

1 SEARCH FOR PRODUCTION OF A HIGGS BOSON AND A SINGLE TOP  
2 QUARK IN MULTILEPTON FINAL STATES IN  $pp$  COLLISIONS AT  $\sqrt{s} = 13$   
3 TeV.

4 by

5 Jose Andres Monroy Montañez

# A DISSERTATION

7 Presented to the Faculty of

8 The Graduate College at the University of Nebraska

In Partial Fulfilment of Requirements

10 For the Degree of Doctor of Philosophy

11 Major: Physics and Astronomy

12 Under the Supervision of Kenneth Bloom and Aaron Dominguez

13 Lincoln, Nebraska

14 July, 2018

15 SEARCH FOR PRODUCTION OF A HIGGS BOSON AND A SINGLE TOP  
16 QUARK IN MULTILEPTON FINAL STATES IN pp COLLISIONS AT  $\sqrt{s} = 13$   
17 TeV.

18 Jose Andres Monroy Montañez, Ph.D.

19 University of Nebraska, 2018

20 Adviser: Kenneth Bloom and Aaron Dominguez

# <sup>21</sup> Table of Contents

<sup>22</sup>	<b>Table of Contents</b>	<b>iii</b>
<sup>23</sup>	<b>List of Figures</b>	<b>vii</b>
<sup>24</sup>	<b>List of Tables</b>	<b>xi</b>
<sup>25</sup>	<b>1 Theoretical approach</b>	<b>1</b>
<sup>26</sup>	1.1 Introduction . . . . .	1
<sup>27</sup>	1.2 Standard model of particle physics . . . . .	2
<sup>28</sup>	1.2.1 Fermions . . . . .	4
<sup>29</sup>	1.2.1.1 Leptons . . . . .	5
<sup>30</sup>	1.2.1.2 Quarks . . . . .	7
<sup>31</sup>	1.2.2 Fundamental interactions . . . . .	11
<sup>32</sup>	1.2.3 Gauge invariance. . . . .	15
<sup>33</sup>	1.2.4 Gauge bosons . . . . .	17
<sup>34</sup>	1.3 Electroweak unification and the Higgs mechanism . . . . .	18
<sup>35</sup>	1.3.1 Spontaneous symmetry breaking (SSB) . . . . .	26
<sup>36</sup>	1.3.2 Higgs mechanism . . . . .	30
<sup>37</sup>	1.3.3 Masses of the gauge bosons . . . . .	33
<sup>38</sup>	1.3.4 Masses of the fermions . . . . .	34

39	1.3.5	The Higgs field . . . . .	35
40	1.3.6	Production of Higgs bosons at LHC . . . . .	36
41	1.3.7	Higgs boson decay channels . . . . .	40
42	1.4	Experimental status of the anomalous Higgs-fermion coupling . . . .	42
43	1.5	Associated production of a Higgs boson and a single top quark . . . .	44
44	1.6	CP-mixing in $tH$ processes . . . . .	49
45	<b>2</b>	<b>The CMS experiment at the LHC</b>	<b>54</b>
46	2.1	Introduction . . . . .	54
47	2.2	The LHC . . . . .	55
48	2.3	The CMS experiment . . . . .	65
49	2.3.1	CMS coordinate system . . . . .	68
50	2.3.2	Tracking system . . . . .	70
51	2.3.3	Silicon strip tracker . . . . .	73
52	2.3.4	Electromagnetic calorimeter . . . . .	74
53	2.3.5	Hadronic calorimeter . . . . .	76
54	2.3.6	Superconducting solenoid magnet . . . . .	77
55	2.3.7	Muon system . . . . .	79
56	2.3.8	CMS trigger system . . . . .	80
57	2.3.9	CMS computing . . . . .	81
58	<b>3</b>	<b>Event generation, simulation and reconstruction</b>	<b>86</b>
59	3.1	Event generation . . . . .	87
60	3.2	Monte Carlo Event Generators. . . . .	90
61	3.3	CMS detector simulation. . . . .	92
62	3.4	Event reconstruction. . . . .	94
63	3.4.1	Particle-Flow Algorithm. . . . .	94

64	3.4.1.1	Missing transverse energy.	108
65	3.4.2	Event reconstruction examples	109
66	<b>5</b>	<b>Statistical methods</b>	<b>112</b>
67	5.1	Multivariate analysis	112
68	5.1.1	Decision trees	116
69	5.1.2	Boosted decision trees (BDT)	119
70	5.1.3	Overtraining	121
71	5.1.4	Variable ranking	122
72	5.1.5	BDT output example	122
73	5.2	Statistical inference	123
74	5.2.1	Nuisance parameters	124
75	5.2.2	Maximum likelihood estimation method	125
76	5.3	Upper limits	126
77	5.4	Asymptotic limits	130
78	<b>6</b>	<b>Search for production of a Higgs boson and a single top quark in multilepton final states in pp collisions at <math>\sqrt{s} = 13</math> TeV</b>	<b>132</b>
80	6.1	Introduction	132
81	6.2	<i>tHq</i> signature	135
82	6.3	Background processes	137
83	6.4	Data and MC Samples	139
84	6.4.1	Full 2016 data set	139
85	6.4.2	Triggers	140
86	6.4.3	Signal modeling and MC samples	143
87	6.5	Object Identification	145
88	6.5.1	Lepton reconstruction and identification	146

89	6.5.2 Lepton selection efficiency . . . . .	152
90	6.5.3 Jets and $b$ -jet tagging . . . . .	156
91	6.5.4 Missing Energy MET . . . . .	157
92	6.6 Event selection . . . . .	158
93	6.7 Background modeling and predictions . . . . .	160
94	6.7.1 Diboson backgrounds . . . . .	160
95	6.8 Signal discrimination . . . . .	166
96	6.8.1 MVA classifiers evaluation . . . . .	166
97	6.8.2 Discriminating variables . . . . .	167
98	6.9 Additional discriminating variables . . . . .	173
99	<b>A Datasets and triggers</b>	<b>180</b>
100	<b>Bibliography</b>	<b>180</b>
101	<b>References</b>	<b>184</b>

# <sup>102</sup> List of Figures

103	1.1	Standard Model of particle physics.	3
104	1.2	Transformations between quarks	11
105	1.3	Fundamental interactions in nature.	12
106	1.4	SM interactions diagrams	13
107	1.5	Neutral current processes	19
108	1.6	Spontaneous symmetry breaking mechanism	27
109	1.7	SSB Potential form	28
110	1.8	Potential for complex scalar field	29
111	1.9	SSB mechanism for complex scalar field	30
112	1.10	Proton-Proton collision	36
113	1.11	Proton PDFs	37
114	1.12	Higgs boson production mechanism Feynman diagrams	38
115	1.13	Higgs boson production cross section and decay branching ratios	39
116	1.14	$\kappa_t$ - $\kappa_V$ plot of the coupling modifiers. ATLAS and CMS combination.	42
117	1.15	Higgs boson production in association with a top quark	45
118	1.16	Cross section for $tHq$ process as a function of $\kappa_t$	48
119	1.17	Cross section for $tHW$ process as a function of $\kappa_{Htt}$	48
120	1.18	NLO cross section for $tX_0$ and $t\bar{t}X_0$ .	52

121	1.19 NLO cross section for $tWX_0, t\bar{t}X_0$ . . . . .	53
122	2.1 CERN accelerator complex . . . . .	55
123	2.2 LHC protons source. First acceleration stage. . . . .	56
124	2.3 The LINAC2 accelerating system at CERN. . . . .	57
125	2.4 LHC layout and RF cavities module. . . . .	58
126	2.5 LHC dipole magnet. . . . .	60
127	2.6 Integrated luminosity delivered by LHC and recorded by CMS during 2016	62
128	2.7 LHC interaction points . . . . .	63
129	2.8 Multiple $pp$ collision bunch crossing at CMS. . . . .	65
130	2.9 Layout of the CMS detector . . . . .	66
131	2.10 CMS detector transverse slice . . . . .	67
132	2.11 CMS detector coordinate system . . . . .	69
133	2.12 CMS tracking system schematic view. . . . .	70
134	2.13 CMS pixel detector . . . . .	71
135	2.14 SST Schematic view. . . . .	73
136	2.15 CMS ECAL schematic view . . . . .	75
137	2.16 CMS HCAL schematic view . . . . .	77
138	2.17 CMS solenoid magnet . . . . .	78
139	2.18 CMS Muon system schematic view . . . . .	79
140	2.19 CMS Level-1 trigger architecture . . . . .	81
141	2.20 WLCG structure . . . . .	82
142	2.21 Data flow from CMS detector through hardware Tiers . . . . .	84
143	3.1 Event generation process. . . . .	87
144	3.2 Particle flow algorithm. . . . .	95
145	3.3 Stable cones identification . . . . .	102

146	3.4	Jet reconstruction.	104
147	3.5	Jet energy corrections.	106
148	3.6	Secondary vertex in a b-hadron decay.	107
149	3.7	HIG-13-004 Event 1 reconstruction.	109
150	3.8	$e\mu$ event reconstruction.	110
151	3.9	Recorded event reconstruction.	111
152	5.1	Scatter plots-MVA event classification.	114
153	5.2	Scalar test statistical.	115
154	5.3	Decision tree.	116
155	5.4	Decision tree output example.	119
156	5.5	BDT output example.	122
157	5.6	$t_r$ p.d.f. assuming each $H_0$ and $H_1$	128
158	5.7	Illustration of the $CL_s$ limit.	129
159	5.8	Example of Brazilian flag plot	130
160	6.1	Analysis strategy workflow	135
161	6.2	$tHq$ event signature	136
162	6.3	$t\bar{t}$ and $t\bar{t}W$ events signature	139
163	6.4	Trigger efficiency for the same-sign $\mu\mu$ category	141
164	6.5	Trigger efficiency for the $e\mu$ category	142
165	6.6	Trigger efficiency for the $3l$ category	143
166	6.7	$tHq$ and $tHW$ cross section in the $\kappa_t$ - $\kappa_V$ phase space	144
167	6.8	Tight vs loose lepton selection efficiencies in the $2lss$ channel.	154
168	6.9	Tight vs loose lepton selection efficiencies in the $3l$ channel.	155
169	6.10	Kinematic distributions in the diboson control region.	162
170	6.11	Input variables to the BDT for signal discrimination normalized.	164

171	6.12 MVA classifiers performance. . . . .	167
172	6.13 BDTG classifier Input variables distributions. . . . .	169
173	6.14 Distributions of input variables to the BDT for signal discrimination, two	
174	lepton same sign channel. . . . .	170
175	6.15 BDTG classifier output. . . . .	171
176	6.16 BDT input variables. Discrimination against $t\bar{t}$ . . . . .	174
177	6.17 BDT input variables. Discrimination against $t\bar{t}V$ . . . . .	175
178	6.18 BDT inputs as seen by TMVA (signal, in blue, is $tHq$ , background, in	
179	red, is $t\bar{t}$ ) for the same sign dilepton channel, discriminated against $t\bar{t}$	
180	background. . . . .	176
181	6.19 BDT inputs as seen by TMVA (signal, in blue, is $tHq$ , background, in red,	
182	is $t\bar{t}W+t\bar{t}Z$ ) for the same sign dilepton channel, discriminated against $t\bar{t}V$	
183	background. . . . .	177
184	6.20 Correlation matrices for the BDT input variables. . . . .	178
185	6.21 Signal and Background correlation matrices for the input variables in the	
186	TMVA analysis for the same sign dilepton channel, for the signal (left), $t\bar{t}$	
187	background (middle), and $t\bar{t}V$ background (right.) . . . . .	178
188	6.22 Additional discriminating variables distributions. . . . .	179

# <sup>189</sup> List of Tables

190	1.1	Fermions of the SM. . . . .	4
191	1.2	Fermion masses. . . . .	5
192	1.3	Lepton properties. . . . .	7
193	1.4	Quark properties. . . . .	8
194	1.5	Fermion weak isospin and weak hypercharge multiplets. . . . .	9
195	1.6	Fundamental interactions features. . . . .	14
196	1.7	SM gauge bosons. . . . .	18
197	1.8	Higgs boson properties. . . . .	36
198	1.9	Predicted branching ratios for a SM Higgs boson with $m_H = 125 \text{ GeV}/c^2$ . . . . .	41
199	1.10	Predicted SM cross sections for $tH$ production at $\sqrt{s} = 13 \text{ TeV}$ . . . . .	46
200	1.11	Predicted enhancement of the $tHq$ and $tHW$ cross sections at LHC . . . . .	49
201	6.1	Trigger efficiency scale factors and associated uncertainties. . . . .	142
202	6.2	MC signal samples. . . . .	144
203	6.3	Effective areas, for electrons and muons. . . . .	150
204	6.4	Requirements on each of the three muon selections. . . . .	152
205	6.5	Criteria for each of the three electron selections. . . . .	153
206	6.6	Summary of event selection. . . . .	158
207	6.7	BDTG input variables. . . . .	168

208	6.8	TMVA input variables ranking for BDTA_GRAD method . . . . .	172
209	6.9	TMVA input variables ranking for BDTA_GRAD method in same-sign	
210		dilepton channel. . . . .	172
211	6.10	TMVA configuration used in the BDT training. . . . .	173
212	6.11	ROC-integral for all the testing cases. . . . .	178
213	A.1	Full 2016 dataset. . . . .	180
214	A.2	HLT . . . . .	181
215	A.3	$\kappa_V$ and $\kappa_t$ combinations. . . . .	182
216	A.4	List of background samples used in this analysis (CMSSW 80X). . . . .	183

# <sup>217</sup> Chapter 1

## <sup>218</sup> Theoretical approach

### <sup>219</sup> 1.1 Introduction

<sup>220</sup> The physical description of the universe is a challenge that physicists have faced by  
<sup>221</sup> making theories that refine existing principles and proposing new ones in an attempt  
<sup>222</sup> to embrace emerging facts and phenomena.

<sup>223</sup> At the end of 1940s Julian Schwinger [1] and Richard P. Feynman [2], based on  
<sup>224</sup> the work of Sin-Itiro Tomonaga [3], developed an electromagnetic theory consistent  
<sup>225</sup> with special relativity and quantum mechanics that describes how matter and light  
<sup>226</sup> interact; the so-called *quantum electrodynamics* (QED) was born.

<sup>227</sup> QED has become the blueprint for developing theories that describe the universe.  
<sup>228</sup> It was the first example of a quantum field theory (QFT), which is the theoretical  
<sup>229</sup> framework for building quantum mechanical models that describes particles and their  
<sup>230</sup> interactions. QFT is composed of a set of mathematical tools that combines classical  
<sup>231</sup> fields, special relativity and quantum mechanics, while keeping the quantum point  
<sup>232</sup> particles and locality ideas.

<sup>233</sup> This chapter gives an overview of the standard model of particle physics, starting

234 with a description of the particles and their interactions, followed by a description of  
 235 the electroweak interaction, the Higgs boson and the associated production of Higgs  
 236 boson and a single top quark ( $tH$ ). The description contained in this chapter is based  
 237 on References [4–6].

## 238 1.2 Standard model of particle physics

239 The *standard model of particle physics (SM)* describes particle physics at the funda-  
 240 mental level in terms of a collection of interacting particles and fields. The full picture  
 241 of the SM is composed of three fields<sup>1</sup> whose excitations are interpreted as particles  
 242 called mediators or force-carriers, a set of fields whose excitations are interpreted as  
 243 elementary particles interacting through the exchange of those mediators, and a field  
 244 that gives the mass to elementary particles. Figure 1.1 shows a scheme of the SM  
 245 particles’ organization. In addition, for each of the particles in the scheme there exists  
 246 an antiparticle with the same mass and opposite quantum numbers. The existence of  
 247 antiparticles is a prediction of the relativistic quantum mechanics from the solution  
 248 of the Dirac equation for which a negative energy solution is also possible. In some  
 249 cases a particle is its own anti-particle, like photon or Higgs boson.

250 The mathematical formulation of the SM is based on group theory and the use of  
 251 Noether’s theorem [8] which states that for a physical system modeled by a Lagrangian  
 252 that is invariant under a group of transformations a conservation law is expected. For  
 253 instance, a system described by a time-independent Lagrangian is invariant (symmet-  
 254 ric) under time changes (transformations) with the total energy conservation law as  
 255 the expected conservation law. In QED, the charge operator ( $Q$ ) is the generator of

---

<sup>1</sup> The formal and complete treatment of the SM is out of the scope of this document, however a plenty of textbooks describing it at several levels are available in the literature. The treatment in References [5, 6] is quite comprehensive and detailed. Note that gravitational field is not included in the standard model formulation

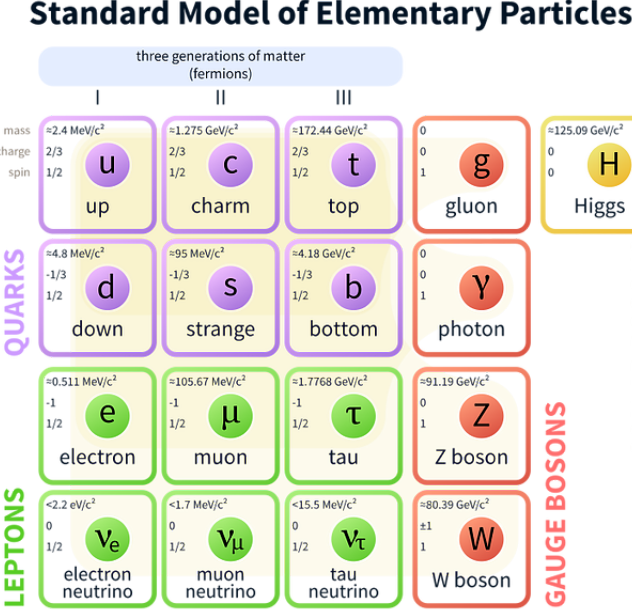


**Figure 1.1:** Schematic representation of the Standard Model of particle physics. The SM is a theoretical model intended to describe three of the four fundamental forces of the universe in terms of a set of particles and their interactions. [7].

256 the U(1) symmetry which according to the Noether's theorem means that there is a  
 257 conserved quantity; this conserved quantity is the electric charge and thus the law  
 258 conservation of electric charge is established.

259 In the SM, the symmetry group  $SU(3)_C \otimes SU(2)_L \otimes U(1)_Y$  describes three of the  
 260 four fundamental interactions in nature (see Section 1.2.2): strong interaction (SI),  
 261 weak interaction (WI) and electromagnetic interactions (EI) in terms of symmetries  
 262 associated to physical quantities:

- 263 • Strong:  $SU(3)_C$  associated to color charge  
 264 • Weak:  $SU(2)_L$  associated to weak isospin and chirality  
 265 • Electromagnetic:  $U(1)_Y$  associated to weak hypercharge and electric charge  
 266 It will be shown that the electromagnetic and weak interactions are combined in

267 the so-called electroweak interaction where chirality, hypercharge, weak isospin and  
 268 electric charge are the central concepts.

269 **1.2.1 Fermions**

270 The basic constituents of the ordinary matter at the lowest level, which form the set  
 271 of elementary particles in the SM formulation, are quarks and leptons. All of them  
 272 have spin 1/2, therefore they are classified as fermions since they obey Fermi-Dirac  
 273 statistics. There are six *flavors* of quarks and three of leptons organized in three  
 274 generations, or families, as shown in Table 1.1.

		Generation		
		1st	2nd	3rd
Leptons	Charged	Electron (e)	Moun( $\mu$ )	Tau ( $\tau$ )
	Neutral	Electron neutrino ( $\nu_e$ )	Muon neutrino ( $\nu_\mu$ )	Tau neutrino ( $\nu_\tau$ )
Quarks	Up-type	Up (u)	Charm (c)	Top (t)
	Down-type	Down (d)	Strange (s)	Bottom (b)

**Table 1.1:** Fermions of the SM. There are six flavors of quarks and three of leptons, organized in three generations, or families, composed of two pairs of closely related particles. The close relationship is motivated by the fact that each pair of particles is a member of an  $SU(2)_L$  doublet that has an associated invariance under isospin transformations. WI between leptons is limited to the members of the same generation; WI between quarks is not limited but greatly favored, to same generation members.

275

276 There is a mass hierarchy between generations (see Table 1.2), where the higher  
 277 generation particles decays to the lower one, which can explain why the ordinary  
 278 matter is made of particles from the first generation. In the SM, neutrinos are modeled  
 279 as massless particles so they are not subject to this mass hierarchy; however, today it  
 280 is known that neutrinos are massive so the hierarchy could be restated. The reason  
 281 behind this mass hierarchy is one of the most important open questions in particle  
 282 physics, and it becomes more puzzling when noticing that the mass difference between

283 first and second generation fermions is small compared to the mass difference with  
 284 respect to the third generation.

Lepton	Mass (MeV/c <sup>2</sup> )	Quark	Mass (MeV/c <sup>2</sup> )
e	0.51	u	2.2
$\mu$	105.65	c	$1.28 \times 10^3$
$\tau$	1776.86	t	$173.1 \times 10^3$
$\nu_e$	Unknown	d	4.7
$\nu_\mu$	Unknown	s	96
$\tau_\mu$	Unknown	b	$4.18 \times 10^3$

**Table 1.2:** Fermion masses [9]. Generations differ by mass in a way that has been interpreted as a mass hierarchy. Approximate values with no uncertainties are used, for comparison purpose.

285

286        Usually, the second and third generation fermions are produced in high energy  
 287 processes, like the ones recreated in particle accelerators.

288 **1.2.1.1 Leptons**

289 A lepton is an elementary particle that is not subject to the SI. As seen in Table 1.1,  
 290 there are two types of leptons, the charged ones (electron, muon and tau) and the  
 291 neutral ones (the three neutrinos). The electric charge (Q) is the property that gives  
 292 leptons the ability to participate in the EI. From the classical point of view, Q plays  
 293 a central role determining, among others, the strength of the electric field through  
 294 which the electromagnetic force is exerted. It is clear that neutrinos are not affected  
 295 by EI because they don't carry electric charge.

296        Another feature of the leptons that is fundamental in the mathematical description  
 297 of the SM is the chirality, which is closely related to spin and helicity. Helicity  
 298 defines the handedness of a particle by relating its spin and momentum such that  
 299 if they are parallel then the particle is right-handed; if spin and momentum are

300 antiparallel the particle is said to be left-handed. The study of parity conservation  
 301 (or violation) in  $\beta$ -decay has shown that only left-handed electrons/neutrinos or right-  
 302 handed positrons/anti-neutrinos are created [10]; the inclusion of that feature in the  
 303 theory was achieved by using projection operators for helicity, however, helicity is  
 304 frame dependent for massive particles which makes it not Lorentz invariant and then  
 305 another related attribute has to be used: *chirality*.

306 Chirality is a purely quantum attribute which makes it not so easy to describe in  
 307 graphical terms but it defines how the wave function of a particle transforms under  
 308 certain rotations. As with helicity, there are two chiral states, left-handed chiral (L)  
 309 and right-handed chiral (R). In the highly relativistic limit where  $E \approx p \gg m$  helicity  
 310 and chirality converge, becoming exactly the same for massless particles.

311 In the following, when referring to left-handed (right-handed) it will mean left-  
 312 handed chiral (right-handed chiral). The fundamental fact about chirality is that  
 313 while EI and SI are not sensitive to chirality, in WI left-handed and right-handed  
 314 fermions are treated asymmetrically, such that only left-handed fermions and right-  
 315 handed anti-fermions are allowed to couple to WI mediators, which is a violation of  
 316 parity. The way to translate this statement in a formal mathematical formulation is  
 317 based on the isospin symmetry group  $SU(2)_L$ .

318 Each generation of leptons is seen as a weak isospin doublet.<sup>2</sup> The left-handed  
 319 charged lepton and its associated left-handed neutrino are arranged in doublets of  
 320 weak isospin  $T=1/2$  while their right-handed partners are singlets:

$$\begin{pmatrix} \nu_l \\ l \end{pmatrix}_L, l_R := \begin{pmatrix} \nu_e \\ e \end{pmatrix}_L, \begin{pmatrix} \nu_\mu \\ \mu \end{pmatrix}_L, \begin{pmatrix} \nu_\tau \\ \tau \end{pmatrix}_L, e_R, \mu_R, \tau_R, \nu_{eR}, \nu_{\mu R}, \nu_{\tau R} \quad (1.1)$$

321 The isospin third component refers to the eigenvalues of the weak isospin operator

---

<sup>2</sup> The weak isospin is an analogy of the isospin symmetry in strong interaction where neutron and proton are affected equally by strong force but differ in their charge.

322 which for doublets is  $T_3 = \pm 1/2$ , while for singlets it is  $T_3 = 0$ . The physical meaning  
 323 of this doublet-singlet arrangement falls in that the WI couples the two particles in  
 324 the doublet by exchanging the interaction mediator while the singlet member is not  
 325 involved in WI. The main properties of the leptons are summarized in Table 1.3.

326 Although all three flavor neutrinos have been observed, their masses remain un-  
 327 known and only some estimations have been made [11]. The main reason is that  
 328 the flavor eigenstates are not the same as the mass eigenstates which implies that  
 329 when a neutrino is created its mass state is a linear combination of the three mass  
 330 eigenstates and experiments can only probe the squared difference of the masses. The  
 331 Pontecorvo-Maki-Nakagawa-Sakata (PMNS) mixing matrix encodes the relationship  
 332 between flavor and mass eigenstates.

Lepton	$Q(e)$	$T_3$	$L_e$	$L_\mu$	$L_\tau$	Lifetime (s)
Electron (e)	-1	-1/2	1	0	0	Stable
Electron neutrino( $\nu_e$ )	0	1/2	1	0	0	Unknown
Muon ( $\mu$ )	-1	-1/2	0	1	0	$2.19 \times 10^{-6}$
Muon neutrino ( $\nu_\mu$ )	0	1/2	0	1	0	Unknown
Tau ( $\tau$ )	-1	-1/2	0	0	1	$290.3 \times 10^{-15}$
Tau neutrino ( $\nu_\tau$ )	0	1/2	0	0	1	Unknown

**Table 1.3:** Lepton properties [9]. Q: electric charge,  $T_3$ : weak isospin. Only left-handed leptons and right-handed anti-leptons participate in the WI. Anti-particles with inverted  $T_3$ , Q and lepton number complete the leptons set but are not listed. Right-handed leptons and left-handed anti-leptons, neither listed, form weak isospin singlets with  $T_3 = 0$  and do not take part in the weak interaction.

333

### 334 1.2.1.2 Quarks

335 Quarks are the basic constituents of protons and neutrons. The way quarks join to  
 336 form bound states, called *hadrons*, is through the SI. Quarks are affected by all the  
 337 fundamental interactions which means that they carry all the four types of charges:  
 338 color, electric charge, weak isospin and mass.

Flavor	$Q(e)$	$I_3$	$T_3$	B	C	S	T	$B'$	Y	Color
Up (u)	2/3	1/2	1/2	1/3	0	0	0	0	1/3	r,b,g
Charm (c)	2/3	0	1/2	1/3	1	0	0	0	4/3	r,b,g
Top(t)	2/3	0	1/2	1/3	0	0	1	0	4/3	r,b,g
Down(d)	-1/3	-1/2	-1/2	1/3	0	0	0	0	1/3	r,b,g
Strange(s)	-1/3	0	-1/2	1/3	0	-1	0	0	-2/3	r,b,g
Bottom(b)	-1/3	0	-1/2	1/3	0	0	0	-1	-2/3	r,b,g

**Table 1.4:** Quark properties [9]. Q: electric charge,  $I_3$ : isospin,  $T_3$ : weak isospin, B: baryon number, C: charmness, S: strangeness, T: topness,  $B'$ : bottomness, Y: hypercharge. Anti-quarks posses the same mass and spin as quarks but all charges (color, flavor numbers) have opposite sign.

339

340     Table 1.4 summarizes the features of quarks, among which the most remarkable  
 341    is their fractional electric charge. Note that fractional charge is not a problem, given  
 342    that quarks are not found isolated, but serves to explain how composed particles are  
 343    formed out of two or more valence quarks<sup>3</sup>.

344     Color charge is responsible for the SI between quarks and is the symmetry ( $SU(3)_C$ )  
 345    that defines the formalism to describe SI. There are three colors: red (r), blue (b)  
 346    and green (g) and their corresponding three anti-colors; thus each quark carries one  
 347    color unit while anti-quarks carries one anti-color unit. As explained in Section 1.2.2,  
 348    quarks are not allowed to be isolated due to the color confinement effect, hence, their  
 349    features have been studied indirectly by observing their bound states created when

- 350       • one quark with a color charge is attracted by an anti-quark with the correspond-  
 351       ing anti-color charge forming a colorless particle called a *meson*.  
  
 352       • three quarks (anti-quarks) with different color (anti-color) charges are attracted  
 353       among them forming a colorless particle called a *baryon (anti-baryon)*.

---

<sup>3</sup> Hadrons can contain an indefinite number of virtual quarks and gluons, known as the quark and gluon sea, but only the valence quarks determine hadrons' quantum numbers.

354        In practice, when a quark is left alone isolated a process called *hadronization* occurs  
 355 where the quark emits gluons (see Section 1.2.4) which eventually will generate new  
 356 quark-antiquark pairs and so on; those quarks will recombine to form hadrons that  
 357 will decay into leptons. This proliferation of particles looks like a *jet* coming from  
 358 the isolated quark. More details about the hadronization process and jet structure  
 359 will be given in chapter3.

360        In the first version of the quark model (1964), M. Gell-Mann [12] and G. Zweig  
 361 [13,14] developed a consistent way to classify hadrons according to their properties.  
 362 Only three quarks (u, d, s) were involved in a scheme in which all baryons have baryon  
 363 number  $B=1$  and therefore quarks have  $B=1/3$ ; non-baryons have  $B=0$ . Baryon  
 364 number is conserved in SI and EI which means that single quarks cannot be created  
 365 but in pairs  $q - \bar{q}$ .

366        The scheme organizes baryons in a two-dimensional space ( $I_3$  - Y); Y (hyper-  
 367 charge) and  $I_3$  (isospin) are quantum numbers related by the Gell-Mann-Nishijima  
 368 formula [15,16]:

$$Q = I_3 + \frac{Y}{2} \quad (1.2)$$

369 where  $Y = B + S + C + T + B'$  are the quantum numbers listed in Table 1.4.

370        There are six quark flavors organized in three generations (see Table 1.1) fol-  
 371 lowing a mass hierarchy which, again, implies that higher generations decay to first  
 372 generation quarks.

	Quarks			$T_3$	$Y_W$	Leptons			$T_3$	$Y_W$
Doublets	$(\frac{u}{d'})_L$	$(\frac{c}{s'})_L$	$(\frac{t}{b'})_L$	$(\frac{1/2}{-1/2})$	$1/3$	$(\nu_e)_L$	$(\nu_\mu)_L$	$(\nu_\tau)_L$	$(\frac{1/2}{-1/2})$	-1
Singlets	$u_R$	$c_R$	$t_R$	0	$4/3$	$\nu_{eR}$	$\nu_{\mu R}$	$\nu_{\tau R}$	0	-2

**Table 1.5:** Fermion weak isospin and weak hypercharge multiplets. Weak hypercharge is calculated through the Gell-Mann-Nishijima formula 1.2 but using the weak isospin and charge for quarks.

373

374 Isospin doublets of quarks are also defined (see Table 1.5), and same as for neutrinos,  
 375 the WI eigenstates are not the same as the mass eigenstates which means that  
 376 members of different quark generations are connected by the WI mediator; thus, up-  
 377 type quarks are coupled not to down-type quarks (the mass eigenstates) directly but  
 378 to a superposition of down-type quarks ( $q'_d$ ; *the weak eigenstates*) via WI according  
 379 to:

380

$$\begin{aligned} q'_d &= V_{CKM} q_d \\ \begin{pmatrix} d' \\ s' \\ b' \end{pmatrix} &= \begin{pmatrix} V_{ud} & V_{us} & V_{ub} \\ V_{cd} & V_{cs} & V_{cb} \\ V_{td} & V_{ts} & V_{tb} \end{pmatrix} \begin{pmatrix} d \\ s \\ b \end{pmatrix} \end{aligned} \quad (1.3)$$

381 where  $V_{CKM}$  is known as Cabibbo-Kobayashi-Maskawa (CKM) mixing matrix [17,18]  
 382 given by

$$\begin{pmatrix} |V_{ud}| & |V_{us}| & |V_{ub}| \\ |V_{cd}| & |V_{cs}| & |V_{cb}| \\ |V_{td}| & |V_{ts}| & |V_{tb}| \end{pmatrix} = \begin{pmatrix} 0.97427 \pm 0.00015 & 0.22534 \pm 0.00065 & 0.00351^{+0.00015}_{-0.00014} \\ 0.22520 \pm 0.00065 & 0.97344 \pm 0.00016 & 0.0412^{+0.0011}_{-0.0005} \\ 0.00867^{+0.00029}_{-0.00031} & 0.0404^{+0.0011}_{-0.0005} & 0.999146^{+0.000021}_{-0.000046} \end{pmatrix}. \quad (1.4)$$

383 The weak decays of quarks are represented in the diagram of Figure 1.2; again  
 384 the CKM matrix plays a central role since it contains the probabilities for the differ-  
 385 ent quark decay channels, in particular, note that quark decays are greatly favored  
 386 between generation members.

387 CKM matrix is a  $3 \times 3$  unitary matrix parametrized by three mixing angles and  
 388 the *CP-mixing phase*; the latter is the parameter responsible for the Charge-Parity

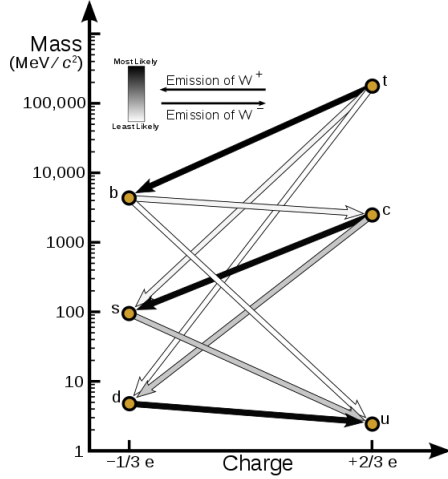


**Figure 1.2:** Transformations between quarks through the exchange of a WI. Higher generations quarks decay to first generation quarks by emitting a W boson. The arrow color indicates the likelihood of the transition according to the grey scale in the top left side which represent the CKM matrix parameters [19].

389 symmetry violation (CP-violation) in the SM. The fact that the top quark decays  
 390 almost all the time to a bottom quark is exploited in this thesis when making the  
 391 selection of the signal events by requiring the presence of a jet tagged as a jet coming  
 392 from a  $b$  quark in the final state.

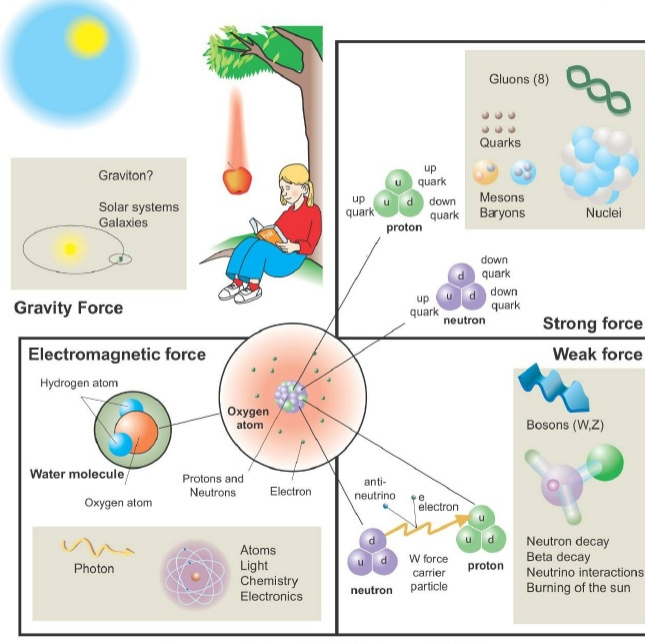
### 393 1.2.2 Fundamental interactions

394 Even though there are many manifestations of force in nature, like the ones repre-  
 395 sented in Figure 1.3, we can classify all of them in four fundamental interactions:

- 396     • *Electromagnetic interaction (EI)* affects particles that are *electrically charged*,  
 397       like electrons and protons. Figure 1.4a. shows a graphical representation, known  
 398       as *Feynman diagram*, of electron-electron scattering.
- 399     • *Strong interaction (SI)* described by Quantum Chromodynamics (QCD). Hadrons  
 400       like the proton and the neutron have internal structure given that they are com-

## Fundamental interactions.

Illustration: Typoform



Summer School KPI 15 August 2009

**Figure 1.3:** Fundamental interactions in nature. Despite the many manifestations of forces in nature, we can track all of them back to one of the fundamental interactions. The most common forces are gravity and electromagnetic given that all of us are subject and experience them in everyday life.

401 posed of two or more valence quarks<sup>4</sup>. Quarks have fractional electric charge  
 402 which means that they are subject to electromagnetic interaction and in the case  
 403 of the proton they should break apart due to electrostatic repulsion; however,  
 404 quarks are held together inside the hadrons against their electrostatic repulsion  
 405 by the *Strong Force* through the exchange of *gluons*. The analog to the electric  
 406 charge is the *color charge*. Electrons and photons are elementary particles as  
 407 quarks but they don't carry color charge, therefore they are not subject to SI. A  
 408 Feynman diagram for gluon exchange between quarks is shown in Figure 1.4b.  
 409 • *Weak interaction (WI)* described by the weak theory (WT), is responsible, for  
 410 instance, for the radioactive decay in atoms and the deuterium production

<sup>4</sup> Particles made of four and five quarks are exotic states not so common.

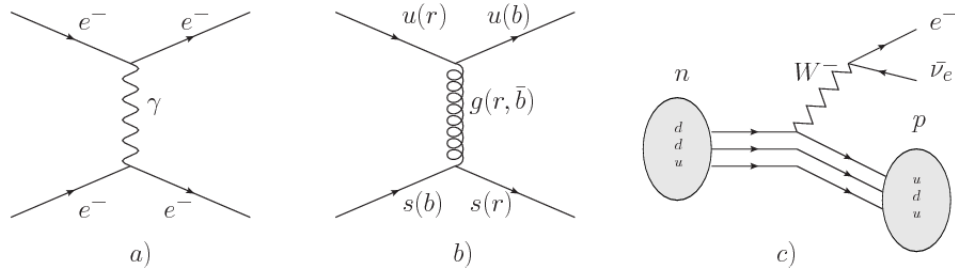


**Figure 1.4:** Feynman diagrams representing the interactions in SM; a) EI:  $e$ - $e$  scattering; b) SI: gluon exchange between quarks ; c) WI:  $\beta$ -decay

within the sun. Quarks and leptons are the particles affected by the weak interaction; they possess a property called *flavor charge* (see 1.2.1) which can be changed by emitting or absorbing one weak force mediator. There are three mediators of the *weak force* known as  $Z$  boson in the case of electrically neutral flavor changes and  $W^\pm$  bosons in the case of electrically charged flavor changes. The *weak isospin* is the WI analog to electric charge in EI, and color charge in SI, and defines how quarks and leptons are affected by the weak force. Figure 1.4c. shows the Feynman diagram of  $\beta$ -decay where a neutron ( $n$ ) is transformed in a proton ( $p$ ) by emitting a  $W^-$  particle.

- *Gravitational interaction (GI)* described by General Theory of Relativity (GR). It is responsible for the structure of galaxies and black holes as well as the expansion of the universe. As a classical theory, in the sense that it can be formulated without even appeal to the concept of quantization, it implies that the space-time is a continuum and predictions can be made without limitation to the precision of the measurement tools. The latter represents a direct contradiction of the quantum mechanics principles. Gravity is deterministic while quantum mechanics is probabilistic; despite that, efforts to develop a quantum theory of gravity have predicted the *graviton* as mediator of the gravitational

429 force<sup>5</sup>.

Interaction	Acts on	Relative strength	Range (m)	Mediators
Electromagnetic (QED)	Electrically charged particles	$10^{-2}$	Infinite	Photon
Strong (QCD)	Quarks and gluons	1	$10^{-15}$	Gluon
Weak (WI)	Leptons and quarks	$10^{-6}$	$10^{-18}$	$W^\pm, Z$
Gravitational (GI)	Massive particles	$10^{-39}$	Infinite	Graviton

Table 1.6: Fundamental interactions features [20].

430

431 Table 1.6 summarizes the main features of the fundamental interactions. The  
 432 strength of the interactions is represented by the coupling constants which depend  
 433 on the energy scale at which the interaction is evaluated, therefore, it is the relative  
 434 strength of the fundamental forces that reveals the meaning of strong and weak; in  
 435 a context where the relative strength of the SI is 1, the EI is about hundred times  
 436 weaker and WI is about million times weaker than the SI. A good description on how  
 437 the relative strength and range of the fundamental interactions are calculated can  
 438 be found in References [20, 21]. In the everyday life, only EI and GI are explicitly  
 439 experienced due to the range of these interactions; i.e., at the human scale distances  
 440 only EI and GI have appreciable effects, in contrast to SI which at distances greater  
 441 than  $10^{-15}$ m become negligible. Is it important to clarify that the weakness of the  
 442 WI is attributed to the fact that its mediators are highly massive which affects the  
 443 propagators of the interaction, as a result, the effect of the coupling constant is  
 444 reduced.

---

<sup>5</sup> Actually a wide variety of theories have been developed in an attempt to describe gravity; some famous examples are string theory and supergravity.

445 **1.2.3 Gauge invariance.**

446 QED was built successfully on the basis of the classical electrodynamics theory (CED)  
 447 of Maxwell and Lorentz, following theoretical and experimental requirements imposed  
 448 by

- 449     • Lorentz invariance: independence on the reference frame.
- 450     • Locality: interacting fields are evaluated at the same space-time point to avoid  
     451       action at a distance.
- 452     • Renormalizability: physical predictions are finite and well defined.
- 453     • Particle spectrum, symmetries and conservation laws already known must emerge  
     454       from the theory.
- 455     • Local gauge invariance.

456     The gauge invariance requirement reflects the fact that the fundamental fields  
 457     cannot be directly measured but associated fields which are the observables. Electric  
 458     (**E**) and magnetic (**B**) fields in CED are associated with the electric scalar potential  
 459      $V$  and the vector potential **A**. In particular, **E** can be obtained by measuring the  
 460     change in the space of the scalar potential ( $\Delta V$ ); however, two scalar potentials  
 461     differing by a constant  $f$  correspond to the same electric field. The same happens  
 462     in the case of the vector potential **A**; thus, different configurations of the associated  
 463     fields result in the same set of values of the observables. The freedom in choosing one  
 464     particular configuration is known as *gauge freedom*; the transformation law connecting  
 465     two configurations is known as *gauge transformation* and the fact that the observables  
 466     are not affected by a gauge transformation is called *gauge invariance*.

467     When the gauge transformation:

$$\begin{aligned} \mathbf{A} &\rightarrow \mathbf{A} - \Delta f \\ V &\rightarrow V - \frac{\partial f}{\partial t} \end{aligned} \tag{1.5}$$

468 is applied to Maxwell equations, they are still satisfied and the fields remain invariant.  
 469 Thus, CED is invariant under gauge transformations and is called a *gauge theory*.  
 470 The set of all gauge transformations form the *symmetry group* of the theory, which  
 471 according to the group theory, has a set of *group generators*. The number of group  
 472 generators determine the number of *gauge fields* of the theory.

473 As mentioned in the first lines of Section 1.2, QED has one symmetry group ( $U(1)$ )  
 474 with one group generator (the  $Q$  operator) and one gauge field (the electromagnetic  
 475 field  $A^\mu$ ). In CED there is not a clear definition, beyond the historical convention,  
 476 of which fields are the fundamental and which are the associated, but in QED the  
 477 fundamental field is  $A^\mu$ . When a gauge theory is quantized, the gauge fields are  
 478 quantized and their quanta are called *gauge bosons*. The word boson characterizes  
 479 particles with integer spin which obey Bose-Einstein statistics.

480 As will be detailed in Section 1.3, interactions between particles in a system can  
 481 be obtained by considering first the Lagrangian density of free particles in the sys-  
 482 tem, which of course is incomplete because the interaction terms have been left out,  
 483 and demanding global phase transformation invariance. Global phase transforma-  
 484 tion means that a gauge transformation is performed identically to every point  
 485 in the space<sup>6</sup> and the Lagrangian remains invariant. Then, the global transforma-  
 486 tion is promoted to a local phase transformation (this time the gauge transforma-  
 487 tion depends on the position in space) and again invariance is required.

---

<sup>6</sup> Here space corresponds to the 4-dimensional space i.e. space-time.

488 Due to the space dependence of the local transformation, the Lagrangian density is  
 489 not invariant anymore. In order to reinstate the gauge invariance, the gauge covariant  
 490 derivative is introduced in the Lagrangian and with it the gauge field responsible for  
 491 the interaction between particles in the system. The new Lagrangian density is gauge  
 492 invariant, includes the interaction terms needed to account for the interactions and  
 493 provides a way to explain the interaction between particles through the exchange of  
 494 the gauge boson.

495 This recipe was used to build QED and the theories that aim to explain the  
 496 fundamental interactions.

#### 497 1.2.4 Gauge bosons

498 The importance of the gauge bosons comes from the fact that they are the force  
 499 mediators or force carriers. The features of the gauge bosons reflect those of the fields  
 500 they represent and they are extracted from the Lagrangian density used to describe  
 501 the interactions. In Section 1.3, it will be shown how the gauge bosons of the EI and  
 502 WI emerge from the electroweak Lagrangian. The SI gauge bosons features are also  
 503 extracted from the SI Lagrangian but it is not detailed in this document. The main  
 504 features of the SM gauge bosons will be briefly presented below and summarized in  
 505 Table 1.7.

- 506 • **Photon.** EI occurs when the photon couples to (is exchanged between) parti-  
 507 cles carrying electric charge; however, The photon itself does not carry electric  
 508 charge, therefore, there is no coupling between photons. Given that the photon  
 509 is massless the EI is of infinite range, i.e., electrically charged particles interact  
 510 even if they are located far away one from each other; this also implies that  
 511 photons always move with the speed of light.

- 512     • **Gluon.** SI is mediated by gluons which just as photons are massless. They  
 513       carry one unit of color charge and one unit of anticolor charge, hence, gluons  
 514       can couple to other gluons. As a result, the range of the SI is not infinite  
 515       but very short due to the attraction between gluons, giving rise to the *color*  
 516       *confinement* which explains why color charged particles cannot be isolated but  
 517       live within composite particles, like quarks inside protons.
- 518     • **W, Z.**  $W^\pm$  and Z, are massive which explains their short-range. Given that  
 519       the WI is the only interaction that can change the flavor of the interacting  
 520       particles, the W boson is the responsible for the nuclear transmutation where  
 521       a neutron is converted into a proton or vice versa with the involvement of an  
 522       electron and a neutrino (see Figure 1.4c). The Z boson is the responsible for the  
 523       neutral weak processes like neutrino elastic scattering where no electric charge  
 524       but momentum transference is involved. WI gauge bosons carry isospin charge  
 525       which makes interaction between them possible.

Interaction	Mediator	Electric charge (e)	Color charge	Weak Isospin	mass (GeV/c <sup>2</sup> )
Electromagnetic	Photon ( $\gamma$ )	0	No	0	0
Strong	Gluon (g)	0	Yes -octet	No	0
Weak	$W^\pm$	$\pm 1$	No	$\pm 1$	$80.385 \pm 0.015$
	Z	0	No	0	$91.188 \pm 0.002$

**Table 1.7:** SM gauge bosons main features [9].

526

### 527    1.3 Electroweak unification and the Higgs 528       mechanism

529    Physicists dream of building a theory that contains all the interactions in one single  
 530       interaction, i.e., showing that at some scale in energy all the four fundamental inter-

actions are unified and only one interaction emerges in a *Theory of everything*. The first sign of the feasibility of such unification came from success in the construction of the CED. Einstein spent years trying to reach that full unification, which by 1920 only involved electromagnetism and gravity, with no success; however, a new partial unification was achieved in the 1960's, when S.Glashow [22], A.Salam [23] and S.Weinberg [24] independently proposed that electromagnetic and weak interactions are two manifestations of a more general interaction called *electroweak interaction* (EWI). EWI was developed by following the useful prescription provided by QED and the gauge invariance principles.

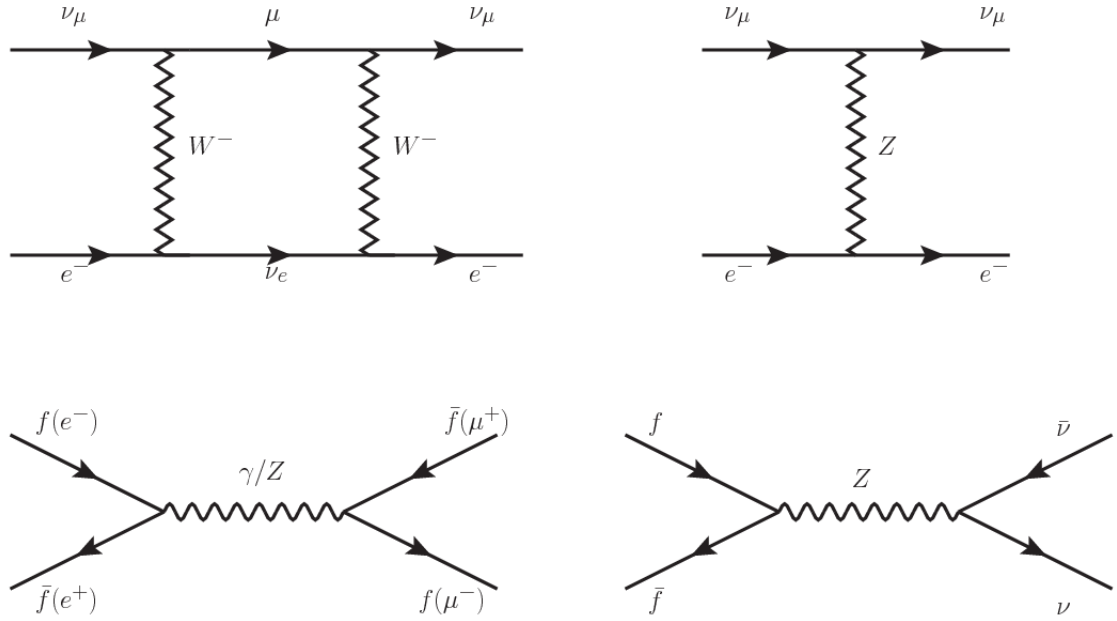


**Figure 1.5:** Top:  $\nu_\mu - e^-$  scattering going through charged currents (left) and neutral currents (right). Bottom: neutral current processes for charged fermions (left) and involving neutrinos (right). While neutral current processes involving only charged fermions can proceed through EI or WI, those involving neutrinos can only proceed via WI.

The *classic* weak theory developed by Fermi, did not have the concept of the W boson but instead it was treated as a point interaction with the dimensionful constant  $G_F$  associated with it. It works really well at low energies very far off the W mass

543 shell. When going up in energy, the theory of weak interactions involving the W  
 544 boson is capable of explaining the  $\beta$ -decay and in general the processes mediated by  
 545  $W^\pm$  bosons. However, there were some processes like the  $\nu_\mu - e$  scattering which  
 546 would require the exchange of two W bosons (see Figure 1.5 top diagrams) giving  
 547 rise to divergent loop integrals and then non-finite predictions. The EWI theory, by  
 548 including neutral currents involving fermions via the exchange of a neutral bosons Z,  
 549 overcomes those divergences and the predictions become realistic.

550 Neutral weak interaction vertices conserve flavor in the same way as the electro-  
 551 magnetic vertices do, but additionally, the Z boson can couple to neutrinos which  
 552 implies that processes involving charged fermions can proceed through EI or WI but  
 553 processes involving neutrinos can proceed only through WI.

554 The prescription to build a gauge theory of the WI consists of proposing a free  
 555 field Lagrangian density that includes the particles involved; next, by requesting  
 556 invariance under global phase transformations first and generalizing to local phase  
 557 transformations invariance later, the conserved currents are identified and interactions  
 558 are generated by introducing gauge fields. Given that the goal is to include the EI  
 559 and WI in a single theory, the group symmetry considered should be a combination of  
 560  $SU(2)_L$  and  $U(1)_{em}$ , however the latter cannot be used directly because the EI treats  
 561 left and right-handed particles indistinctly in contrast to the former. Fortunately, the  
 562 weak hypercharge, which is a combination of the weak isospin and the electric charge  
 563 (Eqn. 1.2) is suitable to be used since it is conserved by the EI and WI. Thus, the  
 564 symmetry group to be considered is

$$G \equiv SU(2)_L \otimes U(1)_Y \quad (1.6)$$

565 The following treatment applies to any of the fermion generations, but for sim-

566 plicity the first generation of leptons will be considered [5, 6, 25, 26].

567 Given the first generation of leptons

$$\psi_1 = \begin{pmatrix} \nu_e \\ e^- \end{pmatrix}_L, \quad \psi_2 = \nu_{eR}, \quad \psi_3 = e_R^- \quad (1.7)$$

568 the charged fermionic currents are given by

$$J_\mu \equiv J_\mu^+ = \bar{\nu}_{eL} \gamma_\mu e_L, \quad J_\mu^\dagger \equiv J_\mu^- = \bar{e}_L \gamma_\mu \nu_{eL} \quad (1.8)$$

569 and the free Lagrangian is given by

$$\mathcal{L}_0 = \sum_{j=1}^3 i\bar{\psi}_j(x) \gamma^\mu \partial_\mu \psi_j(x). \quad (1.9)$$

570 Mass terms are included directly in the QED free Lagrangians since they preserve  
 571 the invariance under the symmetry transformations involved which treat left and right  
 572 handed particles similarly, however mass terms of the form

$$m_W^2 W_\mu^\dagger(x) W^\mu(x) + \frac{1}{2} m_Z^2 Z_\mu(x) Z^\mu(x) - m_e \bar{\psi}_e(x) \psi_e(x) \quad (1.10)$$

573 which represent the mass of  $W^\pm$ , Z and electrons, are not invariant under G trans-  
 574 formations, therefore the gauge fields described by the EWI are in principle massless.

575 Experiments have shown that the EWI gauge fields are not massless [27–30];  
 576 however, they have to acquire mass through a mechanism compatible with the gauge  
 577 invariance; that mechanism is known as the *Higgs mechanism* and will be considered  
 578 later in this Section. The global transformations in the combined symmetry group G  
 579 can be written as

$$\begin{aligned}
\psi_1(x) &\xrightarrow{G} \psi'_1(x) \equiv U_Y U_L \psi_1(x), \\
\psi_2(x) &\xrightarrow{G} \psi'_2(x) \equiv U_Y \psi_2(x), \\
\psi_3(x) &\xrightarrow{G} \psi'_3(x) \equiv U_Y \psi_3(x)
\end{aligned} \tag{1.11}$$

580 where  $U_L$  represent the  $SU(2)_L$  transformation acting only on the weak isospin dou-  
 581 blet and  $U_Y$  represent the  $U(1)_Y$  transformation acting on all the weak isospin mul-  
 582 tiplets. Explicitly

$$U_L \equiv \exp\left(i \frac{\sigma_i}{2} \alpha^i\right), \quad U_Y \equiv \exp(i y_i \beta) \quad (i = 1, 2, 3) \tag{1.12}$$

583 with  $\sigma_i$  the Pauli matrices and  $y_i$  the weak hypercharges. In order to promote the  
 584 transformations from global to local while keeping the invariance, it is required that  
 585  $\alpha^i = \alpha^i(x)$ ,  $\beta = \beta(x)$  and the replacement of the ordinary derivatives by the covariant  
 586 derivatives

$$\begin{aligned}
D_\mu \psi_1(x) &\equiv \left[ \partial_\mu + ig\sigma_i W_\mu^i(x)/2 + ig'y_1 B_\mu(x) \right] \psi_1(x) \\
D_\mu \psi_2(x) &\equiv \left[ \partial_\mu + ig'y_2 B_\mu(x) \right] \psi_2(x) \\
D_\mu \psi_3(x) &\equiv \left[ \partial_\mu + ig'y_3 B_\mu(x) \right] \psi_3(x)
\end{aligned} \tag{1.13}$$

587 introducing in this way four gauge fields,  $W_\mu^i(x)$  and  $B_\mu(x)$ , in the process. The  
 588 covariant derivatives (Eqn. 1.13) are required to transform in the same way as fermion  
 589 fields  $\psi_i(x)$  themselves, therefore, the gauge fields transform as:

$$\begin{aligned} B_\mu(x) &\xrightarrow{G} B'_\mu(x) \equiv B_\mu(x) - \frac{1}{g'} \partial_\mu \beta(x) \\ W_\mu^i(x) &\xrightarrow{G} W_\mu^{i\prime}(x) \equiv W_\mu^i(x) - \frac{i}{g} \partial_\mu \alpha_i(x) - \varepsilon_{ijk} \alpha_i(x) W_\mu^j(x). \end{aligned} \quad (1.14)$$

590 The G invariant version of the Lagrangian density 1.9 can be written as

$$\mathcal{L}_0 = \sum_{j=1}^3 i \bar{\psi}_j(x) \gamma^\mu D_\mu \psi_j(x) \quad (1.15)$$

591 where free massless fermion and gauge fields and fermion-gauge boson interactions  
 592 are included. The EWI Lagrangian density must additionally include kinetic terms  
 593 for the gauge fields ( $\mathcal{L}_G$ ) which are built from the field strengths, according to

$$B_{\mu\nu}(x) \equiv \partial_\mu B_\nu - \partial_\nu B_\mu \quad (1.16)$$

$$W_{\mu\nu}^i(x) \equiv \partial_\mu W_\nu^i(x) - \partial_\nu W_\mu^i(x) - g \varepsilon^{ijk} W_\mu^j W_\nu^k \quad (1.17)$$

594 the last term in Eqn. 1.17 is added in order to hold the gauge invariance; therefore,

$$\mathcal{L}_G = -\frac{1}{4} B_{\mu\nu}(x) B^{\mu\nu}(x) - \frac{1}{4} W_{\mu\nu}^i(x) W_i^{\mu\nu}(x) \quad (1.18)$$

595 which contains not only the free gauge fields contributions, but also the gauge fields  
 596 self-interactions and interactions among them.

597 The three weak isospin conserved currents resulting from the  $SU(2)_L$  symmetry  
 598 are given by

$$J_\mu^i(x) = \frac{1}{2} \bar{\psi}_1(x) \gamma_\mu \sigma^i \psi_1(x) \quad (1.19)$$

599 while the weak hypercharge conserved current resulting from the  $U(1)_Y$  symmetry is  
 600 given by

$$J_\mu^Y = \sum_{j=1}^3 \bar{\psi}_j(x) \gamma_\mu y_j \psi_j(x) \quad (1.20)$$

601 In order to evaluate the electroweak interactions modeled by an isos triplet field  
 602  $W_\mu^i$  that couples to isospin currents  $J_\mu^i$  with strength  $g$  and additionally the singlet  
 603 field  $B_\mu$  which couples to the weak hypercharge current  $J_\mu^Y$  with strength  $g'/2$ . The  
 604 interaction Lagrangian density to be considered is

$$\mathcal{L}_I = -g J^{i\mu}(x) W_\mu^i(x) - \frac{g'}{2} J^{Y\mu}(x) B_\mu(x) \quad (1.21)$$

605 Note that the weak isospin currents are not the same as the charged fermionic cur-  
 606 rents that were used to describe the WI (Eqn. 1.8), since the weak isospin eigenstates  
 607 are not the same as the mass eigenstates, but they are closely related

$$J_\mu = \frac{1}{2}(J_\mu^1 + iJ_\mu^2), \quad J_\mu^\dagger = \frac{1}{2}(J_\mu^1 - iJ_\mu^2). \quad (1.22)$$

608 The same happens with the gauge fields  $W_\mu^i$  which are related to the mass eigen-  
 609 states  $W^\pm$  by

$$W_\mu^+ = \frac{1}{\sqrt{2}}(W_\mu^1 - iW_\mu^2), \quad W_\mu^- = \frac{1}{\sqrt{2}}(W_\mu^1 + iW_\mu^2). \quad (1.23)$$

610 The fact that there are three weak isospin conserved currents is an indication that  
 611 in addition to the charged fermionic currents, which couple charged to neutral leptons,  
 612 there should be a neutral fermionic current that does not involve electric charge  
 613 exchange; therefore, it couples neutral fermions or fermions of the same electric charge.  
 614 The third weak isospin current contains a term that is similar to the electromagnetic

615 current ( $j_\mu^{em}$ ), indicating that there is a relation between them and resembling the  
 616 Gell-Mann-Nishijima formula 1.2 adapted to electroweak interactions

$$Q = T_3 + \frac{Y_W}{2}. \quad (1.24)$$

617 Just as  $Q$  generates the  $U(1)_{em}$  symmetry, the weak hypercharge generates the  
 618  $U(1)_Y$  symmetry as said before. It is possible to write the relationship in terms of  
 619 the currents as

$$j_\mu^{em} = J_\mu^3 + \frac{1}{2} J_\mu^Y. \quad (1.25)$$

620 The neutral gauge fields  $W_\mu^3$  and  $B_\mu$  cannot be directly identified with the  $Z$   
 621 and the photon fields since the photon interacts similarly with left and right-handed  
 622 fermions; however, they are related through a linear combination given by

$$\begin{aligned} A_\mu &= B_\mu \cos \theta_W + W_\mu^3 \sin \theta_W \\ Z_\mu &= -B_\mu \sin \theta_W + W_\mu^3 \cos \theta_W \end{aligned} \quad (1.26)$$

where  $\theta_W$  is known as the *Weinberg angle*. The interaction Lagrangian is now given by

$$\begin{aligned} \mathcal{L}_I = -\frac{g}{\sqrt{2}}(J^\mu W_\mu^+ + J^{\mu\dagger} W_\mu^-) - &\left(g \sin \theta_W J_\mu^3 + g' \cos \theta_W \frac{J_\mu^Y}{2}\right) A^\mu \\ &- \left(g \cos \theta_W J_\mu^3 - g' \sin \theta_W \frac{J_\mu^Y}{2}\right) Z^\mu \end{aligned} \quad (1.27)$$

623 the first term is the weak charged current interaction, while the second term is the

624 electromagnetic interaction under the condition

$$g \sin \theta_W = g' \cos \theta_W = e, \quad \frac{g'}{g} = \tan \theta_W \quad (1.28)$$

625 contained in the Eqn.1.25; the third term is the neutral weak current.

626

627 Note that the neutral fields transformation given by the Eqn. 1.26 can be written  
 628 in terms of the coupling constants  $g$  and  $g'$  as:

$$A_\mu = \frac{g' W_\mu^3 + g B_\mu}{\sqrt{g^2 + g'^2}}, \quad Z_\mu = \frac{g W_\mu^3 - g' B_\mu}{\sqrt{g^2 + g'^2}}. \quad (1.29)$$

629 So far, the Lagrangian density describing the non-massive EWI is:

$$\mathcal{L}_{nmEWI} = \mathcal{L}_0 + \mathcal{L}_G \quad (1.30)$$

630 where fermion and gauge fields have been considered massless because their regular  
 631 mass terms are manifestly non invariant under  $G$  transformations; therefore, masses  
 632 have to be generated in a gauge invariant way. The mechanism by which this goal is  
 633 achieved is known as the *Higgs mechanism* and is closely connected to the concept of  
 634 *spontaneous symmetry breaking*.

### 635 1.3.1 Spontaneous symmetry breaking (SSB)

636 Figure 1.6 left shows a steel nail (top) which is subject to an external force; the form  
 637 of the potential energy is also shown (bottom).

638 Before reaching the critical force value, the system has rotational symmetry with  
 639 respect to the nail axis; however, after the critical force value is reached the nail buck-

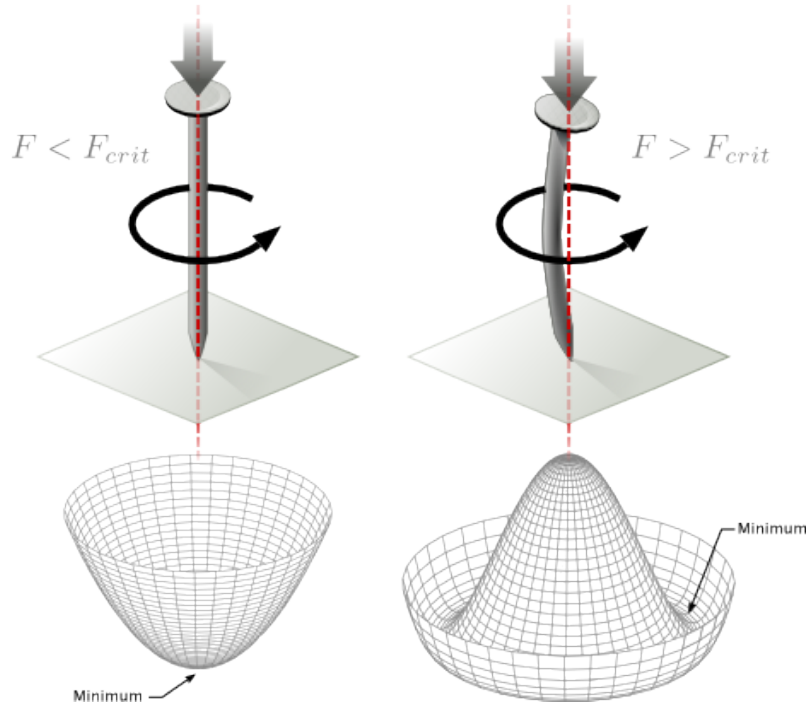


**Figure 1.6:** Spontaneous symmetry breaking mechanism. The steel nail, subject to an external force (top left), has rotational symmetry with respect to its axis. When the external force overcomes a critical value the nail buckles (top right) choosing a minimal energy state (ground state) and thus *breaking spontaneously the rotational symmetry*. The potential energy (bottom) changes but holds the rotational symmetry; however, an infinite number of asymmetric ground states are generated and circularly distributed in the bottom of the potential [31].

640 les (top right). The form of the potential energy (bottom right) changes appearing a  
 641 set of infinity minima but preserving its rotational symmetry. Right before the nail  
 642 buckles there is no indication of the direction the nail will bend because any of the  
 643 directions are equivalent, but once the nail bends, choosing a direction, an arbitrary  
 644 minimal energy state (ground state) is selected and it does not share the system's  
 645 rotational symmetry. This mechanism for reaching an asymmetric ground state is  
 646 known as *spontaneous symmetry breaking*.

647 The lesson from this analysis is that the way to introduce the SSB mechanism  
 648 into a system is by adding the appropriate potential to it.

649 Figure 1.7 shows a plot of the potential  $V(\phi)$  in the case of a scalar field  $\phi$

$$V(\phi) = \mu^2 \phi^\dagger \phi + \lambda (\phi^\dagger \phi)^2 \quad (1.31)$$

650     If  $\mu^2 > 0$  the potential has only one minimum at  $\phi = 0$  and describes a scalar field  
 651    with mass  $\mu$ . If  $\mu^2 < 0$  the potential has a local maximum at  $\phi = 0$  and two minima  
 652    at  $\phi = \pm\sqrt{-\mu^2/\lambda}$  which enables the SSB mechanism to work.

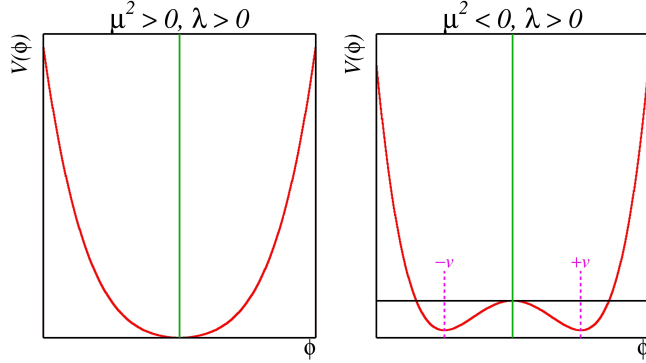


**Figure 1.7:** Shape of the potential  $V(\phi)$  for  $\lambda > 0$  and:  $\mu^2 > 0$  (left) and  $\mu^2 < 0$  (right). The case  $\mu^2 < 0$  corresponds to the potential suitable for introducing the SSB mechanism by choosing one of the two ground states which are connected via reflection symmetry. [31].

653     In the case of a complex scalar field  $\phi(x)$

$$\phi(x) = \frac{1}{\sqrt{2}}(\phi_1 + i\phi_2) \quad (1.32)$$

654    the Lagrangian (invariant under global  $U(1)$  transformations) is given by

$$\mathcal{L} = (\partial_\mu \phi)^\dagger (\partial^\mu \phi) - V(\phi), \quad V(\phi) = \mu^2 \phi^\dagger \phi + \lambda (\phi^\dagger \phi)^2 \quad (1.33)$$

655    where an appropriate potential has been added in order to introduce the SSB.

656     As seen in Figure 1.8, the potential has now an infinite number of minima circularly  
 657    distributed along the  $\xi$ -direction which makes possible the occurrence of the SSB by  
 658    choosing an arbitrary ground state; for instance,  $\xi = 0$ , i.e.  $\phi_1 = v, \phi_2 = 0$

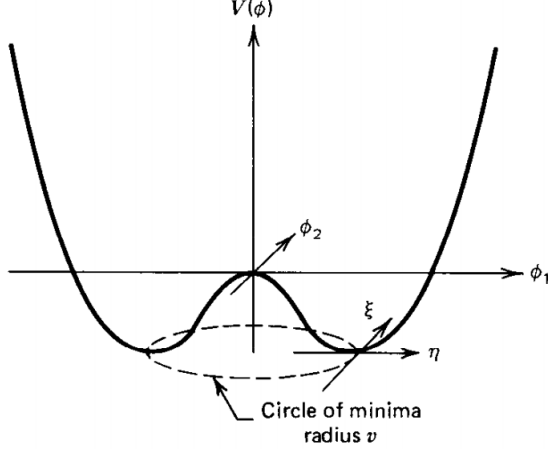


**Figure 1.8:** Potential for complex scalar field. There is a circle of minima of radius  $v$  along the  $\xi$ -direction [6].

$$\phi_0 = \frac{v}{\sqrt{2}} \exp(i\xi) \xrightarrow{\text{SSB}} \phi_0 = \frac{v}{\sqrt{2}} \quad (1.34)$$

659 As usual, excitations over the ground state are studied by making an expansion  
 660 about it; thus, the excitations can be parametrized as:

$$\phi(x) = \frac{1}{\sqrt{2}}(v + \eta(x) + i\xi(x)) \quad (1.35)$$

661 which when substituted into Eqn. 1.33 produces a Lagrangian in terms of the new  
 662 fields  $\eta$  and  $\xi$

$$\mathcal{L}' = \frac{1}{2}(\partial_\mu \xi)^2 + \frac{1}{2}(\partial_\mu \eta)^2 + \mu^2 \eta^2 - V(\phi_0) - \lambda v \eta (\eta^2 + \xi^2) - \frac{\lambda}{4}(\eta^2 + \xi^2)^2 \quad (1.36)$$

663 where the last two terms represent the interactions and self-interaction between the  
 664 two fields  $\eta$  and  $\xi$ . The particular feature of the SSB mechanism is revealed when  
 665 looking to the first three terms of  $\mathcal{L}'$ . Before the SSB, only the massless  $\phi$  field is

666 present in the system; after the SSB there are two fields of which the  $\eta$ -field has  
 667 acquired mass  $m_\eta = \sqrt{-2\mu^2}$  while the  $\xi$ -field is still massless (see Figure 1.9).

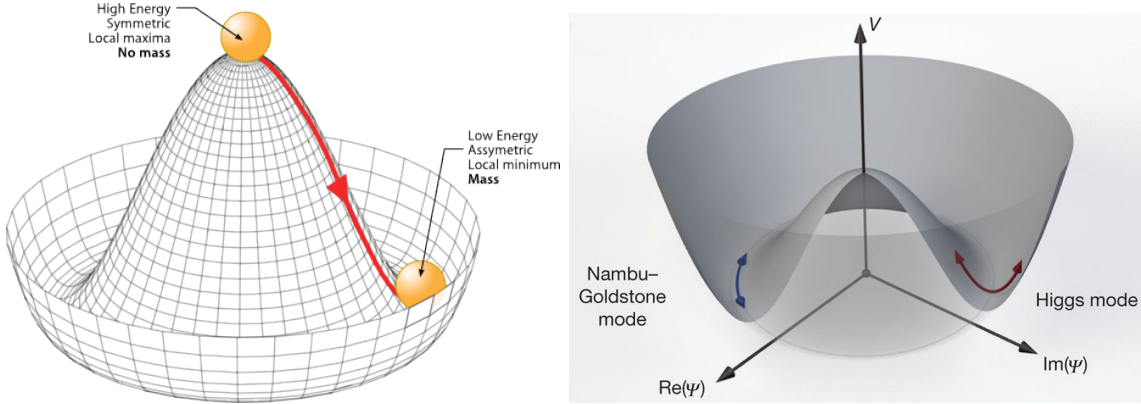


**Figure 1.9:** SSB mechanism for a complex scalar field [31, 32].

668 Thus, the SSB mechanism serves as a method to generate mass but as a side ef-  
 669 fect a massless field is introduced in the system. This fact is known as the Goldstone  
 670 theorem and states that a massless scalar field appears in the system for each con-  
 671 tinuous symmetry spontaneously broken. Another version of the Goldstone theorem  
 672 states that “if a Lagrangian is invariant under a continuous symmetry group  $G$ , but  
 673 the vacuum is only invariant under a subgroup  $H \subset G$ , then there must exist as many  
 674 massless spin-0 particles (Nambu-Goldstone bosons) as broken generators.” [26] The  
 675 Nambu-Goldstone boson can be understood considering that the potential in the  $\xi$ -  
 676 direction is flat so excitations in that direction are not energy consuming and thus  
 677 represent a massless state.

### 678 1.3.2 Higgs mechanism

679 When the SSB mechanism is introduced in the formulation of the EWI in an attempt  
 680 to generate the mass of the so far massless gauge bosons and fermions, an interesting  
 681 effect is revealed. In order to keep the  $G$  symmetry group invariance and generate

682 the mass of the EW gauge bosons, a G invariant Lagrangian density ( $\mathcal{L}_S$ ) has to be  
 683 added to the non massive EWI Lagrangian (Eqn. 1.30)

$$\mathcal{L}_S = (D_\mu \phi)^\dagger (D^\mu \phi) - \mu^2 \phi^\dagger \phi - \lambda (\phi^\dagger \phi)^2, \quad \lambda > 0, \mu^2 < 0 \quad (1.37)$$

$$D_\mu \phi = \left( i\partial_\mu - g \frac{\sigma_i}{2} W_\mu^i - g' \frac{Y}{2} B_\mu \right) \phi \quad (1.38)$$

684  $\phi$  has to be an isospin doublet of complex scalar fields so it preserves the G invariance;  
 685 thus  $\phi$  can be defined as:

$$\phi = \begin{pmatrix} \phi^+ \\ \phi^0 \end{pmatrix} \equiv \frac{1}{\sqrt{2}} \begin{pmatrix} \phi_1 + i\phi_2 \\ \phi_3 + i\phi_4 \end{pmatrix}. \quad (1.39)$$

686 The minima of the potential are defined by

$$\phi^\dagger \phi = \frac{1}{2} (\phi_1^2 + \phi_2^2 + \phi_3^2 + \phi_4^2) = -\frac{\mu^2}{2\lambda}. \quad (1.40)$$

687 The choice of the ground state is critical. By choosing a ground state, invariant  
 688 under  $U(1)_{em}$  gauge symmetry, the photon will remain massless and the  $W^\pm$  and  $Z$   
 689 bosons masses will be generated which is exactly what is needed. In that sense, the  
 690 best choice corresponds to a weak isospin doublet with  $T_3 = -1/2$ ,  $Y_W = 1$  and  $Q = 0$   
 691 which defines a ground state with  $\phi_1 = \phi_2 = \phi_4$  and  $\phi_3 = v$ :

$$\phi_0 \equiv \frac{1}{\sqrt{2}} \begin{pmatrix} 0 \\ v \end{pmatrix}, \quad v^2 \equiv -\frac{\mu^2}{\lambda}. \quad (1.41)$$

692 where the vacuum expectation value  $v$  is fixed by the Fermi coupling  $G_F$  according  
 693 to  $v = (\sqrt{2}G_F)^{1/2} \approx 246$  GeV.

694 The G symmetry has been broken and three Nambu-Goldstone bosons will appear.

695 The next step is to expand  $\phi$  about the chosen ground state as:

$$\phi(x) = \frac{1}{\sqrt{2}} \exp\left(\frac{i}{v} \sigma_i \theta^i(x)\right) \begin{pmatrix} 0 \\ v + H(x) \end{pmatrix} \approx \frac{1}{\sqrt{2}} \begin{pmatrix} \theta_1(x) + i\theta_2(x) \\ v + H(x) - i\theta_3(x) \end{pmatrix} \quad (1.42)$$

696 to describe fluctuations from the ground state  $\phi_0$ . The fields  $\theta_i(x)$  represent the  
 697 Nambu-Goldstone bosons while  $H(x)$  is known as *Higgs field*. The fundamental fea-  
 698 ture of the parametrization used is that the dependence on the  $\theta_i(x)$  fields is factored  
 699 out in a global phase that can be eliminated by taking the physical *unitary gauge*  
 700  $\theta_i(x) = 0$ . Therefore the expansion about the ground state is given by:

$$\phi(x) \frac{1}{\sqrt{2}} \begin{pmatrix} 0 \\ v + H(x) \end{pmatrix} \quad (1.43)$$

701 which when substituted into  $\mathcal{L}_S$  (Eqn. 1.37) results in a Lagrangian containing the  
 702 now massive three gauge bosons  $W^\pm, Z$ , one massless gauge boson (photon) and  
 703 the new Higgs field ( $H$ ). The three degrees of freedom corresponding to the Nambu-  
 704 Goldstone bosons are now integrated into the massive gauge bosons as their lon-  
 705 gitudinal polarizations which were not available when they were massless particles.  
 706 The effect by which vector boson fields acquire mass after an spontaneous symmetry  
 707 breaking, but without an explicit gauge invariance breaking is known as the *Higgs*  
 708 *mechanism*.

709 The mechanism was proposed by three independent groups: F.Englert and R.Brout  
 710 in August 1964 [33], P.Higgs in October 1964 [34] and G.Guralnik, C.Hagen and  
 711 T.Kibble in November 1964 [35]; however, its importance was not realized until  
 712 S.Glashow [22], A.Salam [23] and S.Weinberg [24], independently, proposed that elec-  
 713 tromagnetic and weak interactions are two manifestations of a more general interac-  
 714 tion called *electroweak interaction* in 1967.

715 **1.3.3 Masses of the gauge bosons**

716 The masses of the gauge bosons are extracted by evaluating the kinetic part of La-  
 717 grangian  $\mathcal{L}_S$  in the ground state (known also as the vacuum expectation value), i.e.,

$$\left| \left( \partial_\mu - ig \frac{\sigma_i}{2} W_\mu^i - i \frac{g'}{2} B_\mu \right) \phi_0 \right|^2 = \left( \frac{1}{2} v g \right)^2 W_\mu^+ W^{-\mu} + \frac{1}{8} v^2 (W_\mu^3, B_\mu) \begin{pmatrix} g^2 & -gg' \\ -gg' & g'^2 \end{pmatrix} \begin{pmatrix} W^{3\mu} \\ B^\mu \end{pmatrix} \quad (1.44)$$

718 comparing with the typical mass term for a charged boson  $M_W^2 W^+ W^-$

$$M_W = \frac{1}{2} v g. \quad (1.45)$$

The second term in the right side of the Eqn.1.44 comprises the masses of the neutral bosons, but it needs to be written in terms of the gauge fields  $Z_\mu$  and  $A_\mu$  in order to be compared to the typical mass terms for neutral bosons, therefore using Eqn. 1.29

$$\begin{aligned} \frac{1}{8} v^2 [g^2 (W_\mu^3)^2 - 2gg' W_\mu^3 B^\mu + g'^2 B_\mu^2] &= \frac{1}{8} v^2 [g W_\mu^3 - g' B_\mu]^2 + 0[g' W_\mu^3 + g B_\mu]^2 \quad (1.46) \\ &= \frac{1}{8} v^2 [\sqrt{g^2 + g'^2} Z_\mu]^2 + 0[\sqrt{g^2 + g'^2} A_\mu]^2 \end{aligned}$$

719 and then

$$M_Z = \frac{1}{2} v \sqrt{g^2 + g'^2}, \quad M_A = 0 \quad (1.47)$$

720 **1.3.4 Masses of the fermions**

721 The lepton mass terms can be generated by introducing a gauge invariant Lagrangian  
 722 term describing the Yukawa coupling between the lepton field and the Higgs field

$$\mathcal{L}_{Yl} = -G_l \left[ (\bar{\nu}_l, \bar{l})_L \begin{pmatrix} \phi^+ \\ \phi^0 \end{pmatrix} l_R + \bar{l}_R (\phi^-, \bar{\phi}^0) \begin{pmatrix} \nu_l \\ l \end{pmatrix} \right], \quad l = e, \mu, \tau. \quad (1.48)$$

723 After the SSB and replacing the usual field expansion about the ground state  
 724 (Eqn.1.41) into  $\mathcal{L}_{Yl}$ , the mass term arises

$$\mathcal{L}_{Yl} = -m_l (\bar{l}_L l_R + \bar{l}_R l_L) - \frac{m_l}{v} (\bar{l}_L l_R + \bar{l}_R l_L) H = -m_l \bar{l} \left( 1 + \frac{H}{v} \right) \quad (1.49)$$

725

$$m_l = \frac{G_l}{\sqrt{2}} v \quad (1.50)$$

726 where the additional term represents the lepton-Higgs interaction. The quark masses  
 727 are generated in a similar way as lepton masses but for the upper member of the  
 728 quark doublet a different Higgs doublet is needed:

$$\phi_c = -i\sigma_2 \phi^* = \begin{pmatrix} -\bar{\phi}^0 \\ \phi^- \end{pmatrix}. \quad (1.51)$$

729 Additionally, given that the quark isospin doublets are not constructed in terms  
 730 of the mass eigenstates but in terms of the flavor eigenstates, as shown in Table 1.5,  
 731 the coupling parameters will be related to the CKM matrix elements; thus, the quark  
 732 Lagrangian is given by:

$$\mathcal{L}_{Yq} = -G_d^{i,j} (\bar{u}_i, \bar{d}'_i)_L \begin{pmatrix} \phi^+ \\ \phi^0 \end{pmatrix} d_{jR} - G_u^{i,j} (\bar{u}_i, \bar{d}'_i)_L \begin{pmatrix} -\bar{\phi}^0 \\ \phi^- \end{pmatrix} u_{jR} + h.c. \quad (1.52)$$

733 with  $i, j = 1, 2, 3$ . After SSB and expansion about the ground state, the diagonal form

734 of  $\mathcal{L}_{Yq}$  is:

$$\mathcal{L}_{Yq} = -m_d^i \bar{d}_i d_i \left(1 + \frac{H}{v}\right) - m_u^i \bar{u}_i u_i \left(1 + \frac{H}{v}\right) \quad (1.53)$$

735 Fermion masses depend on arbitrary couplings  $G_l$  and  $G_{u,d}$  and are not predicted  
736 by the theory.

### 737 1.3.5 The Higgs field

738 After the characterization of the fermions and gauge bosons as well as their interac-  
739 tions, it is necessary to characterize the Higgs field itself. The Lagrangian  $\mathcal{L}_S$  in Eqn.  
740 1.37 written in terms of the gauge bosons is given by

$$\mathcal{L}_S = \frac{1}{4} \lambda v^4 + \mathcal{L}_H + \mathcal{L}_{HV} \quad (1.54)$$

741

$$\mathcal{L}_H = \frac{1}{2} \partial_\mu H \partial^\mu H - \frac{1}{2} m_H^2 H^2 - \frac{1}{2v} m_H^2 H^3 - \frac{1}{8v^2} m_H^2 H^4 \quad (1.55)$$

742

$$\mathcal{L}_{HV} = m_H^2 W_\mu^+ W^{\mu-} \left(1 + \frac{2}{v} H + \frac{2}{v^2} H^2\right) + \frac{1}{2} m_Z^2 Z_\mu Z^\mu \left(1 + \frac{2}{v} H + \frac{2}{v^2} H^2\right) \quad (1.56)$$

743 The mass of the Higgs boson is deduced as usual from the mass term in the Lagrangian  
744 resulting in:

$$m_H = \sqrt{-2\mu^2} = \sqrt{2\lambda}v \quad (1.57)$$

745 however, it is not predicted by the theory either. The experimental measurement of  
746 the Higgs boson mass have been performed by the *Compact Muon Solenoid (CMS)*  
747 experiment and the *A Toroidal LHC Appartus (ATLAS)* experiments at the *Large  
748 Hadron Collider (LHC)*, [36–38], and is presented in Table 1.8.

749

Property	Value
Electric charge	0
Color charge	0
Spin	0
Weak isospin	-1/2
Weak hypercharge	1
Parity	1
Mass (GeV/c <sup>2</sup> )	125.09±0.21 (stat.)±0.11 (syst.)

**Table 1.8:** Higgs boson properties. Higgs mass is not predicted by the theory and the value here corresponds to the experimental measurement.

### 1.3.6 Production of Higgs bosons at LHC

751 At the LHC, Higgs bosons are produced as a result of the collision of two counter-  
752 rotating protons beams. A detailed description of the LHC machine will be presented  
in chapter 2.

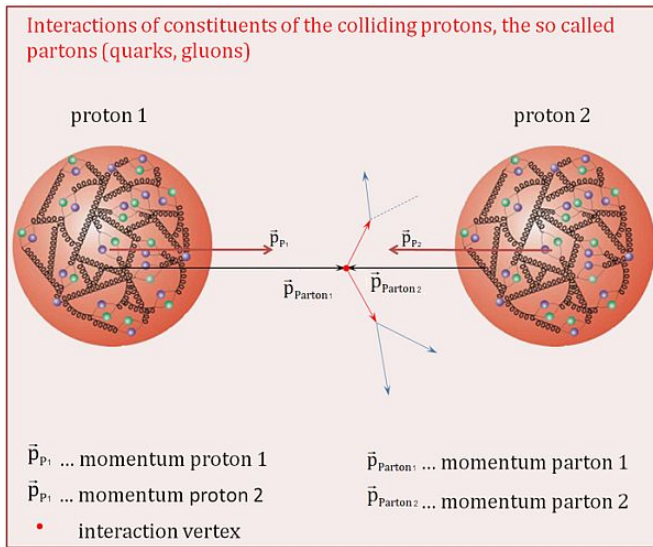


**Figure 1.10:** Proton-proton collision. Protons are composed of 3 valence quarks, a sea of quarks and gluons; therefore in a proton-proton collision, quarks and gluons are those who collide. [39].

753

754 Protons are composed of quarks and these quarks are bound by gluons; however,  
755 what is commonly called the quark content of the proton makes reference to the  
756 valence quarks. In fact, a proton is not just a rigid entity with three balls in it all  
757 tied up with springs, but the gluons exchanged by the valence quarks tend to split

758 spontaneously into quark-antiquark pairs or more gluons, creating *sea of quarks and*  
 759 *gluons* as represented in Figure 1.10.

760 In a proton-proton ( $pp$ ) collision, the proton's constituents, quarks and gluons, are  
 761 those that collide. The  $pp$  cross section depends on the momentum of the colliding  
 762 particles, reason for which it is needed to know how the momentum is distributed  
 763 inside the proton. Quarks and gluons are known as partons, hence, the functions  
 764 that describe how the proton momentum is distributed among partons inside it are  
 765 called *parton distribution functions (PDFs)*; PDFs are determined from experimental  
 766 data obtained in experiments where the internal structure of hadrons is tested, and  
 767 depend on the momentum transfer  $Q$  and the fraction of momentum  $x$  carried by an  
 768 specific parton. Figure 1.11 shows the proton PDFs ( $xf(x, Q^2)$ ) for two values of  $Q$ .

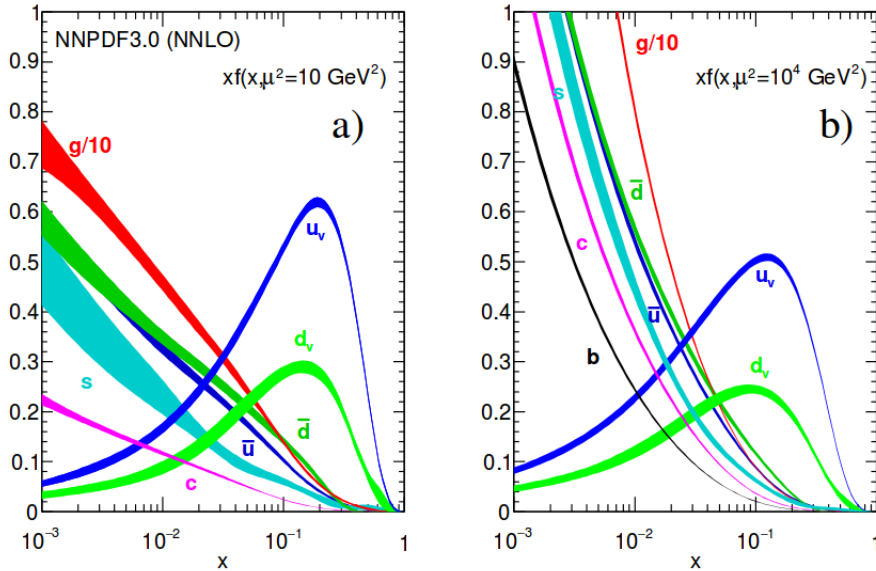


**Figure 1.11:** Proton PDFs for two values of  $Q^2$ : left.  $\mu^2 = Q^2 = 10 \text{ GeV}^2$ , right.  $\mu^2 = Q^2 = 10^4 \text{ GeV}^2$ .  $u_v$  and  $d_v$  correspond to the  $u$  and  $d$  valence quarks,  $s, c, b, \bar{u}, \bar{d}$  correspond to sea quarks, and  $g$  corresponds to gluons. Note that gluons carry a high fraction of the proton's momentum. [9]

769 In physics, a common approach to study complex systems consists of starting  
 770 with a simpler version of them, for which a well known description is available, and

adding an additional *perturbation* which represents a small deviation from the known behavior. If the perturbation is small enough, the physical quantities associated with the perturbed system are expressed as a series of corrections to those of the simpler system. The perturbation series corresponds to an expansion in power series of a small parameter, therefore, the more terms are considered in the series (the higher order in the perturbation series), the more precise is the description of the complex system. If the perturbation does not get progressively smaller, the strategy cannot be applied and new methods have to be employed.

High energy systems, like the Higgs production at LHC explored in this thesis, usually can be treated perturbatively with the expansion made in terms of the coupling constants. The overview presented here will be oriented specifically to the Higgs boson production mechanisms in  $pp$  collisions at LHC.

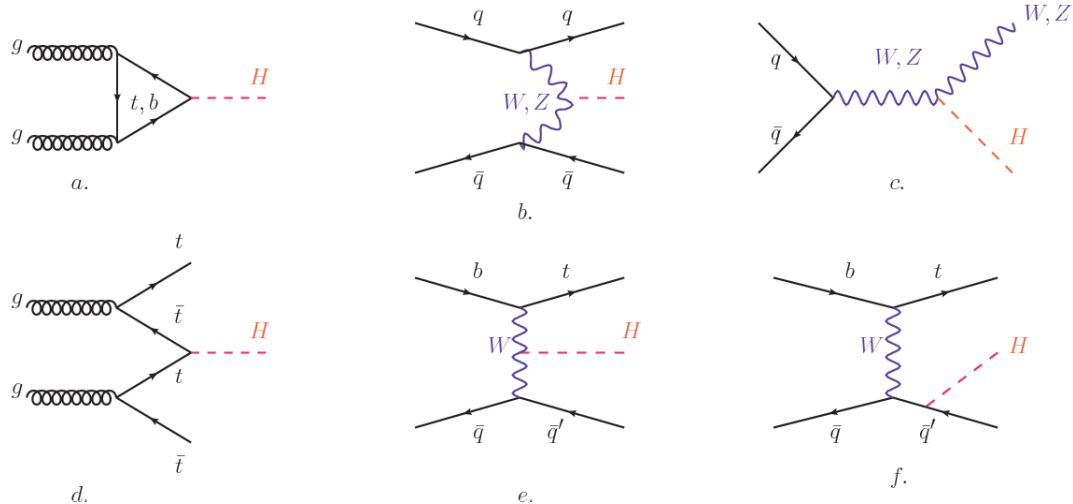


**Figure 1.12:** Main Higgs boson production mechanism Feynman diagrams. a. gluon-gluon fusion, b. vector boson fusion (VBF), c. Higgs-strahlung, d. Associated production with a top or bottom quark pair, e-f. associated production with a single top quark.

Figure 1.12 shows the Feynman diagrams for the leading order (first order) Higgs production processes at LHC; note that in these diagrams the incoming particles are not the protons themselves but the partons from the protons that actually participate

in the interaction, hence, theorists typically calculate the cross section for the parton interaction, and then convolute that cross section with the information from the PDFs to get a production cross section that is actually measured in experiments. The cross section for Higgs production as a function of the center of mass-energy ( $\sqrt{s}$ ) for  $pp$  collisions is showed in Figure 1.13 left. The tags NLO (next to leading order), NNLO (next to next to leading order) and N3LO (next to next to next to leading order) make reference to the order at which the perturbation series have been considered while the tags QCD and EW correspond to the strong and electroweak coupling constants respectively.

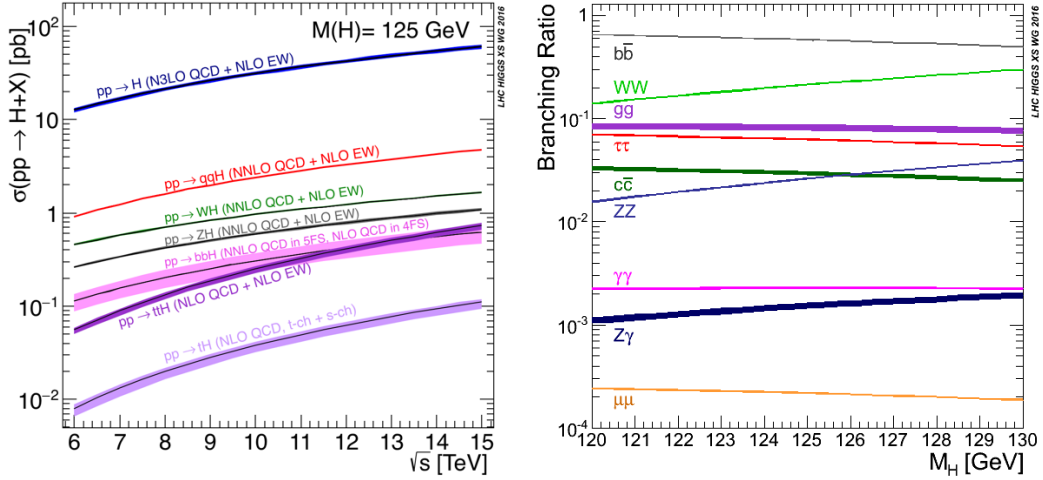


**Figure 1.13:** Higgs boson production cross sections (left) and decay branching ratios (right) for the main mechanisms. The VBF is indicated as  $qqH$  [40].

The main production mechanism is the gluon fusion (Figure 1.12a and  $pp \rightarrow H$  in Figure 1.13) given that gluons carry the highest fraction of momentum of the protons in  $pp$  colliders (as shown in Figure ??). Since the Higgs boson does not couple to gluons, the mechanism proceeds through the exchange of a virtual top-quark loop. Note that in this process the Higgs boson is produced alone, turning out to be problematic for some Higgs decays, because such absence of anything produced in

801 association with the Higgs represent a trouble for triggering, however, this mechanism  
 802 is experimentally clean when combined with the two-photon or the four-lepton decay  
 803 channels (see Section 1.3.7).

804 Vector boson fusion (Figure 1.12b and  $pp \rightarrow qqH$  in Figure 1.13) has the second  
 805 largest production cross section. The scattering of two fermions is mediated by a weak  
 806 gauge boson which later emits a Higgs boson. In the final state, the two fermions tend  
 807 to be located in the central region of the detector; this kind of features are generally  
 808 used as a signature when analyzing the datasets provided by the experiments<sup>7</sup>.

809 In the Higgs-strahlung mechanism (Figure 1.12c and  $pp \rightarrow WH, pp \rightarrow ZH$  in  
 810 Figure 1.13) two fermions annihilate to form a weak gauge boson. If the initial  
 811 fermions have enough energy, the emergent boson might emit a Higgs boson.

812 The associated production with a top or bottom quark pair and the associated  
 813 production with a single top quark (Figure 1.12d-f and  $pp \rightarrow bbH, pp \rightarrow t\bar{t}H, pp \rightarrow tH$   
 814 in Figure 1.13) have a smaller cross section than the main three mechanisms above,  
 815 but they provide a good opportunity to test the Higgs-top coupling. The analysis  
 816 reported in this thesis is developed using these production mechanisms. A detailed  
 817 description of the  $tH$  mechanism will be given in Section 1.5.

### 818 1.3.7 Higgs boson decay channels

819 When a particle can decay through several modes, also known as channels, the prob-  
 820 ability of decaying through a given channel is quantified by the *branching ratio (BR)*  
 821 of the decay channel; thus, the BR is defined as the ratio of number of decays go-  
 822 ing through that given channel to the total number of decays. In regard to the  
 823 Higgs boson decay, the BR can be predicted with accuracy once the Higgs mass is  
 824 known [41, 42]. In Figure 1.13 right, a plot of the BR as a function of the Higgs mass

---

<sup>7</sup> More details about how to identify events of interest in this analysis will be given in chapter 6.

is presented; the largest predicted BR corresponds to the  $b\bar{b}$  pair decay channel (see Table 1.9) given that it is the heaviest particle pair whose on-shell<sup>8</sup> production is kinematically allowed in the decay.

Decay channel	Branching ratio	Rel. uncertainty
$H \rightarrow b\bar{b}$	$5.84 \times 10^{-1}$	$+3.2\% - 3.3\%$
$H \rightarrow W^+W^-$	$2.14 \times 10^{-1}$	$+4.3\% - 4.2\%$
$H \rightarrow \tau^+\tau^-$	$6.27 \times 10^{-2}$	$+5.7\% - 5.7\%$
$H \rightarrow ZZ$	$2.62 \times 10^{-2}$	$+4.3\% - 4.1\%$
$H \rightarrow \gamma\gamma$	$2.27 \times 10^{-3}$	$+5.0\% - 4.9\%$
$H \rightarrow Z\gamma$	$1.53 \times 10^{-3}$	$+9.0\% - 8.9\%$
$H \rightarrow \mu^+\mu^-$	$2.18 \times 10^{-4}$	$+6.0\% - 5.9\%$

**Table 1.9:** Predicted branching ratios and the relative uncertainty for some decay channels of a SM Higgs boson with  $m_H = 125\text{GeV}/c^2$  [9]; the uncertainties are driven by theoretical uncertainties for the different Higgs boson partial widths and by parametric uncertainties associated to the strong coupling and the masses of the quarks which are the input parameters. Further details on these calculations can be found in Reference [43]

828

829 Decays to other lepton and quark pairs, like electron, strange, up, and down  
 830 quark pairs not listed in the table, are also possible but their likelihood is too small  
 831 to measure since they are very lightweight, hence, their interaction with the Higgs  
 832 boson is very weak. On other hand, the decay to top quark pairs is heavily suppressed  
 833 due to the top quark mass ( $\approx 173\text{ GeV}/c^2$ ).

834 Decays to gluons proceed indirectly through a virtual top quark loop while the  
 835 decays to photons proceed through a virtual W boson loop, therefore, their branching  
 836 ratio is smaller compared to direct interaction decays. Same is true for the decay to  
 837 a photon and a Z boson.

---

<sup>8</sup> In general, on-shell or real particles are those which satisfy the energy-momentum relation ( $E^2 - |\vec{p}|^2 c^2 = m^2 c^4$ ); off-shell or virtual particles does not satisfy it which is possible under the uncertainty principle of quantum mechanics. Usually, virtual particles correspond to internal propagators in Feynman diagrams.

838 In the case of decays to pairs of W and Z bosons, the decay proceed with one of  
 839 the bosons being on-shell and the other being off-shell. The likelihood of the process  
 840 diminish depending on how far off-shell are the virtual particles involved, hence, the  
 841 branching ratio for W boson pairs is bigger than for Z boson pairs since Z boson mass  
 842 is bigger than W boson mass.

843 Note that the decay to a pair of virtual top quarks is possible, but the probability  
 844 is way too small.

845 **1.4 Experimental status of the anomalous  
 846 Higgs-fermion coupling**

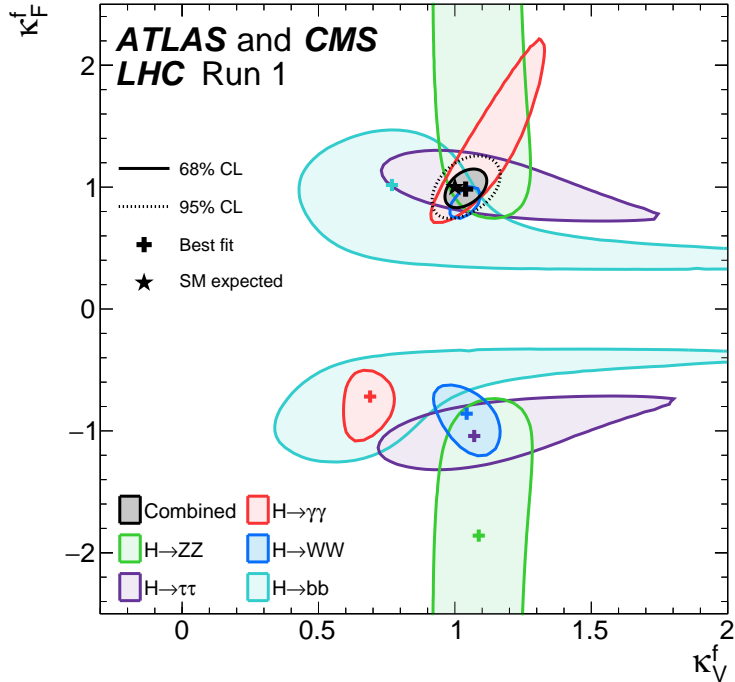


**Figure 1.14:** Combination of the ATLAS and CMS fits for coupling modifiers  $\kappa_t - \kappa_V$ ; also shown the individual decay channels combination and their global combination. No assumptions have been made on the sign of the coupling modifiers [44].

847       ATLAS and CMS have performed analyses of the anomalous Higgs-fermion cou-  
 848       pling by making likelihood scans for the two coupling modifiers,  $\kappa_f$  and  $\kappa_V$ , under  
 849       the assumption that  $\kappa_Z = \kappa_W \equiv \kappa_V$  and  $\kappa_t = \kappa_\tau = \kappa_b \equiv \kappa_f$ . Figure 1.14 shows the  
 850       result of the combination of ATLAS and CMS fits; also the individual decay channels  
 851       combination and the global combination results are shown. Note that from this plot  
 852       there is limited information on the sign of the coupling since the only information  
 853       available about the sign of the coupling comes from decays rather than production.

854       While all the channels are compatible for positive values of the modifiers, for  
 855       negative values of  $\kappa_f$  there is no compatibility. The best fit for individual channels  
 856       is compatible with negative values of  $\kappa_f$  except for the  $H \rightarrow bb$  channel. The best  
 857       fit for the combination yields  $\kappa_f \geq 0$ , in contrast to the yields from the individual  
 858       channels; the reason of this yield resides in the  $H \rightarrow \gamma\gamma$  coupling.  $H \rightarrow \gamma\gamma$  decay  
 859       proceeds through a loop of either top quarks or W bosons, hence, this channel is  
 860       sensitive to  $\kappa_t$  thanks to the interference of these two amplitude contributions; under  
 861       the assumption that no beyond SM particles take part in the loops, a flipped sign  
 862       of  $\kappa_t$  will increase the  $H \rightarrow \gamma\gamma$  branching fraction by a factor of  $\sim 2.4$  which is not  
 863       supported by measurements; thus, this large asymmetry between the positive and  
 864       negative coupling ratios in the  $H \rightarrow \gamma\gamma$  channel drives the yield of the global fit and  
 865       would mean that the anomalous H-t coupling is excluded as stated in Reference [44],  
 866       but there is a caveat, this exclusion holds only if no new particles contribute to the  
 867       loop in the main diagram for that decay.

868       Although the  $H \rightarrow bb$  channel is expected to be the most sensitive channel and  
 869       its best fit value of  $\kappa_t$  is positive, and then the global fit yield is still supported,  
 870       the contributions from all the other decay channels, small compared to the  $H \rightarrow bb$ ,  
 871       indicate that the anomalous H-t coupling cannot be excluded completely, motivating  
 872       to look at  $tH$  processes which can help with both, the limited information on the sign

873 of the H-t coupling and the access to information from the Higgs boson production  
 874 rather than from its decays.

875 It will be shown in Section 1.5 that the same interference effect enhance the  
 876  $tH$  production rate and could reveal evidence of direct production of heavy new par-  
 877 ticles as predicted in composite and little Higgs models [45], or new physics related  
 878 to Higgs boson mediated flavor changing neutral currents [46] as well as probes the  
 879 CP-violating phase of the H-t coupling [47, 48].

## 880 1.5 Associated production of a Higgs boson and a 881 single top quark

882 The production of Higgs boson in association with a top quark has been extensively  
 883 studied [47, 49–52]. While measurements of the main Higgs production mechanisms  
 884 rates are sensitive to the strength of the Higgs coupling to W boson or top quark,  
 885 they are not sensitive to the relative sign between the two couplings. In this thesis,  
 886 the Higgs boson production mechanism explored is the associated production with a  
 887 single top quark ( $tH$ ) which offers sensitivity to the relative sign of the Higgs couplings  
 888 to W boson and to top quark. The description given here is based on Reference [51]

A process where two incoming particles interact and produce a final state with two particles can proceed in three called channels (see, for instance, Figure 1.15 omitting the red line). The t-channel represents processes where an intermediate particle is emitted by one of the incoming particles and absorbed by the other. The s-channel represents processes where the two incoming particles merge into an intermediate particle which eventually will split into the particles in the final state. The third channel, u-channel, is similar to the t-channel but the two outgoing particles interchange their

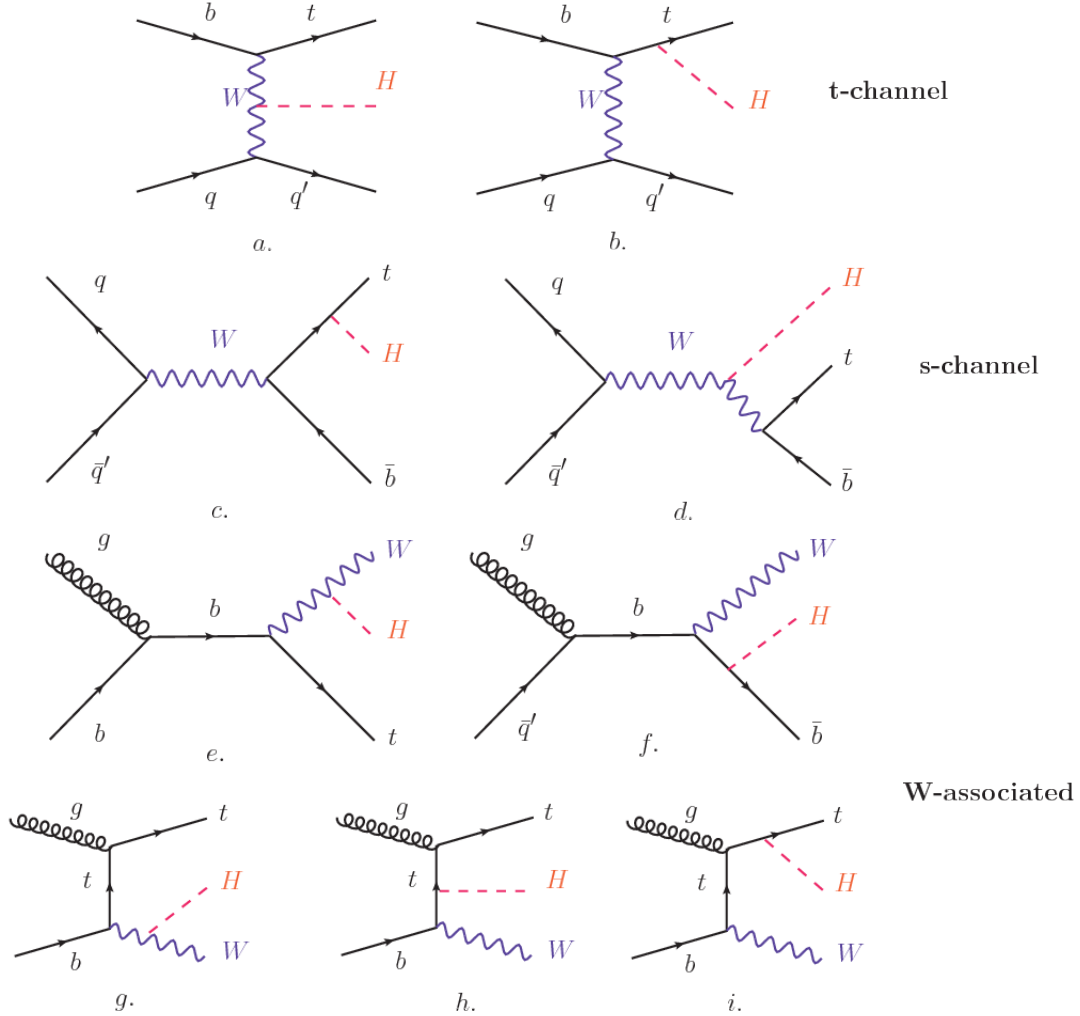


**Figure 1.15:** Associated Higgs boson production with a top quark mechanism Feynman diagrams. a.,b. t-channel ( $tHq$ ), c.,d. s-channel ( $tHb$ ), e-i. W-associated.

roles. These three channels are connected to the so-called Mandelstam variables

$$s = (p_1 + p_2)^2 = (p'_1 + p'_2)^2 \rightarrow \text{square of the center mass-energy.} \quad (1.58)$$

$$t = (p_1 - p'_1)^2 = (p'_2 - p_2)^2 \rightarrow \text{square of the four-momentum transfer.} \quad (1.59)$$

$$u = (p_1 - p'_2)^2 = (p'_1 - p_2)^2 \rightarrow \text{square of the crossed four-momentum transfer.} \quad (1.60)$$

$$s + t + u = m_1^2 + m_2^2 + m'_1^2 + m'_2^2 \quad (1.61)$$

which relate the momentum, energy and the angles of the incoming and outgoing particles in an scattering process of two particles to two particles. The importance of the Mandelstam variables reside in that they form a minimum set of variables needed to describe the kinematics of this scattering process; they are Lorentz invariant which makes them very useful when doing calculations.

The  $tH$  production, where Higgs boson can be radiated either from the top quark or from the W boson, is represented by the leading order Feynman diagrams in Figure 1.15. The cross section for the  $tH$  process is calculated, as usual, summing over the contributions from the different Feynman diagrams; therefore it depends on the interference between the contributions. In the SM, the interference for t-channel ( $tHq$  process) and W-associated ( $tHW$  process) production is destructive [49] resulting in the small cross sections presented in Table 1.10.

tH production channel	Cross section (fb)
t-channel ( $pp \rightarrow tHq$ )	$70.79^{+2.99}_{-4.80}$
W-associated ( $pp \rightarrow tHW$ )	$15.61^{+0.83}_{-1.04}$
s-channel( $pp \rightarrow tHb$ )	$2.87^{+0.09}_{-0.08}$

**Table 1.10:** Predicted SM cross sections for  $tH$  production at  $\sqrt{s} = 13$  TeV [53, 54].

The s-channel contribution can be neglected. It will be shown that a deviation from the SM destructive interference would result in an enhancement of the  $tH$  cross section compared to that in SM, which could be used to get information about the sign of the Higgs-top coupling [51, 52]. In order to describe  $tH$  production processes, Feynman diagram 1.15b will be considered; there, the W boson is radiated by a quark in the proton and eventually it will interact with the b quark. In the high energy regime, the effective W approximation [55] is used to describe the process as the

909 emission of an approximately on-shell W and its hard scattering with the b quark;  
 910 i.e.  $Wb \rightarrow th$ . The scattering amplitude for the process is given by

$$\mathcal{A} = \frac{g}{\sqrt{2}} \left[ (\kappa_t - \kappa_V) \frac{m_t \sqrt{s}}{m_W v} A \left( \frac{t}{s}, \varphi; \xi_t, \xi_b \right) + \left( \kappa_V \frac{2m_W s}{v t} + (2\kappa_t - \kappa_V) \frac{m_t^2}{m_W v} \right) B \left( \frac{t}{s}, \varphi; \xi_t, \xi_b \right) \right], \quad (1.62)$$

911 where  $\kappa_V \equiv g_{HVV}/g_{HVV}^{SM}$  and  $\kappa_t \equiv g_{Ht}/g_{Ht}^{SM} = y_t/y_t^{SM}$  are scaling factors that quantify  
 912 possible deviations of the couplings from the SM values, Higgs-Vector boson (H-  
 913 W) and Higgs-top (H-t) respectively, from the SM couplings;  $s = (p_W + p_b)^2$ ,  $t =$   
 914  $(p_W - p_H)^2$ ,  $\varphi$  is the Higgs azimuthal angle around the  $z$  axis taken parallel to the  
 915 direction of motion of the incoming W; A and B are functions describing the weak  
 916 interaction in terms of the chiral states  $(\xi_t, \xi_b)$  of the quarks  $b$  and  $t$ . Terms that  
 917 vanish in the high energy limit have been neglected as well as the Higgs and  $b$  quark  
 918 masses<sup>9</sup>.

919 The scattering amplitude grows with energy like  $\sqrt{s}$  for  $\kappa_V \neq \kappa_t$ , in contrast to  
 920 the SM ( $\kappa_t = \kappa_V = 1$ ), where the first term in 1.62 cancels out and the amplitude  
 921 is constant for large  $s$ ; therefore, a deviation from the SM predictions represents an  
 922 enhancement in the  $tHq$  cross section. In particular, for a SM H-W coupling and a  
 923 H-t coupling of inverted sign with respect to the SM ( $\kappa_V = -\kappa_t = 1$ ) the  $tHq$  cross  
 924 section is enhanced by a factor greater 10 as seen in the Figure 1.16 taken from  
 925 Reference [51]; Reference [56] has reported similar enhancement results.

926 A similar analysis is valid for the W-associated channel but, in that case, the in-  
 927 terference is more complicated since there are more than two contributions and an ad-  
 928 ditional interference with the production of Higgs boson and a top pair process( $t\bar{t}H$ ).  
 929 The calculations are made using the so-called Diagram Removal (DR) technique where

---

<sup>9</sup> A detailed explanation of the structure and approximations used to derive  $\mathcal{A}$  can be found in Reference [51]

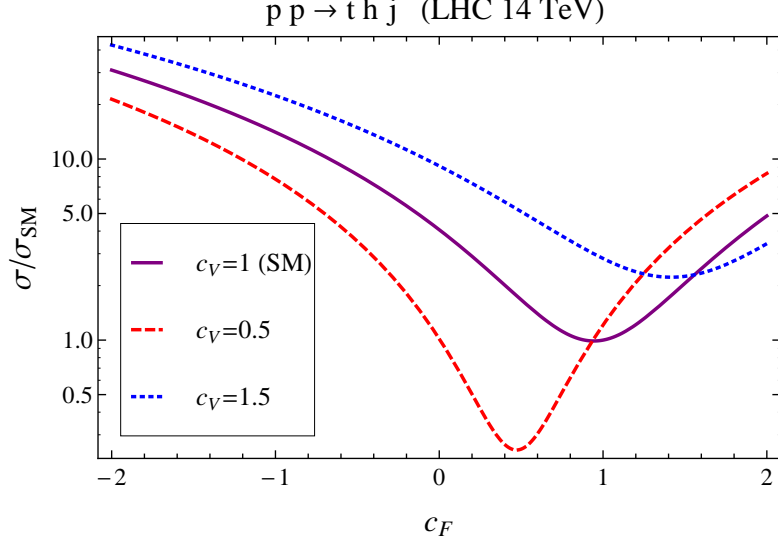


**Figure 1.16:** Cross section for  $tHq$  process as a function of  $\kappa_t$ , normalized to the SM, for three values of  $\kappa_V$ . In the plot  $c_f$  refers to the Higgs-fermion coupling which is dominated by the H-t coupling and represented here by  $\kappa_t$ . Solid, dashed and dotted lines correspond to  $c_V \rightarrow \kappa_V = 1, 0.5, 1.5$  respectively. Note that for the SM ( $\kappa_V = \kappa_t = 1$ ), the destructive effect of the interference is maximal.

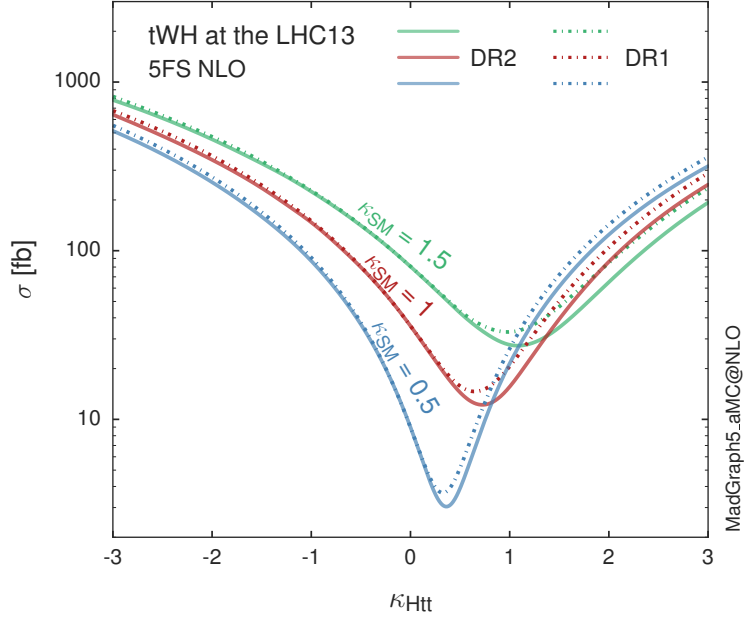


**Figure 1.17:** Cross section for  $tHW$  process as a function of  $\kappa_{Htt}$ , for three values of  $\kappa_{SM}$  at  $\sqrt{s} = 13$  TeV.  $\kappa_{Htt}^2 = \sigma_{Htt}/\sigma_{Htt}^{SM}$  is a simple re-scaling of the SM Higgs interactions.

interfering diagrams are removed (or added) from the calculations in order to evaluate the impact of the removed contributions. DR1 was defined to neglect  $t\bar{t}H$  interference while DR2 was defined to take  $t\bar{t}H$  interference into account [48]. As shown in Figure 1.17, the  $tHW$  cross section is enhanced from about 15 fb (SM:  $\kappa_{Htt} = 1$ ) to about 150 fb ( $\kappa_{Htt} = -1$ ). Differences between curves for DR1 and DR2 help to gauge the impact of the interference with  $t\bar{t}H$ . Results of the calculations of the  $tHq$  and  $tHW$  cross sections at  $\sqrt{s} = 13$  TeV can be found in Reference [57] and a summary of the results is presented in Table 1.11.

	$\sqrt{s}$ TeV	$\kappa_t = 1$	$\kappa_t = -1$
$\sigma^{LO}(tHq)(fb)$ [51]	8	$\approx 17.4$	$\approx 252.7$
	14	$\approx 80.4$	$\approx 1042$
$\sigma^{NLO}(tHq)(fb)$ [51]	8	$18.28^{+0.42}_{-0.38}$	$233.8^{+4.6}_{-0.0}$
	14	$88.2^{+1.7}_{-0.0}$	$982.8^{+28}_{-0.0}$
$\sigma^{LO}(tHq)(fb)$ [56]	14	$\approx 71.8$	$\approx 893$
$\sigma^{LO}(tHW)(fb)$ [56]	14	$\approx 16.0$	$\approx 139$
$\sigma^{NLO}(tHq)(fb)$ [57]	8	$18.69^{+8.62\%}_{-17.13\%}$	-
	13	$74.25^{+7.48\%}_{-15.35\%}$	$848^{+7.37\%}_{-13.70\%}$
	14	$90.10^{+7.34\%}_{-15.13\%}$	$1011^{+7.24\%}_{-13.39\%}$
$\sigma^{LO}(tHW)(fb)$ [48]	13	$15.77^{+15.91\%}_{-15.76\%}$	-
$\sigma^{NLO}DR1(tHW)(fb)$ [48]	13	$21.72^{+6.52\%}_{-5.24\%}$	$\approx 150$
$\sigma^{NLO}DR2(tHW)(fb)$ [48]	13	$16.28^{+7.34\%}_{-15.13\%}$	$\approx 150$

**Table 1.11:** Predicted enhancement of the  $tHq$  and  $tHW$  cross sections at LHC for  $\kappa_V = 1$  and  $\kappa_t = \pm 1$  at LO and NLO; the cross section enhancement of more than a factor of 10 is due to the flipping in the sign of the H-t coupling with respect to the SM one.

938

## 939 1.6 CP-mixing in $tH$ processes

940 In addition to the sensitivity to sign of the H-t coupling, the  $tHq$  and  $tHW$  processes  
 941 have been proposed as a tool to investigate the possibility of a H-t coupling that does

942 not conserve CP [47, 48, 58].

943 In this thesis, the sensitivity of  $tH$ processes to CP-mixing is also studied on the  
 944 basis of References [47, 48] using the effective field theory framework where a generic  
 945 particle ( $X_0$ ) of spin-0 and a general CP violating interaction with the top quark  
 946 ( $Htt$  coupling), can couple to scalar and pseudo-scalar fermionic densities. The H-W  
 947 interaction is assumed to be SM-like. The Lagrangian modeling the H-t interaction  
 948 is given by

$$\mathcal{L}_0^t = -\bar{\psi}_t (c_\alpha \kappa_{Htt} g_{Htt} + i s_\alpha \kappa_{Att} g_{Att} \gamma_5) \psi_t X_0, \quad (1.63)$$

949 where  $\alpha$  is the CP-mixing phase,  $c_\alpha \equiv \cos \alpha$  and  $s_\alpha \equiv \sin \alpha$ ,  $\kappa_{Htt}$  and  $\kappa_{Att}$  are real  
 950 dimensionless re-scaling parameters<sup>10</sup> used to parametrize the magnitude of the CP-  
 951 violating and CP-conserving parts of the amplitude. The model defines  $g_{Htt} =$   
 952  $g_{Att} = m_t/v = y_t/\sqrt{2}$  with  $v \sim 246$  GeV the Higgs vacuum expectation value. In  
 953 this parametrization, three special cases can be recovered

954 • CP-even coupling  $\rightarrow \alpha = 0^\circ$

955 • CP-odd coupling  $\rightarrow \alpha = 90^\circ$

956 • SM coupling  $\rightarrow \alpha = 0^\circ$  and  $\kappa_{Htt} = 1$

957 The loop induced  $X_0$  coupling to gluons can also be described in terms of the  
 958 parametrization above, according to

$$\mathcal{L}_0^g = -\frac{1}{4} \left( c_\alpha \kappa_{Hgg} g_{Hgg} G_{\mu\nu}^a G^{a,\mu\nu} + s_\alpha \kappa_{Agg} g_{Agg} G_{\mu\nu}^a \tilde{G}^{a,\mu\nu} \right) X_0. \quad (1.64)$$

959 where  $g_{Hgg} = -\alpha_s/3\pi v$  and  $g_{Agg} = \alpha_s/2\pi v$  and  $G_{\mu\nu}$  is the gluon field strength tensors.

960 Under the assumption that the top quark dominates the gluon-fusion process at LHC

---

<sup>10</sup> analog to  $\kappa_t$  and  $\kappa_V$

961 energies,  $\kappa_{Hgg} \rightarrow \kappa_{Htt}$  and  $\kappa_{Agg} \rightarrow \kappa_{Att}$ , so that the ratio between the gluon-gluon  
 962 fusion cross section for  $X_0$  and for the SM Higgs prediction can be written as

$$\frac{\sigma_{NLO}^{gg \rightarrow X_0}}{\sigma_{NLO,SM}^{gg \rightarrow H}} = c_\alpha^2 \kappa_{Htt}^2 + s_\alpha^2 \left( \kappa_{Att} \frac{g_{Agg}}{g_{Hgg}} \right)^2. \quad (1.65)$$

963 If the re-scaling parameters are set to

$$\kappa_{Htt} = 1, \quad \kappa_{Att} = \left| \frac{g_{Hgg}}{g_{Agg}} \right| = \frac{2}{3}. \quad (1.66)$$

964 the gluon-fusion SM cross section is reproduced for every value of the CP-mixing  
 965 angle  $\alpha$ ; therefore, by imposing that condition to the Lagrangian density 1.63, the  
 966 CP-mixing angle is not constrained by current data. Figure 1.18 shows the NLO cross  
 967 sections for t-channel  $tX_0$ (blue) and  $t\bar{t}X_0$  (red) associated production processes as a  
 968 function of the CP-mixing angle  $\alpha$ .  $X_0$  is a generic spin-0 particle with top quark  
 969 CP-violating coupling. Re-scaling factors  $\kappa_{Htt}$  and  $\kappa_{Att}$  have been set to reproduce  
 970 the SM gluon-fusion cross sections.

971 It is interesting to notice that the  $tX_0$  cross section is enhanced, by a factor of  
 972 about 10, when a continuous rotation in the scalar-pseudoscalar plane is applied; this  
 973 enhancement is similar to the enhancement produced when the H-t coupling is flipped  
 974 in sign with respect to the SM ( $y_t = -y_{t,SM}$  in the plot), as showed in Section 1.5. In  
 975 contrast, the degeneracy in the  $t\bar{t}X_0$  cross section is still present given that it depends  
 976 quadratically on the H-t coupling, but more interesting is to notice that  $t\bar{t}X_0$  cross  
 977 section is exceeded by  $tX_0$  cross section after  $\alpha \sim 60^\circ$ .

978 A similar parametrization can be used to investigate the  $tHW$  process sensitivity  
 979 to CP-violating H-t coupling. As said in 1.5, the interference in the W-associated  
 980 channel is more complicated because there are more than two contributions and also  
 981 there is interference with the  $t\bar{t}H$  production process.

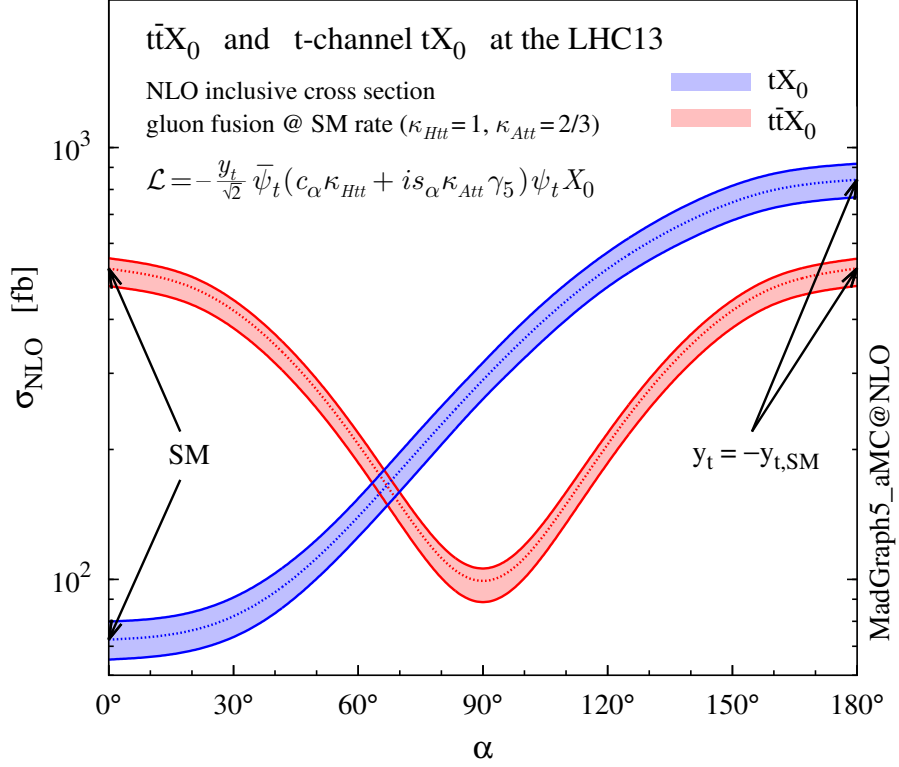


**Figure 1.18:** NLO cross sections for t-channel  $tX_0$ (blue) and  $t\bar{t}X_0$  (red) associated production processes as a function of the CP-mixing angle  $\alpha$ .  $X_0$  is a generic spin-0 particle with top quark CP-violating coupling [47].

982       Figure 1.19 shows the NLO cross sections for t-channel  $tX_0$ (blue),  $t\bar{t}X_0$  (red)  
983       associated production and for the combined  $tWX_0+t\bar{t}X_0+interference$  (orange) as  
984       a function of the CP-mixing angle. It is clear that the effect of the interference in the  
985       combined case is the lifting of the degeneracy present in the  $t\bar{t}X_0$  production. The  
986       constructive interference enhances the cross section from about 500 fb at SM ( $\alpha = 0$ )  
987       to about 600 fb ( $\alpha = 180^\circ \rightarrow y_t = -y_{t,SM}$ ).

988       An analysis combining  $tHq$  and  $tHW$ processes will be made in this thesis taking  
989       advantage of the sensitivity improvement.

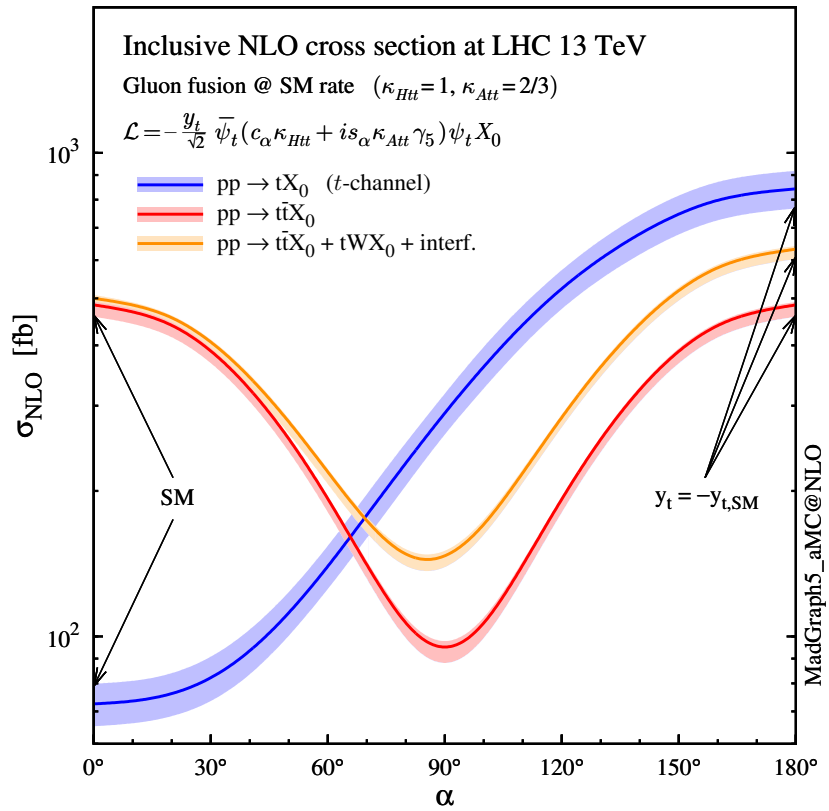


**Figure 1.19:** NLO cross sections for t-channel  $tX_0$ (blue),  $t\bar{t}X_0$  (red) associated production processes and combined  $tWX_0 + t\bar{t}X_0$  (including interference) production as a function of the CP-mixing angle  $\alpha$  [47].

990 **Chapter 2**

991 **The CMS experiment at the LHC**

992 **2.1 Introduction**

993 Located on the Swiss-French border, the European Council for Nuclear Research  
994 (CERN) is the largest scientific organization leading particle physics research. About  
995 13000 people in a broad range of roles including users, students, scientists, engineers,  
996 among others, contribute to the data taking and analysis, with the goal of unveiling  
997 the secrets of nature and revealing the fundamental structure of the universe. CERN  
998 is also the home of the Large Hadron Collider (LHC), the largest particle accelerator  
999 around the world, where protons (or heavy ions) traveling close to the speed of light,  
1000 are made to collide. These collisions open a window to investigate how particles (and  
1001 their constituents if they are composite) interact with each other, providing clues  
1002 about the laws of nature. This chapter presents an overview of the LHC structure  
1003 and operation. A detailed description of the CMS detector is offered, given that the  
1004 data used in this thesis have been taken with this detector.

## 1005 2.2 The LHC

1006 With 27 km of circumference, the LHC is currently the most powerful circular acceler-  
 1007 ator in the world. It is installed in the same tunnel where the Large Electron-Positron  
 1008 (LEP) collider was located, taking advantage of the existing infrastructure. The LHC  
 1009 is part of the CERN's accelerator complex composed of several successive accelerat-  
 1010 ing stages before the particles are injected into the LHC ring where they reach their  
 1011 maximum energy (see Figure 2.1).

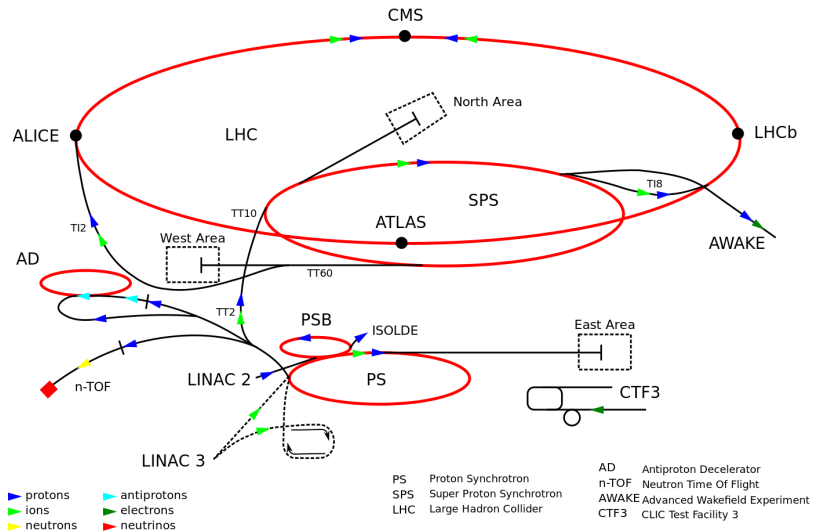


**Figure 2.1:** CERN accelerator complex. Blue arrows show the path followed by protons along the acceleration process [61].

1012 The LHC runs in three collision modes depending on the particles being acceler-  
 1013 ated

1014 • Proton-Proton collisions ( $pp$ ) for multiple physics experiments.

1015 • Lead-Lead collisions ( $Pb-Pb$ ) for heavy ion experiments.

1016 • Proton-Lead collisions ( $p-Pb$ ) for quark-gluon plasma experiments.

1017 In this thesis only  $pp$  collisions will be considered.

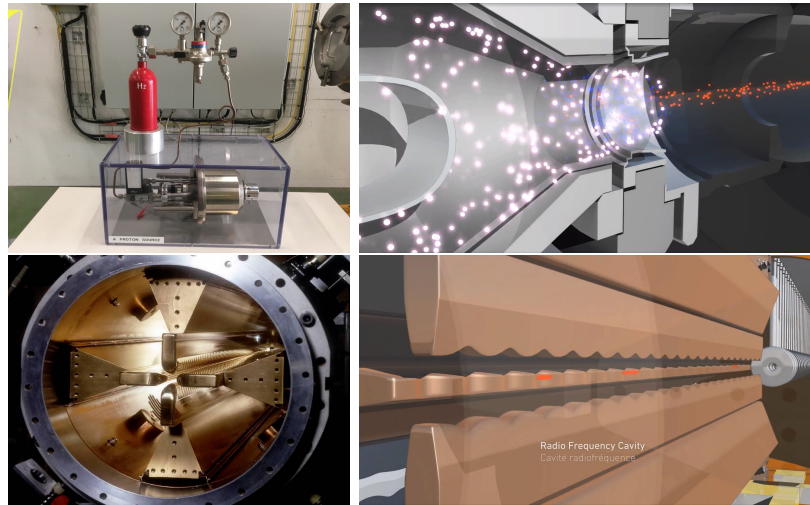


**Figure 2.2:** LHC protons source and the first acceleration stage. Top: the bottle contains hydrogen gas which is injected into the metal cylinder (white dots) to be broken down into electrons (blue dots) and protons (red dots); Bottom: the obtained protons are directed towards the radio frequency quadrupole which perform the first acceleration, focus the beam and create the bunches of protons. Left images are real pictures while right images are drawings [65, 66].

1018      Collection of protons starts with hydrogen atoms taken from a bottle, containing  
 1019     hydrogen gas, and injecting them in a metal cylinder; hydrogen atoms are broken  
 1020     down into electrons and protons by an intense electric field (see Figure 2.2 top).  
 1021     The resulting protons leave the metal cylinder towards a radio frequency quadrupole  
 1022     (RFQ) that focus the beam, accelerates the protons and creates the packets of protons  
 1023     called bunches. In the RFQ, an electric field is generated by a RF wave at a frequency  
 1024     that matches the resonance frequency of the cavity where the electrodes are contained.  
 1025     The beam of protons traveling on the RFQ axis experiences an alternating electric  
 1026     field gradient that generates the focusing forces.

1027     In order to accelerate the protons, a longitudinal time-varying electric field com-  
 1028     ponent is added to the system; it is done by giving the electrodes a sine-like profile as  
 1029     shown in Figure 2.2 bottom. By matching the speed and phase of the protons with  
 1030     the longitudinal electric field the bunching is performed; protons synchronized with

1031 the RFQ (synchronous protons) do not feel an accelerating force, but those protons in  
 1032 the beam that have more (or less) energy than the synchronous proton (asynchronous  
 1033 protons) will feel a decelerating (accelerating) force; therefore, asynchronous protons  
 1034 will oscillate around the synchronous ones forming bunches of protons [63]. From the  
 1035 RFQ protons emerge with energy 750 keV in bunches of about  $1.15 \times 10^{11}$  protons [64].

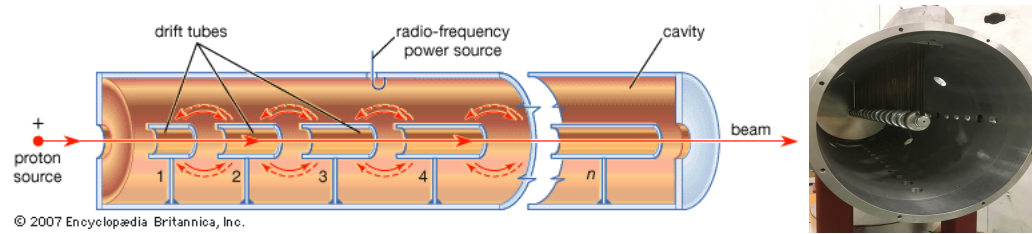


**Figure 2.3:** Left: drawing of the LINAC2 accelerating system at CERN. Electric fields generated by radio frequency (RF) create acceleration and deceleration zones inside the cavity; deceleration zones are blocked by drift tubes where quadrupole magnets focus the proton beam. Right: picture of a real RF cavity [67].

1036 Proton bunches coming from the RFQ go to the linear accelerator 2 (LINAC2)  
 1037 where they are accelerated to reach 50 MeV energy. In the LINAC2 stage, acceleration  
 1038 is performed using electric fields generated by radio frequency which create zones  
 1039 of acceleration and deceleration as shown in Figure 2.3. In the deceleration zones,  
 1040 the electric field is blocked using drift tubes where protons are free to drift while  
 1041 quadrupole magnets focus the beam.

1042 The beam coming from LINAC2 is injected into the proton synchrotron booster  
 1043 (PSB) to reach 1.4 GeV in energy. The next acceleration is provided at the proton  
 1044 synchrotron (PS) up to 26 GeV, followed by the injection into the super proton  
 1045 synchrotron (SPS) where protons are accelerated to 450 GeV. Finally, protons are  
 1046 injected into the LHC where they are accelerated to the target energy of 6.5 TeV.

1047 PSB, PS, SPS and LHC accelerate protons using the same RF acceleration tech-  
 1048 nique described before.

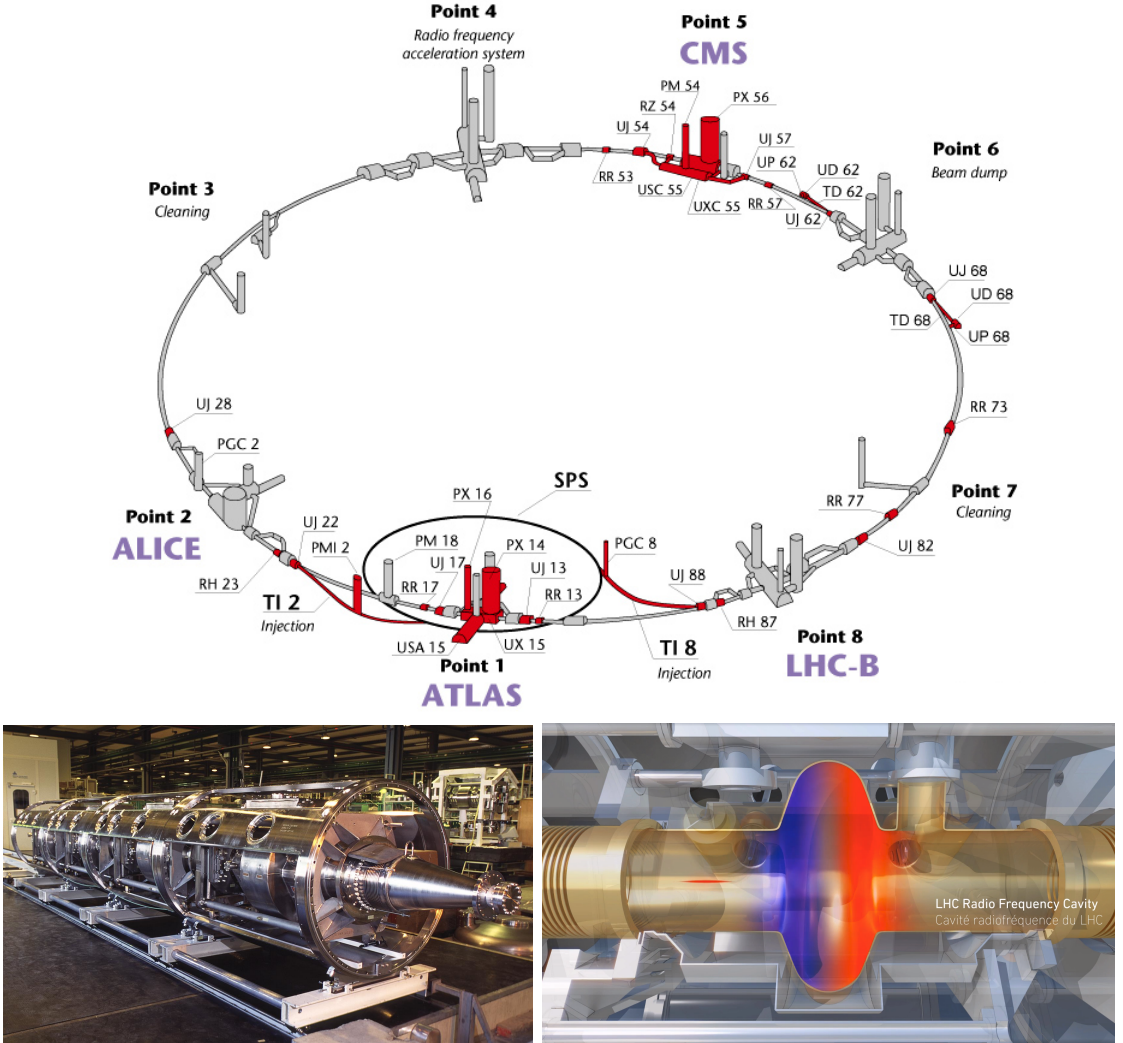


**Figure 2.4:** Top: LHC layout. The red zones indicate the infrastructure additions to the LEP installations, built to accommodate the ATLAS and CMS experiments which exceed the size of the former experiments located there [62]. Bottom: LHC RF cavities. A module (left picture) accommodates 4 cavities, each like the one in the right drawing, that accelerate protons and preserve the bunch structure of the beam. The color gradient pattern represents the strength of the electric field inside the cavity; red zone corresponds to the maximum of the oscillation electric field while the blue zone corresponds to the minimum. [66, 68]

1049 The LHC has a system of 16 RF cavities located in the so-called point 4, as  
 1050 shown in Figure 2.4 top, tuned at a frequency of 400 MHz. The bottom side of  
 1051 Figure 2.4 shows a picture of a RF module composed of 4 RF cavities working in a  
 1052 superconducting state at 4.5 K; also, a representation of the accelerating electric field

1053 that accelerates the protons in the bunch is shown. The maximum of the oscillating  
 1054 electric field (red region) picks the proton bunches at the entrance of the cavity  
 1055 and keeps accelerating them through the whole cavity. The protons are carefully  
 1056 timed so that in addition to the acceleration effect the bunch structure of the beam  
 1057 is preserved.

1058 While protons are accelerated in one section of the LHC ring, where the RF cavities  
 1059 are located, in the rest of their path they have to be kept in the curved trajectory  
 1060 defined by the LHC ring. Technically, LHC is not a perfect circle; RF, injection, beam  
 1061 dumping, beam cleaning and sections before and after the experimental points where  
 1062 protons collide are all straight sections. In total, there are 8 arcs 2.45 km long each  
 1063 and 8 straight sections 545 m long each. In order to curve the proton's trajectory in  
 1064 the arc sections, superconducting dipole magnets are used.

1065 Inside the LHC ring, there are two proton beams traveling in opposite directions  
 1066 in two separated beam pipes; the beam pipes are kept at ultra-high vacuum ( $\sim 10^{-9}$   
 1067 Pa) to ensure that there are no particles that interact with the proton beams. The  
 1068 superconducting dipole magnets used in LHC are made of a NbTi alloy, capable of  
 1069 transporting currents of about 12000 A when cooled at a temperature below 2K using  
 1070 liquid helium (see Figure 2.5).

1071 Protons in the arc sections of LHC feel a centripetal force exerted by the dipole  
 1072 magnets; the magnitude of magnetic field needed to keep the protons in the LHC  
 1073 curved trayectomy can be found assuming that protons travel at  $v \approx c$ , using the  
 1074 standard values for proton mass and charge and the LHC radius, as

$$F_m = \frac{mv^2}{r} = qBv \rightarrow B = 8.33T \quad (2.1)$$

1075 which is about 100000 times the Earth's magnetic field. A representation of the

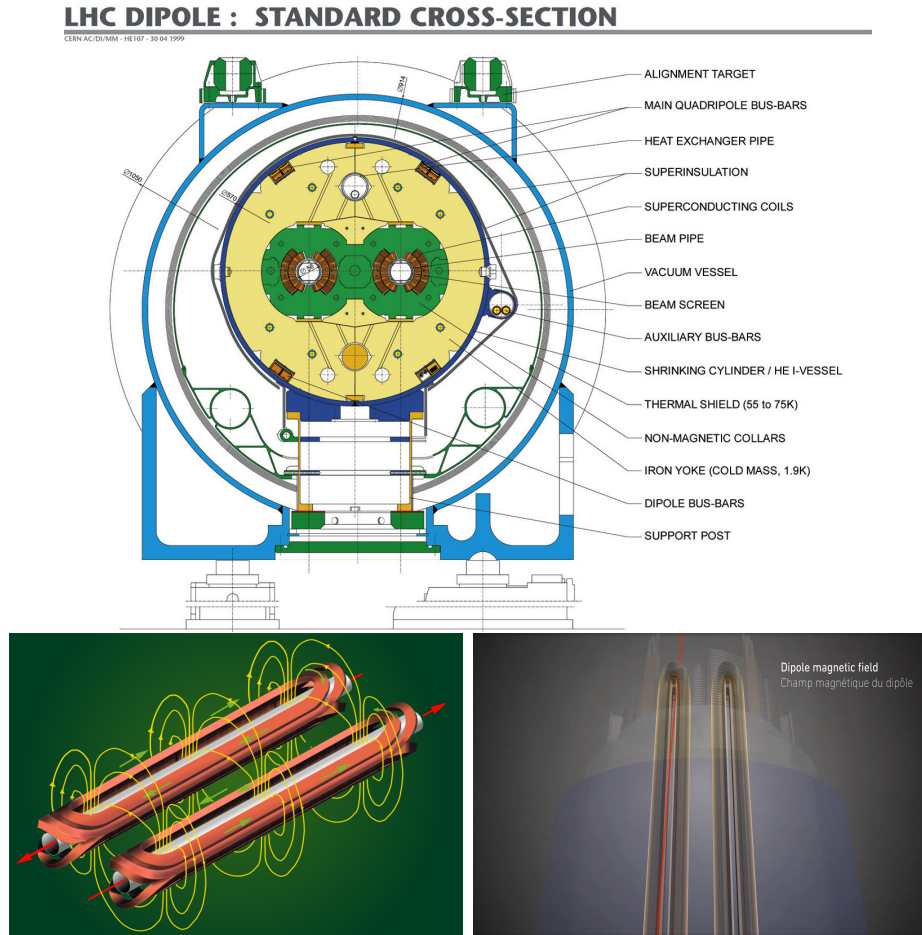


**Figure 2.5:** Top: LHC dipole magnet transverse view; cooling, shielding and mechanical support are indicated. Bottom left: Magnetic field generated by the dipole magnets; note that the direction of the field inside one beam pipe is opposite with respect to the other beam pipe which guarantee that both proton beams are curved in the same direction towards the center of the ring. The effect of the dipole magnetic field on the proton beam is represented on the bottom right side [66, 69, 70].

1076 magnetic field generated by the dipole magnets is shown on the bottom left side of  
 1077 Figure 2.5. The bending effect of the magnetic field on the proton beam is shown on  
 1078 the bottom right side of Figure 2.5. Note that the dipole magnets are not curved;  
 1079 the arc section of the LHC ring is composed of straight dipole magnets of about 15  
 1080 m. In total there are 1232 dipole magnets along the LHC ring.  
 1081 In addition to the bending of the beam trajectory, the beam has to be focused. The

focusing is performed by quadrupole magnets installed in a different straight section; in total 858 quadrupole magnets are installed along the LHC ring. Other effects like electromagnetic interaction among bunches, interaction with electron clouds from the beam pipe, the gravitational force on the protons, differences in energy among protons in the same bunch, among others, are corrected using sextupole and other magnetic multipoles.

The two proton beams inside the LHC ring are made of bunches with a cylindrical shape of about 7.5 cm long and about 1 mm in diameter; when bunches are close to the interaction point (IP), the beam is focused up to a diameter of about 16  $\mu\text{m}$  in order to maximize the probability of collisions between protons. The number of collisions per second is proportional to the cross section of the bunches with the *luminosity* ( $L$ ) as the proportionality factor, thus, the luminosity can be calculated using

$$L = fn \frac{N_1 N_2}{4\pi\sigma_x\sigma_y} \quad (2.2)$$

where  $f$  is the revolution frequency,  $n$  is the number of bunches per beam,  $N_1$  and  $N_2$  are the numbers of protons per bunch,  $\sigma_x$  and  $\sigma_y$  are the gaussian transverse sizes of the bunches. With the expected parameters, the LHC expected luminosity is about

$$f = \frac{v}{2\pi r_{LHC}} \approx \frac{3 \times 10^8 \text{ m/s}}{27 \text{ km}} \approx 11.1 \text{ kHz},$$

$$n = 2808$$

$$N_1 = N_2 \sim 1.5 \times 10^{11}$$

$$\sigma_x = \sigma_y = 16 \mu\text{m}$$

1097

$$L = 1.28 \times 10^{34} \text{ cm}^{-2} \text{ s}^{-1} = 1.28 \times 10^{-5} \text{ fb}^{-1} \text{ s}^{-1} \quad (2.3)$$

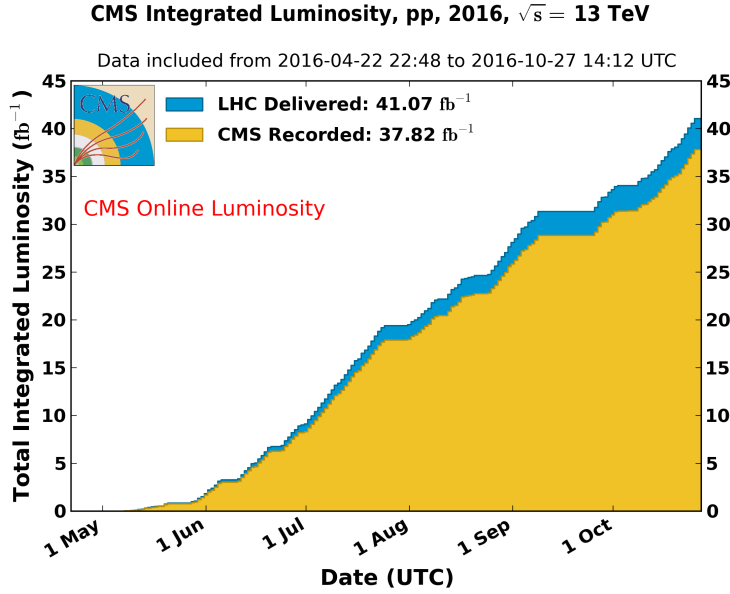


**Figure 2.6:** Integrated luminosity delivered by LHC and recorded by CMS during 2016. The difference between the delivered and the recorded luminosity is due to fails and issues occurred during the data taking in the CMS experiment [71].

1098        Luminosity is a fundamental aspect of LHC given that the bigger luminosity the  
 1099        bigger number of collisions, which means that for processes with a very small cross  
 1100        section the number of expected occurrences is increased and so the chances of being  
 1101        detected. The integrated luminosity, collected by the CMS experiment during 2016  
 1102        is shown in Figure 2.6; the data analyzed in this thesis corresponds to an integrated  
 1103        luminosity of  $35.9 \text{ fb}^{-1}$  at a center of mass-energy  $\sqrt{s} = 13 \text{ TeV}$ .

1104        One way to increase  $L$  is increasing the number of bunches in the beam. Cur-  
 1105        rently, the separation between two consecutive bunches in the beam is 7.5 m which  
 1106        corresponds to a time separation of 25 ns. In the full LHC ring the allowed number  
 1107        of bunches is  $n = 27\text{km}/7.5\text{m} = 3600$ ; however, there are some gaps in the bunch pat-  
 1108        tern intended for preparing the dumping and injection of the beam, thus, the proton  
 1109        beams are composed of 2808 bunches.

1110        Once the proton beams reach the desired energy, they are brought to cross each

other producing  $pp$  collisions. The bunch crossing happens in precise places where the four LHC experiments are located, as seen in the top of Figure 2.7. In 2008  $pp$  collisions of  $\sqrt{s} = 7$  TeV were performed; the energy was increased to 8 TeV in 2012 and to 13 TeV in 2015.

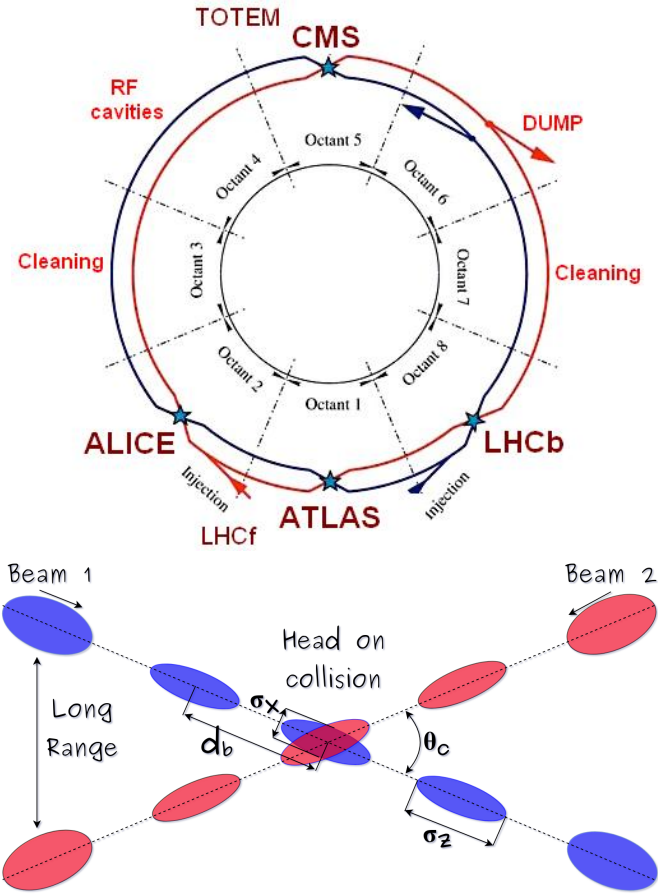


**Figure 2.7:** Top: LHC interaction points. Bunch crossing occurs where the LHC experiments are located [72]. Sections indicated as cleaning are dedicated to collimate the beam in order to protect the LHC ring from collisions with protons in very spreaded bunches. Bottom: bunch crossing scheme. Since the bunch crossing is not perfectly head-on, the luminosity is reduced in a factor of 17%; adapted from Reference [86].

The CMS and ATLAS experiments are multi-purpose experiments, hence, they are enabled to explore physics in any of the LHC collision modes. LHCb experiment is optimized to explore bottom quark physics, while ALICE is optimized for heavy

1118 ion collisions searches; TOTEM and LHCf are dedicated to forward physics studies;  
 1119 MoEDAL (not indicated in the Figure) is intended for monopole or massive pseudo  
 1120 stable particles searches.

1121 At the IP there are two interesting details that need to be addressed. The first  
 1122 one is that the bunch crossing does not occur head-on but at a small crossing angle  $\theta_c$   
 1123 (280  $\mu$ rad in CMS and ATLAS) as shown in the bottom side of Figure 2.7, affecting  
 1124 the overlapping between bunches; the consequence is a reduction of about 17% in  
 1125 the luminosity (represented by a factor not included in eqn. 2.2). The second one  
 1126 is the occurrence of multiple  $pp$  collisions in the same bunch crossing; this effect is  
 1127 called *pileup* (PU). A fairly simple estimation of the PU follows from estimating the  
 1128 probability of collision between two protons, one from each of the bunches in the  
 1129 course of collision; it depends roughly on the ratio of proton size and the cross section  
 1130 of the bunch in the IP, i.e.,

$$P(pp\text{-}collision) \sim \frac{d_{proton}^2}{\sigma_x \sigma_y} = \frac{(1\text{fm})^2}{(16\mu\text{m})^2} \sim 4 \times 10^{-21} \quad (2.4)$$

1131 however, there are  $N = 1.15 \times 10^{11}$  protons in a bunch, thus the estimated number of  
 1132 collisions in a bunch crossing is

$$PU = N^2 * P(pp\text{-}collision) \sim 50pp \text{ collision per bunch crossing}, \quad (2.5)$$

1133 about 20 of which are inelastic. A multiple  $pp$  collision event in a bunch crossing at  
 1134 CMS is shown in Figure 2.8.

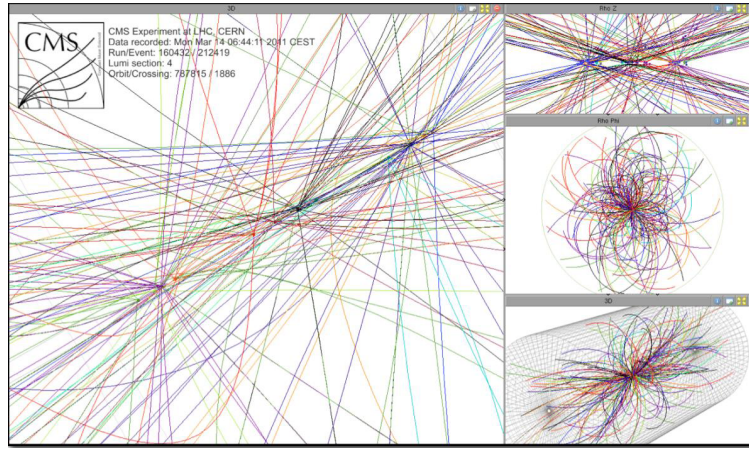


**Figure 2.8:** Multiple  $pp$  collision bunch crossing at CMS. [73].

## 1135 2.3 The CMS experiment

1136 CMS is a general-purpose detector designed to conduct research in a wide range  
 1137 of physics from the standard model to new physics like extra dimensions and dark  
 1138 matter. Located at Point 5 in the LHC layout as shown in Figure 2.4, CMS is  
 1139 composed of several detection systems distributed in a cylindrical structure; in total,  
 1140 CMS weights about 12500 tons in a very compact 21.6 m long and 14.6 m diameter  
 1141 cylinder. It was built in 15 separate sections at the ground level and lowered to the  
 1142 cavern individually to be assembled. A complete and detailed description of the CMS  
 1143 detector and its components is given in Reference [74] on which this section is based.  
 1144 Figure 2.9 shows the layout of the CMS detector. The detection system is composed  
 1145 of (from the innermost to the outermost)

- 1146     • Pixel detector.
- 1147     • Silicon strip tracker.
- 1148     • Preshower detector.
- 1149     • Electromagnetic calorimeter.

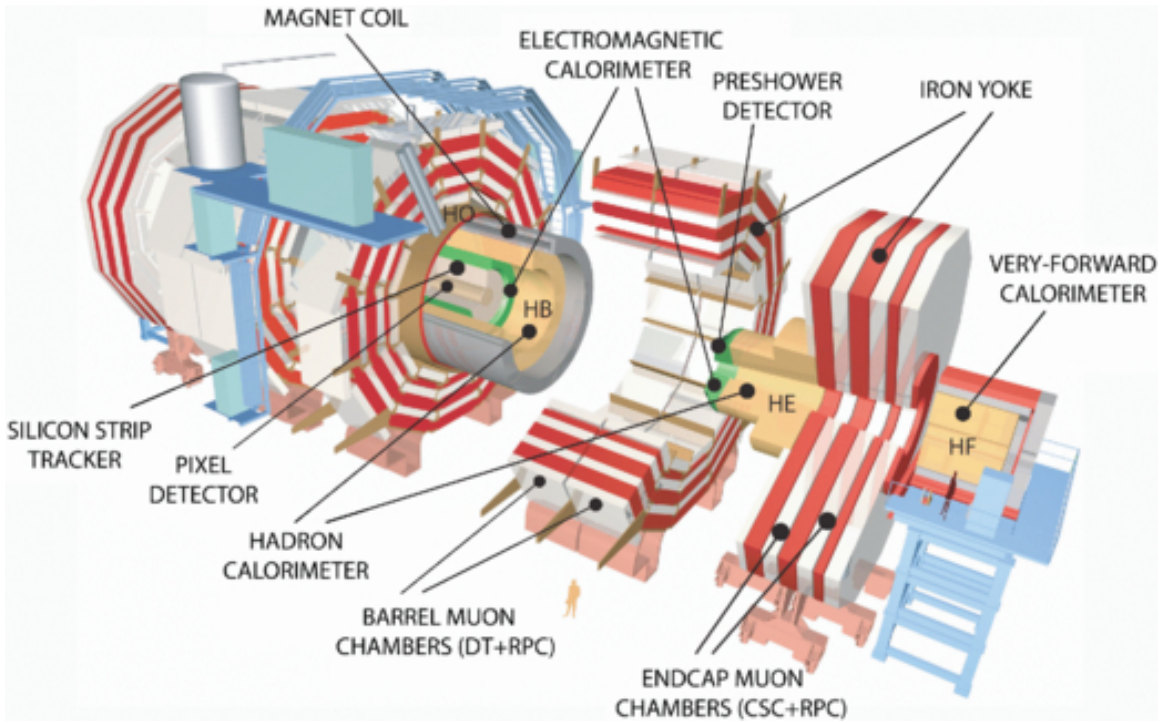


**Figure 2.9:** Layout of the CMS detector. The several subdetectors are indicated. The central region of the detector is referred as the barrel section while the endcaps are referred as the forward sections. [75].

1150 • Hadronic calorimeter.

1151 • Muon chambers (barrel and endcap)

1152 The central region of the detector is commonly referred as the barrel section while  
 1153 the endcaps are referred as the forward sections of the detector; thus, each subdetector  
 1154 is composed of a barrel section and a forward section.

1155 When a  $pp$  collision happens inside the CMS detector, many different particles are  
 1156 produced, but only some of them live long enough to be detected; they are electrons,  
 1157 photons, pions, kaons, protons, neutrons and muons; neutrinos are not detected by  
 1158 the CMS detector. Thus, the CMS detector was designed to detect those particles and  
 1159 measure their properties. Figure 2.10 shows a transverse slice of the CMS detector.  
 1160 The silicon tracker (pixel detector + strip tracker) is capable to register the track of

the charged particles traversing it, while calorimeters (electromagnetic and hadronic) measure the energy of the particles that are absorbed by their materials. Considering the detectable particles, mentioned above, emerging from the IP, a basic description of the detection process is as follows.

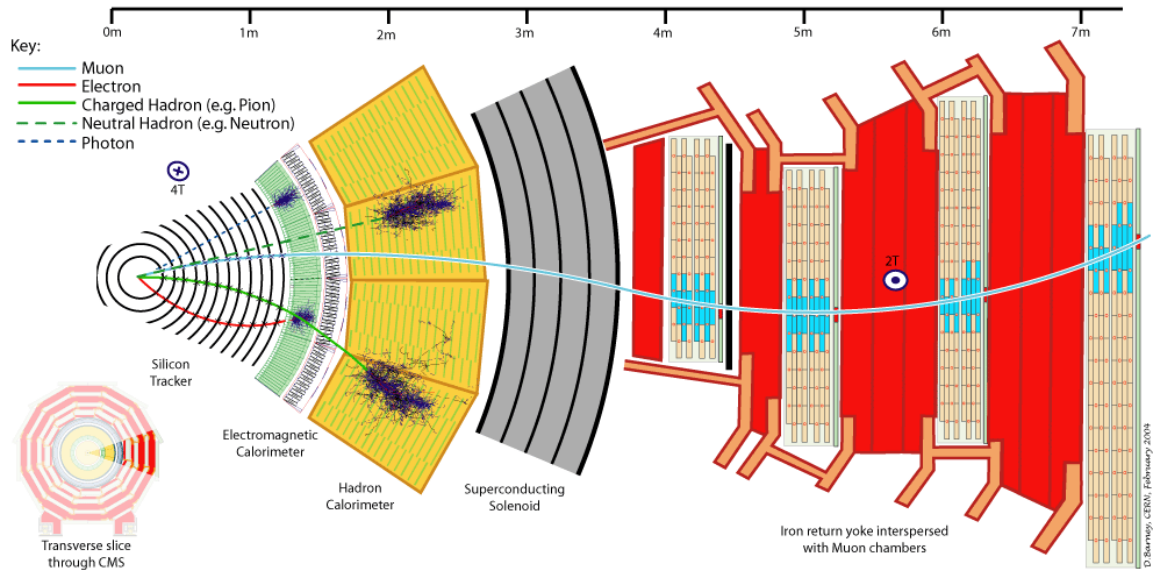


**Figure 2.10:** CMS detector transverse slice [76].

A muon emerging from the IP, will create a track on the silicon tracker and on the muon chambers. The design of the CMS detector is driven by the requirements on the identification, momentum resolution and unambiguous charge determination of the muons; therefore, a large bending power is provided by the solenoid magnet made of superconducting cable capable of generating a 3.8 T magnetic field. The muon track is bent twice since the magnetic field inside the solenoid is directed along the  $z$ -direction but outside its direction is reversed. Muons interact very weakly with the calorimeters, therefore, it is not absorbed but escape away from the detector.

An electron emerging from the IP will create a track along the tracker which will be bent due to the presence of the magnetic field, later, it will be absorbed in the electromagnetic calorimeter where its energy is measured.

1176 A photon will not leave a track because it is neutral, but it will be absorbed in  
 1177 the electromagnetic calorimeter.

1178 A neutral hadron, like the neutron, will not leave a track either but it will lose a  
 1179 small amount of its energy during its passage through the electromagnetic calorimeter  
 1180 and then it will be absorbed in the hadron calorimeter depositing the rest of its energy.

1181 A charged hadron, like the proton or  $\pi^\pm$ , will leave a curved track on the silicon  
 1182 tracker, some of its energy in the electromagnetic calorimeter and finally will be  
 1183 absorbed in the hadronic calorimeter.

1184 A more detailed description of each detection system will be presented in the  
 1185 following sections.

### 1186 2.3.1 CMS coordinate system

1187 The coordinate system used by CMS is centered on the geometrical center of the  
 1188 detector which is the nominal IP as shown in Figure 2.11<sup>1</sup>. The  $z$ -axis is parallel  
 1189 to the beam direction, while the  $Y$ -axis pointing vertically upward, and the  $X$ -axis  
 1190 pointing radially inward toward the center of the LHC.

1191 In addition to the common cartesian and cylindrical coordinate systems, two co-  
 1192 ordinates are of particular utility in particle physics: rapidity ( $y$ ) and pseudorapidity  
 1193 ( $\eta$ ), defined in connection to the polar angle  $\theta$ , energy and longitudinal momentum  
 1194 component (momentum along the  $z$ -axis) according to

$$y = \frac{1}{2} \ln \frac{E + p_z}{E - p_z} \quad \eta = -\ln \left( \tan \frac{\theta}{2} \right) \quad (2.6)$$

1195 Rapidity is related to the angle between the  $XY$ -plane and the direction in which  
 1196 the products of a collision are emitted; it has the nice property that the difference

---

<sup>1</sup> Not all the  $pp$  interaction occur at the nominal IP because of the bunch lenght, therefore, each  $pp$  collision has its own IP location

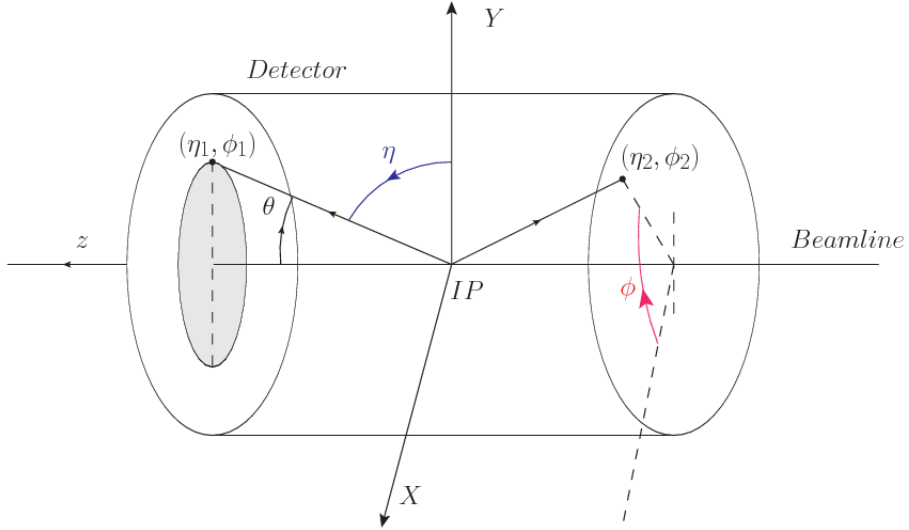


**Figure 2.11:** CMS detector coordinate system.

1197 between the rapidities of two particles is invariant with respect to Lorentz boosts  
 1198 along the  $z$ -axis, hence, data analysis becomes more simple when based on rapid-  
 1199 ity; however, it is not simple to measure the rapidity of highly relativistic particles,  
 1200 as those produced after  $pp$  collisions. Under the highly relativistic motion approxi-  
 1201 mation,  $y$  can be rewritten in terms of the polar angle, concluding that rapidity is  
 1202 approximately equal to the pseudorapidity defined above, i.e.,  $y \approx \eta$ . Note that  $\eta$   
 1203 is easier to measure than  $y$  given the direct relationship between the former and the  
 1204 polar angle.

1205 The angular distance between two objects in the detector ( $\Delta R$ ) is commonly used  
 1206 to judge the isolation of those object; it is defined in terms of their coordinates  $(\eta_1, \phi_1)$ ,  
 1207  $(\eta_2, \phi_2)$  as

$$\Delta R = \sqrt{(\Delta\eta)^2 - (\Delta\phi)^2} \quad (2.7)$$

### 1208 2.3.2 Tracking system

1209 The CMS tracking system is designed to provide a precise measurement of the trajectories (*track*) followed by the charged particles created after the  $pp$  collisions; also, the  
 1210 precise reconstruction of the primary and secondary origins of the tracks (*vertices*) is  
 1211 expected in an environment where, each 25 ns, the bunch crossing produces about 20  
 1212 inelastic collisions and about 1000 particles.  
 1213

1214 Physics requirements guiding the tracking system performance include the precise characterization of events involving gauge bosons, W and Z, and their leptonic  
 1215 decays for which an efficient isolated lepton and photon reconstruction is of capital  
 1216 importance, given that isolation is required to suppress background events to a level  
 1217 that allows observations of interesting processes like Higgs boson decays or beyond  
 1218 SM events.

1220 The ability to identify and reconstruct  $b$ -jets and B-hadrons within these jets is also  
 1221 a fundamental requirement, achieved through the ability to reconstruct accurately  
 1222 displaced vertices, given that  $b$ -jets are part of the signature of top quark physics, like  
 1223 the one treated in this thesis.

1224 An schematic view of the CMS tracking system is shown in Figure 2.12

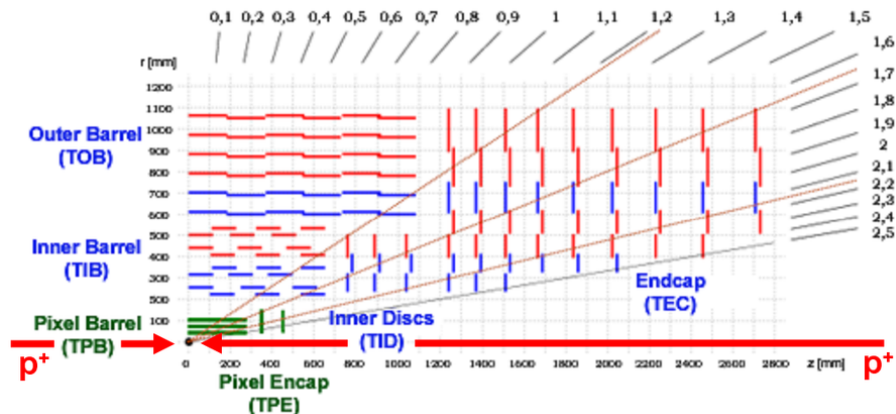


**Figure 2.12:** CMS tracking system schematic view [78].

1225 In order to satisfy these performance requirements, the tracking system uses two  
 1226 different detector subsystems arranged in concentric cylindrical volumes, the pixel  
 1227 detector and the silicon strip tracker; the pixel detector is located in the high particle  
 1228 density region ( $r < 20\text{cm}$ ) while the silicon strip tracker is located in the medium and  
 1229 lower particle density regions  $20\text{cm} < r < 116\text{cm}$ .

1230 **Pixel detector**

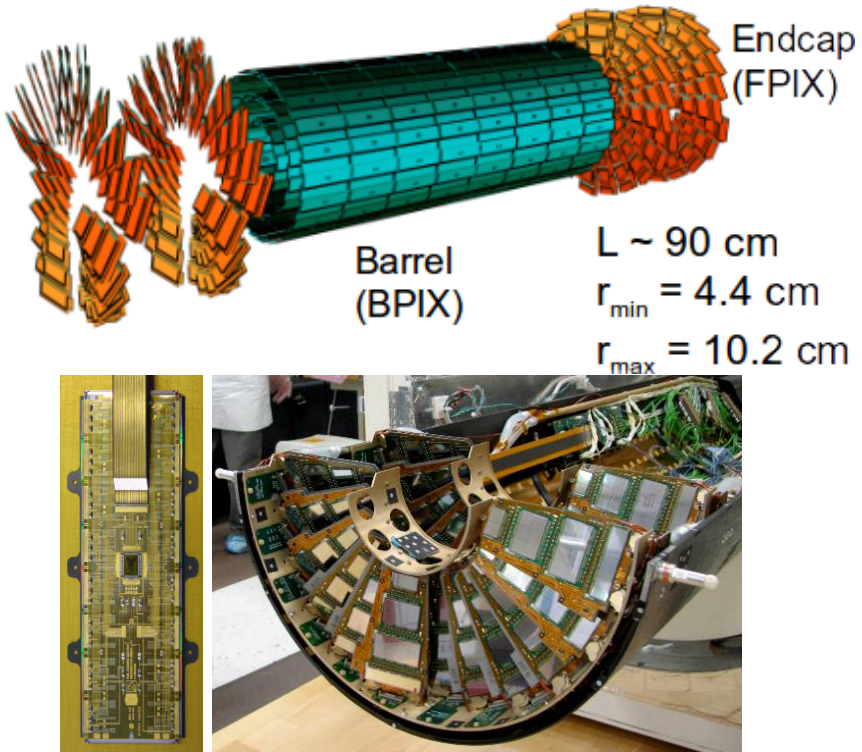


**Figure 2.13:** CMS pixel detector. Top: schematic view; Bottom: pictures of a barrel(BPIX) module(left) and forward modules(right) [74].

1231 The pixel detector was replaced during the 2016-2017 extended year-end technical  
 1232 stop, due to the increasingly challenging operating conditions like the higher particle  
 1233 flux and more radiation harsh environment, among others. The new one is responding  
 1234 as expected, reinforcing its crucial role in the successful way to fulfill the new LHC

physics objectives after the discovery of the Higgs boson. Since the data sets used in this thesis were produced using the previous version of the pixel detector, it will be the subject of the description in this section. The last chapter of this thesis is dedicated to describe my contribution to the *Forward Pixel Phase 1 upgrade*.

The pixel detector was composed of 1440 silicon pixel detector modules organized in three-barrel layers in the central region (BPix) and two disks in the forward region (FPix) as shown in the top side of Figure 2.13; it was designed to record efficiently and with high precision, up to  $20\mu\text{m}$  in the  $XY$ -plane and  $20\mu\text{m}$  in the  $z$ -direction, the first three space-points (*hits*) nearest to the IP region in the range  $|\eta| \leq 2.5$ . The first barrel layer was located at a radius of 44 mm from the beamline, while the third layer was located at a radius of 102 mm, closer to the strip tracker inner barrel layer (see Section 2.3.3) in order to reduce the rate of fake tracks. The high granularity of the detector is represented in its about 66 Mpixels, each of size  $100 \times 150\mu\text{m}^2$ . The transverse momentum resolution of tracks can be measured with a resolution of 1-2% for muons of  $p_T = 100$  GeV.

A charged particle passing through the pixel sensors produce ionization in them, giving energy for electrons to be removed from the silicon atoms, hence, creating electron-hole pairs. The collection of charges in the pixels generates an electrical signal that is read out by an electronic readout chip (ROC); each pixel has its own electronics which amplifies the signal. Combining the signal from the pixels activated by a traversing particle in the several layers of the detector allows one to reconstruct the particle's trajectory in 3D.

Commonly, the charge produced by traversing of a particle is collected by and shared among several pixels; by interpolating between pixels, the spatial resolution is improved. In the barrel section the charge sharing in the  $r\phi$ -plane is due to the Lorentz effect. In the forward pixels the charge sharing is enhanced by arranging the

1261 blades in the turbine-like layout as shown in Figure 2.13 bottom left.

### 1262 2.3.3 Silicon strip tracker

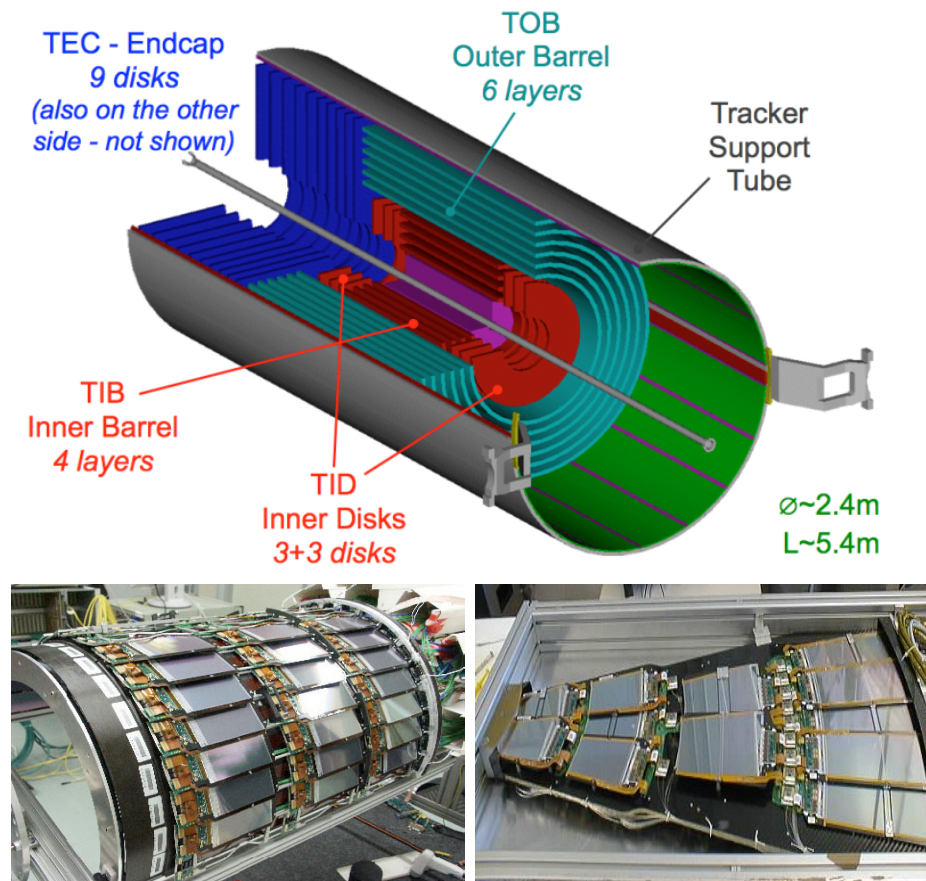


**Figure 2.14:** Top: CMS Silicon Strip Tracker (SST) schematic view. The SST is composed of the tracker inner barrel (TIB), the tracker inner disks (TID), the tracker outer barrel (TOB) and the tracker endcaps (TEC). Each part is made of silicon strip modules; the modules in blue represent two modules mounted back-to-back and rotated in the plane of the module by a stereo angle of 120 mrad in order to provide a 3-D reconstruction of the hit positions. Bottom: pictures of the TIB (left) and TEC (right) modules [80–82].

1263 The silicon strip tracker (SST) is the second stage in the CMS tracking system.

1264 The top side of Figure 2.14 shows a schematic of the SST. The inner tracker region is

1265 composed of the tracker inner barrel (TIB) and the tracker inner disks (TID) covering

1266 the region  $r < 55$  cm and  $|z| < 118$  cm. The TIB is composed of 4 layers while the TID

1267 is composed of 3 disks at each end. The silicon sensors in the inner tracker are 320  
 1268  $\mu\text{m}$  thick, providing a resolution of about 13-38  $\mu\text{m}$  in the  $r\phi$  position measurement.

1269       The modules indicated in blue in the schematic view of Figure 2.14 are two mod-  
 1270 ules mounted back-to-back and rotated in the plane of the module by a *stereo* angle  
 1271 of 100 mrad; the hits from these two modules, known as *stereo hits*, are combined to  
 1272 provide a measurement of the second coordinate ( $z$  in the barrel and  $r$  on the disks)  
 1273 allowing the reconstruction of hit positions in 3-D.

1274       The outer tracker region is composed of the tracker outer barrel (TOB) and the  
 1275 tracker endcaps (TEC). The six layers of the TOB offer coverage in the region  $r > 55$   
 1276 cm and  $|z| < 118$  cm, while the 9 disks of the TEC cover the region  $124 < |z| < 282$   
 1277 cm. The resolution offered by the outer tracker is about 13-38  $\mu\text{m}$  in the  $r\phi$  position  
 1278 measurement. The inner four TEC disks use silicon sensors 320  $\mu\text{m}$  thick; those in  
 1279 the TOB and the outer three TEC disks use silicon sensors of 500  $\mu\text{m}$  thickness. The  
 1280 silicon strips run parallel to the  $z$ -axis and the distance between strips varies from 80  
 1281  $\mu\text{m}$  in the inner TIB layers to 183  $\mu\text{m}$  in the inner TOB layers; in the endcaps the  
 1282 wedge-shaped sensors with radial strips, whose pitch range between 81  $\mu\text{m}$  at small  
 1283 radii and 205  $\mu\text{m}$  at large radii.

1284       The whole SST has 15148 silicon modules, 9.3 million silicon strips and cover a  
 1285 total active area of about 198  $\text{m}^2$ .

### 1286 2.3.4 Electromagnetic calorimeter

1287 The CMS electromagnetic calorimeter (ECAL) is designed to measure the energy of  
 1288 electrons and photons. It is composed of 75848 lead tungstate crystals which have a  
 1289 short radiation length (0.89 cm) and fast response, since 80% of the light is emitted  
 1290 within 25 ns; however, they are combined with Avalanche photodiodes (APDs) as

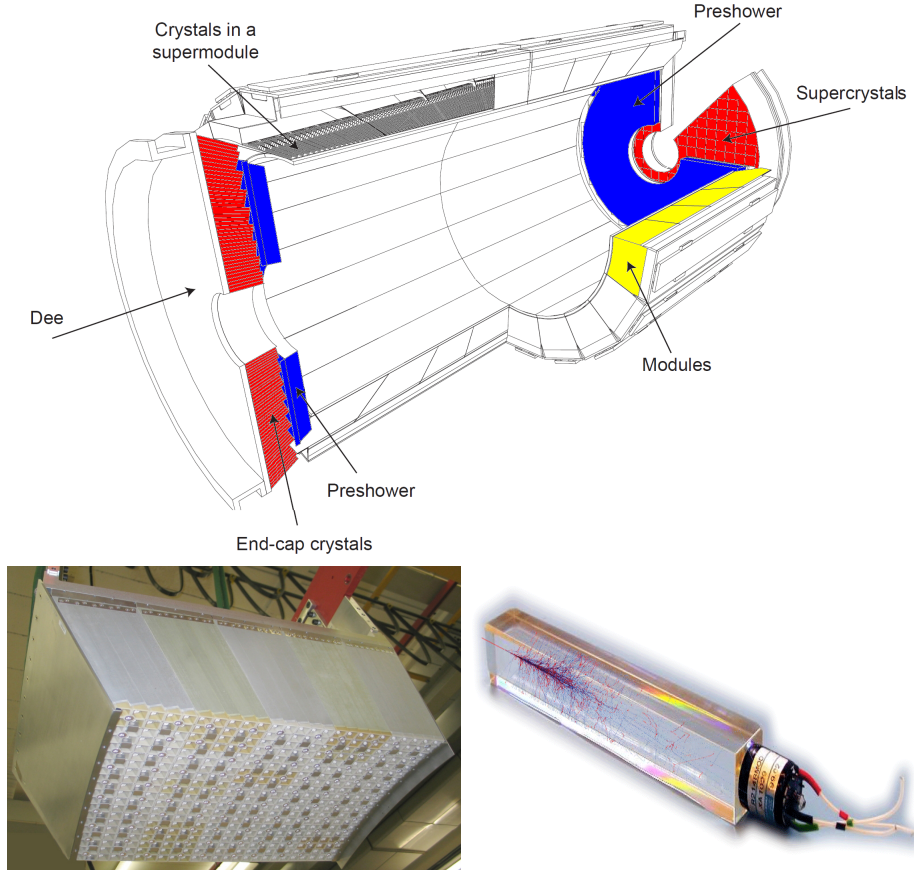


**Figure 2.15:** Top: CMS ECAL schematic view. Bottom: Module equipped with the crystals (left); ECAL crystal(right) with an artistic representation of an electromagnetic shower [74].

1291 photodetectors given that crystals themselves have a low light yield ( $30\gamma/\text{MeV}$ ). A  
 1292 schematic view of the ECAL is shown in Figure 2.15.

1293 Energy is measured when electrons and photons are absorbed by the crystals  
 1294 which generates an electromagnetic *shower*, as seen in bottom right picture of the  
 1295 Figure 2.15; the shower is seen as a *cluster* of energy which depending on the amount  
 1296 of energy deposited can involve several crystals. The ECAL barrel (EB) covers the  
 1297 region  $|\eta| < 1.479$ , using crystals of depth of 23 cm and  $2.2 \times 2.2 \text{ cm}^2$  transverse  
 1298 section; the ECAL endcap (EE) covers the region  $1.479 < |\eta| < 3.0$  using crystals of  
 1299 depth 22 cm and transverse section of  $2.86 \times 2.86 \text{ cm}^2$ ; the photodetectors used are

1300 vacuum phototriodes (VPTs). Each EE is divided in two structures called *Dees*.

1301       The preshower detector (ES) is installed in front of the EE and covers the region  
 1302       $1.653 < |\eta| < 2.6$ . The ES provides a precise measurement of the position of electro-  
 1303      magnetic showers, which allows to distinguish electrons and photon signals from  $\pi^0$   
 1304      decay signals. The ES is composed of a layer of lead radiators followed by a layer of  
 1305      silicon strip sensors. The lead radiators initiate electromagnetic showers when reached  
 1306      by photons and electrons, then, the strip sensors measure the deposited energy and  
 1307      the transverse shower profiles. The full ES thickness is 20 cm.

### 1308     **2.3.5 Hadronic calorimeter**

1309   Hadrons are not absorbed by the ECAL<sup>2</sup> but by the hadron calorimeter (HCAL),  
 1310   which is made of a combination of alternating brass absorber layers and silicon photo-  
 1311   multiplier(SiPM) layers; therefore, particles passing through the scintillator material  
 1312   produce showers, as in the ECAL, as a result of the inelastic scattering of the hadrons  
 1313   with the detector material. Since the particles are not absorbed in the scintillator,  
 1314   their energy is sampled; therefore the total energy is not measured but estimated from  
 1315   the energy clusters, which reduces the resolution of the detector. Brass was chosen  
 1316   as the absorber material due to its short interaction length ( $\lambda_I = 16.42\text{cm}$ ) and its  
 1317   non-magnetivity. Figure 2.16 shows a schematic view of the CMS HCAL.

1318       The HCAL is divided into four sections; the Hadron Barrel (HB), the Hadron  
 1319       Outer (HO), the Hadron Endcap (HE) and the Hadron Forward (HF) sections. The  
 1320       HB covers the region  $0 < |\eta| < 1.4$ , while the HE covers the region  $1.3 < |\eta| < 3.0$ .  
 1321       The HF, made of quartz fiber scintillator and steel as absorption material, covers the  
 1322       forward region  $3.0 < |\eta| < 5.2$ . Both the HB and HF are located inside the solenoid.  
 1323       The HO is placed outside the magnet as an additional layer of scintillators with the

---

<sup>2</sup> Most hadrons are not absorbed, but few low-energy ones might be.

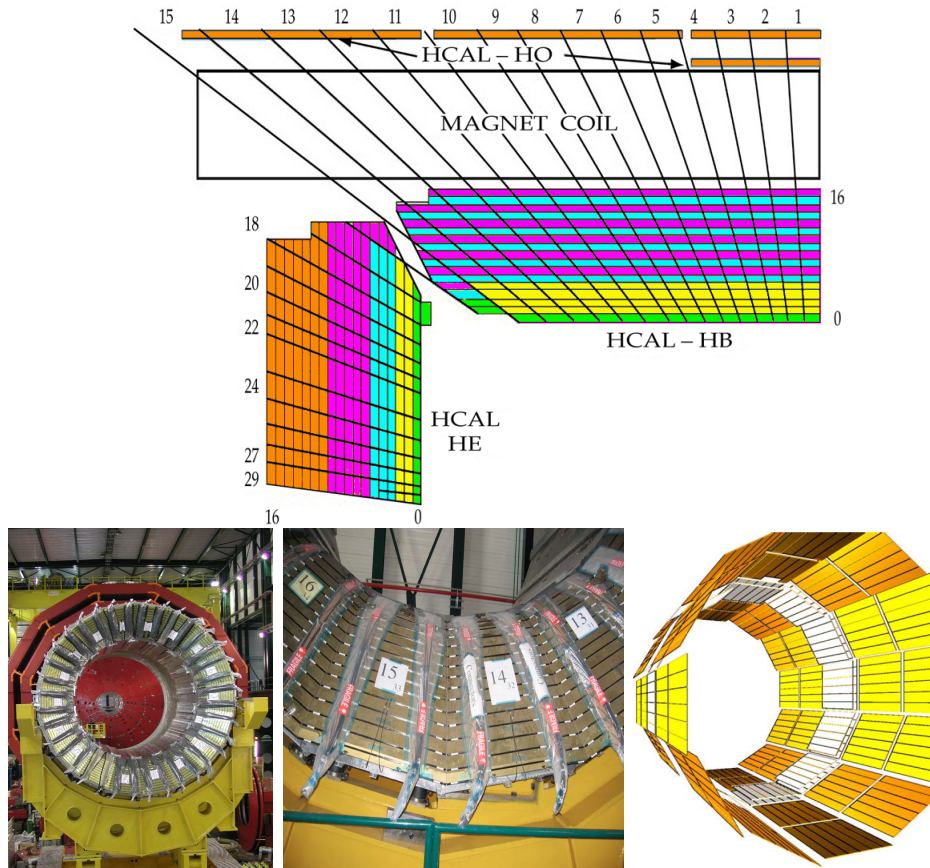


**Figure 2.16:** Top: CMS HCAL schematic view, the colors indicate the layers that are grouped into the same readout channels. Bottom: picture of a section of the HB; the absorber material is the golden region and scintillators are placed in between the absorber material (left and center). Schematic view of the HO (right). [83,84]

1324 purpose of measure the energy tails of particles passing through the HB and the  
 1325 magnet (see Figure 2.16 top and bottom right).

### 1326 **2.3.6 Superconducting solenoid magnet**

1327 The superconducting magnet installed in the CMS detector is designed to provide  
 1328 an intense and highly uniform magnetic field in the central part of the detector.  
 1329 In fact, the tracking system takes advantage of the bending power of the magnetic  
 1330 field to measure with precision the momentum of the particles that traverse it; the

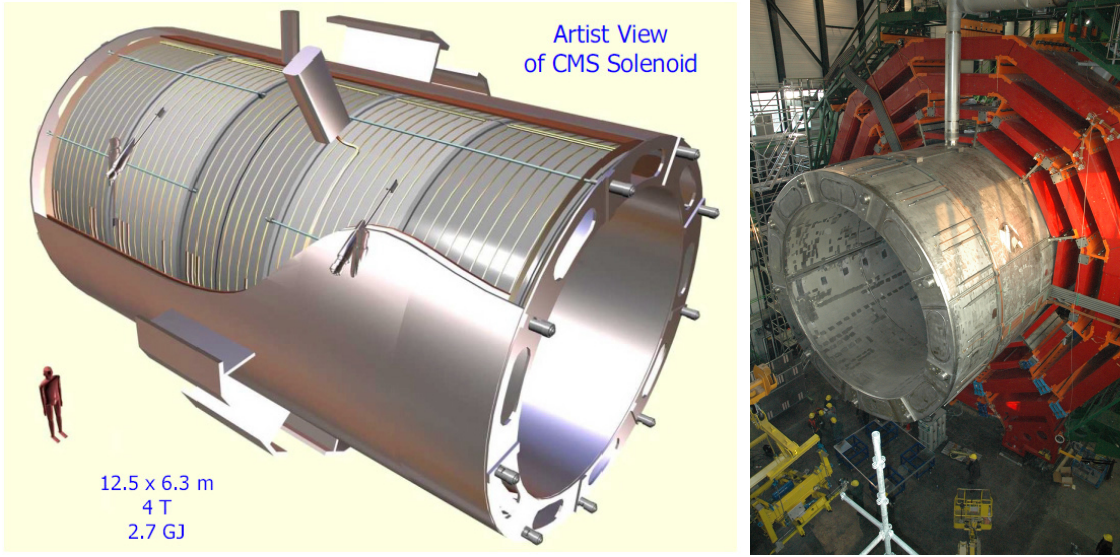


**Figure 2.17:** Artistic representation of the CMS solenoid magnet(left). The magnet is supported on an iron yoke (right) which also serves as the house of the muon detector and as mechanical support for the whole CMS detector [77].

1331 unambiguous determination of the sign for high momentum muons was a driving  
 1332 principle during the design of the magnet. The magnet has a diameter of 6.3 m, a  
 1333 length of 12.5 m and a cold mass of 220 t; the generated magnetic field reaches a  
 1334 strength of 3.8T. Since it is made of Ni-Tb superconducting cable it has to operate at  
 1335 a temperature of 4.7 K by using a helium cryogenic system; the current circulating in  
 1336 the cables reaches 18800 A under normal running conditions. The left side of Figure  
 1337 2.17 shows an artistic view of the CMS magnet, while the right side shows a transverse  
 1338 view of the cold mass where the winding structure is visible.

1339 The yoke (see Figure 2.17), composed of 5 barrel wheels and 6 endcap disks made  
 1340 of iron, serves not only as the media for magnetic flux return but also provides housing  
 1341 for the muon detector system and structural stability to the full detector.

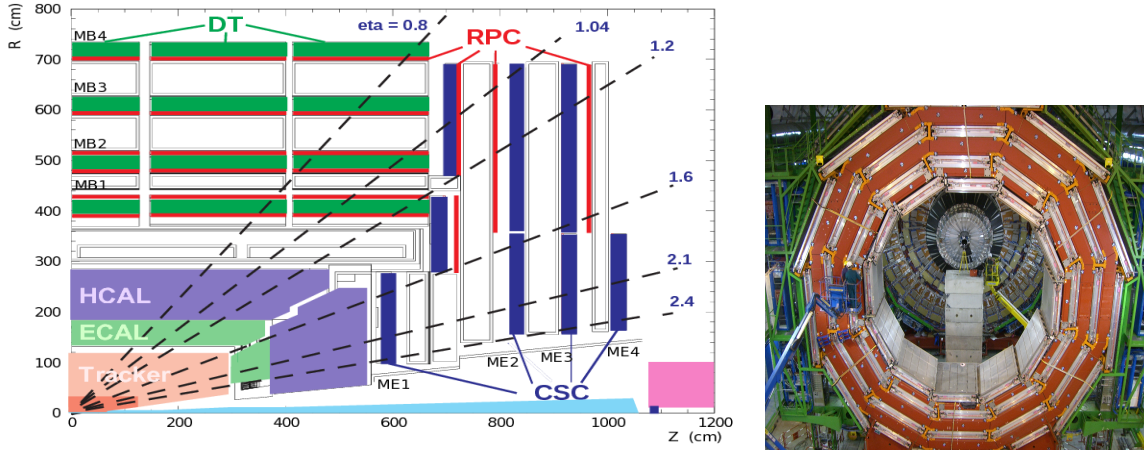


**Figure 2.18:** Left: CMS muon system schematic view; Right: one of the yoke rings with the muon DTs and RPCs installed; in the back it is possible to see the muon endcap [85].

### 1342 2.3.7 Muon system

1343 Muons are the only charged particles able to pass through all the CMS detector due  
 1344 to their low ionization energy loss; thus, muons can be separated easily from the  
 1345 high amount of particles produced in a  $pp$  collision. Also, muons are expected to be  
 1346 produced in the decay of several new particles; therefore, good detection of muons  
 1347 was one of the leading principles when designing the CMS detector.

1348 The CMS muon detection system (muon spectrometer) is embedded in the return  
 1349 yoke as seen in Figure 2.18. It is composed of three different detector types, the drift  
 1350 tube chambers (DT), cathode strip chambers (CSC), and resistive plate chambers  
 1351 (RPC); DT are located in the central region  $\eta < 1.2$  arranged in four layers of drift  
 1352 chambers filled with an Ar/CO<sub>2</sub> gas mixture.

1353 The muon endcaps are made of CSCs covering the region  $\eta < 2.4$  and filled with  
 1354 a mixture of Ar/CO<sub>2</sub>/CF<sub>4</sub>. The reason behind using a different detector type lies on  
 1355 the different conditions in the forward region like the higher muon rate and higher  
 1356 residual magnetic field compared to the central region.

1357 The third type of detector used in the muon system is a set of four disks of RPCs

1358 working in avalanche mode. The RPCs provide good spatial and time resolutions. The  
 1359 track of high- $p_T$  muon candidates is built combining information from the tracking  
 1360 system and the signal from up to six RPCs and four DT chambers.

1361 The muon tracks are reconstructed from the hits in the several layers of the muon  
 1362 system.

### 1363 2.3.8 CMS trigger system

1364 CMS expects  $pp$  collisions every 25 ns, i.e., an interaction rate of 40 MHz for which  
 1365 it is not possible to store the recorded data in full. In order to handle this high event  
 1366 rate data, an online event selection, known as triggering, is performed; triggering  
 1367 reduces the event rate to 100 Hz for storage and further offline analysis.

1368 The trigger system starts with a reduction of the event rate to 100 kHz in the  
 1369 so-called *the level 1 trigger* (L1). L1 is based on dedicated programmable hardware  
 1370 like Field Programmable Gate Arrays (FPGAs) and Application Specific Integrated  
 1371 Circuits (ASICs), partly located in the detector itself; another portion is located in  
 1372 the CMS underground cavern. Hit pattern information from the muon chambers  
 1373 and the energy deposits in the calorimeter are used to decide if an event is accepted  
 1374 or rejected, according to selection requirements previously defined, which reflect the  
 1375 interesting physics processes. Figure 2.19 shows the L1 trigger architecture.

1376 The second stage in the trigger system is called *the high-level trigger* (HLT); events  
 1377 accepted by L1 are passed to HLT in order to make an initial reconstruction of them.  
 1378 HLT is software based and runs on a dedicated server farm, using selection algorithms  
 1379 and high-level object definitions; the event rate at HLT is reduced to 100 Hz. The  
 1380 first HLT stage takes information from the muon detectors and the calorimeters to  
 1381 make the initial object reconstruction; in the next HLT stage, information from the

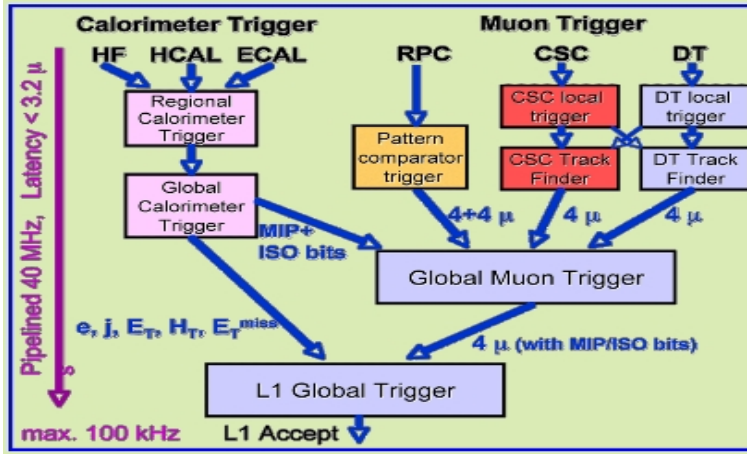


**Figure 2.19:** CMS Level-1 trigger architecture [86].

pixel and strip detectors is used to do first fast tracking and then full tracking online. This initial object reconstruction is used in further steps of the trigger system.

Events and preliminary reconstructed physics objects from HLT are sent to be fully reconstructed at the CERN computing center known also as Tier-0 facility. Again, the pixel detector information provides high-quality seeds for the track reconstruction algorithm offline, primary vertex reconstruction, electron and photon identification, muon reconstruction,  $\tau$  identification, and b-tagging. After full reconstruction, data sets are made available for offline analyses.

### 2.3.9 CMS computing

Data coming from the experiment have to be stored and made available for further analysis; in order to cope with all the tasks implied in the offline data processing, like transfer, simulation, reconstruction and reprocessing, among others, a large computing power is required. The CMS computing system is based on the distributed architecture concept, where users of the system and physical computer centers are distributed worldwide and interconnected by high-speed networks.

The worldwide LHC computing grid (WLCG) is the mechanism used to provide

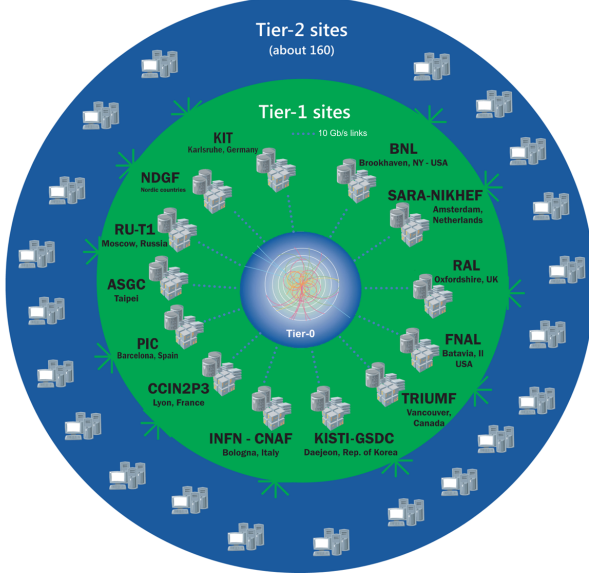


**Figure 2.20:** WLCG structure. The primary computer centers (Tier-0) are located at CERN (data center) and at the Wigner datacenter in Budapest. Tier-1 is composed of 13 centers and Tier-2 is composed of about 160 centers. [87].

1398 that distributed environment. WLCG is a tiered structure connecting computing  
 1399 centers around the world, which provides the necessary storage and computing facil-  
 1400 ties. The primary computing centers of the WLCG are located at the CERN and  
 1401 the Wigner datacenter in Budapest and are known as Tier-0 as shown in Figure 2.20.  
 1402 The main responsibilities for each tier level are [87]

- 1403     • **Tier-0:** initial reconstruction of recorded events and storage of the resulting  
       1404 datasets, the distribution of raw data to the Tier-1 centers.
- 1405     • **Tier-1:** provide storage capacity, support for the Grid, safe-keeping of a pro-  
       1406 portional share of raw and reconstructed data, large-scale reprocessing and safe-  
       1407 keeping of corresponding output, generation of simulated events, distribution  
       1408 of data to Tier 2s, safe-keeping of a share of simulated data produced at these  
       1409 Tier 2s.
- 1410     • **Tier-2:** store sufficient data and provide adequate computing power for spe-

1411       cific analysis tasks and proportional share of simulated event production and  
1412       reconstruction.

1413       Aside from the general computing strategy to manage the huge amount of data  
1414       produced by experiments, CMS uses a software framework to perform a variety of  
1415       processing, selection and analysis tasks. The central concept of the CMS data model  
1416       referred to as *event data model* (EDM) is the *Event*; therefore, an event is the unit  
1417       that contains the information from a single bunch crossing, any data derived from  
1418       that information like the reconstructed objects, and the details of the derivation.

1419       Events are passed as the input to the *physics modules* that obtain information  
1420       from them and create new information; for instance, *event data producers* add new  
1421       data into the events, *analyzers* produce an information summary from an event set,  
1422       *filters* perform selection and triggering.

1423       CMS uses several event formats with different levels of detail and precision

1424       • **Raw format:** events in this format contain the full recorded information from  
1425       the detector as well as trigger decision and other metadata. An extended version  
1426       of raw data is used to store information from the CMS Monte Carlo simulation  
1427       tools (see Chapter 3). Raw data are stored permanently, occupying about  
1428       2MB/event

1429       • **RECO format:** events in this format correspond to raw data that have been  
1430       submitted to reconstruction algorithms like primary and secondary vertex re-  
1431       construction, particle ID, and track finding. RECO events contain physics ob-  
1432       jects and all the information used to reconstruct them; average size is about 0.5  
1433       MB/event.

- 1434     • **AOD format:** Analysis Object Data (AOD) is the data format used in the  
 1435       physics analyses given that it contains the parameters describing the high-level  
 1436       physics objects in addition to enough information to allow a kinematic refitting if  
 1437       needed. AOD events are filtered versions of the RECO events to which skimming  
 1438       or other filtering have been applied, hence AOD events are subsets of RECO  
 1439       events. Requires about 100 kB/event.
- 1440     • **Non-event data** are data needed to interpret and reconstruct events. Some  
 1441       of the non-event data used by CMS contains information about the detector  
 1442       contraction and condition data like calibrations, alignment, and detector status.

1443     Figure 2.21 shows the data flow scheme between CMS detector and tiers.

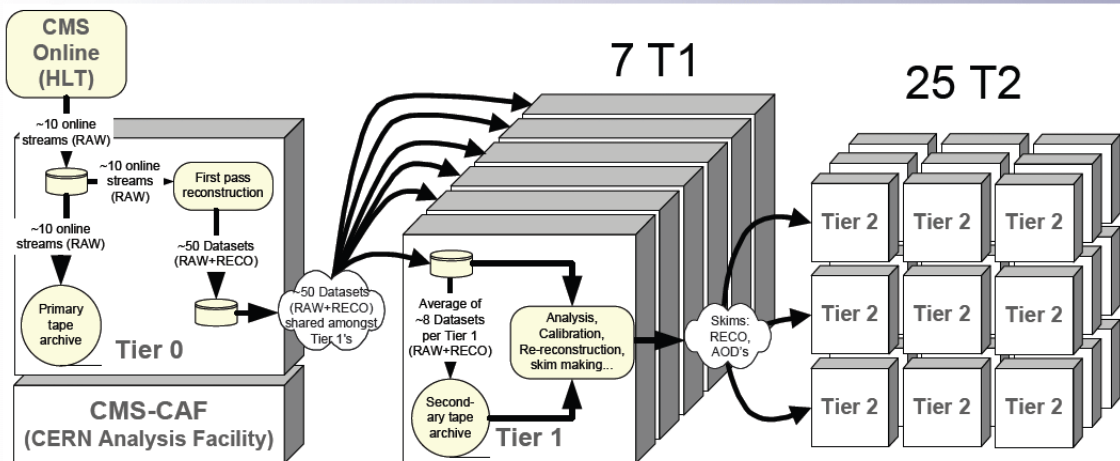


**Figure 2.21:** Data flow from CMS detector through tiers.

1444     The whole collection of software built as a framework is referred to as *CMSSW*. This  
 1445       framework provides the services needed by the simulation, calibration and alignment,  
 1446       and reconstruction modules that process event data, so that physicists can perform  
 1447       analysis. The CMSSW event processing model is composed of one executable, called  
 1448       `cmsRun`, and several plug-in modules which contains all the tools (calibration, recon-

1449 struction algorithms) needed to process an event. The same executable is used for  
1450 both detector data and Monte Carlo simulations [88].

1451 **Chapter 3**

1452 **Event generation, simulation and  
1453 reconstruction**

1454 The process of analyzing data recorded by the CMS experiment involves several stages  
1455 where the data are processed in order to interpret the information provided by all  
1456 the detection systems; in those stages, the particles produced after the  $pp$  collision  
1457 are identified by reconstructing their trajectories and measuring their features. In  
1458 addition, the SM provides a set of predictions that have to be compared with the  
1459 experimental results; however, in most of the cases, theoretical predictions are not  
1460 directly comparable to experimental results due to the diverse source of uncertainties  
1461 introduced by the experimental setup and theoretical approximations, among others.

1462 The strategy to face these conditions consists in using statistical methods imple-  
1463 mented in computational algorithms to produce numerical results that can be con-  
1464 trasted with the experimental results. These computational algorithms are commonly  
1465 known as Monte Carlo (MC) methods and, in the case of particle physics, they are  
1466 designed to apply the SM rules and produce predictions about the physical observ-  
1467 ables measured in the experiments. Since particle physics is governed by quantum

mechanics principles, predictions are not allowed from single events; therefore, a high number of events are *generated* and predictions are produced in the form of statistical distributions for the observables. Effects of the detector presence are included in the predictions by introducing simulations of the detector itself.

This chapter presents a description of the event generation strategy and the tools used to perform the detector simulation and physics objects reconstruction. A comprehensive review of event generators for LHC physics can be found in Reference [89] on which this chapter is based.

### 3.1 Event generation

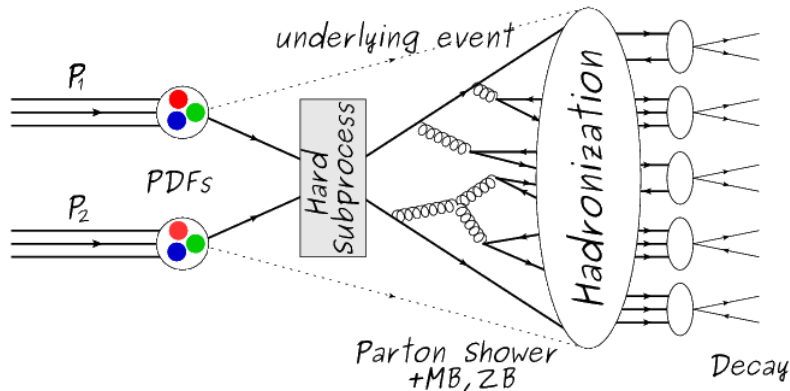


**Figure 3.1:** Event generation process. The actual interaction is generated in the hard subprocess. The parton shower describes the evolution of the partons from the hard subprocess. Modified from Reference [90].

The event generation is intended to create events that mimic the behavior of actual events produced in collisions; they obey a sequence of steps from the particles collision hard process to the decay process into the final state. Figure 3.1 shows a schematic view of the event generation process; the fact that the full process can be treated as several independent steps is motivated by the QCD factorization theorem.

1482 Generation starts by taking into account the PDFs of the incoming particles.  
 1483 Event generators offer the option to chose from several PDF sets depending on the  
 1484 particular process under simulation<sup>1</sup>; in the following,  $pp$  collisions will be consid-  
 1485 ered. The *hard subprocess* describes the actual interaction between partons from the  
 1486 incoming protons; it is represented by the matrix element connecting the initial and  
 1487 final states of the interaction. Normally, the matrix element can be written as a  
 1488 sum over Feynman diagrams and consider interferences between terms in the sum-  
 1489 mation. During the generation of the hard subprocess, the production cross section  
 1490 is calculated.

1491 The order to which the cross section is calculated depends on the order of the Feyn-  
 1492 man diagrams involved in the calculation; therefore, radiative corrections are included  
 1493 by considering a higher order Feynman diagrams where QCD radiation dominates.  
 1494 Currently, cross sections calculated to LO do not offer a satisfactory description of the  
 1495 processes, i.e., the results are only reliable for the shape of distributions; therefore,  
 1496 NLO calculations have to be performed with the implication that the computing time  
 1497 needed is highly increased.

1498 The final parton content of the hard subprocess is subjected to the *parton shower*  
 1499 which generates the gluon radiation. Parton shower evolves the partons, i.e., glouns  
 1500 split into quark-antiquark pairs and quarks with enough energy radiate gluons giv-  
 1501 ing rise to further parton multiplication, following the DGLAP (Dokshitzer-Gribov-  
 1502 Lipatov-Altarelli-Parisi) equations. Showering continues until the energy scale is low  
 1503 enough to reach the non-perturbative limit.

1504 In the simulation of LHC processes that involve  $b$  quarks, like the single top quark  
 1505 or Higgs associated production, it is needed to consider that the  $b$  quark is heavier  
 1506 than the proton; hence, the QCD interaction description is made in two different

---

<sup>1</sup> Tool in Reference [91] allows to plot different PDF sets under customizable conditions.

1507 schemes [95]

- 1508     • four-flavor (4F) scheme.  $b$  quarks appear only in the final state because they  
 1509       are heavier than the proton and therefore they can be produced only from the  
 1510       splitting of a gluon into pairs or singly in association with a  $t$  quark in high  
 1511       energy-scale interactions; furthermore, during the simulation, the  $b$ -PDFs are set  
 1512       to zero. Calculations in this scheme are more complicated due to the presence  
 1513       of the second  $b$  quark but the full kinematics is considered already at LO and  
 1514       therefore the accuracy of the description is better.
  
- 1515     • five-flavor (5F) scheme.  $b$  quarks are considered massless, therefore they can  
 1516       appear in both initial and final states since they can now be part of the proton;  
 1517       thus, during the simulation  $b$ -PDFs are not set to zero. In this scheme, calcula-  
 1518       tions are simpler than in the 4F scheme and possible logarithmic divergences  
 1519       are absorbed by the PDFs through the DGLAP evolution.

1520     In this thesis, the  $tHq$  events are generated using the 4F scheme in order to reduce  
 1521     uncertainties, while the  $tHW$  events are generated using the 5F scheme to eliminate  
 1522     LO interference with  $t\bar{t}H$  process [48].

1523     Partons involved in the  $pp$  collision are the focus of the simulation, however, the  
 1524     rest of the partons inside the incoming protons are also affected because the remnants  
 1525     are colored objects; also, multiple parton interactions can occur. The hadronization  
 1526     of the remnants and multiple parton interactions are known as *underlying event* and  
 1527     it has to be included in the simulation. In addition, multiple  $pp$  collisions in the same  
 1528     bunch crossing (pile-up mentioned in 2.2) occurs, actually in two forms

- 1529     • *in-time PU* which refers to multiple  $pp$  collision in the bunch crossing but that  
 1530       are not considered as primary vertices.

1531       • *Out-of-time PU* which refers to overlapping  $pp$  collisions from consecutive bunch  
 1532       crossings; this can occur due to the time-delays in the detection systems where  
 1533       information from one bunch crossing is assigned to the next or previous one.

1534       While the underlying event effects are included in generation using generator-  
 1535       specific tools, PU effects are added to the generation by overlaying Minimum-bias (MB)  
 1536       and Zero-bias (ZB) events to the generated events. MB events are inelastic events  
 1537       selected by using a loose trigger with as little bias as possible, therefore accepting a  
 1538       large fraction of the overall inelastic event; ZB events correspond to random events  
 1539       recorded by the detector when collisions are likely. MB models in-time PU and ZB  
 1540       models out-of-time PU.

1541       The next step in the generation process is called *hadronization*. Since particles  
 1542       with a net color charge are not allowed to exits isolated, they have to recombine  
 1543       to form bound states. This is precisely the process by which the partons resulting  
 1544       from the parton shower arrange themselves as color singlets to form hadrons. At  
 1545       this step, the energy-scale is low and the strong coupling constant is large, therefore  
 1546       hadronization process is non-perturbative and the evolution of the partons is described  
 1547       using phenomenological models. Most of the baryons and mesons produced in the  
 1548       hadronization are unstable and hence they will decay in the detector.

1549       The last step in the generation process corresponds to the decay of the unstable  
 1550       particles generated during hadronization; it is also simulated in the hadronization  
 1551       step, based on the known branching ratios.

## 1552       **3.2 Monte Carlo Event Generators.**

1553       The event generation described in the previous section has been implemented in  
 1554       several software packages for which a brief description is given.

- 1555     • **PYTHIA 8.** It is a program designed to perform the generation of high energy  
 1556        physics events which describes the collisions between particles such as electrons  
 1557        and protons. Several theories and models are implemented in it, in order to  
 1558        describe physical aspects like hard and soft interaction, parton distributions,  
 1559        initial and final-state parton showers, multiple parton interactions, beam rem-  
 1560        nants, hadronization<sup>2</sup> and particle decay. Thanks to extensive testing, several  
 1561        optimized parametrizations, known as *tunings*, have been defined in order to  
 1562        improve the description of actual collisions to a high degree of precision; for  
 1563        analysis at  $\sqrt{s} = 13$  TeV, the underline event CUETP8M1 tune is employed [97].  
 1564        The calculation of the matrix element is performed at LO which is not enough  
 1565        for the current required level of precision; therefore, pythia is often used for  
 1566        parton shower, hadronization and decays, while other event generators are used  
 1567        to generate the matrix element at NLO.
  
- 1568     • **MadGraph5\_aMC@NLO.** MadGraph is a matrix element generator which  
 1569        calculates the amplitudes for all contributing Feynman diagrams of a given  
 1570        process but does not provide a parton shower while MC@NLO incorporates  
 1571        NLO QCD matrix elements consistently into a parton shower framework; thus,  
 1572        MadGraph5\_aMC@NLO, as a merger of the two event generators MadGraph5  
 1573        and aMC@NLO, is an event generator capable to calculate tree-level and NLO  
 1574        cross sections and perform the matching of those with the parton shower. It is  
 1575        one of the most frequently used matrix element generators; however, it has the  
 1576        particular feature of the presence of negative event weights which reduce the  
 1577        number of events used to reproduce the properties of the objects generated [98].
  
- 1578     • **POWHEG.** It is an NLO matrix element generator where the hardest emis-

---

<sup>2</sup> based in the Lund string model [96]

1579 sion of color charged particles is generated in such a way that the negative event  
 1580 weights issue of MadGraph5\_aMC@NLO is overcome; however, the method re-  
 1581 quires an interface with  $p_T$ -ordered parton shower or a parton shower generator  
 1582 where this highest emission can be vetoed in order to avoid double counting of  
 1583 this highest-energetic emission. PYTHIA is a commonly matched to POWHEG  
 1584 event generator [100].

1585 Events resulting from the whole generation process are known as MC events.

### 1586 3.3 CMS detector simulation.

1587 After generation, MC events contain the physics of the collisions but they are not  
 1588 ready to be compared to the events recorded by the experiment since these recorded  
 1589 events correspond to the response of the detection systems to the interaction with  
 1590 the particles traversing them. The simulation of the CMS detector has to be applied  
 1591 on top of the event generation; it is simulated with a MC toolkit for the simulation  
 1592 of particles passing through matter called Geant4 which is also able to simulate the  
 1593 electronic signals that would be measured by all detectors inside CMS.

1594 The simulation takes the generated particles contained in the MC events as input,  
 1595 makes them pass through the simulated geometry, and models physics processes that  
 1596 particles experience during their passage through matter. The full set of results from  
 1597 particle-matter interactions corresponds to the simulated hit which contains informa-  
 1598 tion about the energy loss, momentum and position. Particles of the input event are  
 1599 called *primary*, while the particles originating from GEANT4-modeled interactions of  
 1600 a primary particle with matter are called a *secondary*. Simulated hits are the input  
 1601 of subsequent modules that emulate the response of the detector readout system and

1602 triggers. The output from the emulated detection systems and triggers is known as  
 1603 digitization [101, 102].

1604 The modeling of the CMS detector corresponds to the accurate modeling of the  
 1605 interaction among particles, the detector material, and the magnetic field. This  
 1606 simulation procedure includes the following standard steps

1607 • Modeling of the Interaction Region.

1608 • Modeling of the particle passage through the hierarchy of volumes that compose  
 1609 CMS detector and of the accompanying physics processes.

1610 • Modeling of the effect of multiple interactions per beam crossing and/or the  
 1611 effect of events overlay ( Pile-Up simulation).

1612 • Modeling of the detector's electronics response, signal shape, noise, calibration  
 1613 constants (digitization).

1614 In addition to the full simulation, i.e., a detailed detector simulation, a faster  
 1615 simulation (FastSim) have been developed, that may be used where much larger  
 1616 statistics are required. In FastSim, detector material effects are parametrized and  
 1617 included in the hits; those hits are used as input of the same higher-level algorithms<sup>3</sup>  
 1618 used to analyze the recorded events. In this way, comparisons between fast and full  
 1619 simulations can be performed [104].

1620 After the full detector simulation, the output events can be directly compared  
 1621 to events actually recorded in the CMS detector. The collection of MC events that  
 1622 reproduces the expected physics for a given process is known as MC sample.

---

<sup>3</sup> track fitting, calorimeter clustering, b tagging, electron identification, jet reconstruction and calibration, trigger algorithms which will be considered in the next sections

1623 **3.4 Event reconstruction.**

1624 The CMS experiment use the *particle-flow event reconstruction algorithm (PF)* to do  
1625 the reconstruction of particles produced in  $pp$  collisions. Next sections will present  
1626 a basic description of the *Elements* used by PF (tracker tracks, energy clusters, and  
1627 muon tracks), based in the References [105, 106] where more detailed descriptions can  
1628 be found.

1629 **3.4.1 Particle-Flow Algorithm.**

1630 Each of the several sub detection systems of the CMS detector is dedicated to identify  
1631 an specific type of particles, i.e., photons and electrons are absorbed by the ECAL  
1632 and their reconstruction is based on ECAL information; hadrons are reconstructed  
1633 from clusters in the HCAL while muons are reconstructed from hits in the muon  
1634 chambers. PF is designed to correlate signals from all the detector layers (tracks and  
1635 energy clusters) in order to reconstruct and identify each final state particle and its  
1636 properties as sketched in Figure 3.2.

1637 For instance, a charged hadron is identified by a geometrical connection, known  
1638 as *link*, between one or more calorimeter clusters and a track in the tracker, provided  
1639 there are no hits in the muon system; combining several measurements allows a better  
1640 determination of the energy and charge sign of the charged hadron.

1641 **Charged-particle track reconstruction.**

1642 The strategy used by PF in order to reconstruct tracks is called *Iterative Tracking*  
1643 which occurs in four steps

- 1644 • Seed generation where initial track candidates are found by looking for a combi-  
1645 nation of hits in the pixel detector, strip tracker, and muon chambers. In total

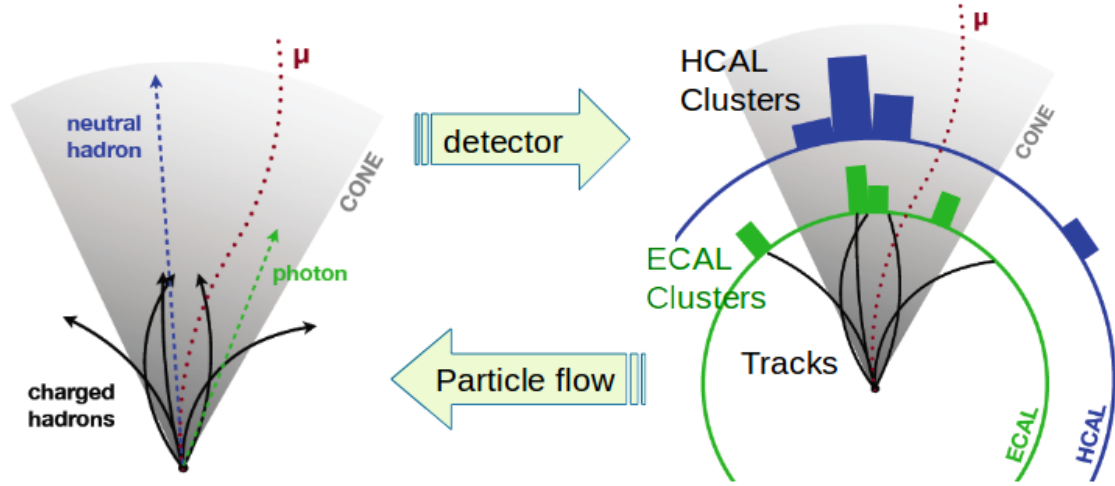


**Figure 3.2:** Particle flow algorithm. Information from the several CMS detection systems is provided as input to the algorithm which then combine it to identify and reconstruct all the particles in the final state and their properties. Reconstruction of simulated events is also performed by providing information from MC samples, detector and trigger simulation [107].

1646 ten iterations are performed, each one with a different seeding requirement.  
 1647 Seeds are used to estimate the trajectory parameters and uncertainties at the  
 1648 time of the full track reconstruction. Seeds are also considered track candidates.

- 1649     • Track finding using a tracking software known as Combinatorial Track Finder  
  1650       (CTF) [108]. The seed trajectories are extrapolated along the expected flight  
  1651       path of a charged particle, in agreement to the trajectory parameters obtained  
  1652       in the first step, in an attempt to find additional hits that can be assigned to  
  1653       the track candidates.
- 1654     • Track-fitting where the found tracks are passed as input to a module which  
  1655       provides the best estimate of the parameters of each trajectory.
- 1656     • Track selection where track candidates are submitted to a selection which dis-  
  1657       cards those that fail a set of defined quality criteria.

1658 Iterations differ in the seeding configuration and the final track selection as elab-

1659 orated in References [105, 106]. In the first iteration, high  $p_T$  tracks and tracks pro-  
 1660 duced near to the interaction region are identified and those hits are masked thereby  
 1661 reducing the combinatorial complexity. Next, iterations search for more complicated  
 1662 tracks, like low  $p_T$  tracks and tracks from b hadron decays, which tend to be displaced  
 1663 from the interaction region.

1664 **Vertex reconstruction.**

1665 During the track reconstruction, an extrapolation toward to the calorimeters is per-  
 1666 formed in order to match energy deposits; that extrapolation is performed also toward  
 1667 the beamline in order to find the origin of the track known as *vertex*. The vertex re-  
 1668 construction is performed by selecting from the available reconstructed tracks, those  
 1669 that are consistent with being originated in the interaction region where  $pp$  collisions  
 1670 are produced. The selection involves a requirement on the number of tracker (pixel  
 1671 and strip) hits and the goodness of the track fit.

1672 Selected tracks are clustered using a *deterministic annealing algorithm* (DA)<sup>4</sup>. A  
 1673 set of candidate vertices and their associated tracks, resulting from the DA, are then  
 1674 fitted with an *adaptive vertex fitter* (AVF) to produce the best estimate of the vertices  
 1675 locations.

1676 The  $p_T$  of the tracks associated to a reconstructed vertex is added, squared and  
 1677 used to organize the vertices; the vertex with the highest squared sum is designated  
 1678 as the *primary vertex* (*PV*) while the rest are designated as PU vertices.

1679 **Calorimeter clustering.**

1680 After traversing the CMS tracker system, electrons, photons and hadrons deposit their  
 1681 energy in the ECAL and HCAL cells. The PF clustering algorithm aims to provide

---

<sup>4</sup> DA algorithm and AVF are described in detail in References [110, 111]

1682 a high detection efficiency even for low-energy particles and an efficient distinction  
 1683 between close energy deposits. The clustering runs independently in the ECAL barrel  
 1684 and endcaps, HCAL barrel and endcaps, and the two preshower layers, following two  
 1685 steps

- 1686     • cells with an energy larger than a given seed threshold and larger than the energy  
 1687        of the neighboring cells are identified as cluster seeds. The neighbor cells are  
 1688        those that either share a side with the cluster seed candidate, or the eight closest  
 1689        cells including cells that only share a corner with the seed candidate.
- 1690     • cells with at least a corner in common with a cell already in the cluster seed  
 1691        and with an energy above a cell threshold are grouped into topological clusters.

1692 Clusters formed in this way are known as *particle-flow clusters*. With this cluster-  
 1693 ing strategy, it is possible to detect and measure the energy and direction of photons  
 1694 and neutral hadrons as well as differentiate these neutral particles from the charged  
 1695 hadron energy deposits. In cases involving charged hadrons for which the track pa-  
 1696 rameters are not determined accurately, for instance, low-quality and high- $p_T$  tracks,  
 1697 clustering helps in the energy measurements.

### 1698 Electron track reconstruction.

1699 Although the charged-particle track reconstruction described above works for elec-  
 1700 trons, they lose a significant fraction of their energy via bremsstrahlung photon radi-  
 1701 ation before reaching the ECAL; thus, the reconstruction performance depends on the  
 1702 ability to measure also the radiated energy. The reconstruction strategy, in this case,  
 1703 requires information from the tracking system and from the ECAL. Bremsstrahlung  
 1704 photons are emitted at similar  $\eta$  values to that of the electron but at different values  
 1705 of  $\phi$ ; therefore, the radiated energy can be recovered by grouping ECAL clusters in a

1706  $\eta$  window over a range of  $\phi$  around the electron direction. The group is called ECAL  
 1707 supercluster.

1708 Electron candidates from the track-seeding and ECAL super clustering are merged  
 1709 into a single collection which is submitted to a full electron tracking fit with a  
 1710 Gaussian-sum filter (GSF) [109]. The electron track and its associated ECAL su-  
 1711 percluster form a *particle-flow electron*.

## 1712 Muon track reconstruction.

1713 Given that the CMS detector is equipped with a muon spectrometer capable to iden-  
 1714 tify and measure the momentum of the muons traversing it, the muon reconstruction  
 1715 is not specific to PF; therefore, three different muon types are defined

- 1716     ● *Standalone muon.* A clustering on the DTs or CSCs hits is performed to form  
 1717       track segments; those segments are used as seeds for the reconstruction in the  
 1718       muon spectrometer. All DTs, CSCs, and RPCs hits along the muon trajectory  
 1719       are combined and fitted to form the full track. The fitting output is called a  
 1720       *standalone-muon track*.
- 1721     ● *Tracker muon.* Each track in the inner tracker with  $p_T$  larger than 0.5 GeV and  
 1722       a total momentum  $p$  larger than 2.5 GeV is extrapolated to the muon system.  
 1723       A *tracker muon track* corresponds to a extrapolated track that matches at least  
 1724       one muon segment.
- 1725     ● *Global muon.* When tracks in the inner tracker (inner tracks) and standalone-  
 1726       muon tracks are matched and turn out being compatibles, their hits are com-  
 1727       bined and fitted to form a *global-muon track*.

1728        Global muons sharing the same inner track with tracker muons are merged into  
 1729      a single candidate. PF muon identification uses the muon energy deposits in ECAL,  
 1730      HCAL, and HO associated with the muon track to improve the muon identification.

1731 **Particle identification and reconstruction.**

1732      PF elements are connected by a linker algorithm that tests the connection between any  
 1733      pair of elements; if they are found to be linked, a geometrical distance that quantifies  
 1734      the quality of the link is assigned. Two elements may be linked indirectly through  
 1735      common elements. Linked elements form *PF blocks* and each PF block may contain  
 1736      elements originating in one or more particles. Links can be established between  
 1737      tracks, between calorimeter clusters, and between tracks and calorimeter clusters.  
 1738      The identification and reconstruction start with a PF block and proceed as follows

1739        • Muons. An *isolated global muon* is identified by evaluating the presence of  
 1740      inner track and energy deposits close to the global muon track in the  $(\eta, \phi)$   
 1741      plane, i.e., in a particular point of the global muon track, inner tracks and  
 1742      energy deposits are sought within a radius of  $\Delta R = 0.3$  (see eqn. 2.7) from the  
 1743      muon track; if they exist and the  $p_T$  of the found track added to the  $E_T$  of the  
 1744      found energy deposit does not exceed 10% of the muon  $p_T$  then the global muon  
 1745      is an isolated global muon. This isolation condition is stringent enough to reject  
 1746      hadrons misidentified as muons.

1747        *Non-isolated global muons* are identified using additional selection requirements  
 1748      on the number of track segments in the muon system and energy deposits along  
 1749      the muon track. Muons inside jets are identified with more stringent criteria  
 1750      in isolation and momentum as described in Reference [112]. The PF elements  
 1751      associated with an identified muon are masked from the PF block.

- 1752     ● Electrons are identified and reconstructed as described above plus some addi-  
 1753       tional requirements on fourteen variables like the amount of energy radiated,  
 1754       the distance between the extrapolated track position at the ECAL and the po-  
 1755       sition of the associated ECAL supercluster, among others, which are combined  
 1756       in an specialized multivariate analysis strategy that improves the electron iden-  
 1757       tification. Tracks and clusters used to identify and reconstruct electrons are  
 1758       masked in the PF block.
- 1759     ● Isolated photons are identified from ECAL superclusters with  $E_T$  larger than 10  
 1760       GeV, for which the energy deposited at a distance of 0.15, from the supercluster  
 1761       position on the  $(\eta, \phi)$  plane, does not exceed 10% of the supercluster energy;  
 1762       note that this is an isolation requirement. In addition, there must not be links  
 1763       to tracks. Clusters involved in the identification and reconstruction are masked  
 1764       in the PF block.
- 1765     ● Bremsstrahlung photons and prompt photons tend to convert to electron-positron  
 1766       pairs inside the tracker, therefore, a dedicated finder algorithm is used to link  
 1767       tracks that seem to originate from a photon conversion; in case those two tracks  
 1768       are compatible with the direction of a bremsstrahlung photon, they are also  
 1769       linked to the original electron track. Photon conversion tracks are also masked  
 1770       in the PF block.
- 1771     ● The remaining elements in the PF block are used to identify hadrons. In the  
 1772       region  $|\eta| \leq 2.5$ , neutral hadrons are identified with HCAL clusters not linked  
 1773       to any track while photons from neutral pion decays are identified with ECAL  
 1774       clusters without links to tracks. In the region  $|\eta| > 2.5$  ECAL clusters linked to  
 1775       HCAL clusters are identified with a charged or neutral hadron shower; ECAL  
 1776       clusters with no links are identified with photons. HCAL clusters not used yet,

1777       are linked to one or more unlinked tracks and to an unlinked ECAL in order to  
 1778       reconstruct charged-hadrons or a combination of photons and neutral hadrons  
 1779       according to certain conditions on the calibrated calorimetric energy.

- 1780       • Charged-particle tracks may be liked together when they converge to a *sec-*  
 1781       *ondary vertex (SV)* displaced from the IP where the PV and PU vertices are  
 1782       reconstructed; at least three tracks are needed in that case, of which at most  
 1783       one has to be an incoming track with hits in tracker region between a PV and  
 1784       the SV.

1785       The linker algorithm, as well as the whole PF algorithm, has been validated and  
 1786       commissioned; results from that validation are presented in the Reference [105].

1787       **Jet reconstruction.**

1788       Quarks and gluons may be produced in the  $pp$  collisions, therefore, their hadronization  
 1789       will be seen in the detector as a shower of hadrons and their decay products in the  
 1790       form of a *jet*. Two classes of clustering algorithms have been developed based in  
 1791       their jet definition [113]:

- 1792       • Iterative cone algorithms (IC). Jets are defined in terms of circles of fixed radius  
 1793        $R$  in the  $\eta\text{-}\phi$  plane, known as *stable cones*, for which the sum of the momenta  
 1794       of all the particles within the cone points in the same direction as the center  
 1795       of the circle. The seed of the iteration is the hardest non-isolated particle in  
 1796       the event, then, the resulting momentum direction is assigned as the new cone  
 1797       direction and a new iteration starts; iteration process stops when the cone if  
 1798       found to be stable.

1799     • Sequential recombination algorithms. The distance between non-isolated par-  
 1800     ticles is calculated; if that distance is below a threshold, these particles are  
 1801     recombined into a new object. The sequence is repeated until the separation  
 1802     between the recombined object and any other particle is above certain thresh-  
 1803     old; the recombined object is called a jet and the algorithm starts again with  
 1804     the remaining particles.

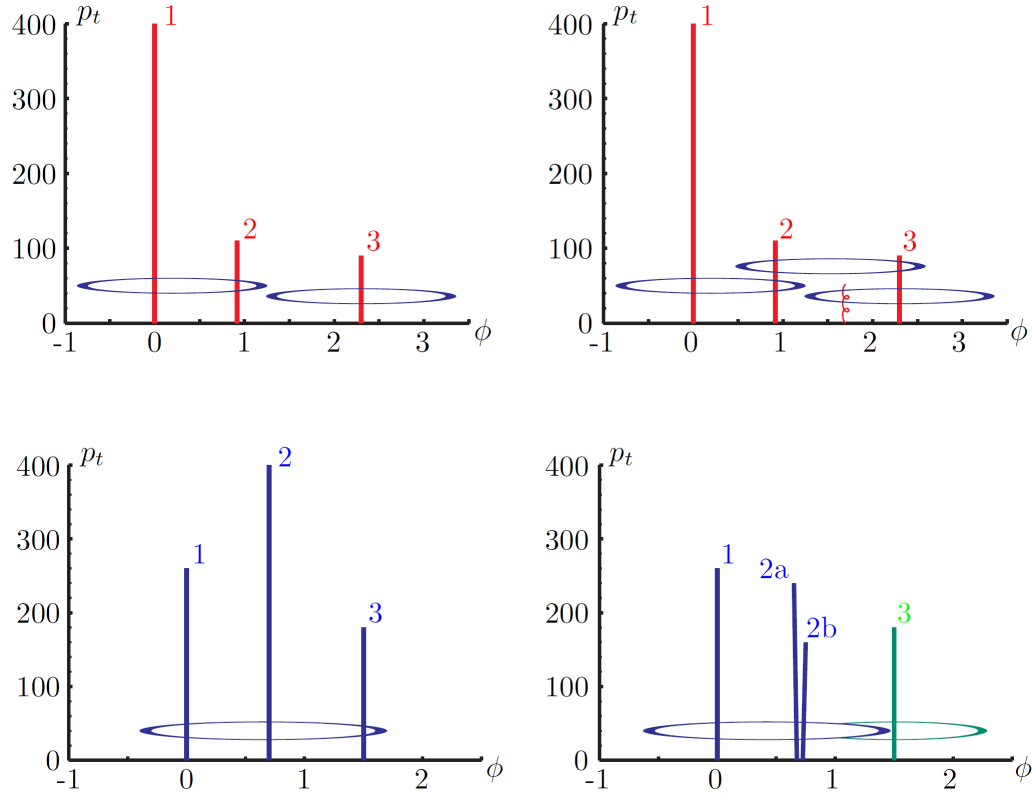


**Figure 3.3:** Stable cones identification using IC algorithms [113].

1805     Two conditions are of particular importance for the clustering algorithms, *infrared*  
 1806     and *collinear (IRC) safety*. In order to explain the concept of infrared (IR) safety,  
 1807     consider an event with three hard particles as shown in the top left side of Figure 3.3,  
 1808     two stable cones are found and then two jets are identified; if a soft gluon is added, as  
 1809     shown in the top right side of Figure 3.3, three stable cones are found and the three

1810 hard particles are now clustered into a single jet. If the addition of soft particles  
 1811 change the outcome of the clustering, then it is said that the algorithm is IR unsafe.  
 1812 Soft radiation is highly likely in perturbative QCD, which dominates the physics of  
 1813 the jets, and then IR unsafe effect leads to divergences [113].

1814 The concept of collinear safety can also be explained considering a three hard  
 1815 particles event, as shown in the bottom left side of Figure 3.3, where one stable cone  
 1816 containing all three particles is found and one jet is identified; if the hardest particle  
 1817 is split into two collinear particles (2a and 2b) in the bottom right side of Figure 3.3,  
 1818 then the clustering results in a different jet identification and the algorithm is said  
 1819 to be collinear unsafe. The collinear unsafe effect leads to divergences in jet cross  
 1820 section calculations [114].

1821 It has been determined that IC algorithms are IRC unsafe, and therefore, they  
 1822 have to be replaced by algorithms that not only provide the finite perturbative results  
 1823 from theoretical computations, but also that are not highly dependent on underlying  
 1824 event and pileup effects which leads to significant corrections [113].

1825 The sequential recombination algorithms arise as the IRC safe alternative used by  
 1826 the CMS experiment; in particular the anti- $k_t$  algorithm which is a generalization of  
 1827 the previously existing  $k_t$  [115] and Cambridge/Aachen [116] jet clustering algorithms.

1828 The anti- $k_t$  algorithm is used to perform the jet reconstruction by clustering those  
 1829 PF particles within a cone (see Figure 3.4); previously, isolated electrons, isolated  
 1830 muons, and charged particles associated with other interaction vertices are excluded  
 1831 from the clustering.

1832 The anti- $k_t$  algorithm proceeds in a sequential recombination of PF particles; the  
 1833 distance between particles  $i$  and  $j$  ( $d_{ij}$ ) and the distance between particles and the  
 1834 beam are defined as

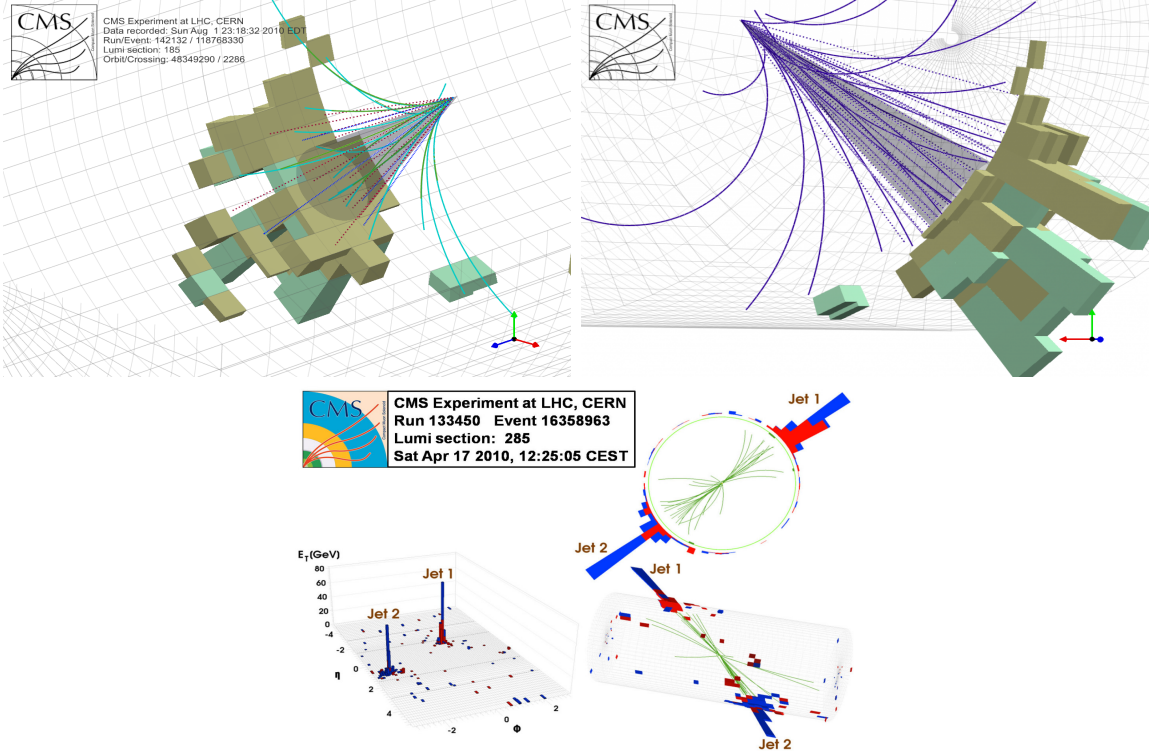


**Figure 3.4:** Jet reconstruction performed by the anti- $k_t$  algorithm. Top: Two different views of a CMS recorded event are presented. Continuous lines correspond to tracks left by charged particles in the tracker while dotted lines are the imaginary paths followed by neutral particles. The green cubes represent the ECAL cells while the blue ones represent the HCAL cells; in both cases, the height of the cube represent the amount of energy deposited in the cells [117]. Bottom: Reconstruction of a recorded event with two jets [118].

$$d_{ij} = \min\left(\frac{1}{k_{ti}^2}, \frac{1}{k_{tj}^2}\right) \frac{\Delta_{ij}^2}{R^2}$$

$$d_{iB} = \frac{1}{k_{ti}^2} \quad (3.1)$$

1835 where  $\Delta_{ij}^2 = (y_i - y_j)^2 + (\phi_i - \phi_j)^2$ ,  $k_{ti}$ ,  $y_i$  and  $\phi_i$  are the transverse momentum, ra-  
1836 pidity and azimuth of particle  $i$  respectively and  $R$  is the called jet radius. For all  
1837 the remaining PF particles, after removing the isolated ones,  $d_{ij}$  and  $d_{iB}$  are calcu-

lated<sup>5</sup> and the smallest is identified; if it is a  $d_{ij}$ , particles  $i$  and  $j$  are replaced with  
 a new object whose momentum is the vectorial sum of the combined particles. If the  
 smallest distance is a  $d_{iB}$  the clustering process ends, the object  $i$  (which at this stage  
 should be a combination of several PF particles) is declared as a *Particle-flow-jet* (PF  
 jet) and all the associated PF particles are removed from the detector. The clustering  
 process is repeated until no PF particles remain.  $R$  is a free parameter that can be  
 adjusted according to the specific analysis conditions; usually, two values are used,  
 $R=0.4$  and  $R=0.5$ , giving the name to the so-called AK4-jet and AK5-jet respectively.

An advantage of the anti- $k_t$  algorithm over other clustering algorithms is the reg-  
 ularity of the boundaries of the resulting jets. For all known IRC safe algorithms,  
 soft radiation can introduce irregularities in the boundaries of the final jets; however,  
 anti- $k_t$  algorithm is soft-resilient, meaning that jets shape is not affected by soft radi-  
 ation, which is a valuable property considering that knowing the typical shape of jets  
 makes experimental calibration of jets more simple. In addition, that soft-resilience  
 is expected to simplify certain theoretical calculations and reduce the momentum-  
 resolution loss caused by underlying-event (UE) and pileup contamination [114].

The effect of the UE and pileup contamination over a jet identification, can be  
 seen as if soft events are added to the jet; for instance, if a soft event representing UE  
 or pileup is added to an event for which a set of jets  $J$  have been identified, and the  
 clustering is rerun on that new extended event, the outcome will be different in two  
 aspects: jets will contain some additional soft energy and the distribution of particles  
 in jets may have change; that effect is called *back-reaction*. The back-reaction effect in  
 the anti- $k_t$  algorithm is suppressed not by the amount of momentum added to the jet  
 but by the jet transverse momentum  $p_{T,J}$ , which means that this strong suppression  
 leads to a smaller correction due to EU and pileup effect [114].

---

<sup>5</sup> Notice that this is a combinatorial calculation.

1863 Jet energy Corrections

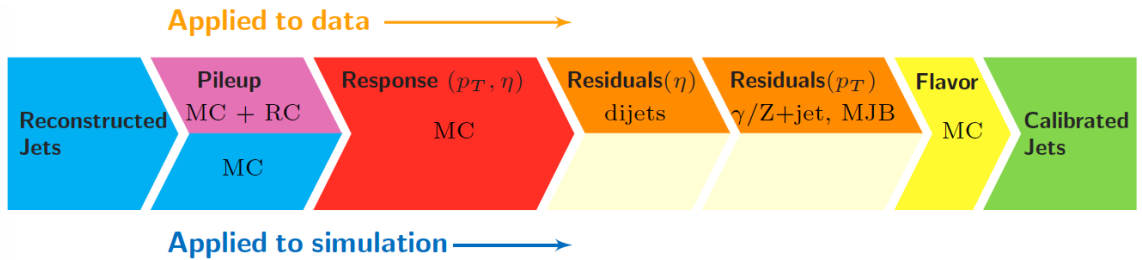


**Figure 3.5:** Jet energy correction diagram. Correction levels are applied sequentially in the indicated fixed order [120].

Even though jets can be reconstructed efficiently, there are some effects that are not included in the reconstruction and that lead to discrepancies between the reconstructed results and the predicted results; in order to overcome these discrepancies, a factorized model has been designed in the form of jet energy corrections (JEC) [119, 120] applied sequentially as shown in the diagram of Figure 3.5.

1869 At each level, the jet four-momentum is multiplied by a scaling factor based on  
1870 jet properties, i.e.,  $\eta$ , flavor, etc.

- Level 1 correction removes the energy coming from pile-up. The scale factor is determined using a MC sample of QCD dijet (2 jets) events with and without pileup overlay; it is parametrized in terms of the offset energy density  $\rho$ , jet area  $A$ , jet  $\eta$  and jet  $p_T$ . Different corrections are applied to data and MC due to the detector simulation.
  - MC-truth correction accounts for differences between the reconstructed jet energy and the MC particle-level energy. The correction is determined on a QCD dijet MC sample and is parametrized in terms of the jet  $p_T$  and  $\eta$ .
  - Residuals correct remaining small differences within jet response in data and MC. The Residuals  $\eta$ -dependent correction compares jets of similar  $p_T$  in the

1881 barrel reference region. The Residuals  $p_T$ -dependent correct the jet absolute  
 1882 scale (JES vs  $p_T$ ).

- 1883 • Jet-flavor corrections are derived in the same way as MC-truth corrections but  
 1884 using QCD pure flavor samples.

1885 ***b*-tagging of jets.**

1886 A particular feature of the hadrons containing bottom quarks (*b*-hadrons) is that  
 1887 their lifetime is long enough to travel some distance before decaying, but it is not as  
 1888 long as those of light quark hadrons; therefore, when looking at the hadrons produced  
 1889 in  $pp$  collisions, *b*-hadrons decay typically inside the tracker rather than reaching the  
 1890 calorimeters as some light-hadrons do. As a result, a *b*-hadron decay gives rise to a  
 1891 displaced vertex (secondary vertex) with respect to the primary vertex as shown in  
 1892 Figure 3.6; the SV displacement is in the order of a few millimeters. A jet resulting  
 1893 from the decay of a *b*-hadron is called *b* jet; other jets are called light jets.

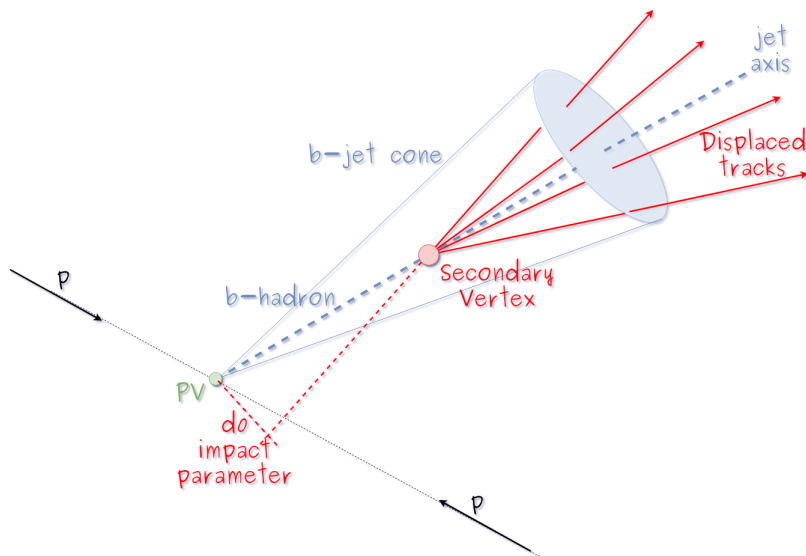


**Figure 3.6:** Secondary vertex in a *b*-hadron decay.

1894 Several methods to identify *b*-jets (*b*-tagging) have been developed; the method

1895 used in this thesis is known as *Combined Secondary Vertex* algorithm in its second  
 1896 version (CSVv2) [121]. By using information of the impact parameter, the recon-  
 1897 structed secondary vertices, and the jet kinematics as input in a multivariate analysis  
 1898 that combines the discrimination power of each variable in one global discrimina-  
 1899 tor variable, three working points (references): loose, medium and tight, are defined  
 1900 which quantify the probabilities of mistag jets from light quarks as jets from  $b$  quarks;  
 1901 10, 1 and 0.1 % respectively. Although the mistagging probability decreases with the  
 1902 working point strength, the efficiency to correctly tag  $b$ -jets also decreases as 83, 69  
 1903 and 49 % for the respective working point; therefore, a balance needs to be achieved  
 1904 according to the specific requirements of the analysis.

### 1905 3.4.1.1 Missing transverse energy.

1906 The fact that proton bunches carry momentum along the  $z$ -axis implies that for  
 1907 each event it is expected that the momentum in the transverse plane is balanced.  
 1908 Imbalances are quantified by the missing transverse energy (MET) and are attributed  
 1909 to several sources including particles escaping undetected through the beam pipe,  
 1910 neutrinos produced in weak interactions processes which do not interact with the  
 1911 detector and thus escaping without leaving a sign, or even undiscovered particles  
 1912 predicted by models beyond the SM.

1913 The PF algorithm assigns the negative sum of the momenta of all reconstructed  
 1914 PF particles to the *particle-flow MET* according to

$$\vec{E}_T = - \sum_i \vec{p}_{T,i} \quad (3.2)$$

1915 JEC are propagated to the calculation of the  $\vec{E}_T$  as described in the Reference [122].

### 1916 3.4.2 Event reconstruction examples

1917 Figures 3.7-3.9 show the results of the reconstruction performed on 3 recorded events.

1918 Descriptions are taken directly from the source.

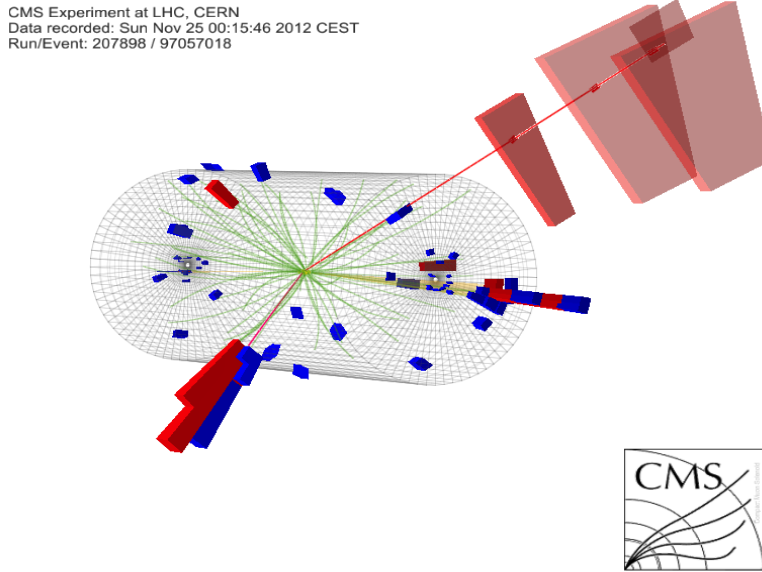


**Figure 3.7:** HIG-13-004 Event 1 reconstruction results; “HIG-13-004 Event 1: Event recorded with the CMS detector in 2012 at a proton-proton center-of-mass energy of 8 TeV. The event shows characteristics expected from the decay of the SM Higgs boson to a pair of  $\tau$  leptons. Such an event is characterized by the production of two forward-going jets, seen here in opposite endcaps. One of the  $\tau$  decays to a muon (red lines on the right) and neutrinos, while the other  $\tau$  decays into a charged hadron and a neutrino.” [123].

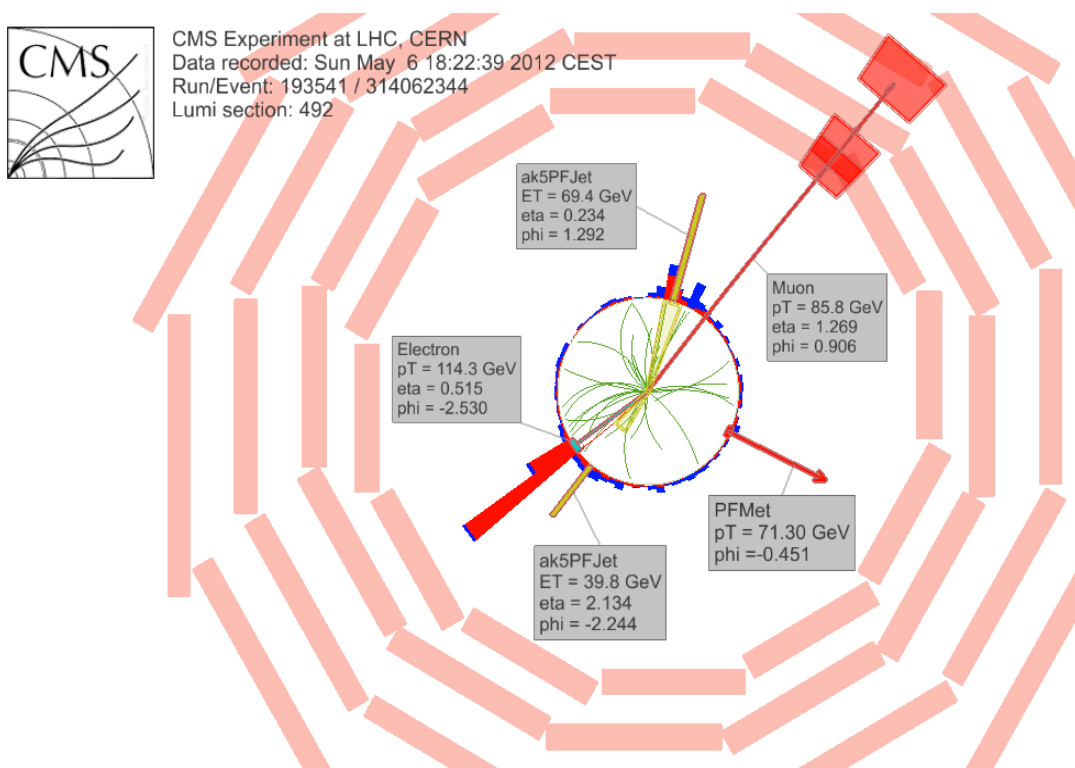


**Figure 3.8:**  $e\mu$  event reconstruction results; “An  $e\mu$  event candidate selected in 8 TeV data, as seen from the direction of the proton beams. The kinematics of the main objects used in the event selection are highlighted: two isolated leptons and two particle-flow jets. The reconstructed missing transverse energy is also displayed for reference” [124].

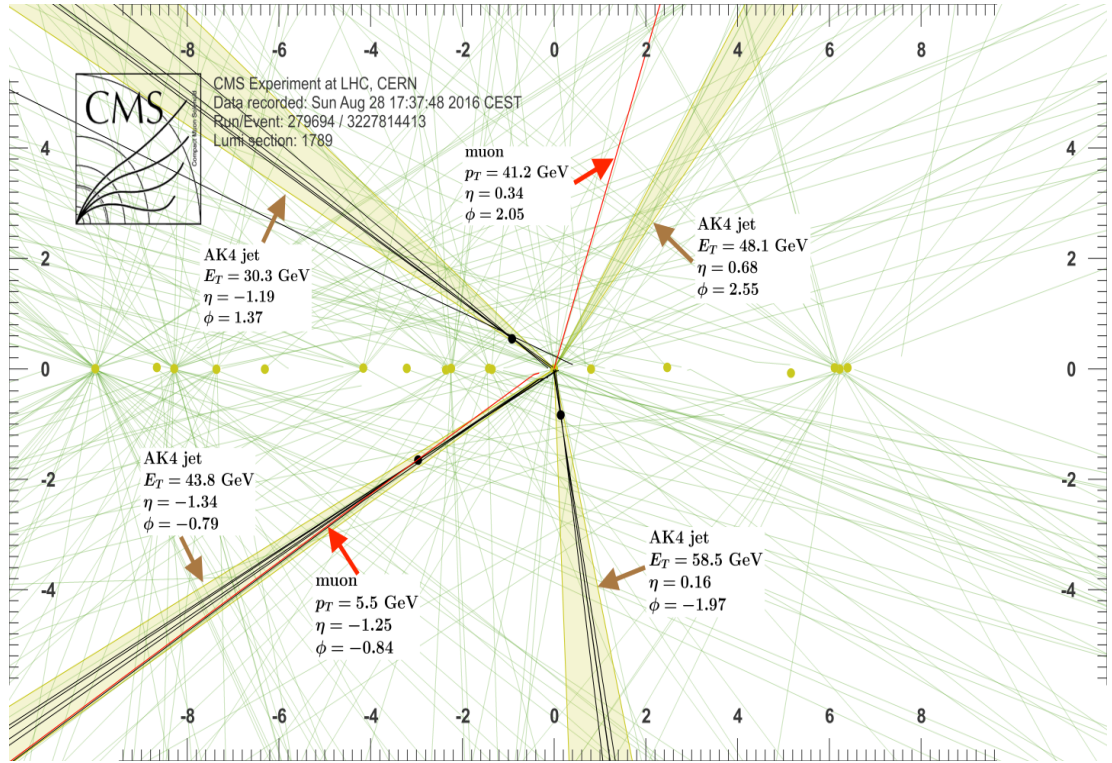


**Figure 3.9:** Recorded event reconstruction results; “Recorded event ( $\rho$ - $z$  projection) with three jets with  $p_T > 30$  GeV with one displaced muon track in 2016 data collected at 13 TeV. Each of the three jets has a displaced reconstructed vertex. The jet with  $p_T(j) = 43.8$  GeV,  $\eta(j) = -1.34$ ,  $\phi(j) = -0.79$  contains muon with  $p_T(\mu) = 5.5$  GeV,  $\eta(\mu) = -1.25$ ,  $\phi(\mu) = -0.84$ . Event contains reconstructed isolated muon with  $p_T(\mu) = 41.2$  GeV,  $\eta(\mu) = 0.34$ ,  $\phi(\mu) = 2.05$  and MET with  $p_T = 72.5$  GeV,  $\phi = -0.32$ . Jet candidates for a  $b$ -jet from top quark leptonic and hadronic decays are tagged by CSVv2T algorithm. One of the other two jets is tagged by CharmT algorithm. Tracks with  $p_T > 0.5$  GeV are shown. The number of reconstructed primary vertices is 18. Reconstructed  $m_T(W)$  is 101.8 GeV. Beam spot position correction is applied. Reconstructed primary vertices are shown in yellow color, while reconstructed displaced vertices and associated tracks are presented in black color. Dimensions are given in cm” [125].

# 1919 Chapter 5

## 1920 Statistical methods

1921 In the course of analyzing the data sets provided by the CMS experiment and used in  
1922 this thesis, several statistical tools have been employed; in this chapter, a description  
1923 of these tools will be presented, starting with the general statement of the multivariate  
1924 analysis methods, followed by the particularities of the Boosted Decision Trees (BDT)  
1925 method and its application to the classification problem. Statistical inference methods  
1926 used will also be presented. This chapter is based mainly on References [126–128].

### 1927 5.1 Multivariate analysis

1928 Multivariate data analysis (MVA) makes use of the statistical techniques developed to  
1929 analyze more than one variable at once, taking into account all the correlations among  
1930 variables. MVA is employed in a variety of fields like consumer and market research,  
1931 quality control and process optimization. Using MVA it is possible to identify the  
1932 dominant patterns in a data sample, like groups, outliers and trends, and determine  
1933 to which group a set of values belong; in the particle physics context, MVA methods  
1934 are used to perform the selection of certain type of events from a large data set.

1935 Processes with small cross section, such as the  $tHq$  process ( $\sigma_{SM}(\sqrt{s} = 13\text{TeV}) =$   
 1936  $70.96 \text{ fb}$ ), are hard to detect in the presence of the processes with larger cross sections,  
 1937  $\sigma_{SM}^{t\bar{t}}(\sqrt{s} = 13\text{TeV}) = 823.44 \text{ fb}$  for instance; therefore, only a small fraction of the data  
 1938 contains events of interest (signal), the major part is signal-like events, which mimic  
 1939 signal characteristics but belong to different processes, so they are a background to  
 1940 the process of interest. This implies that it is not possible to say with certainty  
 1941 that a given event is a signal or a background and statistical methods should be  
 1942 involved. In that sense, the challenge can be formulated as one where a set of events  
 1943 have to be classified according to certain special features; these features correspond  
 1944 to the measurements of several parameters like energy or momentum, organized in a  
 1945 set of *input variables*. The measurements for each event can be written in a vector  
 1946  $\mathbf{x} = (x_1, \dots, x_n)$  for which

- 1947 •  $f(\mathbf{x}|s)$  is the probability density (*likelihood function*) that  $\mathbf{x}$  is the set of mea-  
 1948 sured values given that the event is a signal event (signal hypothesis).
- 1949 •  $f(\mathbf{x}|b)$  is the probability density (*likelihood function*) that  $\mathbf{x}$  is the set of mea-  
 1950 sured values given that the event is a background event (background hypothe-  
 1951 sis).

1952 Figure 5.1 shows three ways to perform a classification of events for which mea-  
 1953 surements of two properties, i.e., two input variables  $x_1$  and  $x_2$ , have been performed;  
 1954 blue circles represent signal events while red triangles represent background events.  
 1955 The classification on the left is *cut-based* requiring  $x_1 < c_1$  and  $x_2 < c_2$ ; usually the  
 1956 cut values ( $c_1$  and  $c_2$ ) are chosen according to some knowledge about the event pro-  
 1957 cess. In the middle plot, the classification is performed using a linear function of  
 1958 the input variables, hence the boundary is a straight line, while in the right plot the

1959 the relationship between input variables is not linear thus the boundary is not linear  
 1960 either.

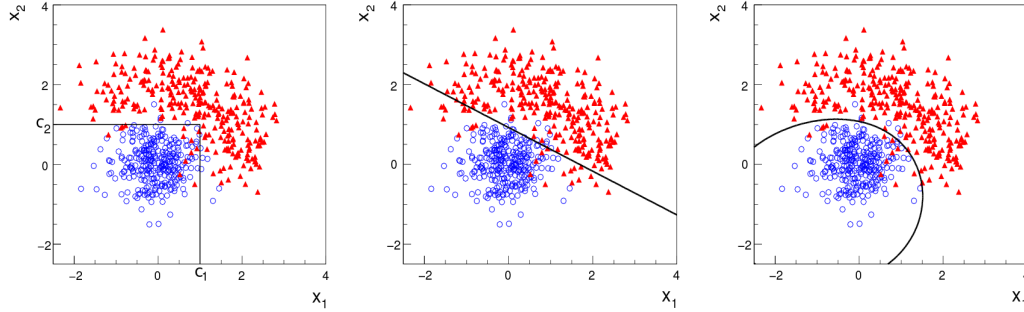


**Figure 5.1:** Scatter plots-MVA event classification. Distribution of two input variables  $x_1$  and  $x_2$  measured for a set of events; blue circles represent signal events and red triangles represent background events. The classification is based on cuts (left), linear boundary (center), and nonlinear boundary (right) [126]

1961 In general, the boundary can be parametrized in terms of the input variables such  
 1962 that the cut is set on the parametrization instead of on the variables, i.e.,  $y(\mathbf{x}) = y_{cut}$   
 1963 with  $y_{cut}$  being a constant; thus, the acceptance or rejection of an event is based on  
 1964 which side of the boundary the event is located. If  $y(\mathbf{x})$ , usually called *test statistic*,  
 1965 has functional form, it can be used to determine the probability distribution functions  
 1966  $p(y|s)$  and  $p(y|b)$  and then perform a test statistic with a single cut on the scalar  
 1967 variable  $y$ .

1968 Figure 5.2 shows an example of what would be the probability distribution func-  
 1969 tions under the signal and background hypotheses for a scalar test statistic with a cut  
 1970 on the classifier  $y$ . Note that the tails of the distributions indicate that some signal  
 1971 events fall in the rejection region and some background events fall on the acceptance  
 1972 region; therefore, it is convenient to define the *efficiency* with which events of a given  
 1973 type are accepted. The signal and background efficiencies are given by

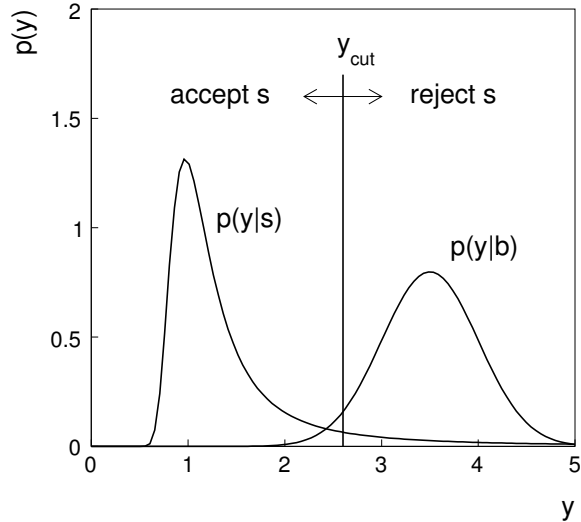


**Figure 5.2:** Distributions of the scalar test statistic  $y(\mathbf{x})$  under the signal and background hypotheses. [126]

$$\varepsilon_s = P(\text{accept event}|s) = \int_A f(\mathbf{x}|s) d\mathbf{x} = \int_{-\infty}^{y_{cut}} p(y|s) dy , \quad (5.1)$$

$$\varepsilon_b = P(\text{accept event}|b) = \int_A f(\mathbf{x}|b) d\mathbf{x} = \int_{-\infty}^{y_{cut}} p(y|b) dy , \quad (5.2)$$

1974 where  $A$  is the acceptance region. If the background hypothesis is the *null hypothesis*  
 1975 ( $H_0$ ), the signal hypothesis would be *alternative hypothesis* ( $H_1$ ); in this context, the  
 1976 background efficiency corresponds to the significance level of the test ( $\alpha$ ) and describes  
 1977 the misidentification probability, while the signal efficiency corresponds to the power  
 1978 of the test ( $1-\beta$ )<sup>1</sup> and describes the probability of rejecting the background hypothesis  
 1979 if the signal hypothesis is true. What is sought in an analysis is to maximize the power  
 1980 of the test relative to the significance level, i.e., set a selection with the largest possible  
 1981 selection efficiency and the smallest possible misidentification probability.

---

<sup>1</sup>  $\beta$  is the fraction of signal events that fall out of the acceptance region

1982 **5.1.1 Decision trees**

1983 For this thesis, the implementation of the MVA strategy, described above, is per-  
 1984 formed through decision trees by using the TMVA software package [127] included  
 1985 in the ROOT analysis framework [129]. In a simple picture, a decision tree classifies  
 1986 events according to their input variables values by setting a cut on each input variable  
 1987 and checking which events are on which side of the cut, just as proposed in the MVA  
 1988 strategy, but in addition, as a machine learning algorithm, decision trees offer the  
 1989 possibility to be trained and then perform the classification efficiently.

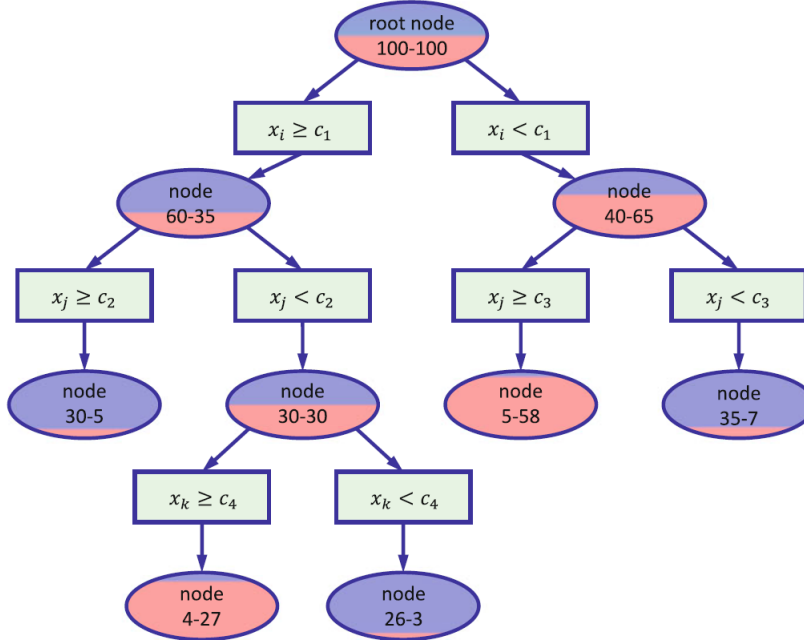


**Figure 5.3:** Example of a decision tree. Each node is fed with a MC sample mixing signal and background events (left-right numbers); nodes colors represent the relative number of signal/background events [128].

1990 The training or growing of a decision tree is the process where the rules for clas-  
 1991 sifying events are defined; this process is represented in Figure 5.3 and consists of  
 1992 several steps:

- 1993 • take MC samples of signal and background events and split them into two parts

1994        each; the first parts will be used in the decision tree training, while the second  
 1995        parts will be used for testing the final classifier obtained from the training.  
 1996        Each event has associated a set of input variables  $\mathbf{x} = (x_1, \dots, x_n)$  which serve  
 1997        to distinguish between signal and background events. The training sample is  
 1998        taken in at the *root node*.

1999        • Pick one variable, say  $x_i$ .  
 2000        • Pick one value of  $x_i$ , each event has its own value of  $x_i$ , and split the training  
 2001        sample into two subsamples  $B_1$  and  $B_2$ ;  $B_1$  contains events for which  $x_i < c_1$   
 2002        while  $B_2$  contains the rest of the training events;  
 2003        • scan all possible values of  $x_i$  and find the splitting value that provides the *best*  
 2004        classification<sup>2</sup>, i.e.,  $B_1$  is mostly made of signal events while  $B_2$  is mostly made  
 2005        of background events.  
 2006        • It is possible that variables other than the picked one produce a better classi-  
 2007        fication, hence, all the variables have to be evaluated. Pick the next variable,  
 2008        say  $x_j$ , and repeat the scan over its possible values.  
 2009        • At the end, all the variables and their values will have been scanned, the *best*  
 2010        variable and splitting value will have been identified, say  $x_1, c_1$ , and there will  
 2011        be two nodes fed with the subsamples  $B_1$  and  $B_2$ .

2012        Nodes are further split by repeating the decision process until a given number of  
 2013        final nodes is obtained, nodes are largely dominated by either signal or background  
 2014        events, or nodes have too few events to continue. Final nodes are called *leaves* and  
 2015        they are classified as signal or background leaves according to the class of the majority  
 2016        of events in them. Each *branch* in the tree corresponds to a sequence of cuts.

---

<sup>2</sup> Quality of the classification will be treated in the next paragraph.

2017        The quality of the classification at each node is evaluated through a separation  
 2018 criteria; there are several of them but the *Gini Index* ( $G$ ) is the one used in the  
 2019 decision trees trained for the analysis in this thesis.  $G$  is written in terms of the  
 2020 purity ( $P$ ), i.e., the fraction of signal events in the samples after the separation is  
 2021 made; it is given by

$$G = P(1 - P) \quad (5.3)$$

2022 note that  $P=0.5$  at the root node while  $G=0$  for pure leaves. For a node  $A$  split into  
 2023 two nodes  $B_1$  and  $B_2$  the  $G$  gain is

$$\Delta G = G(A) - G(B_1) - G(B_2). \quad (5.4)$$

2024        The *best* classification corresponds to that for which the gain of  $G$  is maximized;  
 2025 hence, the scanning over all the variables in an event and their values is of great  
 2026 importance.

2027        In order to provide a numerical output for the classification, events in a sig-  
 2028 nal(background) leaf are assigned a score of 1(-1) each, defining in this way the  
 2029 decision tree *classifier/weak learner* as

$$f(\mathbf{x}) = \begin{cases} 1 & \mathbf{x} \text{ in signal region,} \\ -1 & \mathbf{x} \text{ in background region.} \end{cases}$$

2030        Figure 5.4 shows an example of the classification of a sample of events, containing  
 2031 two variables, performed by a decision tree.

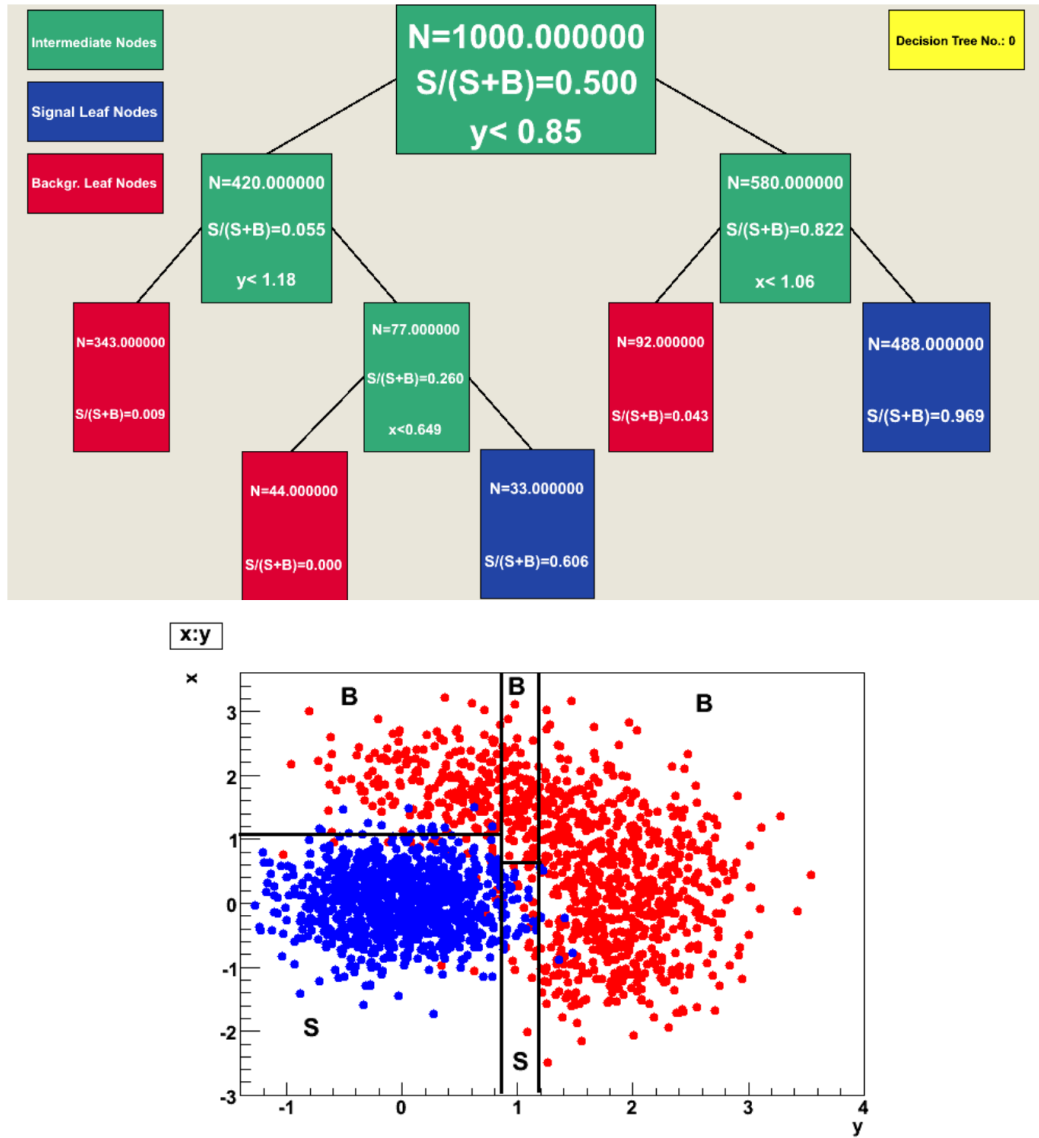


**Figure 5.4:** Example of a decision tree output. Each leaf, blue for signal events and red for background events, is represented by a region in the variables phase space [130].

### 2032 5.1.2 Boosted decision trees (BDT).

2033 Event misclassification occurs when a training event ends up in the wrong leaf, i.e., a  
 2034 signal event ends up in a background leaf or a background event ends up in a signal  
 2035 leaf. A way to correct it is to assign a weight to the misclassified events and train  
 2036 a second tree using the reweighted events; the event reweighting is performed by a

2037 boosting algorithm in such a way that when used in the training of a new decision  
 2038 tree the *boosted events* get correctly classified. The process is repeated iteratively  
 2039 adding a new tree to the forest and creating a set of classifiers, which are combined  
 2040 to create the next classifier; the final classifier offers more stability<sup>3</sup> and has a smaller  
 2041 misclassification rate than any individual ones. The resulting tree collection is known  
 2042 as a *boosted decision tree (BDT)*.

2043 Thus, purity of the sample is generalized to

$$P = \frac{\sum_s w_s}{\sum_s w_s + \sum_b w_b} \quad (5.5)$$

2044 where  $w_s$  and  $w_b$  are the weights of the signal and background events respectively;  
 2045 the Gini index is also generalized

$$G = \left( \sum_i^n w_i \right) P(1 - P) \quad (5.6)$$

2046 with  $n$  the number of events in the node. The final score of an event, after pass-  
 2047 ing through the forest, is calculated as the renormalized sum of all the individual  
 2048 (possibly weighted) scores; thus, high(low) score implies that the event is most likely  
 2049 signal(background).

2050 The boosting procedure, implemented in the *Gradient boosting* algorithm used in  
 2051 this thesis, produces a classifier  $F(\mathbf{x})$  which is the weighted sum of the individual  
 2052 classifiers obtained after each iteration, i.e.,

$$F(\mathbf{x}) = \sum_{m=1}^M \beta_m f(\mathbf{x}; a_m) \quad (5.7)$$

2053 where  $M$  is the number of trees in the forest. The *loss function*  $L(F, y)$  represents the

---

<sup>3</sup> Decision trees suffer from sensitivity to statistical fluctuations in the training sample which may lead to very different results with a small change in the training samples.

2054 deviation between the classifier  $F(\mathbf{x})$  response and the true value  $y$  obtained from the  
 2055 training sample (1 for signal events and -1 for background event), according to

$$L(F, y) = \ln(1 + e^{-2F(\mathbf{x})y}) \quad (5.8)$$

2056 thus, the reweighting is employed to ensure the minimization of the loss function; a  
 2057 more detailed description of the minimization procedure can be found in Reference  
 2058 [131]. The final classifier output is later used as a final discrimination variable, labeled  
 2059 as *BDT output/response*.

### 2060 5.1.3 Overtraining

2061 Decision trees offer the possibility to have as many nodes as desired in order to  
 2062 reduce the misclassification to zero (in theory); however, when a classifier is too much  
 2063 adjusted to a particular training sample, the classifier's response to a slightly different  
 2064 sample may leads to a completely different classification results; this effect is known  
 2065 as *overtraining*.

2066 An alternative to reduce the overtraining in BDTs consists in pruning the tree  
 2067 by removing statistically insignificant nodes after the tree growing is completed but  
 2068 this option is not available for BDTs with gradient boosting in the TMVA-toolkit,  
 2069 therefore, the overtraining has to be reduced by tuning the algorithm, number of  
 2070 nodes, minimum number of events in the leaves, etc. The overtraining can be evaluated  
 2071 by comparing the responses of the classifier when running over the training and  
 2072 test samples.

### 2073 5.1.4 Variable ranking

2074 BDTs have a couple of particular advantages related to the input variables; they are  
 2075 relatively insensitive to the number of input variables used in the vector  $\mathbf{x}$ . The  
 2076 ranking of the BDT input variables is determined by counting the number of times a  
 2077 variable is used to split decision tree nodes; in addition, the separation gain-squared  
 2078 achieved in the splitting and the number of events in the node are accounted by  
 2079 applying a weighting to that number. Thus, those variables with small or no power  
 2080 to separate signal and background events are rarely chosen to split the nodes, i.e., are  
 2081 effectively ignored.

2082 In addition, variables correlations play an important role for some MVA methods  
 2083 like the Fisher discriminant algorithm in which the first step consist of performing a  
 2084 linear transformation to a phase space where the correlations between variables are  
 2085 removed; in the case of BDT algorithm, correlations do not affect the performance.

### 2086 5.1.5 BDT output example

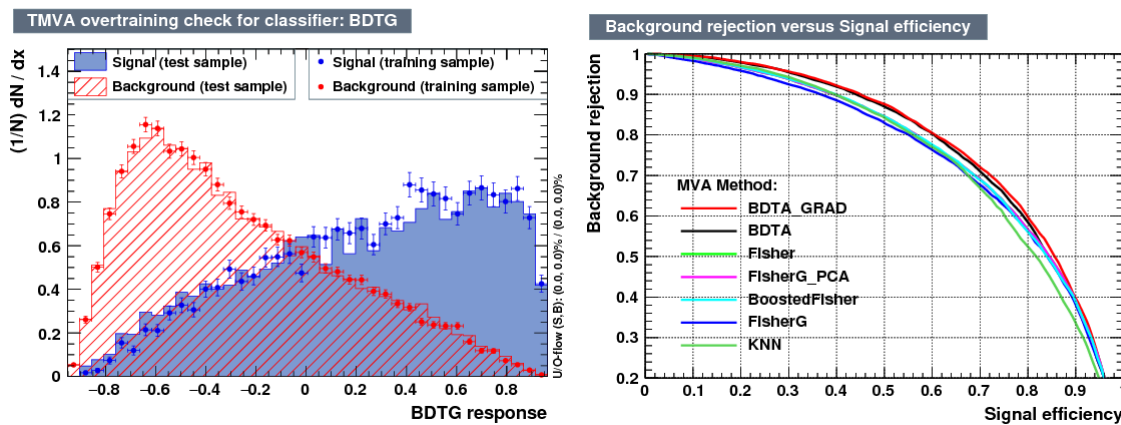


**Figure 5.5:** Left: Output distributions for the gradient boosted decision tree (BDTG) classifier using a sample of signal ( $pp \rightarrow tHq$ ) and background ( $pp \rightarrow tt$ ) events. Right: Background rejection vs signal efficiency (ROC curves) for various MVA classifiers running over the same sample used to produce the plot on the left.

2087        The left side of figure 5.5 shows the BDT output distributions for signal ( $pp \rightarrow$   
 2088  $tHq$ ) and background ( $pp \rightarrow t\bar{t}$ ) events; this plot is the equivalent to the one showed  
 2089 in Figure 5.2. A forest with 800 trees, maximum depth per tree = 3, and gradient  
 2090 boosting have been used as training parameters. The BDTG classifier offers a good  
 2091 separation power. There is a small overtraining in the signal distribution, while the  
 2092 background distribution is very well predicted which might indicate that the sample  
 2093 is composed of more background than signal events.

2094        The right side of figure 5.5 shows the background rejection vs signal efficiency  
 2095 curves for several combinations of MVA classifiers-boosting algorithms running over  
 2096 the same MC sample; these curves are known as ROC curves and give an indication  
 2097 of the performance of the classifier. In this particular example, the best performance  
 2098 is achieved with the BDTG classifier (BDTA\_GRAD), which motivate its use in this  
 2099 thesis.

## 2100 5.2 Statistical inference

2101 Once events are classified, the next step consists of finding the parameters that define  
 2102 the likelihood functions  $f(\mathbf{x}|s)$ ,  $f(\mathbf{x}|b)$  for signal and background events respectively.  
 2103 In general, likelihood functions depend not only on the measurements but also on  
 2104 parameters ( $\theta_m$ ) that define their shapes; the process of estimating these *unknown*  
 2105 *parameters* and their uncertainties from the experimental data is called *inference*.

2106        The statistical inference tools used in this analysis are implemented in the RooFit  
 2107 toolkit [132] and COMBINE package [133] included in the CMSSW software frame-  
 2108 work.

2109 **5.2.1 Nuisance parameters**

2110 The unknown parameter vector  $\theta$  is made of two types of parameters: those pa-  
 2111 rameters that provide information about the physical observables of interest for the  
 2112 experiment or *parameters of interest*, and the *nuisance parameters* that are not of  
 2113 direct interest for the experiment but that need to be included in the analysis in  
 2114 order to achieve a satisfactory description of the data; they represent effects of the  
 2115 detector response like the finite resolutions of the detection systems, miscalibrations,  
 2116 and in general any source of uncertainty introduced in the analysis.

2117 Nuisance parameters can be estimated from experimental data; for instance, data  
 2118 samples from a test beam are usually employed for calibration purposes. In cases  
 2119 where experimental samples are not availables, the estimation of nuisance parameters  
 2120 makes use of dedicated simulation programs to provide the required samples.

2121 The estimation of the unknown parameters involves certain deviations from their  
 2122 true values, hence, the measurement of the nuisance parameter is written in terms  
 2123 of an estimated value, also called central value,  $\hat{\theta}$  and its uncertainty  $\delta\theta$  using the  
 2124 notation

$$\theta = \hat{\theta} \pm \delta\theta \quad (5.9)$$

2125 where the interval  $[\hat{\theta} - \delta\theta, \hat{\theta} + \delta\theta]$  is called *confidence interval*; it is usually interpreted,  
 2126 in the limit of infinite number of experiments, as the interval where the true value  
 2127 of the unknown parameter  $\theta$  is contained with a probability of 0.6827 (if no other  
 2128 convention is stated); this interval represents the area under a Gaussian distribution  
 2129 in the interval  $\pm 1\sigma$ .

2130 The uncertainties associated with nuisance parameters produce *systematic uncer-*  
 2131 *tainties* in the final measurement, while the uncertainties related only to fluctuations

2132 in data and that affect the determination of parameters of interest produce *statistical*  
 2133 *uncertainties*.

2134 **5.2.2 Maximum likelihood estimation method**

2135 The estimation of the unknown parameters that are in best agreement with the ob-  
 2136 served data is performed through a function of the data sample that returns the  
 2137 estimate of those parameters; that function is called an *estimator*. Estimators are  
 2138 usually constructed using mathematical expressions encoded in algorithms.

2139 In this thesis, the estimator used is the likelihood function  $f(\mathbf{x}|\boldsymbol{\theta})$ <sup>4</sup> which depends  
 2140 on a set of measured variables  $\mathbf{x}$  and a set of unknown parameters  $\boldsymbol{\theta}$ . The likelihood  
 2141 function for N events in a sample is the combination of all the individual likelihood  
 2142 functions, i.e.,

$$L(\boldsymbol{\theta}) = \prod_{i=1}^N f(\mathbf{x}^i|\boldsymbol{\theta}) = \prod_{i=1}^N f(x_1^i, \dots, x_n^i; \theta_1, \dots, \theta_m) \quad (5.10)$$

2143 and the estimation method used is the *Maximum Likelihood Estimation* method  
 2144 (MLE); it is based on the combined likelihood function defined by eqn. 5.10 and  
 2145 the procedure seeks for the parameter set that corresponds to the maximum value of  
 2146 the combined likelihood function, i.e., the *maximum likelihood estimator* of the un-  
 2147 known parameter vector  $\boldsymbol{\theta}$  is the function that produces the vector of *best estimators*  
 2148  $\hat{\boldsymbol{\theta}}$  for which the likelihood function  $L(\boldsymbol{\theta})$  evaluated at the measured  $\mathbf{x}$  is maximum.

2149 Usually, the logarithm of the likelihood function is used in numerical algorithm  
 2150 implementations in order to avoid underflow the numerical precision of the computers  
 2151 due to the product of low likelihoods. In addition, it is common to minimize the  
 2152 negative logarithm of the likelihood function, therefore, the negative log-likelihood

---

<sup>4</sup> analogue to the likelihood functions described in previous sections

2153 function is

$$F(\boldsymbol{\theta}) = -\ln L(\boldsymbol{\theta}) = -\sum_{i=1}^N f(\mathbf{x}^i | \boldsymbol{\theta}). \quad (5.11)$$

2154 The minimization process is performed by the software MINUIT [134] implemented in the ROOT analysis framework. In case of data samples with large number 2155 of measurements, the computational resources necessary to calculate the likelihood 2156 function are too big; therefore, the parameter estimation is performed using binned 2157 distributions of the variables of interest for which the *binned likelihood function* is 2158 given by

$$L(\mathbf{x}|r, \boldsymbol{\theta}) = \prod_{i=1} \frac{(r \cdot s_i(\boldsymbol{\theta}) + b_i(\boldsymbol{\theta}))^{n_i}}{n_i!} e^{-r \cdot s_i(\boldsymbol{\theta}) - b_i(\boldsymbol{\theta})} \prod_{j=1} \frac{1}{\sqrt{2\pi}\sigma_{\theta_j}^2} e^{-(\theta_j - \theta_{0,j})^2/2\sigma_{\theta_j}^2}, \quad (5.12)$$

2160 with  $s_i$  and  $b_i$  the expected number of signal and background yields for the bin  $i$ ,  $n_i$  2161 is the observed number of events in the bin  $i$  and  $r = \sigma/\sigma_{SM}$  is the signal strength. 2162 Note that the number of entries per bin follows a Poisson distribution. The effect 2163 of the nuisance parameters have been included in the likelihood function through 2164 the multiplication by a Gaussian distribution that models the nuisance. The three 2165 parameters,  $r$ ,  $s_i$  and  $b_i$  are jointly fitted to estimate the value of  $r$ .

## 2166 5.3 Upper limits

2167 In this analysis, two hypotheses are considered; the background only hypothesis 2168 ( $H_0(b)$ ) and the signal plus background hypothesis ( $H_1(s+b)$ ), i.e., the sample of 2169 events is composed of background only events ( $r=0$ ) or it is a mixture of signal plus 2170 background events ( $r=1$ ). The exclusion of one hypothesis against the other means 2171 that the observed data sample better agrees with  $H_0$  or rather with  $H_1$ . In order 2172 to discriminate these hypotheses, a test statistic is constructed on the basis of the

2173 likelihood function evaluated for each of the hypothesis.

2174 The *Neyman-Pearson* lemma [135] states that the test statistic that provides the  
 2175 maximum power for  $H_1$  for a given significance level (background misidentification  
 2176 probability  $\alpha$ ), is given by the ratio of the likelihood functions  $L(\mathbf{x}|H_1)$  and  $L(\mathbf{x}|H_0)$ ;  
 2177 however, in order to use that definition it is necessary to know the true likelihood  
 2178 functions, which in practice is not always possible. Approximate functions obtained  
 2179 by numerical methods, like the BDT method described above, have to be used, so  
 2180 that the *profile likelihood* test statistic is defined by

$$\lambda(\mathbf{r}) = \frac{L(\mathbf{x}|r, \hat{\boldsymbol{\theta}}(r))}{L(\mathbf{x}|\hat{r}, \hat{\boldsymbol{\theta}})}, \quad (5.13)$$

2181 where,  $\hat{r}$  and  $\hat{\boldsymbol{\theta}}$  maximize the likelihood function, and  $\hat{\boldsymbol{\theta}}$  maximizes the likelihood  
 2182 function for a given value of the signal strength modifier  $r$ . In practice, the test  
 2183 statistic  $t_r$

$$t_r = -2\ln\lambda(r) \quad (5.14)$$

2184 is used to evaluate the presence of signal in the sample, since the minimum of  $t_r$  at  
 2185  $r = \hat{r}$  suggests the presence of signal with signal strength  $\hat{r}$ . The uncertainty interval  
 2186 for  $r$  is determined by the values of  $r$  for which  $t_r = +1$ .

2187 The expected probability density function (p.d.f)  $f(t_r|r, \boldsymbol{\theta})$  of the test statistic  $t_r$   
 2188 can be obtained numerically by generating MC samples where one hypothesis,  $H_0(b)$   
 2189 or  $H_1(s+b)$ , is assumed; thus, MC samples contain the possible values of  $t_r$  obtained  
 2190 from *pseudo-experiments* as shown in Figure 5.6. The probability that  $t_r$  takes a value  
 2191 equal or greater than the observed value ( $t_{r,obs}$ ) when a signal with a signal modifier  
 2192  $r$  is present in the data sample, is called the *p-value* of the observation; it can be  
 2193 calculated using

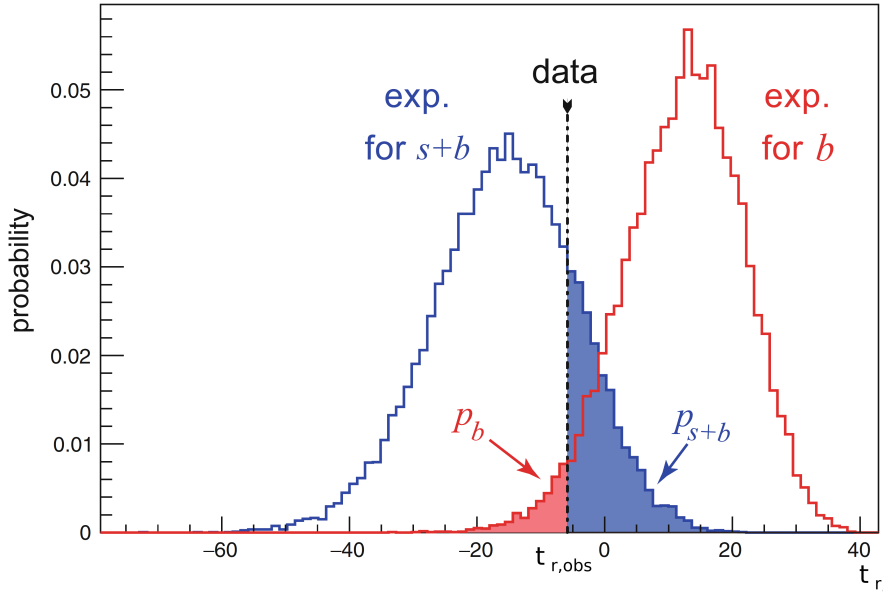


**Figure 5.6:**  $t_r$  p.d.f. from MC pseudo experiments assuming  $H_0$  (red) and  $H_1$  (blue). The black dashed line shows the value of the test statistic as measured from data. Adapted from Reference [128].

$$p_r = \int_{t_{r,obs}}^{\infty} f(t'_r | r, \boldsymbol{\theta}) dt'_r, \quad (5.15)$$

thus,  $p_r < 0.05$  means that, for that particular value of  $r$ ,  $H_1$  could be excluded at 95% Confidence Level (CL). The corresponding background-only p-value is given by

$$1 - p_b = \int_{t_{r,obs}}^{\infty} f(t'_r | 0, \boldsymbol{\theta}) dt'_r, \quad (5.16)$$

If the  $t_r$  p.d.f.s for both hypotheses are well separated, as shown in the top side of Figure 5.7, the experiment is sensitive to the presence of signal in the sample. If the signal presence is small, both p.d.f.s will be largely overlapped (bottom of Figure ??) and either the signal hypothesis could be rejected with not enough justification because the experiment is not sensitive to the signal or a fluctuation of the background could be misinterpreted as presence of signal with the corresponding rejection of the

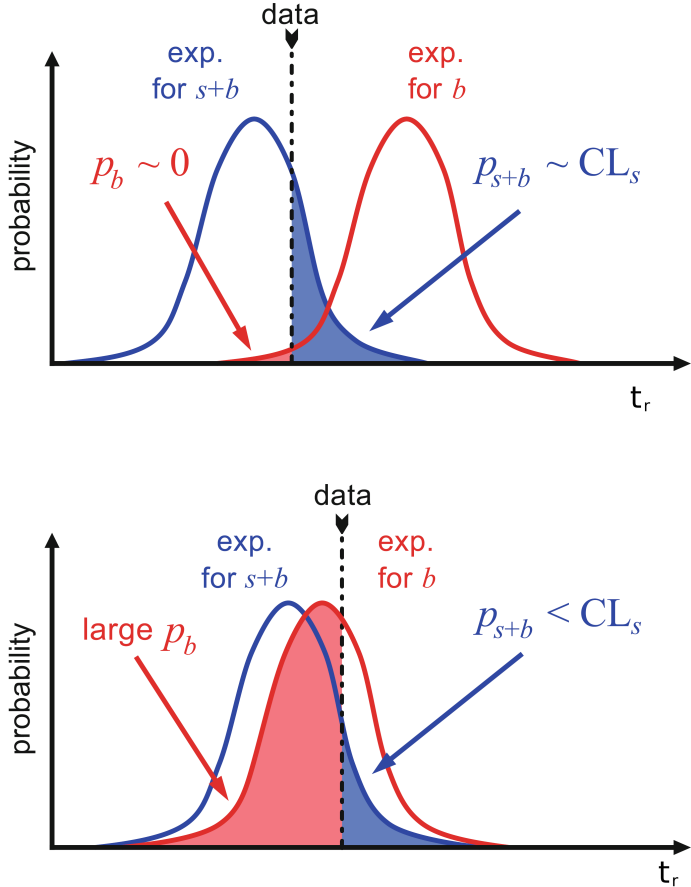


**Figure 5.7:**  $CL_s$  limit illustration. When the test statistic p.d.f. for the two hypotheses  $H_0$  and  $H_1$  are well separated (top) and when they are largely overlapped (bottom). Adapted from Reference [128].

2202 background-only hypothesis. These issues are corrected by using the modified p-  
2203 value [136]

$$p'_r = \frac{p_r}{1 - p_b} \equiv CL_s. \quad (5.17)$$

2204 If  $H_1$  is true, then  $p_b$  is small,  $CL_s \simeq p_r$  and  $H_0$  is rejected; if there is large  
2205 overlap and an statistical fluctuation cause that  $p_b$  is large, then both numerator and  
2206 denominator in Eqn. 5.17 become small but  $CL_s$  would allow the rejection of  $H_1$   
2207 even if there is poor sensitivity to signal.

2208        The upper limit of the parameter of interest  $r^{up}$  is determined by excluding the  
 2209        range of values of  $r$  for which  $CL_s(r, \theta)$  is lower than the confidence level desired,  
 2210        normally 90% or 95%, e.g, scanning over  $r$  and finding the value for which  $p_r'^{up} =$   
 2211        0.05. The expected upper limit can be calculated using pseudo-experiments based on  
 2212        the background-only hypothesis and obtaining a distribution for  $r_{ps}^{up}$ ; the median of  
 2213        that distribution corresponds to the expected upper limit, while the  $\pm 1\sigma$  and  $\pm 2\sigma$   
 2214        deviations correspond to the values of the distribution that defines the 68% and 95%  
 2215        of the area under the distribution centered in the median. It is usual to present all  
 2216        the information about the expected and observed limits in the so-called *Brazilian-flag*  
 2217        *plot* as the one showed in Figure 5.8. The solid line represent the observed  $CL_s$

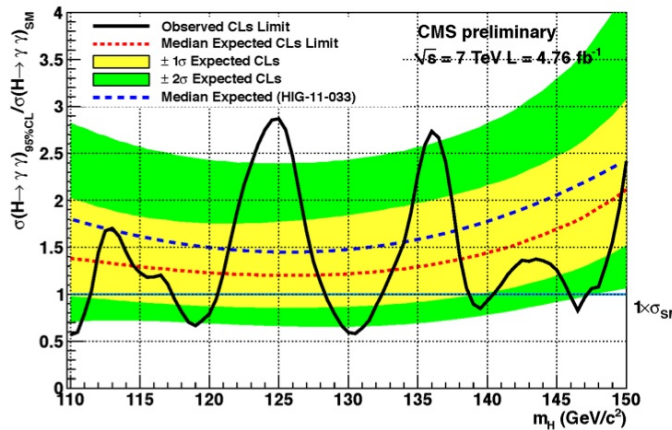


**Figure 5.8:** Brazilian flag plot of CMS experiment limits for Higgs boson decaying to photons [137].

## 2218 5.4 Asymptotic limits

2219        As said before, the complexity of the likelihood functions, the construction of test  
 2220        statistics, and the calculation of the limits and their uncertainties is not always man-  
 2221        ageable and requires extensive computational resources; in order to overcome those  
 2222        issues, asymptotic approximations for likelihood-based test statistics, like the ones

described in previous sections, have been developed [138, 139] using Wilks' theorem.  
Asymptotic approximations replace the construction of the test statistics p.d.f.s using  
MC pseudo-experiments, with the approximate calculation of the test statistics p.d.f.s  
by employing the so-called *Asimov dataset*.

The Asimov dataset is defined as the dataset that produce the true values of the  
nuisance parameters when it is used to evaluate the estimators for all the parameters;  
it is obtained by setting the values of the variables in the dataset to their expected  
values [139].

Limits calculated by using the asymptotic approximation and the Asimov dataset  
are know as *asymptotic limits*.

<sup>2233</sup> **Chapter 6**

<sup>2234</sup> **Search for production of a Higgs**

<sup>2235</sup> **boson and a single top quark in**

<sup>2236</sup> **multilepton final states in pp**

<sup>2237</sup> **collisions at  $\sqrt{s} = 13$  TeV**

<sup>2238</sup> **6.1 Introduction**

<sup>2239</sup> The Higgs boson discovery, supported on experimental observations and theoretical  
<sup>2240</sup> predictions made about the SM, gives the clue of the way in that elementary particles  
<sup>2241</sup> acquire mass through the Higgs mechanism; therefore, knowing the Higgs mass, the  
<sup>2242</sup> Higgs-vector boson and Higgs-fermion couplings can be determined. In order to test  
<sup>2243</sup> the Higgs-top coupling, several measurements have been performed, as stated in the  
<sup>2244</sup> chapter 1, but they are limited in sensitivity to measure the square of the coupling.  
<sup>2245</sup> The production of a Higgs boson in association with a single top quark ( $tH$ ) not  
<sup>2246</sup> only offers access to the sign of the coupling, but also, to the CP phase of the Higgs

2247 couplings.

2248 This chapter presents the search for the associated production of a Higgs boson  
 2249 and a single top quark ( $tHq$ ) events, focusing on leptonic signatures provided by the  
 2250 Higgs decay modes to  $WW$ ,  $ZZ$ , and  $\tau\tau$ ; the 13 TeV dataset produced in 2016, which  
 2251 corresponds to an integrated luminosity of  $35.9\text{fb}^{-1}$ , is used.

2252 As shown in Section 1.5, the SM cross section of  $tHq$  process is driven by a  
 2253 destructive interference between two contributions (see Figure 1.15), where the Higgs  
 2254 couples to either the W boson or the top quark; however, if the sign of the Higgs-  
 2255 top coupling is flipped with respect to the SM prediction, a large enhancement of  
 2256 the cross section occurs, making this analysis sensitive to such deviation. A second  
 2257 process, where the Higgs boson and top quark are accompanied by a W boson ( $tHW$ )  
 2258 has similar behavior, albeit with a weaker interference pattern and lower contribution  
 2259 to the cross section, therefore, a combination of both processes would increase the  
 2260 sensitivity to the sign of the coupling; in this analysis both contributions are combined  
 2261 and referred as  $tH$ channel. A third contribution comes from  $t\bar{t}H$  process. The purpose  
 2262 of this analysis is to investigate the exclusion of the presence of the  $tH + t\bar{t}H$  processes  
 2263 under the assumption of the anomalous Higgs-top coupling modifier ( $\kappa_t = -1$ ). The  
 2264 analysis exploits signatures with two leptons of the same sign ( $\cancel{2}lss$ ) channel and three  
 2265 leptons ( $\cancel{3}l$ ) channel in the final state.

2266 Constraints on the sign of the Higgs-top coupling ( $y_t$ ) have been derived from the  
 2267 decay rate of Higgs boson to photon pairs [50] and from the cross section for associated  
 2268 production of Higgs and Z bosons via gluon fusion [141], with recent results disfavoring  
 2269 negative signs of the coupling [44, 59, 142], although the negative sign coupling have  
 2270 not been completely excluded.

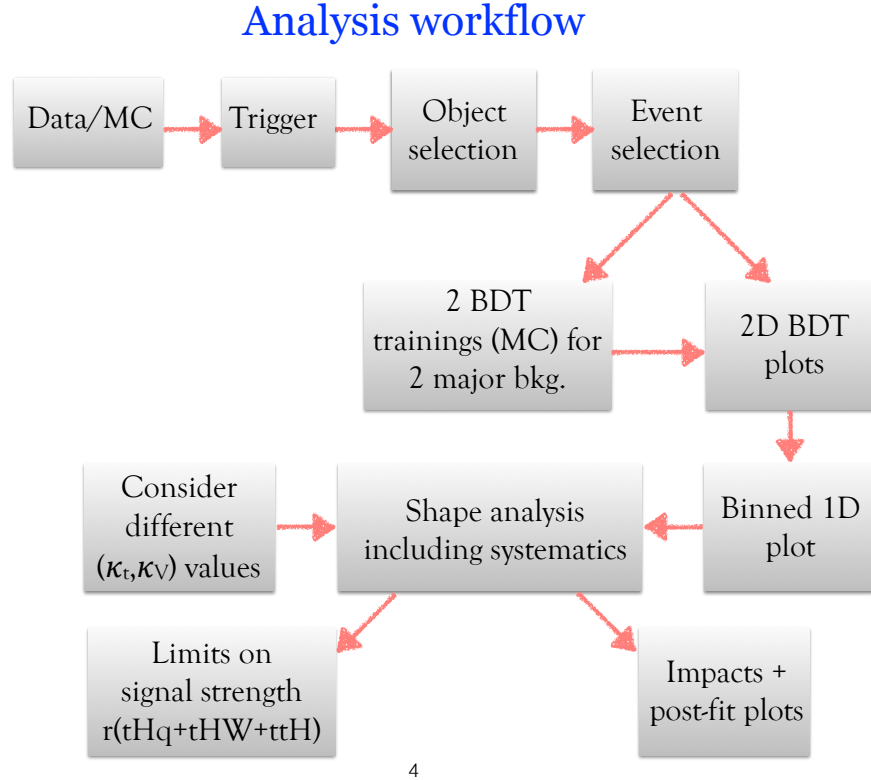
2271 The analysis presented here, expands previous analyses performed at 8 TeV [143,  
 2272 144] and searches for associated production of  $t\bar{t}$  pair and a Higgs boson in the multi-

2273 lepton final state channel [145]; it also complements searches in other decay channels  
 2274 targeting  $H \rightarrow b\bar{b}$  [146].

2275 The first sections present the characteristic  $tHq$  signature as well as the expected  
 2276 backgrounds. The MC samples, data sets, and the physics object definitions are  
 2277 then defined. Following, the background predictions, the signal extraction, and the  
 2278 statistical treatment of the selected events as well as the systematic uncertainties are  
 2279 described. The final section present the results for the exclusion limits as a function  
 2280 of the ratio of  $\kappa_t$  and the dimensionless modifier of the Higgs-vector boson coupling  
 2281  $\kappa_V$ .

2282 The analysis is designed to efficiently identify and select prompt leptons from on-  
 2283 shell W and Z boson decays and to reject non-prompt leptons from  $b$  quark decays  
 2284 and spurious lepton signatures from hadronic jets. Events are then selected in the  
 2285  $2lss$  and  $3l$  channels, and are required to contain hadronic jets, some of which must  
 2286 be consistent with  $b$  quark hadronization. Finally, the signal yield is extracted by  
 2287 simultaneously fitting the output of two dedicated multivariate discriminants, trained  
 2288 to separate the  $tHq$  signal from the two dominant backgrounds, in all categories. The  
 2289 fit result is then used to set an upper limit on the combined  $t\bar{t}H + tH$  production  
 2290 cross section, as a function of the relative coupling strengths of Higgs-top quark and  
 2291 Higgs-Vector boson. Figure 6.1 shows an schematic overview of the analysis strategy  
 2292 workflow.

2293 With respect to the 8 TeV analysis, the object selections have been adjusted for  
 2294 the updated LHC running conditions at 13 TeV, the lepton identification has been  
 2295 improved, and more powerful multivariate analysis techniques are used for the signal  
 2296 extraction.



4

**Figure 6.1:** A schematic overview of the analysis workflow. Based on sets of optimized physics object definitions and selection criteria, signal and background events in a data sample are discriminated. The discrimination is performed by a BDT, previously trained using MC samples of the dominant backgrounds, using discriminant variables based on the  $b$ -jet multiplicity, the activity in the forward region of the detector, and the kinematic properties of leptons. The  $CL_s$  limits on the combined  $t\bar{t}H + tH$  production cross section, as a function of the relative coupling strengths are calculated.

## 2297 6.2 $tHq$ signature

2298 In order to select events of  $tHq$  process, its features are translated into a set of  
 2299 selection rules; Figure 6.2 shows the Feynman diagram and an schematic view of the  
 2300  $tHq$  process from the  $pp$  collision to the final state configuration. A single top quark  
 2301 is produced accompanied by a light quark, denoted as  $q$ ; this light quark is produced  
 2302 predominantly in the forward region of the detector. The Higgs boson can be either  
 2303 emitted by the exchanged  $W$  boson or directly by the singly produced top quark.

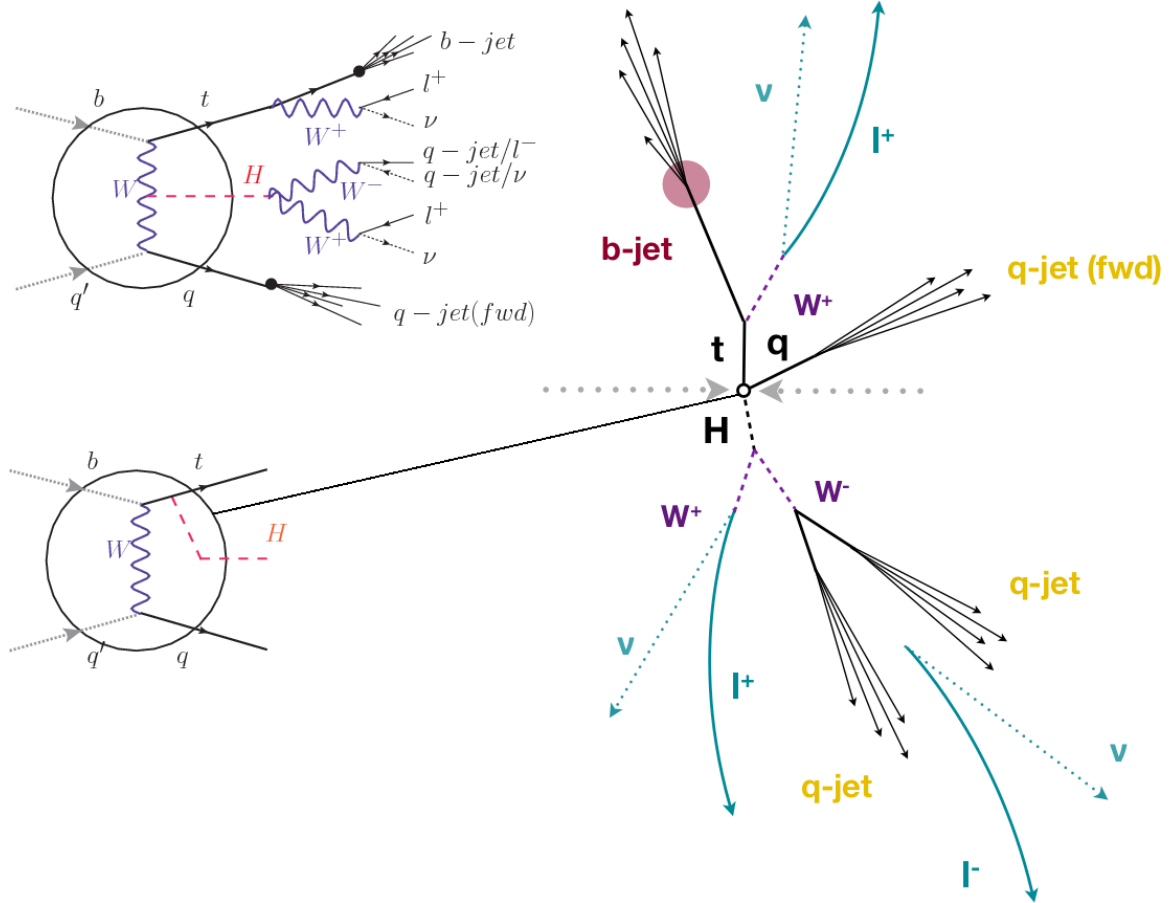


**Figure 6.2:**  $tHq$  event signature. Left: Feynman diagram including the whole evolution up to the final state for the case of the Higgs boson emitted by the  $W$  boson (top); Feynman diagram for the case where the Higgs boson is emitted by the top quark. Right: Schematic view as it would be seen in the detector; the circle in the Feynman diagrams on the left corresponds to the circle in the center of the schematic view as indicated by the line connecting them. In the  $2lss$  channel, one of the  $W$  bosons from the Higgs boson decays to two light-quark jets while in the  $3l$  channel both  $W$  bosons decay to leptons.

2304 Due to their high masses/short lifetimes, top quark and Higgs boson decay after  
 2305 their production within the detector. The Higgs boson is required to decay into a  $W$   
 2306 boson pair<sup>1</sup>. The top quark almost always decays into a bottom quark and a  $W$  boson,  
 2307 as encoded in the CMK matrix. The  $W$  bosons are required to decay leptonically  
 2308 either all the three in the  $3l$  channel or the pair with equal electrical charge in the

<sup>1</sup> ZZ and  $\tau\tau$  decays are also included in the analysis but they are not separately reconstructed

2309  $2lss$  channel case;  $\tau$  leptons are not reconstructed separately and only their leptonic  
 2310 decays into either electrons or muons are considered in this analysis.

2311 In summary, the signal process is characterized by a the final state with

2312 • one light-flavored forward jet,

2313 • one central b-jet,

2314 •  $2lss$  channel  $\rightarrow$  two leptons of the same sign, two neutrinos and two light (often  
 2315 soft) jets,

2316 •  $3l$  channel  $\rightarrow$  three leptons, three neutrinos and no central light-flavored jets,

2317 The presence of neutrinos is inferred from the presence of MET. The analysis has  
 2318 been made public by CMS as a Physics Analysis Summary [147] combining the result  
 2319 for the three lepton and two lepton same-sign channels. Currently, an effort to turn  
 2320 the analysis into a paper is ongoing.

## 2321 6.3 Background processes

2322 The background processes are those that can mimic the signal signature or at least  
 2323 can be reconstructed as that as a result of certain circumstances. The backgrounds  
 2324 can be classified as

2325 • irreducible backgrounds: where genuine prompt leptons are produced in on-  
 2326 shell W and Z boson decays; they can be reliably estimated directly from MC  
 2327 simulated events, using higher-order cross sections or data control regions for  
 2328 the overall normalization.

2329     • reducible backgrounds: where at least one of the leptons is *non-prompt*, i.e.,  
 2330       produced within a hadronic jet; genuine leptons from heavy flavor decays and  
 2331       misreconstructed jets, also known as *mis-ID leptons* or *fake leptons*, are consid-  
 2332       ered non-prompt leptons. These non-prompt leptons leave tracks and hits in  
 2333       the detection systems as would a prompt lepton, but correlating those hits with  
 2334       nearby jets could be a way of removing them. The misassignment of electron  
 2335       charge in processes like  $t\bar{t}$  or Drell-Yan, represent an additional source of back-  
 2336       ground, but it is relevant only for the  $2lss$  channel. Reducible backgrounds are  
 2337       not well predicted by simulation, hence, they are estimated using data-driven  
 2338       methods.

2339       The main sources of background events for  $tHq$  process are  $t\bar{t}$  process and  $t\bar{t} +$   
 2340        $X$  ( $X = W, Z, \gamma$ ) processes, the latter regarded together as  $t\bar{t}V$  process. Figure 6.3  
 2341       shows the signature for  $t\bar{t}$  and  $t\bar{t}W$  processes.

2342       The largest contribution to irreducible backgrounds comes from  $t\bar{t}W$  and  $t\bar{t}Z$  processes  
 2343       for which the number of ( $b-$ )jets (( $b-$ )jet multiplicity) is higher than that of the sig-  
 2344       nal events, while for other contributing background events,  $WZ$ ,  $ZZ$ , and rare SM  
 2345       processes like  $W^\pm W^\pm qq$ ,  $t\bar{t}t\bar{t}$ ,  $tZq$ ,  $tZW$ ,  $WWW$ ,  $WWZ$ ,  $WZZ$ ,  $ZZZ$ , the ( $b-$ )jet  
 2346       multiplicity is lower compared to that of the signal events. None of the irreducible  
 2347       backgrounds present activity in the forward region of the detector.

2348       On the side of the reducible backgrounds, the largest contribution comes from the  
 2349        $t\bar{t}$  events which have a very similar signature to the signal events but does no present  
 2350       activity in the forward region of the detector either; A particular feature of the  $t\bar{t}$   
 2351       events is their charge-symmetry, which is also a difference with respect to the signal  
 2352       events.

2353       The charge misidentification plays an important role in the the  $2lss$  channel since

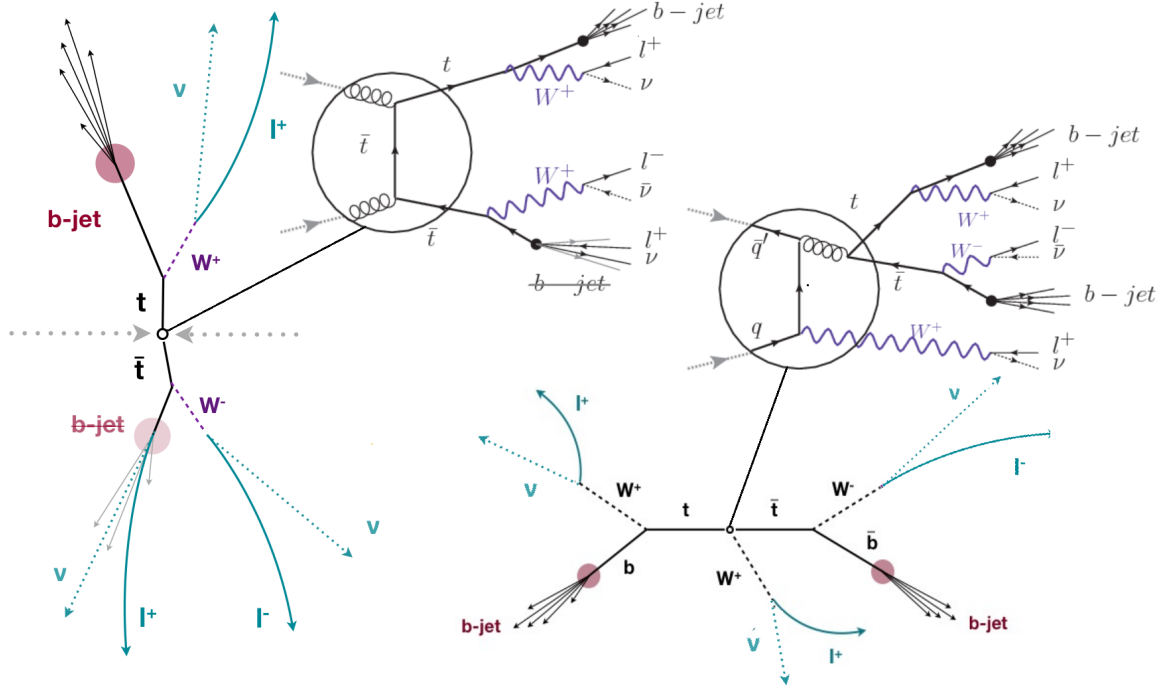


**Figure 6.3:**  $t\bar{t}$  (left) and  $t\bar{t}W$  (right) events signature as they would be seen in the detector; the Feynman diagrams including the whole evolution up to the final state are also showed. The  $t\bar{t}$  process signature is very similar to that of the signal process with one fake lepton and no forward activity. The  $t\bar{t}W$  process present a higher  $b$ -jet multiplicity compared to the signal process, a prompt lepton and no forward activity.

2354 leptons in processes like  $t\bar{t} + \text{jets}$  or  $Z + \text{jets}$  can be charge misidentified, leading to  
 2355 backgrounds increments. An identification variable have been designed in order to  
 2356 reject this type of background events.

## 2357 6.4 Data and MC Samples

### 2358 6.4.1 Full 2016 data set

2359 The data set used in this analysis was collected by the CMS experiment during 2016  
 2360 at while running at  $\sqrt{s} = 13\text{TeV}$  and corresponds to a total integrated luminosity  
 2361 of  $35.9\text{fb}^{-1}$ . Only periods when the CMS magnet was on were considered when

2362 selecting the data samples; that corresponds to the 23Sep2016 (Run B to G) and  
 2363 PromptReco (Run H) versions of the datasets.

2364 Multilepton final states with either two same-sign leptons or three leptons tar-  
 2365 get the case where the Higgs boson decays to a pair of W bosons,  $\tau$  leptons, or Z  
 2366 bosons, and where the top quark decays leptonically, hence, the SingleElectron,  
 2367 SingleMuon, DoubleEG, MuonEG, DoubleMuon dataset (see Table A.1) compose the  
 2368 full dataset. The certified luminosity sections are selected using the golden JSON file  
 2369 defined by the CMS experiment [148].

## 2370 6.4.2 Triggers

2371 The events considered are those online-reconstructed events triggered by one, two, or  
 2372 three leptons. Single-lepton triggers are included in order to boost the acceptance  
 2373 of events where the  $p_T$  of the sub-leading lepton falls below the threshold of the  
 2374 double-lepton triggers. The trigger efficiency is increased by including double-lepton  
 2375 triggers in the  $3l$  category, and single-lepton triggers in all categories; it is possible  
 2376 given the logical “or” of the trigger decisions of all the individual triggers in a given  
 2377 category. Table A.2 shows the lowest-threshold non-prescaled triggers present in the  
 2378 High-Level Trigger (HLT) menus for both Monte-Carlo and data in 2016.

### 2379 Trigger efficiency scale factors

2380 Trigger efficiency describes the ability of events to pass the trigger requirements. It  
 2381 is measured in simulated events using generator information given that there is no  
 2382 trigger bias with the MC sample. Measuring the trigger efficiency in data requires a  
 2383 more elaborated procedure; first, select a set of events collected by a trigger that is  
 2384 uncorrelated with the lepton triggers such that the selected events form an unbiased

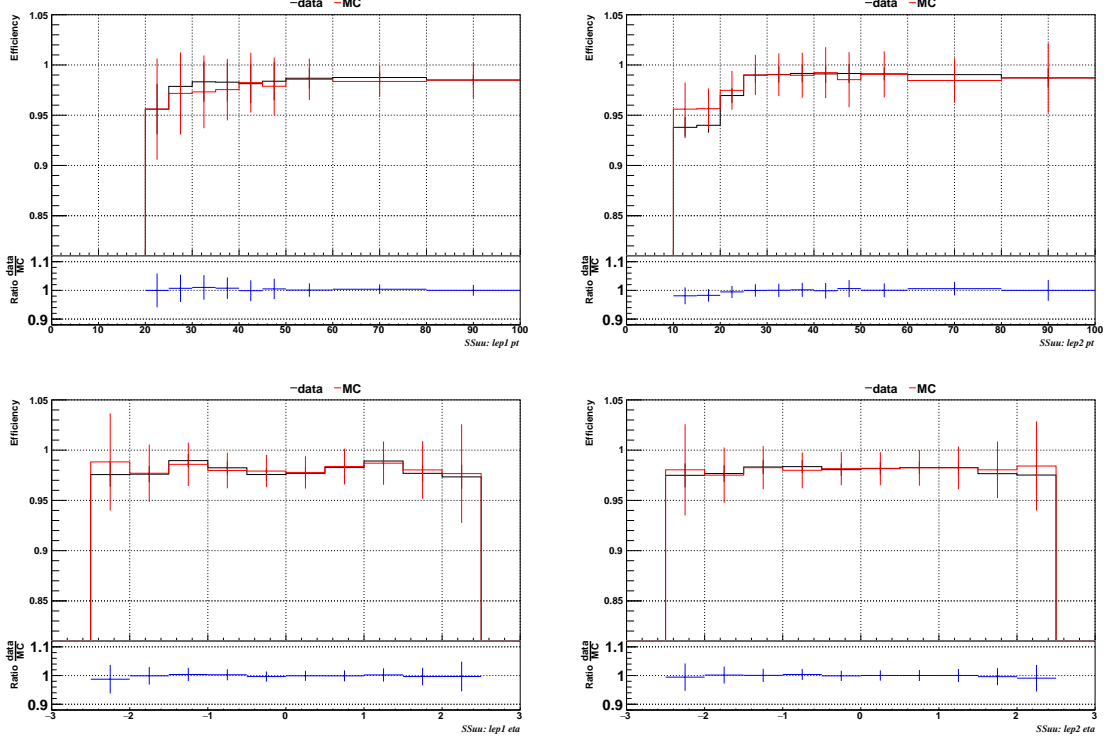


**Figure 6.4:** Comparison between data and MC trigger efficiencies in the same-sign  $\mu\mu$  category, as a function of the  $p_T$  and  $\eta$  of the leading lepton (left) and the sub-leading lepton (right) [149].

sample. In this analysis, that uncorrelated trigger is a MET trigger. Second step is looking for candidate events with exactly two good leptons (exactly three good leptons for the  $3l$  channel). Finally, measure the efficiency for the candidate events to pass the logical “or” of triggers being considered in a given event category as defined in Table A.2.

Comparisons between the data and MC efficiencies for each category, showed in Figures 6.4, 6.5, and 6.6, reveal that they are in good agreement; the difference is corrected by applying scale factors derived from the ratio between both efficiencies.

Applied flat scale factors in each category are shown in Tab. 6.1; they have been inherited from Reference [149].

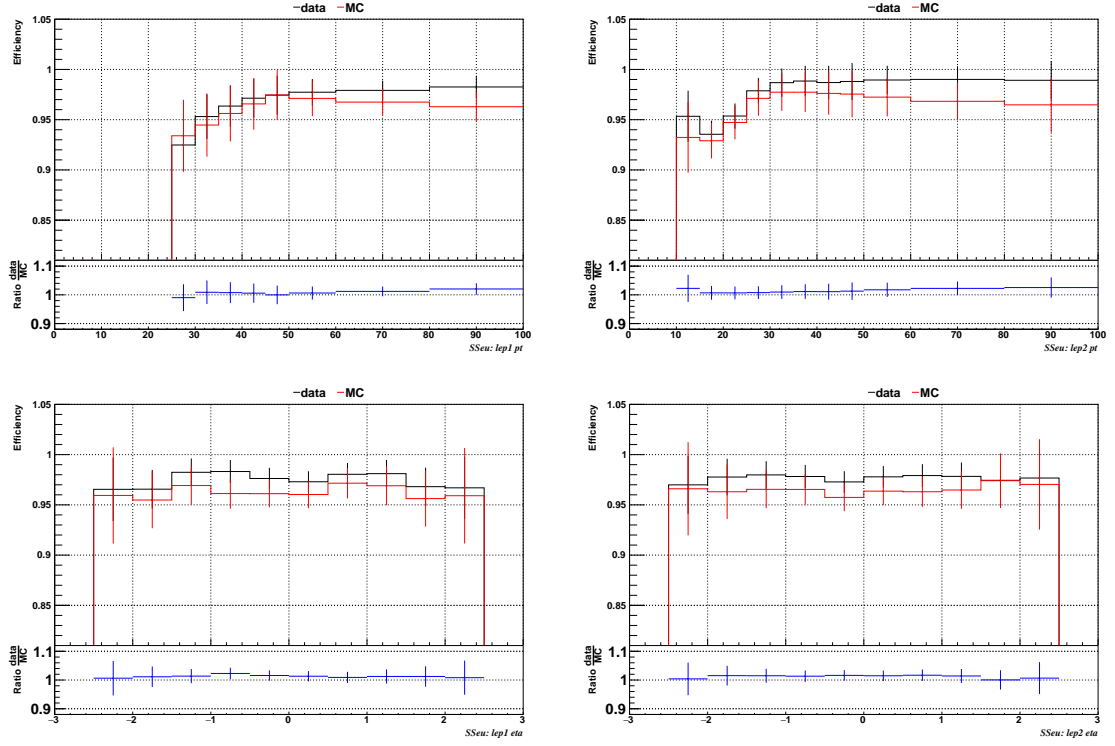


**Figure 6.5:** Comparison between data and MC trigger efficiencies in the same-sign  $e\mu$  category as a function of the  $p_T$  and  $\eta$  of the leading lepton (left) and the sub-leading lepton (right) [149].

Category	Scale Factor
ee	$1.01 \pm 0.02$
$e\mu$	$1.01 \pm 0.01$
$\mu\mu$	$1.00 \pm 0.01$
3l	$1.00 \pm 0.03$

**Table 6.1:** Trigger efficiency scale factors and associated uncertainties, shown here rounded to the nearest percent.

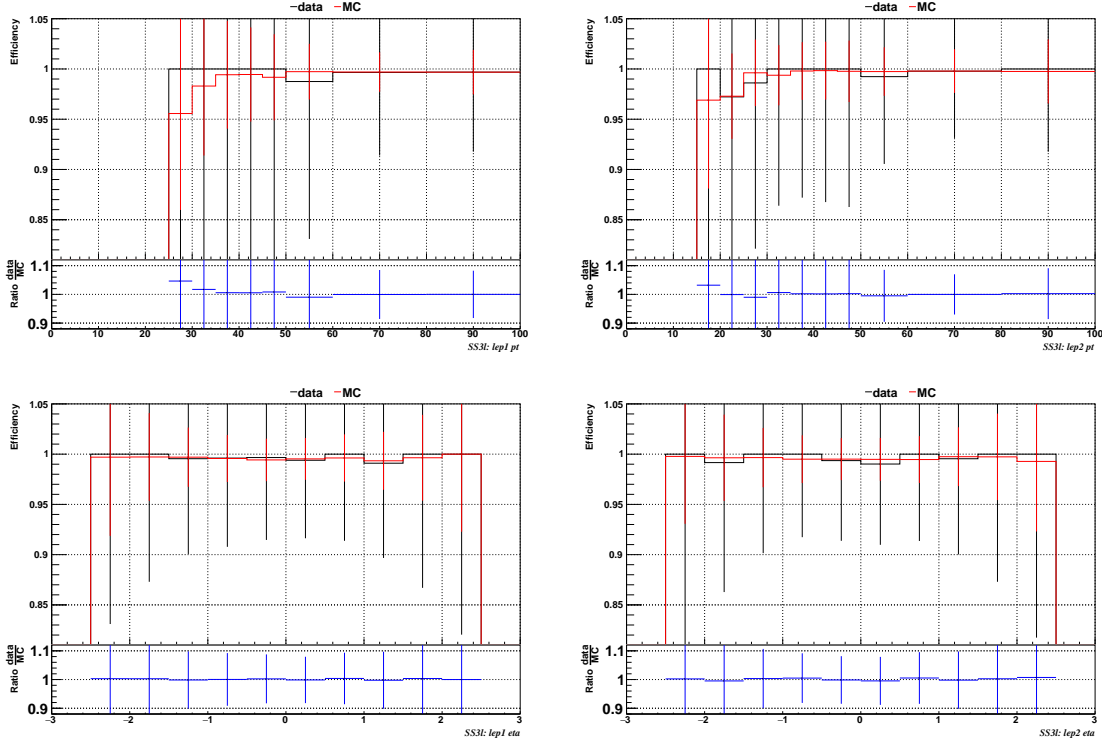


**Figure 6.6:** Comparison between data and MC trigger efficiencies in the  $3l$  category, as a function of the  $p_T$  and  $\eta$  of the leading lepton (left) and the sub-leading lepton (right) [149].

### 2395 6.4.3 Signal modeling and MC samples

2396 Current event generators allow for adjusting the kinematics of the generated events,  
 2397 based on an event-wise reweighting; in this way, several generation parameters phase  
 2398 spaces can be explored according to the experimental interests. The signal samples  
 2399 used in this analysis were generated in such a way that not only the case  $\kappa_t = -1$ , but  
 2400 an extended range of  $\kappa_t$  and  $\kappa_V$  values may be investigated.

2401  $tHq$  and  $tHW$  cross section in the  $\kappa_t$ - $\kappa_V$  phase space are shown in Figure 6.7. As  
 2402 said in section 3.1, the  $tHq$  sample was generated using the 4F scheme which provides  
 2403 a better description of the additional  $b$  quark from the initial gluon splitting, while the  
 2404  $tHW$  sample was generated using the 5F scheme in order to remove its interference  
 2405 with  $t\bar{t}H$  at LO.

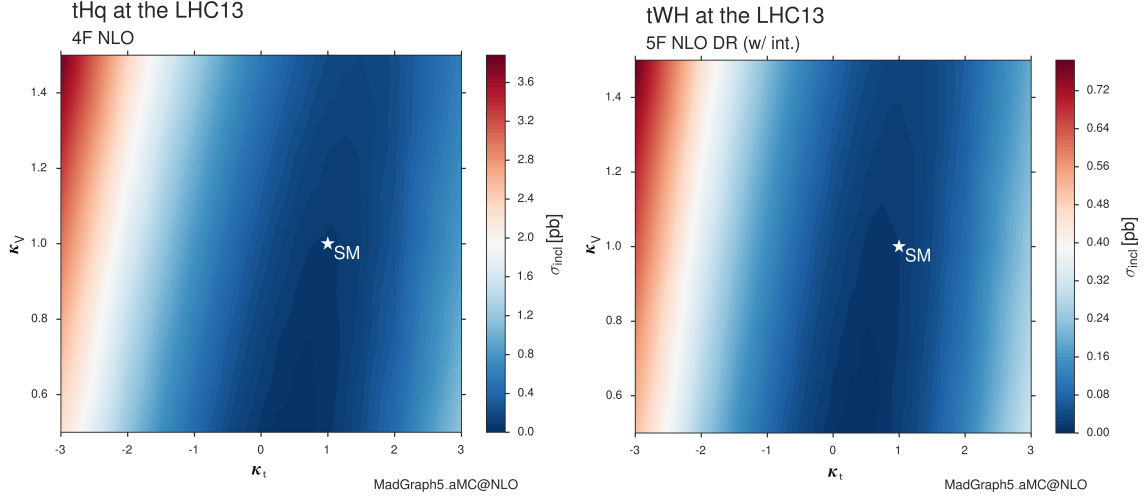


**Figure 6.7:**  $tHq$  and  $tHW$  cross section in the  $\kappa_t$ - $\kappa_V$  phase space [150].

#### 2406 MC signal samples

2407 The two signal samples,  $tHq$  and  $tHW$ , correspond to the `RunIISummer16MiniAODv2`  
 2408 campaign produced with `CMSSW_80X`; they were produced with `MG5_aMC@NLO`  
 2409 (version 5.2.2.3), in LO order mode at  $\sqrt{s} = 13$  TeV, and are normalized to NLO cross  
 2410 sections (see Table 6.2). The Higgs boson is assumed to be SM-like except for the  
 2411 values of its couplings to the top quark and W boson. Each sample was generated  
 2412 with a set of event weights corresponding to 51 different values of  $(\kappa_t, \kappa_V)$  couplings,  
 2413 accessible in terms of LHE event weights as shown in Table A.3; however, the main  
 2414 interest is the  $(\kappa_t = -1, \kappa_V = 1)$  case.

Sample	$\sigma$ [pb]	BF
<code>/THQ_Hincl_13TeV-madgraph-pythia8_TuneCUETP8M1/</code>	0.7927	0.324
<code>/THW_Hincl_13TeV-madgraph-pythia8_TuneCUETP8M1/</code>	0.1472	1.0
<code>/tthJetToNonbb_M125_13TeV_amcatnloFXFX_madspin_pythia8_mWCutfix/</code>	0.2151	1.0

**Table 6.2:** MC signal samples used in this analysis; cross section and branching fraction are also listed [150].

2415 The  $t\bar{t}H$  sample was produced using `AMC@NLO` interfaced to `PYTHIA 8` for  
 2416 the parton shower, and is scaled to NLO cross sections. The  $t\bar{t}H$  cross section depends

2417 quadratically on  $\kappa_t$ ; however, in contrast to the  $tHq$  and tHW samples, the scaling  
 2418 is not performed during the sample generation process but in the analysis code since  
 2419 it was decided to include the  $t\bar{t}H$  process as part of the signal in the course of the  
 2420 analysis.

2421 **MC background samples**

2422 Several MC generators were used to generate the samples of the background processes.  
 2423 The dominant background sources ( $t\bar{t}$ ,  $t\bar{t}W$ ,  $t\bar{t}Z$ ) were produced using AMC@NLO  
 2424 interfaced to PYTHIA8, and are scaled to NLO cross sections. Other minor back-  
 2425 ground processes are simulated using POWHEG interfaced to PYTHIA, or bare  
 2426 PYTHIA as stated in the sample names in Table A.4. Pileup interactions are in-  
 2427 cluded in the simulation in order to reflect the observed multiplicity in data; the  
 2428 simulated events are weighted according to the actual pileup in data, estimated from  
 2429 the measured bunch-to-bunch instantaneous luminosity and the total inelastic cross  
 2430 section, 69.2 mb. All events are finally passed through a full simulation of the CMS  
 2431 detector based on GEANT4, and reconstructed using the same algorithms as used for  
 2432 the data.

2433 **6.5 Object Identification**

2434 In this section, the specific definitions of the physical objects in terms of the numerical  
 2435 values assigned to the reconstruction parameters are presented; thus, the provided  
 2436 details summarize and complement the descriptions presented in previous chapters.  
 2437 The object reconstruction and selection strategy used in this thesis is inherited from  
 2438 the analyses in References [145, 149], thus, the information in this section is extracted  
 2439 from those documents unless other References are stated.

### 2440 6.5.1 Lepton reconstruction and identification

2441 Two types of leptons are defined in this analysis: *signal leptons* are those coming from  
 2442  $W, Z$  and  $\tau$  decays which usually are isolated from other particles; *background leptons*  
 2443 are defined as leptons produced in  $b$ -jet hadron decays, light-jets misidentification,  
 2444 and photon conversions.

2445 The process of reconstruction and identification of electron and muon candidates  
 2446 was described in chapter3, hence, the identification variables used in order to retain  
 2447 the highest possible efficiency for signal leptons while maximizing the rejection of  
 2448 background leptons are listed and described in the following sections <sup>2</sup>.

2449 The identification variables include not only observables related directly to the re-  
 2450 constructed leptons themselves, but also to the clustered energy deposits and charged  
 2451 particles in a cone around the lepton direction (jet-related variables); an initial loose  
 2452 preselection of leptons candidates is performed and then an MVA discriminator, re-  
 2453 ferred to as *lepton MVA* discriminator, is used to distinguish signal leptons from  
 2454 background leptons.

### 2455 Muons

2456 The Physics Objects Groups (POG) at CMS, are in charge of studying and defining  
 2457 the set of selection criteria applied on the course of reconstruction and identification  
 2458 of particles. These selection criteria are implemented in the CMS framework in the  
 2459 form of several object identification working points according to the strength of the  
 2460 requirements.

2461 The muon candidates are reconstructed by combining information from the tracker  
 2462 system and the muon detection system of CMS detector and the POG defined three

---

<sup>2</sup> the studies performed to optimize the identification are far from the scope of this thesis, therefore, only general descriptions are provided

2463 working points for muon identification *MuonID* [153];

- 2464     • *POG Loose Muon ID* is a particle identified as a muon by the PF event re-  
 2465         construction and also reconstructed either as a global-muon or as an arbitrated  
 2466         tracker-muon. This identification criteria is designed to be highly efficient for  
 2467         prompt muons and for muons from heavy and light quark decays; it can be com-  
 2468         plemented by applying impact parameter cuts in analyses with prompt muon  
 2469         signals.
- 2470     • *POG Medium Muon ID* is a Loose muon with additional track-quality and  
 2471         muon-quality (spatial matching between the individual measurements in the  
 2472         tracker and the muon system) requirements. This identification criteria is de-  
 2473         signed to be highly efficient in the separation of the muons coming from decay  
 2474         in flight of heavy quarks and muons coming from B meson decays as well as  
 2475         prompt muons. An additional category *MVA Prompt ID* is defined in this iden-  
 2476         tification criteria directed to discriminated muons from B mesons and prompt  
 2477         muons (from W,Z and  $\tau$  decays). The Medium ID provides the same fake rate as  
 2478         the Tight Muon ID but a higher efficiency on prompt and B-decays muons. [154]
- 2479     • *POG Tight Muon ID* is a global muon with additional muon-quality require-  
 2480         ments Tight Muon ID selects a subset of the PF muons.

2481         Only muons within the muon system acceptance  $|\eta| < 2.4$  and minimum  $p_T$  of 5  
 2482         GeV are considered.

### 2483     **Electrons**

2484         Electrons are reconstructed using information from the tracker and from the electro-  
 2485         magnetic calorimeter and identified by an MVA algorithm (*MVA eID* discriminant)

2486 using the shape of the calorimetric shower variables like the shape in  $\eta$  and  $\phi$ , the clus-  
 2487 ter circularity, widths along  $\eta$  and  $\phi$ ; track-cluster matching variables like  $E_{tot}/p_{in}$ ,  
 2488  $E_{Ele}/p_{out}$ ,  $\Delta\eta_{in}$ ,  $\Delta\eta_{out}$ ,  $\Delta\phi_{in}$ ,  $1/E - 1/p$ ; and track quality variables like  $\chi^2$  of the  
 2489 GSF tracks, the number of hits used by the GSF filter [155].

2490 A loose selection based on  $\eta$ -dependent cuts on this discriminant is used to prese-  
 2491 lect electron candidates, the full shape of the discriminant is used in the lepton MVA  
 2492 selection to separate signal leptons from background leptons (described in Section  
 2493 6.5.1).

2494 In order to reject electrons from photon conversions, electron candidates with  
 2495 missing hits in the pixel tracker layers or matched to a conversion secondary vertex  
 2496 are discarded. Electrons are selected for the analysis if they have  $p_T > 7$  GeV and  
 2497 are located within the tracker system acceptance region ( $|\eta| < 2.5$ ).

#### 2498 Lepton vertexing and pile-up rejection

2499 The impact parameter in the transverse plane  $d_0$ , impact parameter along the  $z$ -  
 2500 axis  $d_z$ , and the impact parameter significance in the detector space  $SIP_{3D}$ , are  
 2501 considered to perform the identification and rejection of pile-up, misreconstructed  
 2502 tracks, and background leptons from b-hadron decays; pile-up and misreconstructed  
 2503 track mitigation is achieved by imposing loose cuts on the impact parameter variables.  
 2504 The full shape of the those variables is used in a lepton MVA classifier to achieve the  
 2505 best separation between the signal and the background leptons.

#### 2506 Lepton isolation

2507 PF is able to recognize leptons from two different sources: on one side, leptons from  
 2508 the decays of heavy particles, such as W and Z bosons, which are normally isolated  
 2509 in space from the hadronic activity in the event; on the other side, leptons from the

2510 decays of hadrons and jets misidentified as leptons, which are not isolated as the  
 2511 former. For highly boosted systems, like the lepton and the  $b$ -jet generated in the  
 2512 semileptonic decay of a boosted top, the decay products tend to be more closer and  
 2513 sometimes they even overlap; thus, the PF standard definition of isolation in terms of  
 2514 the separation between the lepton candidates and other PF objects in the  $\eta$ - $\phi$  plane,

$$\Delta R = \sqrt{(\eta^l - \eta^i)^2 + (\phi^l - \phi^i)^2} < 0.3 \quad (6.1)$$

2515 which considers all the neutral, charged hadrons and photons in a cone around the  
 2516 leptons, is refocused to the local isolation of the leptons through the mini-isolation  
 2517  $I_{mini}$  [156] defined as the sum of particle flow candidates  $p_T$  within a cone around  
 2518 the lepton, corrected for the effects of pileup and divided by the lepton  $p_T$

$$I_{mini} = \frac{\sum_R p_T(h^\pm) - \max\left(0, \sum_R p_T(h^0) + p_T(\gamma) - \rho \mathcal{A}\left(\frac{R}{0.3}\right)^2\right)}{p_T(l)} \quad (6.2)$$

2519 where  $\rho$  is the pileup energy density,  $h^\pm, h^0, \gamma, l$ , represent the charged hadron, neutral  
 2520 hadrons, photons, and the lepton, respectively. The radius  $R$  of the cone depends on  
 2521 the  $p_T$  of the lepton according to

$$R = \frac{10\text{GeV}}{\min(\max(p_T(l), 50\text{GeV}), 200\text{GeV})}, \quad (6.3)$$

2522 The  $p_T$  dependence of the cone size allows for greater signal efficiency. Setting a  
 2523 cut on  $I_{mini}$  below a given threshold ensures that the lepton is locally isolated, even  
 2524 in boosted systems. The effect of pileup is mitigated using the so-called effective area  
 2525 correction  $\mathcal{A}$  listed in Table 6.3.

2526 A loose cut on  $I_{mini}$  is applied to pre-select the muon and electron candidates;

$ \eta $ range	$\mathcal{A}(e)$ neutral/charged	$A(\mu)$ neutral/charged
0.0 - 0.8	0.1607 / 0.0188	0.1322 / 0.0191
0.8 - 1.3	0.1579 / 0.0188	0.1137 / 0.0170
1.3 - 2.0	0.1120 / 0.0135	0.0883 / 0.0146
2.0 - 2.2	0.1228 / 0.0135	0.0865 / 0.0111
2.2 - 2.5	0.2156 / 0.0105	0.1214 / 0.0091

**Table 6.3:** Effective areas, for electrons and muons used to mitigate the effect of pileup by using the so-called effective area correction.

however, the full shape is used in the lepton MVA discriminator when performing the signal lepton selection.

### Jet-related variables

In order to reject misidentified leptons from  $b$ -jets, mostly coming from  $t\bar{t}$ +jets, Drell-Yan+jets, and  $W$ +jets events, the vertexing and isolation described in previous sections are complemented with additional variables related to the closest reconstructed jet to the lepton, i.e., the PF jets reconstructed<sup>3</sup> around the leptons with  $\Delta R = \sqrt{(\eta^l - \eta^{jet})^2 + (\phi^l - \phi^{jet})^2} < 0.5$ . The identification variables used in the lepton MVA discriminator are the ratio  $p_T^l/p_T^{jet}$ , the CSV b-tagging discriminator value of the jet, the number of charged tracks of the jet, and the relative  $p_T$  given by

$$p_T^{rel} = \frac{(\vec{p}_{jet} - \vec{p}_l) \cdot \vec{p}_l}{||\vec{p}_{jet} - \vec{p}_l||}. \quad (6.4)$$

### LeptonMVA discriminator

Electrons and muons passing the basic selection process described above are referred to as *loose leptons*. Additional discrimination between signal leptons and background leptons is crucial considering that the rate of  $t\bar{t}$  production is much larger than the signal, hence, an overwhelming background from  $t\bar{t}$  production. To maximally ex-

<sup>3</sup> charged hadrons from PU vertices are not removed prior to the jet clustering.

2542 exploit the available information in each event to that end, the dedicated lepton MVA  
 2543 discriminator, based on a boosted decision tree (BDT) algorithm, has been built so  
 2544 that all the identification variables can be used together.

2545 The lepton MVA discriminator training is performed using simulated signal Loose  
 2546 leptons from the  $t\bar{t}H$  MC sample and fake leptons from the  $t\bar{t}$  + jets MC sample,  
 2547 separately for muons and electrons. The input variables used include vertexing, iso-  
 2548 lation and jet-related variables, the  $p_T$  and  $\eta$  of the lepton, the electron MVA eID  
 2549 discriminator and the muon segment-compatibility variables. An additional require-  
 2550 ment known as *tight-charge* requirement, is imposed by comparing two independent  
 2551 measurement of the charge, one from the ECAL supercluster and the other from the  
 2552 tracker; thus, the consistency in the measurements of the electron charge is ensured  
 2553 so that events with a wrong electron charge assignment are rejected; this variable is  
 2554 particularly used in the  $2lss$  channel to suppress opposite-sign events for which the  
 2555 charge of one of the leptons has been mismeasured. The tight-charge requirement for  
 2556 muons is represented by the requirement of a consistently well measured track trans-  
 2557 verse momentum given by  $\Delta p_T/p_T < 0.2$ . Leptons are selected for the final analysis  
 2558 if they pass a given threshold of the BDT output, and are referred to as *tight leptons*  
 2559 in the following.

2560 The validation of the lepton MVA algorithm and the lepton identification variables  
 2561 is performed using data in various control regions; the details about that validation  
 2562 are not discussed here but can be found in Reference [149].

### 2563 Selection definitions

2564 Electron and muon object identification is defined in three different sets of selections  
 2565 criteria; the *Loose*, *Fakeable Object*, and *Tight* selection. These three levels of selection  
 2566 are designed to serve for event level vetoes, the fake rate estimation application region,

and the final signal selection, respectively. The  $p_T$  of fakeable objects is defined as  $0.85 \times p_T(\text{jet})$ , where the jet is the one associated to the lepton object. This mitigates the dependence of the fake rate on the momentum of the fakeable object and thereby improves the precision of the method.

Tables 6.4 and 6.5 list the full criteria for the different selections of muons and electrons.

Cut	Loose	Fakeable object	Tight
$ \eta  < 2.4$	✓	✓	✓
$p_T$	$> 5\text{GeV}$	$> 15\text{GeV}$	$> 15\text{GeV}$
$ d_{xy}  < 0.05$ (cm)	✓	✓	✓
$ d_z  < 0.1$ (cm)	✓	✓	✓
$\text{SIP}_{3D} < 8$	✓	✓	✓
$I_{\text{mini}} < 0.4$	✓	✓	✓
is Loose Muon	✓	✓	✓
jet CSV	–	$< 0.8484$	$< 0.8484$
is Medium Muon	–	–	✓
tight-charge	–	–	✓
lepMVA $> 0.90$	–	–	✓

**Table 6.4:** Requirements on each of the three muon selections. In the cases where the cut values change between the selections, those values are listed in the table. Otherwise, whether the cut is applied is indicated.

In addition to the previously defined requirements for jets, they are required to be separated from any lepton candidates passing the fakeable object selections by  $\Delta R > 0.4$ .

## 6.5.2 Lepton selection efficiency

Efficiencies of reconstruction and selecting loose leptons are measured both for muons and electrons using a tag and probe method on both data and MC, using  $Z \rightarrow \ell^+ \ell^-$  [157]. The scale factors are derived from the ratio of efficiencies  $\varepsilon_i(p_T, \eta)$  measured

Cut	Loose	Fakeable Object	Tight
$ \eta  < 2.5$	✓	✓	✓
$p_T$	$> 7\text{GeV}$	$> 15\text{GeV}$	$> 15\text{GeV}$
$ d_{xy}  < 0.05 \text{ (cm)}$	✓	✓	✓
$ d_z  < 0.1 \text{ (cm)}$	✓	✓	✓
$\text{SIP}_{3D} < 8$	✓	✓	✓
$I_{\text{mini}} < 0.4$	✓	✓	✓
MVA eID $> (0.0, 0.0, 0.7)$	✓	✓	✓
$\sigma_{in\eta} < (0.011, 0.011, 0.030)$	—	✓	✓
$\text{H/E} < (0.10, 0.10, 0.07)$	—	✓	✓
$\Delta\eta_{in} < (0.01, 0.01, 0.008)$	—	✓	✓
$\Delta\phi_{in} < (0.04, 0.04, 0.07)$	—	✓	✓
$-0.05 < 1/E - 1/p < (0.010, 0.010, 0.005)$	—	✓	✓
$p_T^{\text{ratio}}$	—	$> 0.5^\dagger / -$	—
jet CSV	—	$< 0.3^\dagger / < 0.8484$	$< 0.8484$
tight-charge	—	—	✓
conversion rejection	—	—	✓
Number of missing hits	$< 2$	$== 0$	$== 0$
lepton MVA $> 0.90$	—	—	✓

**Table 6.5:** Criteria for each of the three electron selections. In cases where the cut values change between selections, those values are listed in the table. Otherwise, whether the cut is applied is indicated. In some cases, the cut values change for different  $\eta$  ranges. These ranges are  $0 < |\eta| < 0.8$ ,  $0.8 < |\eta| < 1.479$ , and  $1.479 < |\eta| < 2.5$  and the respective cut values are given in the form (value<sub>1</sub>, value<sub>2</sub>, value<sub>3</sub>). For the two  $p_T^{\text{ratio}}$  and CSV rows, the cuts marked with a  $\dagger$  are applied to leptons that fail the lepton MVA cut, while the loose cut value is applied to those that pass the lepton MVA cut.

for a given lepton in data/MC, according to

$$\rho(p_T, \eta) = \frac{\varepsilon_{\text{data}}(p_T, \eta)}{\varepsilon_{\text{MC}}(p_T, \eta)}. \quad (6.5)$$

The scale factor for each event is used to correct the weight of the event in the full sample; therefore, the full simulation correction is given by the product of all the individual scale factors. The scale factors used in this thesis are inherited from Reference [149] which in turns inherited them from leptonic SUSY analyses using equivalent lepton selections.

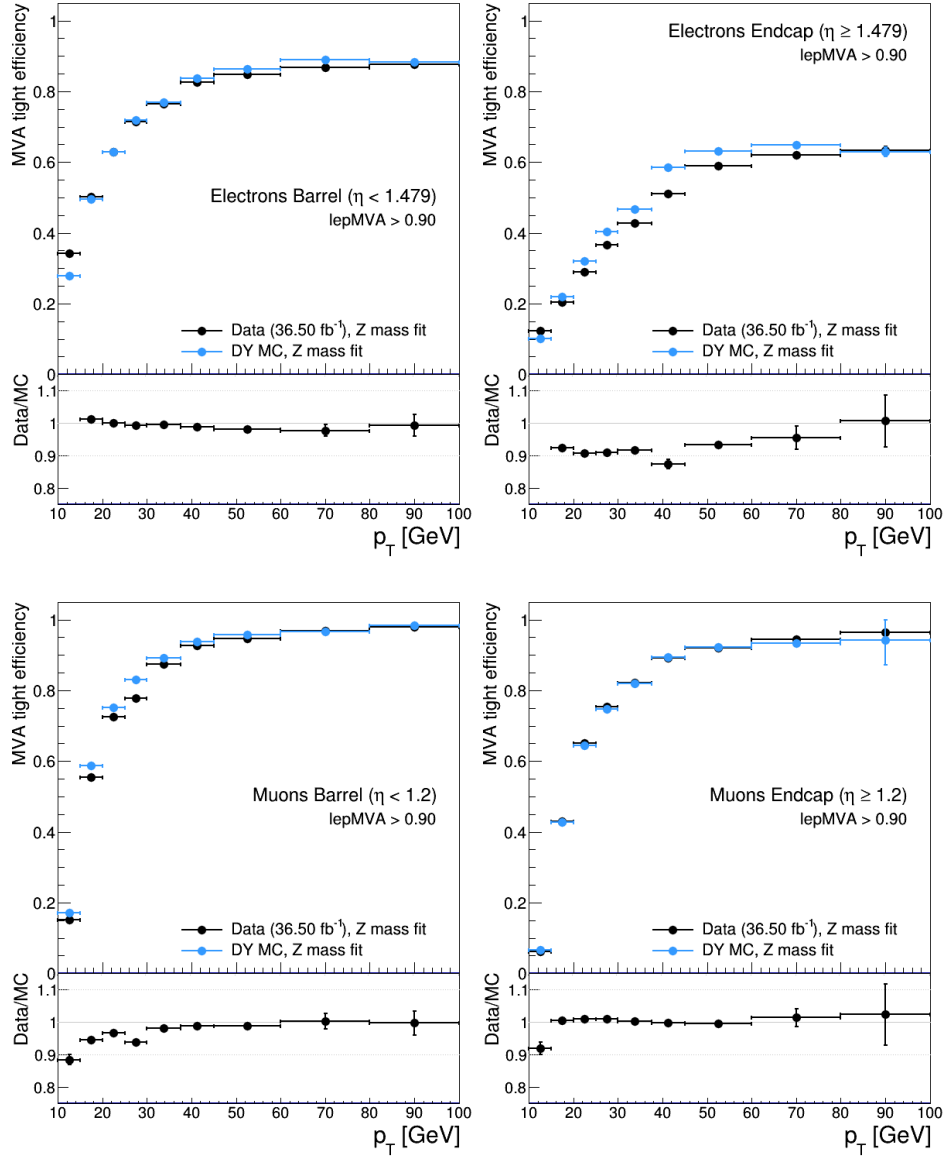


**Figure 6.8:** Tight vs loose selection efficiencies for electrons (top), and muons (bottom), for the  $2lss$  definition, i.e., including the tight-charge requirement.

2586        The efficiency of applying the tight selection as defined in Tables 6.4 and 6.5, on the  
 2587        loose leptons are determined by using a tag and probe method on a sample of Drell-  
 2588        Yan enriched events. Figures 6.8 and 6.9 show the efficiencies for the  $2lss$  channel and  
 2589         $3l$  channel respectively. Efficiencies in the  $2lss$  channel have been produced including  
 2590        the tight-charge requirement, while for the  $3l$  channel it is not included. Number

of passed and failed probes are determined from a fit to the invariant mass of the dilepton system. Simulation is corrected using these scale factors; note that they depends on  $\eta$  and  $p_T$ .

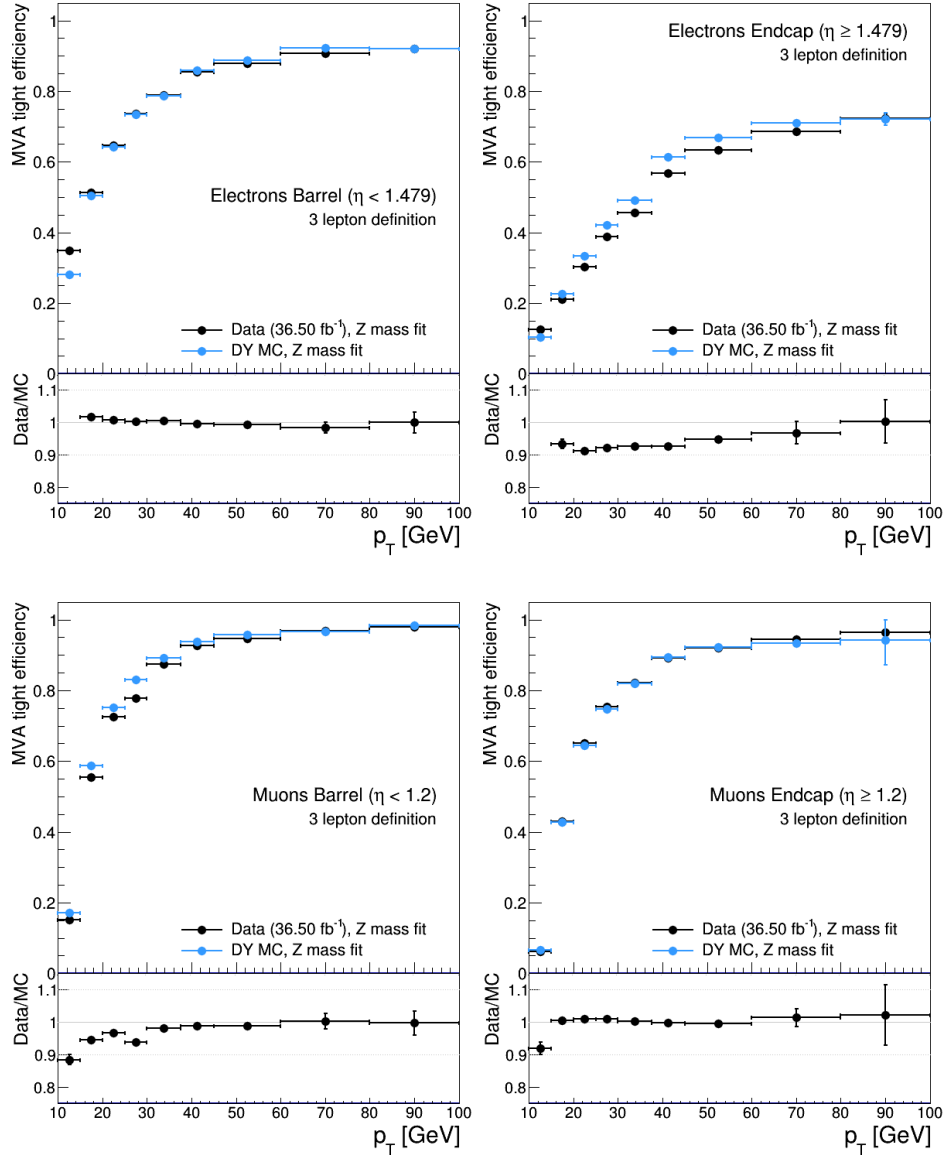


**Figure 6.9:** Tight vs loose selection efficiencies for electrons (top), and muons (bottom), for the  $3l$  channel not including the tight-charge requirement.

2594 **6.5.3 Jets and  $b$ -jet tagging**

2595 In this analysis, jets are reconstructed by clustering PF candidates using the anti- $k_t$   
 2596 algorithm with parameter distance  $\Delta R = 0.4$ ; those charged hadrons that are not  
 2597 consistent with the selected primary vertex are discarded from the clustering. The  
 2598 jet energy is then corrected for the varying response of the detector as a function  
 2599 of transverse momentum  $p_T$  and pseudorapidity  $\eta$ . Jets are selected for use in the  
 2600 analysis only if they have  $p_T > 25$  GeV and are separated from any selected leptons  
 2601 by  $\Delta R > 0.4$ .

2602 Jets coming from the primary vertex and jets coming from pile-up vertices are  
 2603 distinguished using a MVA discriminator based on the differences in the jet shapes,  
 2604 in the relative multiplicity of charged and neutral components, and in the different  
 2605 fraction of transverse momentum which is carried by the hardest components. Jet  
 2606 tracks are also required to be compatible with the primary vertex.

2607 Jets originated from the hadronization of a  $b$  quark are selected using a MVA  
 2608 likelihood discriminant which uses track-based lifetime information and reconstructed  
 2609 secondary vertices (CSV algorithm). Only jets within the CMS tracker acceptance  
 2610 ( $\eta < 2.4$ ) are identified with this tool. Data samples are used to measure the efficiency  
 2611 of the  $b$ -jet tagging and the probability to misidentify jets from light quarks or gluons;  
 2612 in both cases the measurements are parametrized as a function of the jet  $p_T$  and  $\eta$   
 2613 and later used to correct differences between the data and MC simulation in the  $b$   
 2614 tagging performance, by applying per-jet weights to the simulation, dependent on  
 2615 the jet  $p_T$ ,  $\eta$ ,  $b$  tagging discriminator, and flavor (from simulation truth) [151]. The  
 2616 per-event weight is taken as the product of the per-jet weights, including those of the  
 2617 jets associated to the leptons. The weights are derived on  $t\bar{t}$  and Z+jets events.

2618 Two working points are defined, based on the CSV algorithm output: ‘*loose*’ work-

ing point ( $\text{CSV} > 0.46$ ) with a  $b$  signal tagging efficiency of about 83% and a mistagging rate of about 8%; and *medium* working point ( $\text{CSV} > 0.80$ ) with  $b$ -tagging efficiency of about 69% and mistagging rate of order 1% [152]. Tagging of jets from charm quarks have efficiencies of about 40% and 18% for loose and medium working points respectively. Separate scale factors are applied to jets originating from bottom/charm quarks and from light quarks in simulated events to match the tagging efficiencies measured in the data.

#### 6.5.4 Missing Energy MET

As stated in Section 3.4.1.1, the MET vector is calculated as the negative of the vector sum of transverse momenta of all PF candidates in the event and its magnitude is referred to as  $E_T^{\text{miss}}$ . Due to pile-up interactions, the performance in determining MET is degraded; in order to correct for that, the energy from the selected jets and leptons that compose the event is assigned to the variable  $H_T^{\text{miss}}$ . It is calculated in the same way as  $E_T^{\text{miss}}$  and although it has worse resolution than  $E_T^{\text{miss}}$ , it is more robust in the sense that it does not rely on the soft part of the event. The event selection uses a linear discriminator based on the two variables given by

$$E_T^{\text{miss}} \text{LD} = 0.00397 * E_T^{\text{miss}} + 0.00265 * H_T^{\text{miss}} \quad (6.6)$$

taking advantage of the fact that the correlation between  $E_T^{\text{miss}}$  and  $H_T^{\text{miss}}$  is less for events with instrumental missing energy than for events with real missing energy. The working point  $E_T^{\text{miss}} \text{LD} > 0.2$  was chosen to ensure a good signal efficiency while keeping a good background rejection.

## 2639 6.6 Event selection

2640 Events are selected considering the features of the signal process and the decay sig-  
 2641 nature as described in Section 6.2. At the trigger level, events are selected to contain  
 2642 either one, two, or three leptons with minimal  $p_T$  thresholds:

- 2643 • single-lepton trigger → 24 GeV for muons and at 27 GeV for electrons
- 2644 • double-lepton triggers → leading and sub-leading leptons: 17 and 8 GeV for  
 2645 muons and 23 and 12 GeV for electrons.
- 2646 • three-lepton triggers → threshold on the third hardest lepton in the event: 5  
 2647 and 9 GeV for muons and electrons, respectively.

2648 The offline event selection level targets the specific topology of the  $tHq$  signal  
 2649 with  $H \rightarrow WW$  and  $t \rightarrow Wb \rightarrow l\nu b$ ; therefore, the resulting state is composed of three  
 2650 W bosons, one  $b$  quark, and a light spectator quark at high rapidity. The selection  
 2651 criteria for the two channels exploited in this analysis are summarized in Table 6.6.

Same-sign $\ell\ell$ channel	$\ell\ell\ell$ channel
have fired one of the corresponding trigger paths	
No loose leptons with $m_{\ell\ell} < 12\text{GeV}$	
One or more $b$ tagged jets $ \eta  < 2.4$	
One or more non-tagged jets: central → $p_T > 25\text{ GeV}$ , $\eta < 2.4$	
	forward → $p_T > 40\text{ GeV}$ , $\eta > 2.4$
	$E_T^{\text{miss}} \text{LD} > 0.2$
Exactly two tight same-sign leptons	Exactly three tight leptons
Lepton $p_T > 25/15\text{GeV}$	Lepton $p_T > 25/15/15\text{GeV}$
Electrons are triple-charge consistent.	No OSSF lepton pair with $ m_{\ell\ell} - m_Z  < 15\text{GeV}$
Muon $p_T$ resolution: $\Delta p_T/p_T < 0.2$ .	

**Table 6.6:** Summary of event selection.

2652 In the  $2lss$  channel, events with additional tight leptons are vetoed as well as those  
 2653 for which a loose lepton pair has an invariant mass below 12 GeV. A threshold in  $p_T$  of

2654 the leading and sub-leading leptons is also required. events where the two electrons  
2655 have invariant mass within 10 GeV of the Z boson mass (*Z-veto*) are discarded in  
2656 order to reject events from DY+jets production with charge misidentified electrons.

2657 In the  $3l$  lepton channel, leptons are required to have respectively  $p_T > 25\text{GeV}$ ,  $>$   
2658 15 GeV, and  $> 15$  GeV. Events with an opposite-sign, same-flavor lepton combina-  
2659 tion (OSSF) with invariant mass within 15 GeV of the Z boson mass are discarded in  
2660 order to reject events from  $WZ + \text{jets}$  production.

2661 The selection criteria in Table 6.6 represent a relatively loose selection that allows  
2662 to maintain a large signal efficiency while suppressing the main backgrounds. This  
2663 selection includes contributions from  $H \rightarrow \tau\tau$  and  $H \rightarrow ZZ$  as well. The events  
2664 obtained from the selection are then used to extract the signal contribution in a  
2665 second analysis step, using BDT discriminators against the main backgrounds of  
2666  $t\bar{t}W/t\bar{t}Z$  and non-prompt leptons from  $t\bar{t}$ . The shape of the discriminator variables  
2667 is then fit to the observed data distribution to estimate the signal and background  
2668 yields, simultaneously for all channels.

## 2669 6.7 Background modeling and predictions

2670 Irreducible backgrounds are reliably estimated from MC simulated events; there-  
 2671 fore, in this analysis all backgrounds involving prompt leptons are estimated in this  
 2672 way. Reducible backgrounds, are not well predicted by simulation, hence, they are  
 2673 estimated using data-driven methods; in the case of non-prompt leptons, a fake rate  
 2674 method is used.

2675 Drell-Yan contribution is reduced in the  $3l$  channel due to the requirement of an  
 2676 additional lepton, the jet counting and the Z-veto. Three boson contributions are  
 2677 reduced by rejecting events with extra leptons and by requiring forward jets or  $b$ -jets

2678 The  $2lss$  channel receives contribution from the associated production of two W  
 2679 bosons of equal charge and two light jets  $W^\pm W^\pm qq$  and from same-sign W boson  
 2680 pairs can also be produced in double parton scattering (DPS) processes, where each  
 2681 of the colliding protons gives two partons, resulting in two hard interactions.

2682 Backgrounds from  $t\bar{t}W$  and  $t\bar{t}Z$  processes are estimated using simulated events,  
 2683 corrected for data/MC differences and inefficiencies (trigger and lepton selection) in  
 2684 the same way as signal events. Their production cross sections are calculated at  
 2685 NLO order of QCD and EWK, considering theoretical uncertainties from unknown  
 2686 higher orders of 12% for  $t\bar{t}W$  and 10% for  $t\bar{t}Z$ . Additional uncertainties arise from the  
 2687 knowledge of PDFs and  $\hat{\text{S}}$  of about 4% each for  $t\bar{t}W$  and  $t\bar{t}Z$ .

### 2688 6.7.1 Diboson backgrounds

2689 Background contamination from diboson processes is strongly suppressed by imposing  
 2690 the Z-veto, vetoing additional leptons and requiring  $b$ -jets in the event. The diboson  
 2691 contribution is also estimated from simulated events; however, the overall normal-  
 2692 ization of this process is obtained from a dedicated control region. The motivation

behind that strategy is that even though the measured inclusive cross section for diboson processes (WZ,ZZ) is in good agreement with the NLO calculations [149], that agreement is perturbed when leptonic Z decays and hadronic jets in the final state are required; those requirements are precisely the ones that make the diboson production a background for the  $tHq$  signal. Thus, by using a dedicated control region dominated by WZ production<sup>4</sup>, the overall normalization is constrained.

The control region is defined by the presence of at least three leptons, of which one opposite-sign pair must be compatible with a Z boson decay, i.e., invert the Z-veto which makes the control region orthogonal to signal region; the b-jet tagging requirements is also inverted with respect to the signal region, i.e., require two not  $b$ -jets. A scale factor is extracted from the predicted distribution of WZ events in the control region, and the observed data, while keeping other processes fixed; this factor is used to scale the diboson prediction in the signal selection region. More details about the procedure used can be found in Reference [149] from where the scale factor is taken.

In order to test the usability of the diboson background scale factor in this analysis, a Z-enriched control region<sup>5</sup> was defined by inverting the Z-veto and requiring exactly three tight leptons with  $p_T > 25/15/15$  GeV, one or more jets passing the CSVv2 loose working point and less than four central jets. Figure 6.10 shows the distribution of three variables in the diboson control region; the good agreement between MC and data motivates the adoption of the diboson background scale factor.

. Their production cross sections are calculated at NLO of QCD and EWK, with theoretical uncertainties from unknown higher orders of 12% for  $t\bar{t}W$  and 10% for  $t\bar{t}Z$ . Further uncertainties arise from the knowledge of PDFs and  $\alpha_s$  of about 4% each for

---

<sup>4</sup> ZZ background is strongly reduced by the cut on MET.

<sup>5</sup> This control region is different to the one used to find the scale factor.

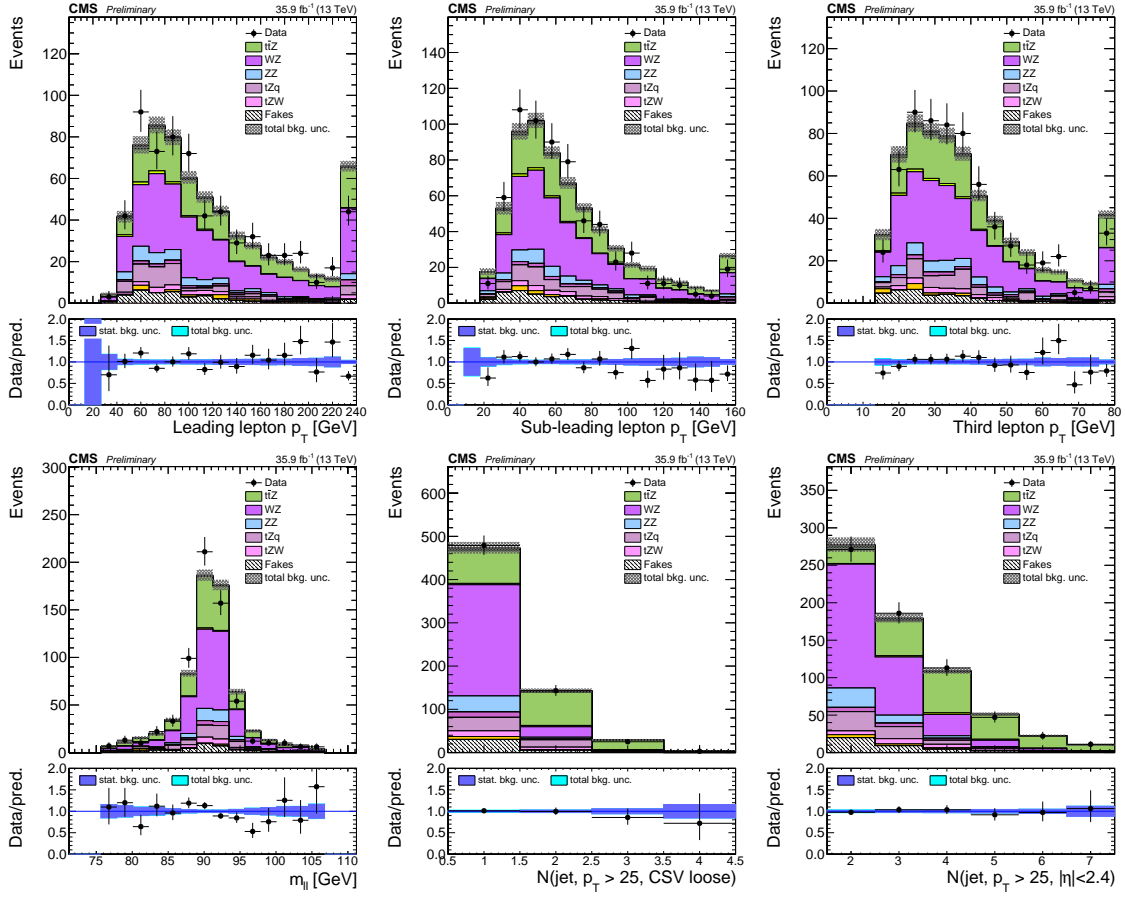


**Figure 6.10:** Kinematic distributions in the diboson control region.

2717  $t\bar{t}W$  and  $t\bar{t}Z$ .

2718 In the  $2lss$  channel case, additional background arises when the charge of a lepton  
 2719 in events with an originally opposite-sign pair is misidentified; usually this happens  
 2720 due to strongly asymmetric conversions of hard bremsstrahlung photons emitted from  
 2721 the initial lepton, therefore, it is more likely to happen for electrons than for muons.

2722 Additional identification criteria are applied for electrons with  $p_T$  greater than 30  
 2723 GeV to mimic the identification applied at trigger level in order to ensure consistency  
 2724 between the measurement region and application region of the fake-rate.

2725 where the contribution to the final selection is estimated by extrapolating from a  
 2726 sideband (or *application region*) with a looser lepton definition (the fakeable object

definitions in Tabs. 6.4 and 6.5) to the signal selection. The tight-to-loose ratios (or *fake rates*) are measured in several background dominated data events with dedicated triggers, subtracting the residual prompt lepton contribution using MC. Non-prompt leptons in our signal regions are predominantly produced in  $t\bar{t}$  events, with a much smaller contribution, from Drell–Yan production. The systematic uncertainty on the normalization of the non-prompt background estimation is on the order of 50%, and thereby one of the dominant limitations on the performance of multilepton analyses in general and this analysis in particular. It consists of several individual sources, such as the result of closure tests of the method using simulated events, limited statistics in the data control regions due to necessary prescaling of lepton triggers, and the uncertainty in the subtraction of residual prompt leptons from the control region.

The fake background where the leptons pass the looser selection are weighted according to how many of them fail the tight criteria. Events with a single failing lepton are weighted with the factor  $f/(1-f)$  for the estimate to the tight selection region, where  $f$  is the fake rate. Events with two failing leptons are given the negative weight  $-f_i f_j / (1-f_i)(1-f_j)$ , and for three leptons the weight is positive and equal to the product of  $f/(1-f)$  factor evaluated for each failing lepton.

Figures 6.11 show the distributions of some relevant kinematic variables, normalized to the cross section of the respective processes and to the integrated luminosity.

2746

The modeling of reducible and irreducible backgrounds in this analysis uses the exact methods, analysis code, and ROOT trees used for the  $t\bar{t}H$  multilepton analysis. We give a brief description of the methods and refer to the documentation of that analysis in Refs. [145, 149] for any details.

Once the events are selected in agreement with the signal characteristics, the extraction of the signal contribution is performed using multivariate discriminators

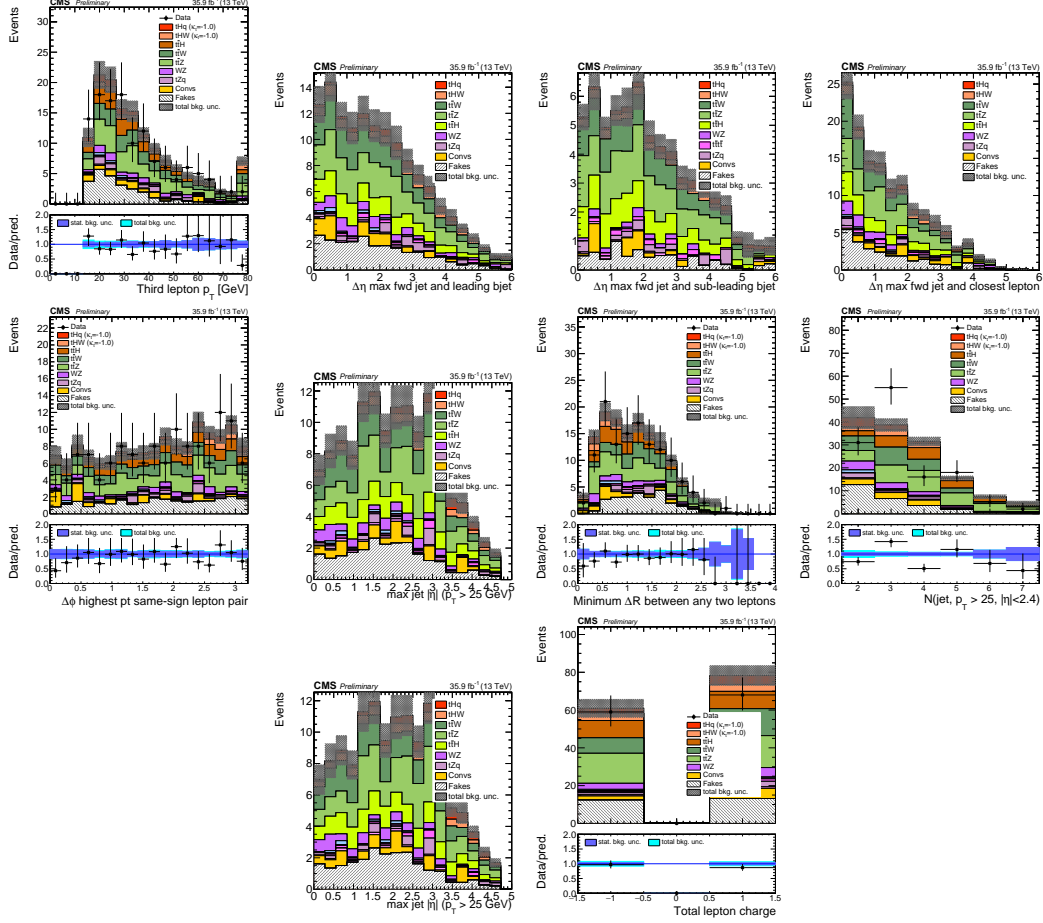


**Figure 6.11:** Distributions of input variables to the BDT for signal discrimination, three lepton channel, normalized to their cross section and to  $35.9\text{fb}^{-1}$ .

against the main backgrounds of  $t\bar{t}W/t\bar{t}Z$  and non-prompt leptons from  $t\bar{t}$ . The shape of the discriminator variables is then fit to the observed data distribution to estimate the signal and background yields, simultaneously for all channels.

A significant fraction of selected data events (about 50% in the dilepton channels, and about 80% in the trilepton channel) also passes the selection used in the dedicated search for  $tth$  in multilepton channels [17]. The expected and observed event yields of this selection are shown in Tab. 2. For the  $tH$  and  $t\bar{t}H$  processes, the largest contribution comes from Higgs decays to  $WW$  (about 75%), followed by  $\tilde{D}\tilde{D}$  (about 20%) and  $ZZ$  (about 5%). Other Higgs production modes contribute negligible event

2762 yields ( $< 5\%$  of the tH +ttH yield).

2763 .

2764 .

2765 .

2766 .

2767 .

2768 .

2769 .

2770 .

2771 .

2772 . . .

2773 . Multivariate techniques are used to discriminate the signal from the dominant  
2774 backgrounds. The analysis yields a 95% confidence level (C.L.) upper limit on the  
2775 combined tH + ttH production cross section times branching ratio of 0.64 pb, with  
2776 an expected limit of 0.32 pb, for a scenario with  $kt = \sqrt{1.0}$  and  $kV = 1.0$ . Values  
2777 of  $kt$  outside the range of  $\sqrt{1.25}$  to  $\sqrt{1.60}$  are excluded at 95% C.L., assuming  $kV$   
2778 = 1.0.

2779 Dont forget to mention previous constrains to ct check Reference ?? and Refer-  
2780 ences <https://link.springer.com/content/pdf/10.1007%2FJHEP01%282013%29088.pdf>  
2781 (paragraph after eq 2)

2782 **6.8 Signal discrimination**

2783 The production cross section for the signal processes  $tHq$ ,  $tHW$ , and  $t\bar{t}H$  is only  
 2784 about 600 fb (the enhancement provided by inverted couplings,  $\kappa_t = -1$  almost double  
 2785 it), resulting in a small signal to background ratio even for a tight selection. A  
 2786 multivariate method is hence employed to train a discriminator to separate  $tH$  signal  
 2787 events from the dominant background events ( $t\bar{t}$  and  $t\bar{t}V$ ).

2788 **6.8.1 MVA classifiers evaluation**

2789 Several MVA classifier algorithms were evaluated in order to determine the most  
 2790 appropriate method for this analysis<sup>6</sup>. The comparison is based on the performance  
 2791 of the classifiers, encoded in the plot of the background rejection as a function of the  
 2792 signal efficiency (ROC curve). The top side of Figure 6.12 shows the ROC curves  
 2793 for the several methods evaluated; two separate training were performed in the  $3l$   
 2794 channel against  $t\bar{t}$  and  $t\bar{t}V$  processes.

2795 In both cases the gradient boosted decision tree (*BDTA\_GRAD*) classifier offers  
 2796 the best results, followed by the adaptive BDT classifier (*BDTA*); the several Fisher  
 2797 classifiers tested, differ in their parameters and/or boosting method but they offer  
 2798 similar performance among them, while the k-Nearest Neighbour (kNN) classifier  
 2799 performance is below the rest of the classifiers. The corresponding ROC curves and  
 2800 in the  $2lss$  channel for trainings against  $t\bar{t}V$ (left) and  $t\bar{t}$  (right) processes are shown  
 2801 in the bottom side of Figure 6.12; the BDTG performance is similar to that in the  
 2802  $3l$  channel.

---

<sup>6</sup> The choice of the tested algorithms was based on the experience from previous analyses and considering the expertise of the members of the  $tHq$  and  $t\bar{t}H$  analyses groups. Only the BDT classifier is described in this thesis and a detailed description of all available methods can be found in Reference [127]

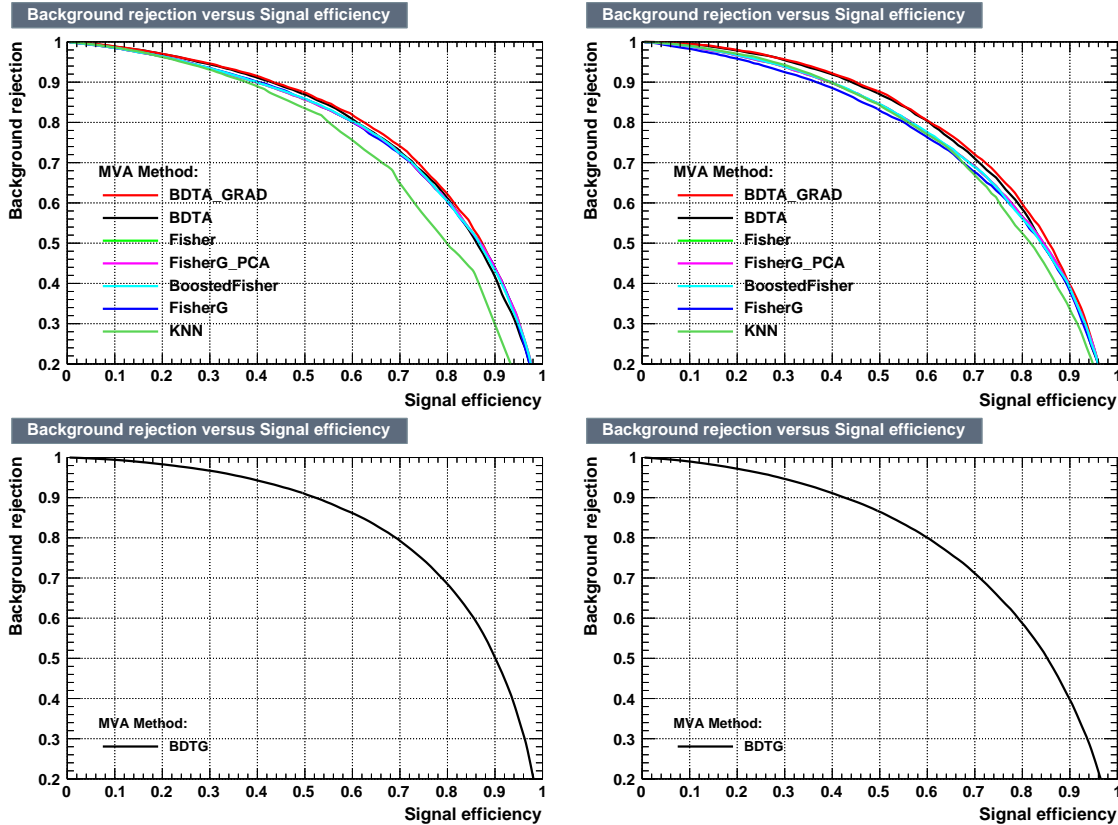


**Figure 6.12:** Top: Background rejection vs signal efficiency (ROC curves) for various MVA classifiers in the  $3l$  channel for training against  $t\bar{V}$  (left) and  $t\bar{t}$  (right). Bottom: background rejection vs signal efficiency (ROC curve) in the  $2lss$  channel for a single discriminator: BDTG, against  $t\bar{V}$  (left) and  $t\bar{t}$  (right).

## 2803 6.8.2 Discriminating variables

2804 The classifier chosen to separate the  $tHq$  signal from the main backgrounds is the  
 2805 boosted decision tree (BDTG) classifier, trained on simulated signal and background  
 2806 events. The samples used in the training are the  $tHq$  sample in Table 6.2, the samples  
 2807 in the third section of table A.4 and the samples marked with an \* in the same table.

2808 As explained in Section 5.1.1, a set of discriminating variables are given as input to  
 2809 the BDTG which combines the individual discrimination power of each input variable  
 2810 to produce a discriminator with the maximum discrimination power. Table 6.7 lists  
 2811 the input variables used in the BDTG trainings for this analysis.

2812        The same set of input variables was used to produce the plots for MVA classifiers  
 2813        evaluation.

Variable name	Description
nJet25	Number of jets with $p_T > 25$ GeV, $ \eta  < 2.4$
nJetEta1	Number of jets with $ \eta  > 1.0$ , non-CSV-loose
MaxEtaJet25	Max. $ \eta $ of any (non-CSV-loose) jet with $p_T > 25$ GeV
detaFwdJetClosestLep	$\Delta\eta$ forward light jet and closest lepton
detaFwdJetBJet	$\Delta\eta$ forward light jet and hardest CSV loose jet
detaFwdJet2BJet	$\Delta\eta$ forward light jet and second hardest CSV loose jet
Lep3Pt/Lep2Pt	$p_T$ of the 3 <sup>rd</sup> lepton (2 <sup>nd</sup> for ss2l)
totCharge	Sum of lepton charges
minDRll	Min $\Delta R$ any two leptons
dphiHighestPtSSPair	$\Delta\phi$ of highest $p_T$ same-sign lepton pair

**Table 6.7:** BDTG input variables. First section lists variables related to jet multiplicities; second section lists variables related to forward jet activity, and third section lists variables related to lepton kinematics.

2814        Plots in Figures 6.13 and 6.14 show the BDTG input variables distributions for  
 2815        the signal and background samples, in the 2lss and 3l channels respectively.

2816        The BDTA\_GRAD classifier output distributions for signal and backgrounds are  
 2817        shown on the bottom of Figure 6.12. As expected, a good discrimination power is  
 2818        obtained using default discriminator parameter values, with minimal overtraining., ,  
 2819        while a reduction in the overtraining is visible.

2820        Figure 6.15 shows the ROC curves and the BDTG classifier outputs in the 2lss  
 2821        channel for trainings against  $t\bar{t}V$  and  $t\bar{t}$  (right) processes. The BDTG performance is  
 2822        similar to that in the 3l channel, while a reduction in the overtraining is visible.

2823        Two BDTG classifiers are trained for the two main backgrounds expected in the  
 2824        analysis: events with prompt leptons from  $t\bar{t}W$  and  $t\bar{t}Z$ (also referred to as  $t\bar{t}V$ ), and  
 2825        events with non-prompt leptons from  $t\bar{t}$ . The datasets used in the training are the  $tHq$   
 2826        signal (see Tab. 6.2), and LO MADGRAPH samples of  $t\bar{t}W$  and  $t\bar{t}Z$ , in an admixture  
 2827        proportional to their respective cross sections (see Tab. ??).

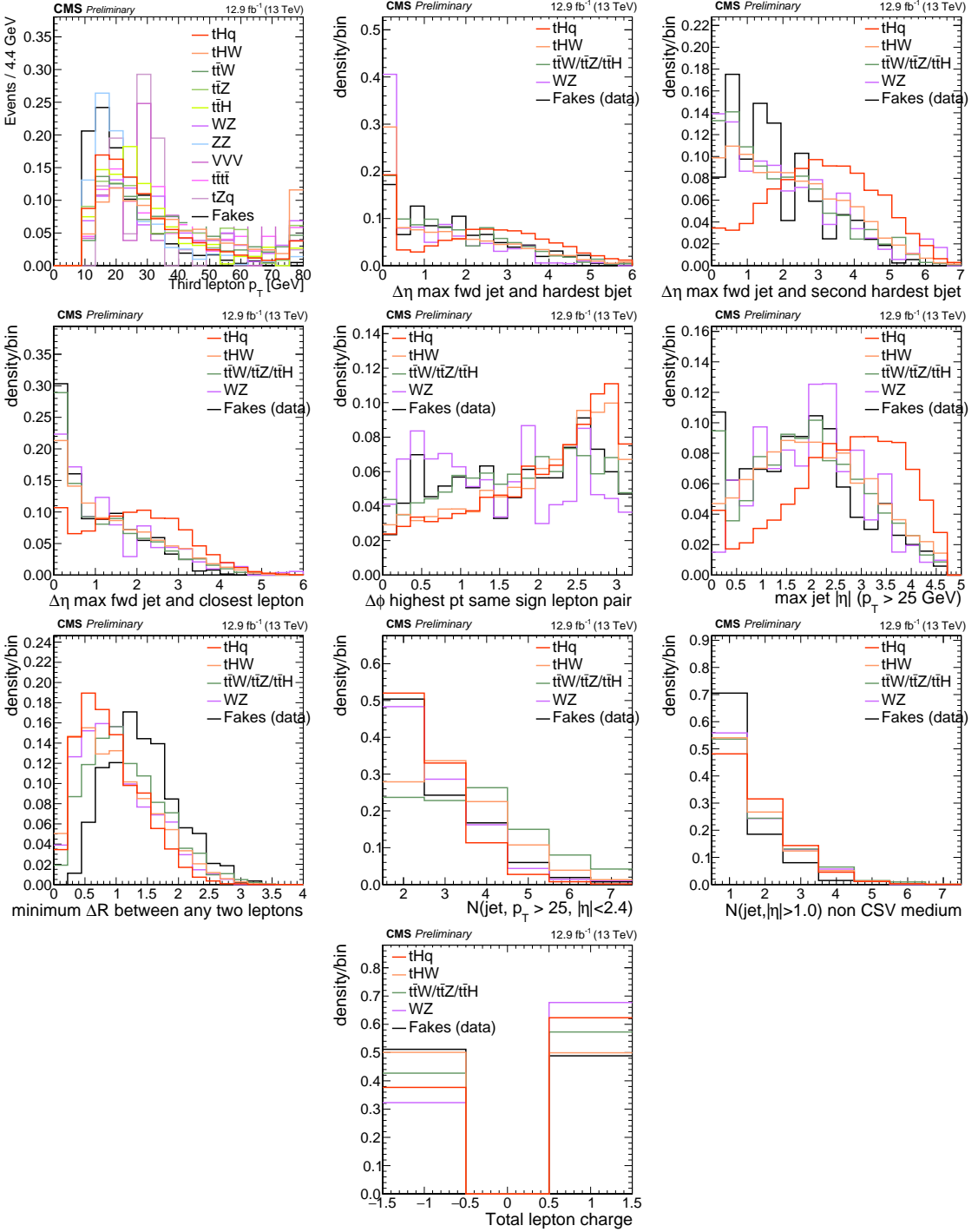


**Figure 6.13:** Distributions of the BDTG classifier input variables (not normalized) for signal discrimination in the  $3l$  channel.

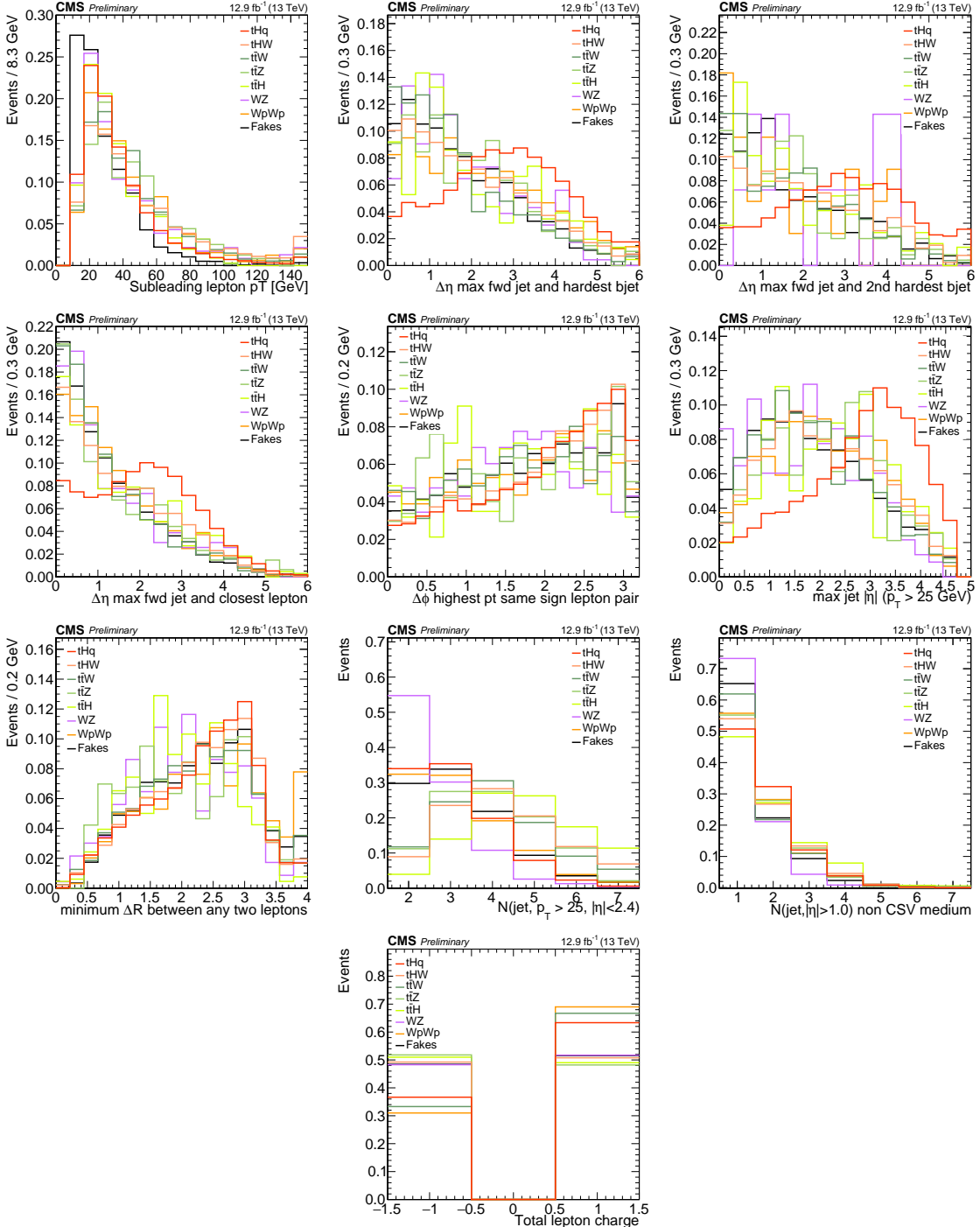


**Figure 6.14:** Distributions of input variables to the BDT for signal discrimination, two lepton same sign channel.

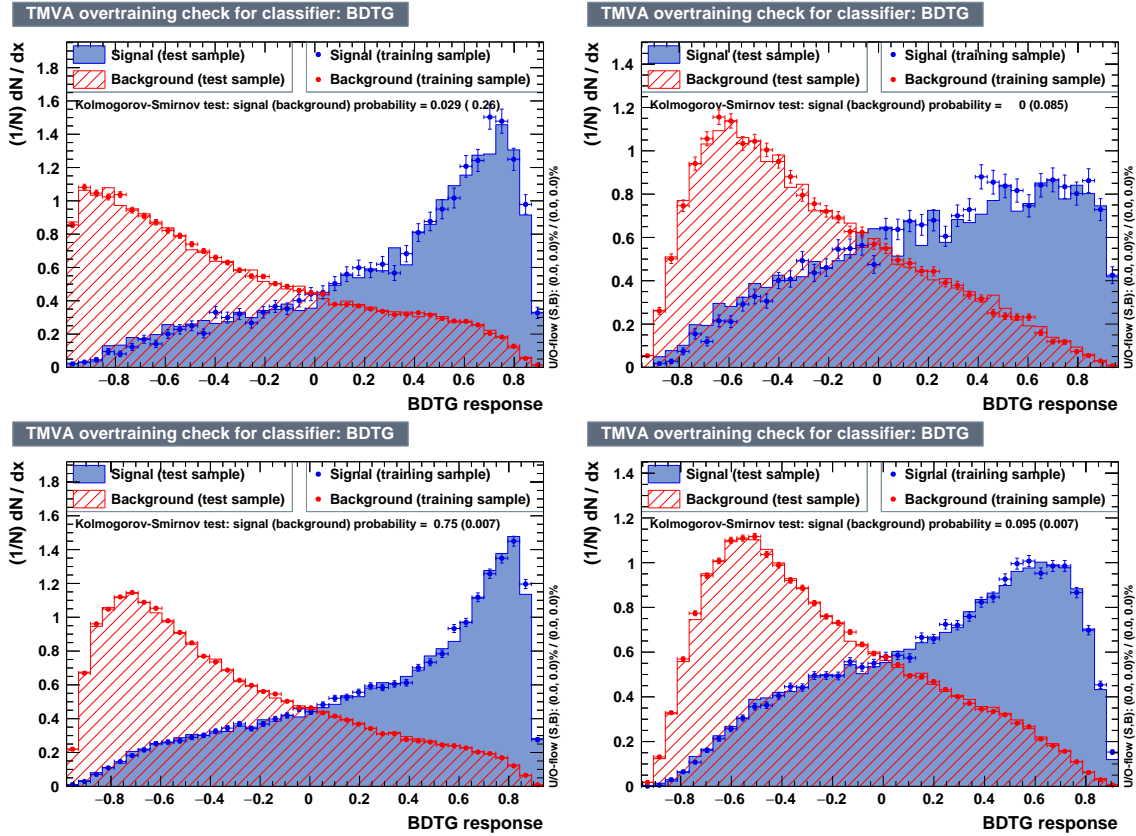


**Figure 6.15:** Top: Bottom: The output from the BDTG (BDTA\_GRAD label in the ROC curve) classifier training against  $t\bar{t}V$ (left) and  $t\bar{t}$  (right) Bottom: classifier output distribution, for training against  $t\bar{t}V$  (left) and against  $t\bar{t}$  (right).

2828 TMVA provides a ranking of the input variables by their importance in the clas-  
2829 sification process, shown in Table 6.9.

2830 The TMVA settings used in the BDT training are shown in Tab. 6.10.

2831 The MVA analysis consist of two stages: first a *training* where the MVA method is  
2832 trained to discriminate between simulated signal and background events, then a *test*  
2833 stage where the trained algorithm is used to classify different events from the samples.  
2834 The sample is obtained from a pre-selection (see Tab. ?? with pre-selection cuts).  
2835 Figures 6.16 show the input variables distributions as seen by the MVA algorithm.  
2836 Note that in contrast to the distributions in Fig. 6.13 only the main backgrounds ( $t\bar{t}$   
2837 from simulation,  $t\bar{t}V$ ) are included.

ttbar training			ttV training		
Rank	Variable	Importance	Variable	Importance	Importance
1	minDRll	1.329e-01	dEtaFwdJetBJet	1.264e-01	
2	dEtaFwdJetClosestLep	1.294e-01	Lep3Pt	1.224e-01	
3	dEtaFwdJetBJet	1.209e-01	maxEtaJet25	1.221e-01	
4	dPhiHighestPtSSPair	1.192e-01	dEtaFwdJet2BJet	1.204e-01	
5	Lep3Pt	1.158e-01	dEtaFwdJetClosestLep	1.177e-01	
6	maxEtaJet25	1.121e-01	minDRll	1.143e-01	
7	dEtaFwdJet2BJet	9.363e-02	dPhiHighestPtSSPair	9.777e-02	
8	nJetEta1	6.730e-02	nJet25_Recl	9.034e-02	
9	nJet25_Recl	6.178e-02	nJetEta1	4.749e-02	
10	lepCharge	4.701e-02	lepCharge	4.116e-02	

**Table 6.8:** TMVA input variables ranking for BDTA\_GRAD method for the trainings in the three lepton channel. For both trainings the rankings show almost the same 5 variables in the first places.

ttbar training			ttV training		
Rank	Variable	Importance	Variable	Importance	Importance
1	dEtaFwdJetClosestLep	1.394e-01	maxEtaJet25	1.357e-01	
2	minDRll	1.359e-01	dEtaFwdJet2BJet	1.267e-01	
3	maxEtaJet25	1.308e-01	dEtaFwdJetBJet	1.200e-01	
4	dPhiHighestPtSSPair	1.116e-01	Lep2Pt	1.196e-01	
5	Lep2Pt	1.111e-01	dEtaFwdJetClosestLep	1.145e-01	
6	dEtaFwdJetBJet	1.067e-01	minDRll	1.077e-01	
7	dEtaFwdJet2BJet	8.906e-02	nJet25_Recl	1.020e-01	
8	nJetEta1	6.445e-02	dPhiHighestPtSSPair	8.232e-02	
9	nJet25_Recl	6.254e-02	nJetEta1	5.948e-02	
10	lepCharge	4.848e-02	lepCharge	3.198e-02	

**Table 6.9:** TMVA input variables ranking for BDTA\_GRAD method in same-sign dilepton channel.

2838     The input variables distributions for  $2lss$  channel for signal against the  $t\bar{t}$  and  $t\bar{t}V$   
 2839    are shown in Figure 6.18 and Figure 6.19 respectively.

2840     Note that splitting the training in two groups reveals that some variables show  
 2841    opposite behavior for the two background sources; potentially screening the discrimi-  
 2842    nation power if they were to be used in a single discriminant. For some other variables  
 2843    the distributions are similar in both background cases.

2844     From table 6.7, it is clear that the input variables are correlated to some extend.  
 2845    These correlations play an important role for some MVA methods like the Fisher  
 2846    discriminant method in which the first step consist of performing a linear transfor-

---

```

TMVA.Types.kBDT
NTrees=800
BoostType=Grad
Shrinkage=0.10
!UseBaggedGrad
nCuts=50
MaxDepth=3
NegWeightTreatment=PairNegWeightsGlobal
CreateMVAPdfs

```

---

**Table 6.10:** TMVA configuration used in the BDT training.

2847 mation to an phase space where the correlations between variables are removed. In  
 2848 case a boosted decision tree (BDT) method however, correlations do not affect the  
 2849 performance. Figure 6.20 show the linear correlation coefficients for signal and back-  
 2850 ground for the two training cases (the signal values are identical by construction). As  
 2851 expected, strong correlations appears for variables related to the forward jet activity.  
 2852 Same trend is seen in case of the same sign dilepton channel in Figure 6.21.

## 2853 6.9 Additional discriminating variables

2854 Two additional discriminating variables were tested considering the fact that the  
 2855 forward jet in the background could come from the pileup; since we have a real forward  
 2856 jet in the signal, it could give some improvement in the discriminating power. The  
 2857 additional variables describe the forward jet momentum (fwdJetPt25) and the forward  
 2858 jet identification(fwdJetPUID). Distributions for these variables in the three lepton  
 2859 channel are shown in the Figure 6.22. The forward jet identification distribution  
 2860 show that for both, signal and background, jets are mostly real jets.

2861 The testing was made including in the MVA input one variable at a time, so we  
 2862 can evaluate the dicrimination power of each variable, and then both simultaneously.  
 2863 fwdJetPUID was ranked in the last place in importance (11) in both training (ttV

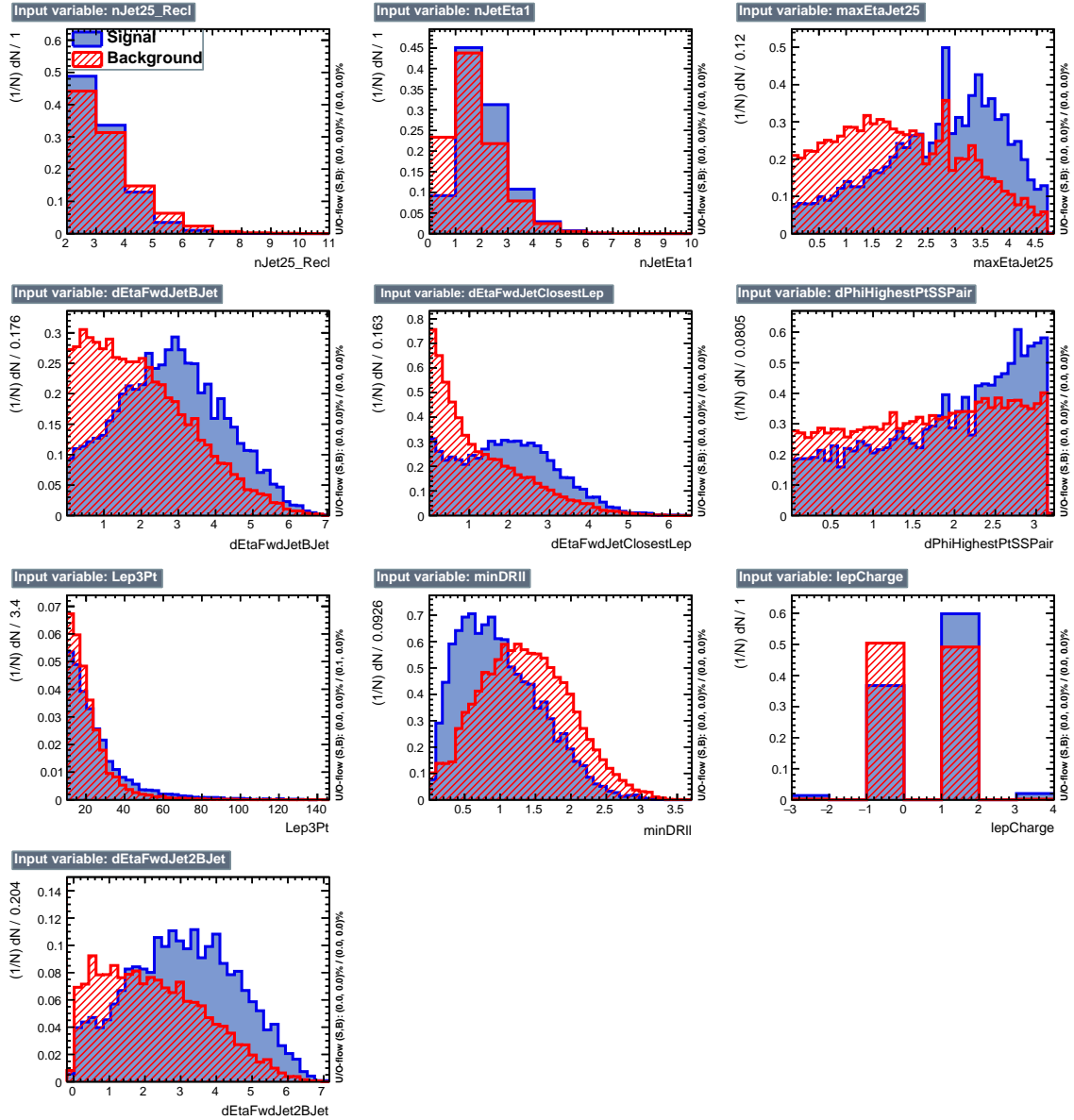


**Figure 6.16:** BDT inputs as seen by TMVA (signal, in blue, is  $tHq$ , background, in red, is  $t\bar{t}$ ) for the three lepton channel, discriminated against  $t\bar{t}$  (fakes) background.

and  $t\bar{t}$ ) while fwdJetPt25 was ranked 3 in the  $t\bar{t}V$  training and 7 in the  $t\bar{t}$  training.  
When training using 12 variables, fwdJetPt25 was ranked 5 and 7 in the  $t\bar{t}V$  and  $t\bar{t}$  trainings respectively, while fwdJetPUID was ranked 12 in both cases.  
The improvement in the discrimination performance provided by the additional variables is about 1%, so it was decided not to include them in the procedure. Table

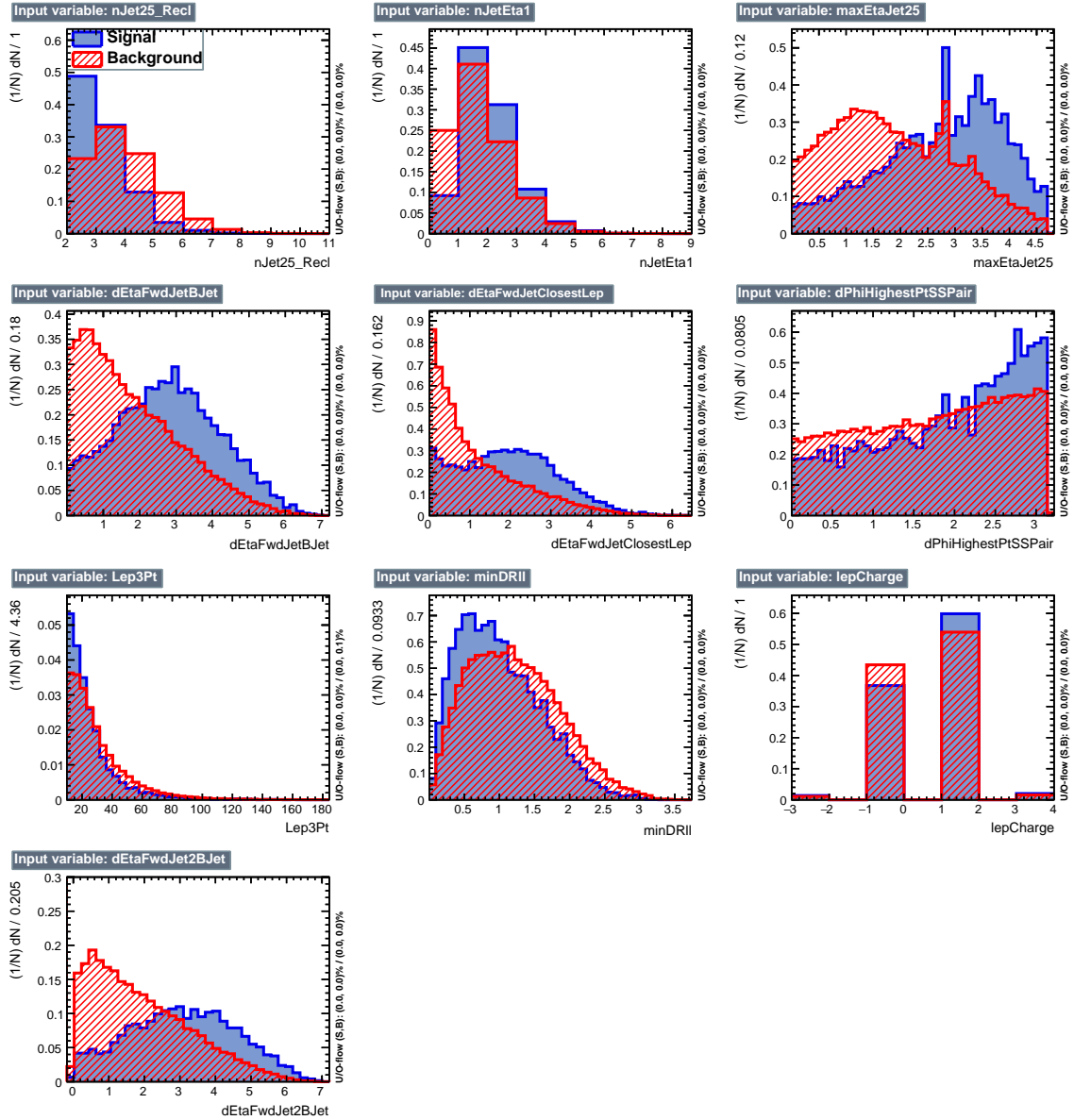


**Figure 6.17:** BDT inputs as seen by TMVA (signal, in blue, is  $tHq$ , background, in red, is  $t\bar{t}W+t\bar{t}Z$ ) for the three lepton channel, discriminated against  $t\bar{t}V$  background.

2869 6.11 show the ROC-integral for all the testing cases we made.

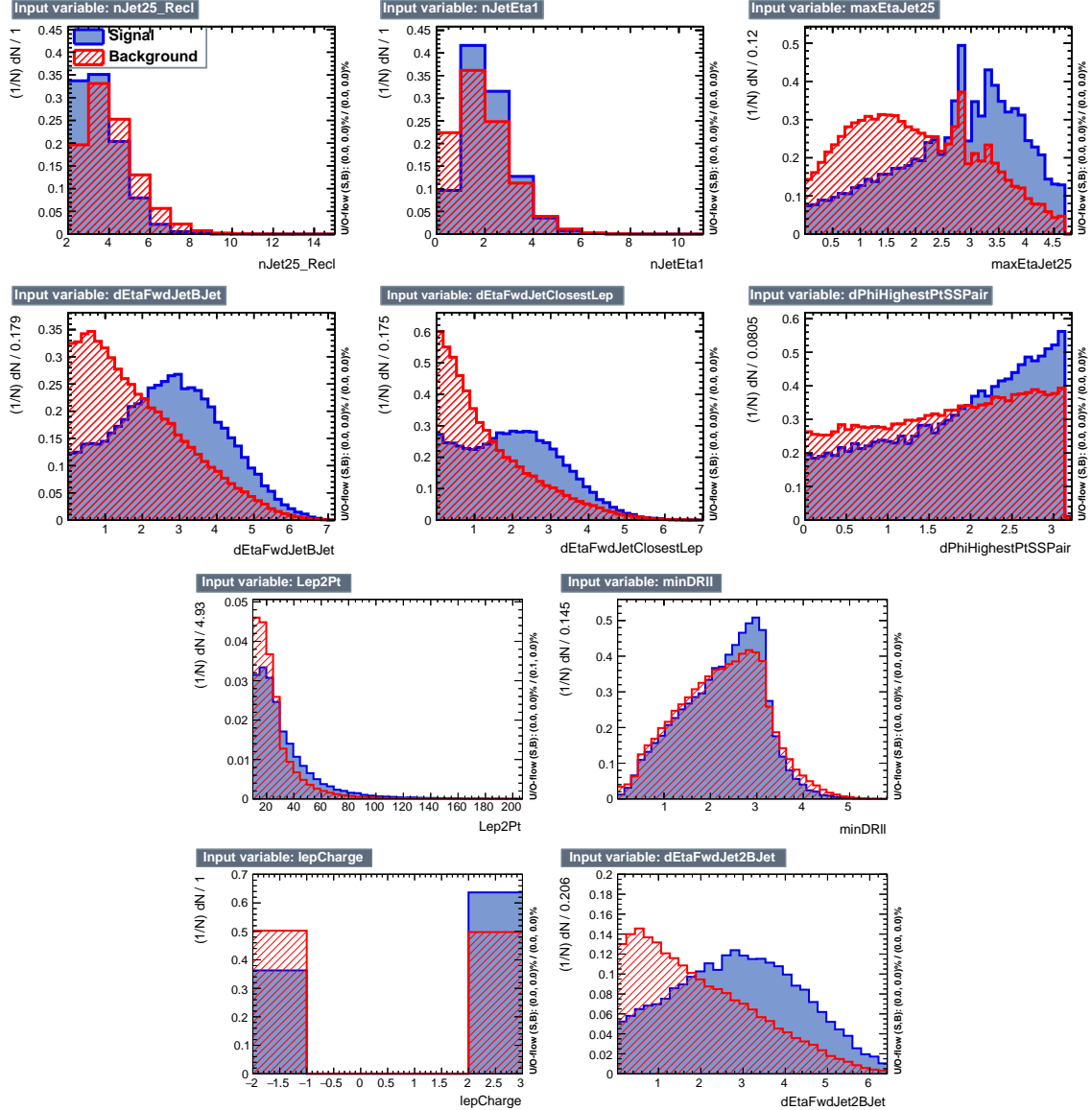


**Figure 6.18:** BDT inputs as seen by TMVA (signal, in blue, is  $tHq$ , background, in red, is  $t\bar{t}$ ) for the same sign dilepton channel, discriminated against  $t\bar{t}$  background.

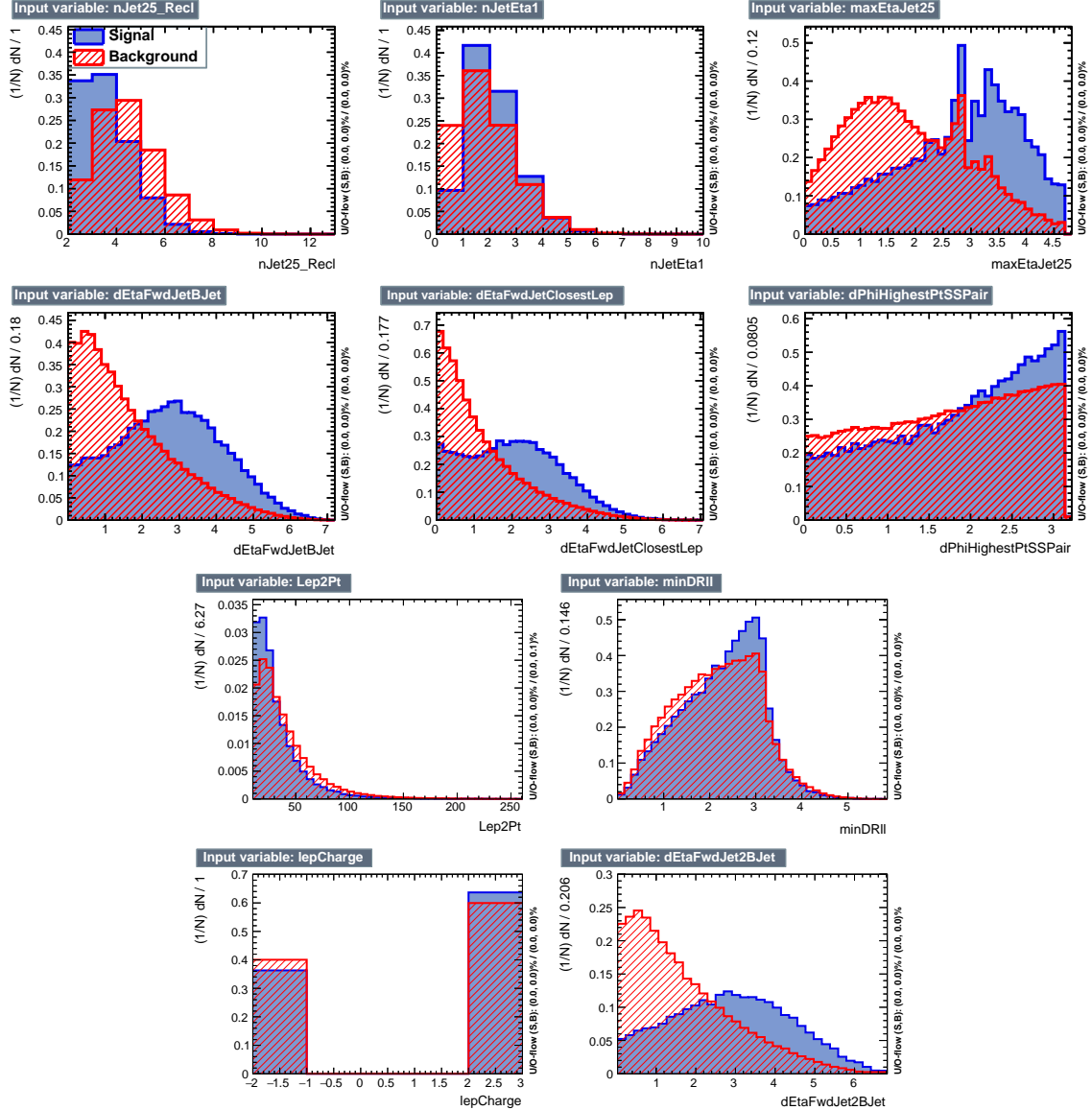


**Figure 6.19:** BDT inputs as seen by TMVA (signal, in blue, is  $tHq$ , background, in red, is  $t\bar{t}W+t\bar{t}Z$ ) for the same sign dilepton channel, discriminated against  $t\bar{t}V$  background.

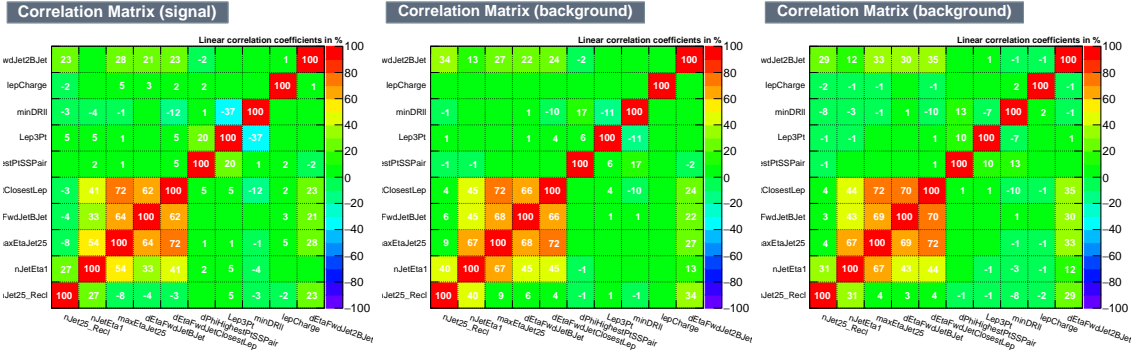


**Figure 6.20:** Signal (left),  $t\bar{t}$  background (middle), and  $t\bar{t}V$  background (right.) correlation matrices for the input variables in the TMVA analysis for the three lepton channel.

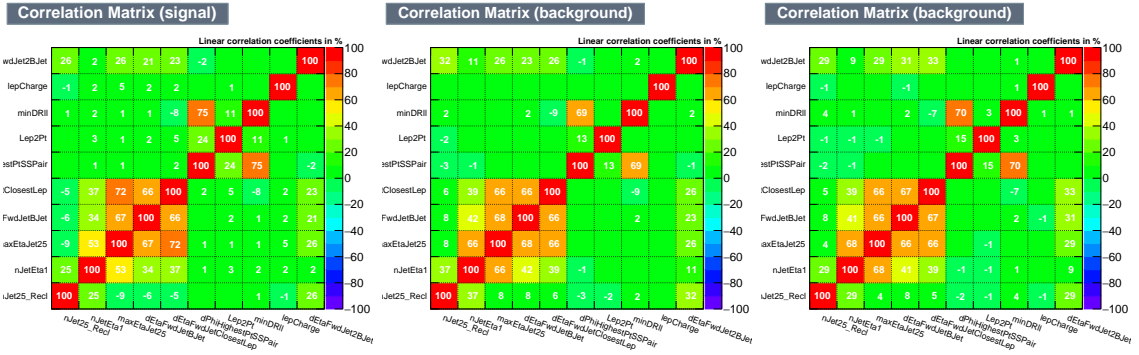


**Figure 6.21:** Signal and Background correlation matrices for the input variables in the TMVA analysis for the same sign dilepton channel, for the signal (left),  $t\bar{t}$  background (middle), and  $t\bar{t}V$  background (right.)

ROC-integral	
base 10 var ttv	0.848
+ fwdJetPUID ttv	0.849
+ fwdJetPt25 ttv	0.856
12 var ttv	0.856
base 10 var tt	0.777
+ fwdJetPUID tt	0.777
+ fwdJetPt25 tt	0.787
12 var	0.787

**Table 6.11:** ROC-integral for all the testing cases we made in the evaluation of the additional variables discriminating power. The improvement in the discrimination performance provided by the additional variables is about 1%

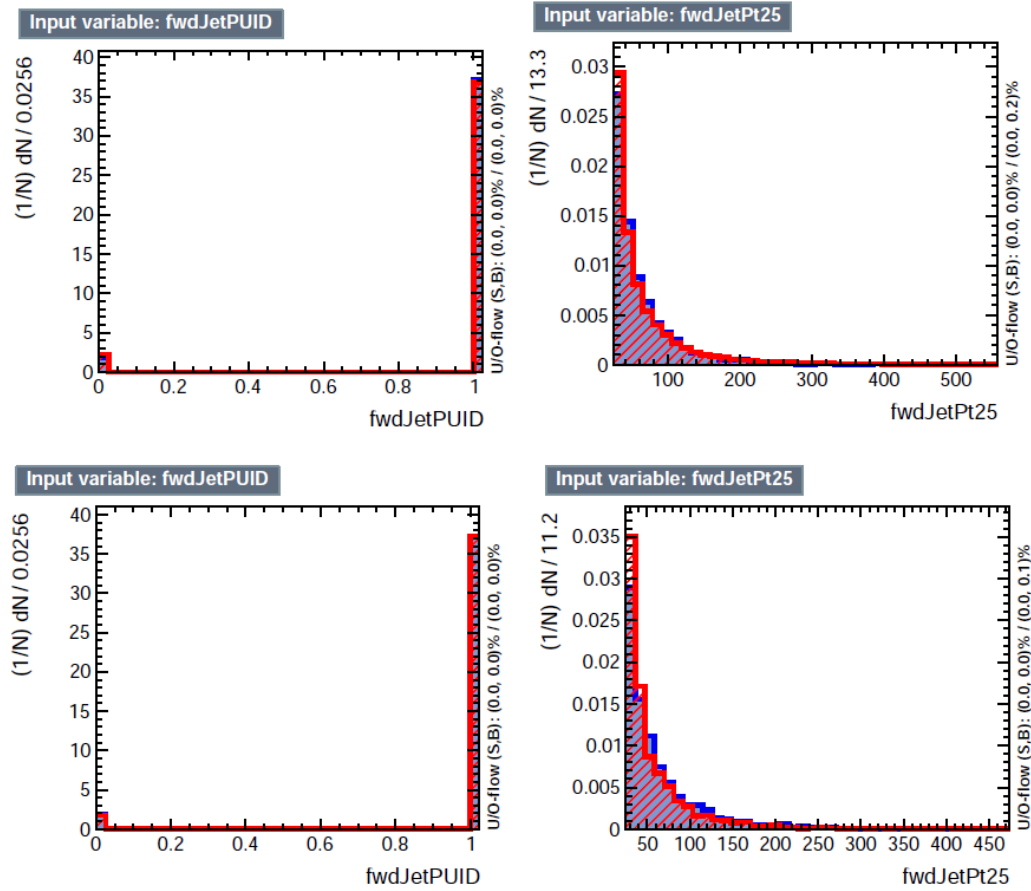


**Figure 6.22:** Additional discriminating variables distributions for ttv training (Top row) and tt training (bottom row) in the three lepton channel. The origin of the jets in the forward jet identification distribution is tagged as 0 for *pileup jets* while *real jets* are tagged as 1.

<sup>2870</sup> **Appendix A**

<sup>2871</sup> **Datasets and triggers**

Dataset name
/JetHT/Run2016X-23Sep2016-vY/MINIAOD
/HTMHT/Run2016X-23Sep2016-vY/MINIAOD
/MET/Run2016X-23Sep2016-vY/MINIAOD
/SingleElectron/Run2016X-23Sep2016-vY/MINIAOD
/SingleMuon/Run2016X-23Sep2016-vY/MINIAOD
/SinglePhoton/Run2016X-23Sep2016-vY/MINIAOD
/DoubleEG/Run2016X-23Sep2016-vY/MINIAOD
/MuonEG/Run2016X-23Sep2016-vY/MINIAOD
/DoubleMuon/Run2016X-23Sep2016-vY/MINIAOD
/Tau/Run2016B-23Sep2016-v3/MINIAOD
/JetHT/Run2016H-PromptReco-v3/MINIAOD
/HTMHT/Run2016H-PromptReco-v3/MINIAOD
/MET/Run2016H-PromptReco-v3/MINIAOD
/SingleElectron/Run2016H-PromptReco-v3/MINIAOD
/SingleMuon/Run2016H-PromptReco-v3/MINIAOD
/SinglePhoton/Run2016H-PromptReco-v3/MINIAOD
/DoubleEG/Run2016H-PromptReco-v3/MINIAOD
/MuonEG/Run2016H-PromptReco-v3/MINIAOD
/DoubleMuon/Run2016H-PromptReco-v3/MINIAOD

**Table A.1:** Full 2016 dataset used in the analysis. In the first section of the table are listed the 23Sep2016 samples; in the Run2016X-23Sep-vY label, X:B-G tag the run while Y:1,3 tag the version of the data sample. Second section list the PromptReco version of the dataset.

Same-sign dilepton (==2 muons)
HLT_Mu17_TrkIsoVVL_Mu8_TrkIsoVVL_DZ_v*
HLT_Mu17_TrkIsoVVL_TkMu8_TrkIsoVVL_DZ_v*
HLT_IsoMu22_v*
HLT_IsoTkMu22_v*
HLT_IsoMu22_eta2p1_v*
HLT_IsoTkMu22_eta2p1_v*
HLT_IsoMu24_v*
HLT_IsoTkMu24_v*
Same-sign dilepton (==2 electrons)
HLT_Ele23_Ele12_CaloIdL_TrackIdL_IsoVL_DZ_v*
HLT_Ele27_eta2p1_WP Loose_Gsf_v*
HLT_Ele27_WPTight_Gsf_v*
HLT_Ele25_eta2p1_WPTight_Gsf_v*
Same-sign dilepton (==1 muon, ==1 electron)
HLT_Mu23_TrkIsoVVL_Ele8_CaloIdL_TrackIdL_IsoVL_v*
HLT_Mu8_TrkIsoVVL_Ele23_CaloIdL_TrackIdL_IsoVL_v*
HLT_Mu23_TrkIsoVVL_Ele8_CaloIdL_TrackIdL_IsoVL_DZ_v*
HLT_Mu8_TrkIsoVVL_Ele23_CaloIdL_TrackIdL_IsoVL_DZ_v*
HLT_IsoMu22_v*
HLT_IsoTkMu22_v*
HLT_IsoMu22_eta2p1_v*
HLT_IsoTkMu22_eta2p1_v*
HLT_IsoMu24_v*
HLT_IsoTkMu24_v*
HLT_Ele27_WPTight_Gsf_v*
HLT_Ele25_eta2p1_WPTight_Gsf_v*
HLT_Ele27_eta2p1_WP Loose_Gsf_v*
Three lepton
HLT_DiMu9_Ele9_CaloIdL_TrackIdL_v*
HLT_Mu8_DiEle12_CaloIdL_TrackIdL_v*
HLT_TripleMu_12_10_5_v*
HLT_Ele16_Ele12_Ele8_CaloIdL_TrackIdL_v*
HLT_Mu23_TrkIsoVVL_Ele8_CaloIdL_TrackIdL_IsoVL_v*
HLT_Mu23_TrkIsoVVL_Ele8_CaloIdL_TrackIdL_IsoVL_DZ_v*
HLT_Mu8_TrkIsoVVL_Ele23_CaloIdL_TrackIdL_IsoVL_v*
HLT_Mu8_TrkIsoVVL_Ele23_CaloIdL_TrackIdL_IsoVL_DZ_v*
HLT_Ele23_Ele12_CaloIdL_TrackIdL_IsoVL_DZ_v*
HLT_Mu17_TrkIsoVVL_Mu8_TrkIsoVVL_DZ_v*
HLT_Mu17_TrkIsoVVL_TkMu8_TrkIsoVVL_DZ_v*
HLT_IsoMu22_v*
HLT_IsoTkMu22_v*
HLT_IsoMu22_eta2p1_v*
HLT_IsoTkMu22_eta2p1_v*
HLT_IsoMu24_v*
HLT_IsoTkMu24_v*
HLT_Ele27_WPTight_Gsf_v*
HLT_Ele25_eta2p1_WPTight_Gsf_v*
HLT_Ele27_eta2p1_WP Loose_Gsf_v*

**Table A.2:** Table of high-level triggers considered in the analysis.

		<i>tHq</i>			<i>tHW</i>		
$\kappa_V$	$\kappa_t$	sum of weights	cross section [pb]	sum of weights	cross section [pb]	LHE weights	
1.0	-3.0	35.700022	2.991	11.030445	0.6409	LHEweight_wgt[446]	
1.0	-2.0	20.124298	1.706	5.967205	0.3458	LHEweight_wgt[447]	
1.0	-1.5	14.043198	1.205	4.029093	0.2353	LHEweight_wgt[448]	
1.0	-1.25	11.429338	0.9869	3.208415	0.1876	LHEweight_wgt[449]	
1.0	-1.0		0.7927		0.1472		
1.0	-0.75	7.054998	0.6212	1.863811	0.1102	LHEweight_wgt[450]	
1.0	-0.5	5.294518	0.4723	1.339886	0.07979	LHEweight_wgt[451]	
1.0	-0.25	3.818499	0.3505	0.914880	0.05518	LHEweight_wgt[452]	
1.0	0.0	2.627360	0.2482	0.588902	0.03881	LHEweight_wgt[453]	
1.0	0.25	1.719841	0.1694	0.361621	0.02226	LHEweight_wgt[454]	
1.0	0.5	1.097202	0.1133	0.233368	0.01444	LHEweight_wgt[455]	
1.0	0.75	0.759024	0.08059	0.204034	0.01222	LHEweight_wgt[456]	
1.0	1.0	0.705305	0.07096	0.273617	0.01561	LHEweight_wgt[457]	
1.0	1.25	0.936047	0.0839	0.442119	0.02481	LHEweight_wgt[458]	
1.0	1.5	1.451249	0.1199	0.709538	0.03935	LHEweight_wgt[459]	
1.0	2.0	3.335034	0.2602	1.541132	0.08605	LHEweight_wgt[460]	
1.0	3.0	10.516125	0.8210	4.391335	0.2465	LHEweight_wgt[461]	
1.5	-3.0	45.281492	3.845	13.426212	0.7825	LHEweight_wgt[462]	
1.5	-2.0	27.606715	2.371	7.809713	0.4574	LHEweight_wgt[463]	
1.5	-1.5	20.476088	1.784	5.594971	0.3290	LHEweight_wgt[464]	
1.5	-1.25	17.337465	1.518	4.635978	0.2749	LHEweight_wgt[465]	
1.5	-1.0	14.483302	1.287	3.775902	0.2244	LHEweight_wgt[466]	
1.5	-0.75	11.913599	1.067	3.014744	0.1799	LHEweight_wgt[467]	
1.5	-0.5	9.628357	0.874	2.352505	0.1410	LHEweight_wgt[468]	
1.5	-0.25	7.627574	0.702	1.789184	0.1081	LHEweight_wgt[469]	
1.5	0.0	5.911882	0.5577	1.324946	0.08056	LHEweight_wgt[470]	
1.5	0.25	4.479390	0.4365	0.959295	0.05893	LHEweight_wgt[471]	
1.5	0.5	3.331988	0.3343	0.692727	0.04277	LHEweight_wgt[472]	
1.5	0.75	2.469046	0.2558	0.525078	0.03263	LHEweight_wgt[473]	
1.5	1.0	1.890565	0.2003	0.456347	0.02768	LHEweight_wgt[474]	
1.5	1.25	1.596544	0.1689	0.486534	0.02864	LHEweight_wgt[475]	
1.5	1.5	1.586983	0.1594	0.615638	0.03509	LHEweight_wgt[476]	
1.5	2.0	2.421241	0.2105	1.170602	0.06515	LHEweight_wgt[477]	
1.5	3.0	7.503280	0.5889	3.467546	0.1930	LHEweight_wgt[478]	
0.5	-3.0	27.432685	2.260	8.929074	0.5136	LHEweight_wgt[479]	
0.5	-2.0	13.956013	1.160	4.419093	0.2547	LHEweight_wgt[480]	
0.5	-1.5	8.924438	0.7478	2.757611	0.1591	LHEweight_wgt[481]	
0.5	-1.25	6.835341	0.5726	2.075247	0.1204	LHEweight_wgt[482]	
0.5	-1.0	5.030704	0.4273	1.491801	0.08696	LHEweight_wgt[483]	
0.5	-0.75	3.510528	0.2999	1.007273	0.05885	LHEweight_wgt[484]	
0.5	-0.5	2.274811	0.1982	0.621663	0.03658	LHEweight_wgt[485]	
0.5	-0.25	1.323555	0.1189	0.334972	0.01996	LHEweight_wgt[486]	
0.5	0.0	0.656969	0.06223	0.147253	0.008986	LHEweight_wgt[487]	
0.5	0.25	0.274423	0.02830	0.058342	0.003608	LHEweight_wgt[488]	
0.5	0.5	0.176548	0.01778	0.068404	0.003902	LHEweight_wgt[489]	
0.5	0.75	0.363132	0.03008	0.177385	0.009854	LHEweight_wgt[490]	
0.5	1.0	0.834177	0.06550	0.385283	0.02145	LHEweight_wgt[491]	
0.5	1.25	1.589682	0.1241	0.692099	0.03848	LHEweight_wgt[492]	
0.5	1.5	2.629647	0.2047	1.097834	0.06136	LHEweight_wgt[493]	
0.5	2.0	5.562958	0.4358	2.206057	0.1246	LHEweight_wgt[494]	
0.5	3.0	14.843102	1.177	5.609519	0.3172	LHEweight_wgt[495]	

**Table A.3:**  $\kappa_V$  and  $\kappa_t$  combinations generated for the two signal samples and their NLO cross sections. The *tHq* cross section is multiplied by the branching fraction of the enforced leptonic decay of the top quark (0.324) [150].

Sample	$\sigma$ [pb]	*
TTWJetsToLNu_TuneCUETP8M1_13TeV-amcatnloFXFX-madspin-pythia8	0.2043	*
TTZToLLNuNu_M-10_TuneCUETP8M1_13TeV-amcatnlo-pythia8	0.2529	*
/store/cmst3/group/susy/gpetrucc/13TeV/u/TTLL_m1to10_L0_NoMS_for76X/	0.0283	
WGToLNuG_TuneCUETP8M1_13TeV-madgraphMLM-pythia8	585.8	
ZGTo2LG_TuneCUETP8M1_13TeV-amcatnloFXFX-pythia8	131.3	
TGJets_TuneCUETP8M1_13TeV_amcatnlo_madspin_pythia8	2.967	
TGJets_TuneCUETP8M1_13TeV_amcatnlo_madspin_pythia8	2.967	
TTGJets_TuneCUETP8M1_13TeV-amcatnloFXFX-madspin-pythia8	3.697	
WpWpJJ_EWK-QCD_TuneCUETP8M1_13TeV-madgraph-pythia8	0.03711	
ZZZ_TuneCUETP8M1_13TeV-amcatnlo-pythia8	0.01398	
WWZ_TuneCUETP8M1_13TeV-amcatnlo-pythia8	0.1651	
WZZ_TuneCUETP8M1_13TeV-amcatnlo-pythia8	0.05565	
WW_DoubleScattering_13TeV-pythia8	1.64	
tZq_ll_4f_13TeV-amcatnlo-pythia8_TuneCUETP8M1	0.0758	
ST_tW1l_5f_L0_13TeV-MadGraph-pythia8	0.01123	
TTTT_TuneCUETP8M1_13TeV-amcatnlo-pythia8	0.009103	
WZTo3LNu_TuneCUETP8M1_13TeV-powheg-pythia8	4.4296	
ZZTo4L_13TeV_powheg_pythia8	1.256	
TTJets_SingleLeptFromTbar_TuneCUETP8M1_13TeV-madgraphMLM-pythia8	182.1754	*
TTJets_SingleLeptFromT_TuneCUETP8M1_13TeV-madgraphMLM-pythia8	182.1754	*
TTJets_DiLept_TuneCUETP8M1_13TeV-madgraphMLM-pythia8	87.3	*
DYJetsToLL_M-10to50_TuneCUETP8M1_13TeV-amcatnloFXFX-pythia8	18610	
DYJetsToLL_M-50_TuneCUETP8M1_13TeV-madgraphMLM-pythia8	6024	
WJetsToLNu_TuneCUETP8M1_13TeV-amcatnloFXFX-pythia8	61526.7	
ST_tW_top_5f_inclusiveDecays_13TeV-powheg-pythia8_TuneCUETP8M1	35.6	
ST_tW_antitop_5f_inclusiveDecays_13TeV-powheg-pythia8_TuneCUETP8M1	35.6	
ST_t-channel_4f_leptonDecays_13TeV-amcatnlo-pythia8_TuneCUETP8M1	70.3144	
ST_t-channel_antitop_4f_leptonDecays_13TeV-powheg-pythia8_TuneCUETP8M1	26.2278	
ST_s-channel_4f_leptonDecays_13TeV-amcatnlo-pythia8_TuneCUETP8M1	3.68064	
WWTo2L2Nu_13TeV-powheg	10.481	
ttWJets_13TeV_madgraphMLM	0.6105	
ttZJets_13TeV_madgraphMLM	0.5297/0.692	

**Table A.4:** List of background samples used in this analysis (CMSSW 80X). The first section of the table lists the samples used in simulation to extract the final yields and shapes; the second section lists the samples of the processes for which the yields are estimated from data. The MC simulation is used to design the data driven methods and in the derivation of the associated systematic uncertainties. The third section list the leading order  $t\bar{t}W$  and  $t\bar{t}Z$  samples, which in addition to the ones market with a \*, where used in the BDT training.

2872 

# References

- 2873 [1] J. Schwinger. "Quantum Electrodynamics. I. A Covariant Formulation". Phys-  
2874       ical Review. 74 (10): 1439-61, (1948). <https://doi.org/10.1103/PhysRev.74.1439>
- 2876 [2] R. P. Feynman. "Space-Time Approach to Quantum Electrodynamics". Physical  
2877       Review. 76 (6): 769-89, (1949). <https://doi.org/10.1103/PhysRev.76.769>
- 2878 [3] S. Tomonaga. "On a Relativistically Invariant Formulation of the Quantum  
2879       Theory of Wave Fields". Progress of Theoretical Physics. 1 (2): 27-42, (1946).  
2880       <https://doi.org/10.1143/PTP.1.27>
- 2881 [4] D.J. Griffiths, "Introduction to electrodynamics". 4th ed. Pearson, (2013).
- 2882 [5] F. Mandl, G. Shaw. "Quantum field theory." Chichester, Wiley (2009).
- 2883 [6] F. Halzen, and A.D. Martin, "Quarks and leptons: An introductory course in  
2884       modern particle physics". New York: Wiley, (1984) .
- 2885 [7] File: Standard\_Model\_of\_Elementary\_Particle\_dark.svg. (2017, June 12)  
2886       Wikimedia Commons, the free media repository. Retrieved November 27, 2017  
2887       from <https://www.collegiate-advanced-electricity.com/single-post/2017/04/10/The-Standard-Model-of-Particle-Physics>.

- 2889 [8] E. Noether, "Invariante Variationsprobleme", Nachrichten von der Gesellschaft  
2890 der Wissenschaften zu Göttingen, mathematisch-physikalische Klasse, vol. 1918,  
2891 pp. 235-257, (1918).
- 2892 [9] C. Patrignani et al. (Particle Data Group), Chin. Phys. C, 40, 100001 (2016)  
2893 and 2017 update.
- 2894 [10] M. Goldhaber, L. Grodzins, A.W. Sunyar "Helicity of Neutrinos", Phys. Rev.  
2895 109, 1015 (1958).
- 2896 [11] Palanque-Delabrouille N et al. "Neutrino masses and cosmology with Lyman-  
2897 alpha forest power spectrum", JCAP 11 011 (2015).
- 2898 [12] M. Gell-Mann. "A Schematic Model of Baryons and Mesons". Physics Letters.  
2899 8 (3): 214-215 (1964).
- 2900 [13] G. Zweig. "An SU(3) Model for Strong Interaction Symmetry and its Breaking"  
2901 (PDF). CERN Report No.8182/TH.401 (1964).
- 2902 [14] G. Zweig. "An SU(3) Model for Strong Interaction Symmetry and its Breaking:  
2903 II" (PDF). CERN Report No.8419/TH.412(1964).
- 2904 [15] M. Gell-Mann. "The Interpretation of the New Particles as Displaced Charged  
2905 Multiplets". Il Nuovo Cimento 4: 848. (1956).
- 2906 [16] T. Nakano, K. Nishijima. "Charge Independence for V-particles". Progress of  
2907 Theoretical Physics 10 (5): 581-582. (1953).
- 2908 [17] N. Cabibbo, "Unitary symmetry and leptonic decays" Physical Review Letters,  
2909 vol. 10, no. 12, p. 531, (1963).

- 2910 [18] M.Kobayashi, T.Maskawa, “CP-violation in the renormalizable theory of weak  
2911 interaction,” Progress of Theoretical Physics, vol. 49, no. 2, pp. 652-657, (1973).
- 2912 [19] File: Weak Decay (flipped).svg. (2017, June 12). Wikimedia Com-  
2913 mons, the free media repository. Retrieved November 27, 2017  
2914 from [https://commons.wikimedia.org/w/index.php?title=File:  
2915 Weak\\_Decay\\_\(flipped\)\.svg&oldid=247498592](https://commons.wikimedia.org/w/index.php?title=File:Weak_Decay_(flipped)\.svg&oldid=247498592).
- 2916 [20] Georgia Tech University. Coupling Constants for the Fundamental Forces(2005).  
2917 Retrieved January 10, 2018, from [http://hyperphysics.phy-astr.gsu.edu/  
2918 hbase/Forces/couple.html#c2](http://hyperphysics.phy-astr.gsu.edu/hbase/Forces/couple.html#c2)
- 2919 [21] M. Strassler. (May 31, 2013).The Strengths of the Known Forces. Retrieved Jan-  
2920 uary 10, 2018, from [https://profmattstrassler.com/articles-and-posts/  
2921 particle-physics-basics/the-known-forces-of-nature/  
2922 the-strength-of-the-known-forces/](https://profmattstrassler.com/articles-and-posts/particle-physics-basics/the-known-forces-of-nature/the-strength-of-the-known-forces/)
- 2923 [22] S.L. Glashow. “Partial symmetries of weak interactions”, Nucl. Phys. 22 579-  
2924 588, (1961).
- 2925 [23] A. Salam, J.C. Ward. “Electromagnetic and weak interactions”, Physics Letters  
2926 13 168-171, (1964).
- 2927 [24] S. Weinberg, “A model of leptons”, Physical Review Letters, vol. 19, no. 21, p.  
2928 1264, (1967).
- 2929 [25] M. Peskin, D. Schroeder, “An introduction to quantum field theory”. Perseus  
2930 Books Publishing L.L.C., (1995).
- 2931 [26] A. Pich. “The Standard Model of Electroweak Interactions” <https://arxiv.org/abs/1201.0537>
- 2932

- 2933 [27] G. Arnison et al. (UA1 Collaboration), Phys. Lett. B 122, 103 (1983).
- 2934 [28] M. Banner et al. (UA2 Collaboration), Phys. Lett. B 122, 476 (1983).
- 2935 [29] G. Arnison et al. (UA1 Collaboration), Phys. Lett. B 126, 398 (1983).
- 2936 [30] P. Bagnaia et al. (UA2 Collaboration), Phys. Lett. B 129, 130 (1983).
- 2937 [31] F.Bellaiche. (2012, 2 September). “What’s this Higgs boson anyway?”. Retrieved  
2938 from: <https://www.quantum-bits.org/?p=233>
- 2939 [32] M. Endres et al. Nature 487, 454-458 (2012) doi:10.1038/nature11255
- 2940 [33] F. Englert, R. Brout. “Broken Symmetry and the Mass of Gauge  
2941 Vector Mesons”. Physical Review Letters. 13 (9): 321-23.(1964)  
2942 doi:10.1103/PhysRevLett.13.321
- 2943 [34] P.Higgs. “Broken Symmetries and the Masses of Gauge Bosons”. Physical Re-  
2944 view Letters. 13 (16): 508-509,(1964). doi:10.1103/PhysRevLett.13.508.
- 2945 [35] G.Guralnik, C.R. Hagen and T.W.B. Kibble. “Global Conservation Laws  
2946 and Massless Particles”. Physical Review Letters. 13 (20): 585-587, (1964).  
2947 doi:10.1103/PhysRevLett.13.585.
- 2948 [36] CMS collaboration. “Observation of a new boson at a mass of 125 GeV with  
2949 the CMS experiment at the LHC”. Physics Letters B. 716 (1): 30-61 (2012).  
2950 arXiv:1207.7235. doi:10.1016/j.physletb.2012.08.021
- 2951 [37] ATLAS collaboration. “Observation of a New Particle in the Search for the Stan-  
2952 dard Model Higgs Boson with the ATLAS Detector at the LHC”. Physics Letters  
2953 B. 716 (1): 1-29 (2012). arXiv:1207.7214. doi:10.1016/j.physletb.2012.08.020.

- 2954 [38] ATLAS collaboration; CMS collaboration (26 March 2015). “Combined Mea-  
 2955 surement of the Higgs Boson Mass in pp Collisions at  $\sqrt{s}=7$  and 8 TeV with  
 2956 the ATLAS and CMS Experiments”. Physical Review Letters. 114 (19): 191803.  
 2957 arXiv:1503.07589. doi:10.1103/PhysRevLett.114.191803.
- 2958 [39] LHC InternationalMasterclasses“When protons collide”. Retrieved from [http://atlas.physicsmasterclasses.org/en/zpath\\_protoncollisions.htm](http://atlas.physicsmasterclasses.org/en/zpath_protoncollisions.htm)
- 2960 [40] CMS Collaboration, “SM Higgs Branching Ratios and Total Decay Widths (up-  
 2961 date in CERN Report4 2016)”. <https://twiki.cern.ch/twiki/bin/view/LHCPhysics/CERNYellowReportPageBR>, last accessed on 17.12.2017.
- 2963 [41] R.Grant V. “Determination of Higgs branching ratios in  $H \rightarrow W^+W^- \rightarrow l\nu jj$   
 2964 and  $H \rightarrow ZZ \rightarrow l^+l^-jj$  channels”. Physics Department, University of Ten-  
 2965 nessee (Dated: October 31, 2012). Retrieved from <http://aesop.phys.utk.edu/ph611/2012/projects/Riley.pdf>
- 2967 [42] LHC Higgs Cross Section Working Group, Denner, A., Heinemeyer, S. et al.  
 2968 “Standard model Higgs-boson branching ratios with uncertainties”. Eur. Phys.  
 2969 J. C (2011) 71: 1753. <https://doi.org/10.1140/epjc/s10052-011-1753-8>
- 2970 [43] D. de Florian et al., LHC Higgs Cross Section Working Group,  
 2971 CERNâš2017âš002-M, arXiv:1610.07922[hep-ph] (2016).
- 2972 [44] ATLAS and CMS Collaborations, “Measurements of the Higgs boson produc-  
 2973 tion and decay rates and constraints on its couplings from a combined ATLAS  
 2974 and CMS analysis of the LHC pp collision data at  $\sqrt{s} = 7$  and 8 TeV,” (2016).  
 2975 CERN-EP-2016-100, ATLAS-HIGG-2015-07, CMS-HIG-15-002.

- 2976 [45] J. A. Aguilar-Saavedra, R. Benbrik, S. Heinemeyer, and M. Perez-Victoria,  
2977 “Handbook of vector-like quarks: Mixing and single production”, Phys. Rev. D  
2978 88 (2013) 094010, doi:10.1103/PhysRevD.88.094010, arXiv:1306.0572.
- 2979 [46] A. Greljo, J. F. Kamenik, and J. Kopp, “Disentangling flavor vio-  
2980 lation in the top-Higgs sector at the LHC”, JHEP 07 (2014) 046,  
2981 doi:10.1007/JHEP07(2014)046, arXiv:1404.1278.
- 2982 [47] F. Demartin, F. Maltoni, K. Mawatari, and M. Zaro, “Higgs production in  
2983 association with a single top quark at the LHC,” European Physical Journal C,  
2984 vol. 75, p. 267, (2015). doi:10.1140/epjc/s10052-015-3475-9, arXiv:1504.00611.
- 2985 [48] F. Demartin, B. Maier, F. Maltoni, K. Mawatari, and M. Zaro, “tWH associated  
2986 production at the LHC”, European Physical Journal C, vol. 77, p. 34, (2017).  
2987 arXiv:1607.05862
- 2988 [49] F. Maltoni, K. Paul, T. Stelzer, and S. Willenbrock, “Associated production  
2989 of Higgs and single top at hadron colliders”, Phys.Rev. D64 (2001) 094023,  
2990 [hep-ph/0106293].
- 2991 [50] S. Biswas, E. Gabrielli, F. Margaroli, and B. Mele, “Direct constraints on the  
2992 top-Higgs coupling from the 8 TeV LHC data,” Journal of High Energy Physics,  
2993 vol. 07, p. 073, (2013).
- 2994 [51] M. Farina, C. Grojean, F. Maltoni, E. Salvioni, and A. Thamm, “Lifting de-  
2995 generacies in Higgs couplings using single top production in association with a  
2996 Higgs boson,” Journal of High Energy Physics, vol. 05, p. 022, (2013).
- 2997 [52] T.M. Tait and C.-P. Yuan, “Single top quark production as a window to physics  
2998 beyond the standard model”, Phys. Rev. D 63 (2000) 014018 [hep-ph/0007298].

- 2999 [53] CMS Collaboration, “Modelling of the single top-quark production in associa-  
 3000 tion with the Higgs boson at 13 TeV.” <https://twiki.cern.ch/twiki/bin/viewauth/CMS/SingleTopHiggsGeneration13TeV>, last accessed on 16.01.2018.  
 3001
- 3002 [54] CMS Collaboration, “SM Higgs production cross sections at  $\sqrt{s} =$   
 3003 13 TeV.” <https://twiki.cern.ch/twiki/bin/view/LHCPhysics/CERNYellowReportPageAt13TeV>, last accessed on 16.01.2018.  
 3004
- 3005 [55] S. Dawson, The effective W approximation, Nucl. Phys. B 249 (1985) 42.
- 3006 [56] S. Biswas, E. Gabrielli and B. Mele, JHEP 1301 (2013) 088 [arXiv:1211.0499  
 3007 [hep-ph]].
- 3008 [57] LHC Higgs Cross Section Working Group, “Handbook of LHC Higgs Cross  
 3009 Sections: 4.Deciphering the Nature of the Higgs Sector”, arXiv:1610.07922.
- 3010 [58] J. Ellis, D. S. Hwang, K. Sakurai, and M. Takeuchi.“Disentangling Higgs-Top  
 3011 Couplings in Associated Production”, JHEP 1404 (2014) 004, [arXiv:1312.5736].
- 3012 [59] CMS Collaboration, V. Khachatryan et al., “Precise determination of the mass  
 3013 of the Higgs boson and tests of compatibility of its couplings with the standard  
 3014 model predictions using proton collisions at 7 and 8 TeV,” arXiv:1412.8662.
- 3015 [60] ATLAS Collaboration, G. Aad et al., “Updated coupling measurements of the  
 3016 Higgs boson with the ATLAS detector using up to  $25 \text{ fb}^{-1}$  of proton-proton  
 3017 collision data”, ATLAS-CONF-2014-009.
- 3018 [61] File:Cern-accelerator-complex.svg. Wikimedia Commons, the free media repos-  
 3019 itory. Retrieved January, 2018 from <https://commons.wikimedia.org/wiki/File:Cern-accelerator-complex.svg>  
 3020

- 3021 [62] J.L. Caron , “Layout of the LEP tunnel including future LHC infrastructures.”,  
3022 (Nov, 1993). A C Collection. Legacy of AC. Pictures from 1992 to 2002. Re-  
3023 trieved from <https://cds.cern.ch/record/841542>
- 3024 [63] M. Vretenar, “The radio-frequency quadrupole”. CERN Yellow Report CERN-  
3025 2013-001, pp.207-223 DOI:10.5170/CERN-2013-001.207. arXiv:1303.6762
- 3026 [64] L.Evans. P. Bryant (editors). “LHC Machine”. JINST 3 S08001 (2008).
- 3027 [65] CERN Photographic Service.“Radio-frequency quadrupole, RFQ-1”, March  
3028 1983, CERN-AC-8303511. Retrieved from <https://cds.cern.ch/record/615852>.
- 3030 [66] CERN Photographic Service “Animation of CERN’s accelerator network”, 14  
3031 October 2013. DOI: 10.17181/cds.1610170 Retrieved from <https://videos.cern.ch/record/1610170>
- 3033 [67] C.Sutton. “Particle accelerator”.Encyclopedia Britannica. July 17,  
3034 2013. Retrieved from <https://www.britannica.com/technology/particle-accelerator>.
- 3036 [68] L.Guiraud. “Installation of LHC cavity in vacuum tank.”. July 27 2000. CERN-  
3037 AC-0007016. Retrieved from <https://cds.cern.ch/record/41567>.
- 3038 [69] J.L. Caron, “Magnetic field induced by the LHC dipole’s superconducting coils”.  
3039 March 1998. AC Collection. Legacy of AC. Pictures from 1992 to 2002. LHC-  
3040 PHO-1998-325. Retrieved from <https://cds.cern.ch/record/841511>.
- 3041 [70] AC Team. “Diagram of an LHC dipole magnet”. June 1999. CERN-DI-9906025  
3042 retrieved from <https://cds.cern.ch/record/40524>.

- 3043 [71] CMS Collaboration “Public CMS Luminosity Information”. [https://twiki.cern.ch/twiki/bin/view/CMSPublic/LumiPublicResults#2016\\\_\\\_proton\\_proton\\_13\\_TeV\\_collis](https://twiki.cern.ch/twiki/bin/view/CMSPublic/LumiPublicResults#2016\_\_proton_proton_13_TeV_collis), last accessed 24.01.2018
- 3044
- 3045
- 3046 [72] J.L Caron. “LHC Layout” AC Collection. Legacy of AC. Pictures from 1992  
3047 to 2002. September 1997, LHC-PHO-1997-060. Retrieved from <https://cds.cern.ch/record/841573>.
- 3048
- 3049 [73] J.A. Coarasa. “The CMS Online Cluster:Setup, Operation and Maintenance  
3050 of an Evolving Cluster”. ISGC 2012, 26 February - 2 March 2012, Academia  
3051 Sinica, Taipei, Taiwan.
- 3052 [74] CMS Collaboration. “The CMS experiment at the CERN LHC” JINST 3 S08004  
3053 (2008).
- 3054 [75] CMS Collaboration. “CMS detector drawings 2012” CMS-PHO-GEN-2012-002.  
3055 Retrieved from <http://cds.cern.ch/record/1433717>.
- 3056 [76] Davis, Siona Ruth. “Interactive Slice of the CMS detector”, Aug. 2016,  
3057 CMS-OUTREACH-2016-027, retrieved from <https://cds.cern.ch/record/2205172>
- 3058
- 3059 [77] R. Breedon. “View through the CMS detector during the cooldown of the  
3060 solenoid on February 2006. CMS Collection”, February 2006, CMS-PHO-  
3061 OREACH-2005-004, Retrieved from <https://cds.cern.ch/record/930094>.
- 3062 [78] Halyo, V. and LeGresley, P. and Lujan, P. “Massively Parallel Computing and  
3063 the Search for Jets and Black Holes at the LHC”, Nucl.Instrum.Meth. A744  
3064 (2014) 54-60, DOI: 10.1016/j.nima.2014.01.038”
- 3065

- 3065 [79] A. Dominguez et. al. “CMS Technical Design Report for the Pixel Detector  
3066 Upgrade”, CERN-LHCC-2012-016. CMS-TDR-11.
- 3067 [80] CMS Collaboration. “Description and performance of track and primary-vertex  
3068 reconstruction with the CMS tracker,” Journal of Instrumentation, vol. 9, no.  
3069 10, p. P10009,(2014).
- 3070 [81] CMS Collaboration and M. Brice. “Images of the CMS Tracker Inner Bar-  
3071 rel”, November 2008, CMS-PHO-TRACKER-2008-002. Retrieved from <https://cds.cern.ch/record/1431467>.
- 3073 [82] M. Weber. “The CMS tracker”. 6th international conference on hyperons, charm  
3074 and beauty hadrons Chicago, June 28-July 3 2004.
- 3075 [83] CMS Collaboration. “Projected Performance of an Upgraded CMS Detector at  
3076 the LHC and HL-LHC: Contribution to the Snowmass Process”. Jul 26, 2013.  
3077 arXiv:1307.7135
- 3078 [84] L. Veillet. “End assembly of HB with EB rails and rotation inside SX ”,Jan-  
3079 uary 2002. CMS-PHO-HCAL-2002-002. Retrieved from <https://cds.cern.ch/record/42594>.
- 3081 [85] J. Puerta-Pelayo.“First DT+RPC chambers installation round in the UX5 cav-  
3082 ern.”. January 2007, CMS-PHO-OREACH-2007-001. Retrieved from <https://cds.cern.ch/record/1019185>
- 3084 [86] X. Cid Vidal and R. Cid Manzano. “CMS Global Muon Trigger” web site:  
3085 Taking a closer look at LHC. Retrieved from [https://www.lhc-closer.es/taking\\_a\\_closer\\_look\\_at\\_lhc/0.lhc\\_trigger](https://www.lhc-closer.es/taking_a_closer_look_at_lhc/0.lhc_trigger)

- 3087 [87] WLCG Project Office, “Documents & Reference - Tiers - Structure,”  
 3088 (2014). <http://wlcg.web.cern.ch/documents-reference> , last accessed on  
 3089 30.01.2018.
- 3090 [88] CMS Collaboration. “CMSSW Application Framework”, <https://twiki.cern.ch/twiki/bin/view/CMSPublic/WorkBookCMSSWFramework>,  
 3091 last accesses 06.02.2018
- 3093 [89] A. Buckleya, J. Butterworthb, S. Giesekec, et. al. “General-purpose event gen-  
 3094 erators for LHC physics”. arXiv:1101.2599v1 [hep-ph] 13 Jan 2011
- 3095 [90] A. Quadt. “Top Quark Physics at Hadron Colliders”. Advances in the Physics  
 3096 of Particles and Nuclei. Springer-Verlag Berlin Heidelberg. DOI: 10.1007/978-  
 3097 3-540-71060-8 (2007)
- 3098 [91] DurhamHep Data Project, “The Durham HepData Project - PDF Plotter.”  
 3099 <http://hepdata.cedar.ac.uk/pdf/pdf3.html> , last accessed on 02.02.2018.
- 3100 [92] G. Altarelli and G. Parisi. “ASYMPTOTIC FREEDOM IN PARTON LAN-  
 3101 GUAGE”, Nucl.Phys. B126:298 (1977).
- 3102 [93] Yu.L. Dokshitzer. Sov.Phys. JETP 46:641 (1977)
- 3103 [94] V.N. Gribov, L.N. Lipatov. “Deep inelastic e p scattering in perturbation the-  
 3104 ory”, Sov.J.Nucl.Phys. 15:438 (1972)
- 3105 [95] F. Maltoni, G. Ridolfi, and M. Ubiali, “b-initiated processes at the LHC: a  
 3106 reappraisal,” Journal of High Energy Physics, vol. 07, p. 022, (2012).
- 3107 [96] B. Andersson, G. Gustafson, G. Ingelman and T. Sjostrand, “Parton fragmen-  
 3108 tation and string dynamics”, Physics Reports, Vol. 97, No. 2-3, pp. 31-145,  
 3109 1983.

- 3110 [97] CMS Collaboration, “Event generator tunes obtained from underlying event  
3111 and multiparton scattering measurements;” European Physical Journal C, vol.  
3112 76, no. 3, p. 155, (2016).
- 3113 [98] J. Alwall et. al., “The automated computation of tree-level and next-to-leading  
3114 order differential cross sections, and their matching to parton shower simula-  
3115 tions,” Journal of High Energy Physics, vol. 07, p. 079, (2014).
- 3116 [99] T. Sjöstrand and P. Z. Skands, “Transverse-momentum-ordered showers and  
3117 interleaved multiple interactions,” European Physical Journal C, vol. 39, pp.  
3118 129–154, (2005).
- 3119 [100] S. Frixione, P. Nason, and C. Oleari, “Matching NLO QCD computations with  
3120 Parton Shower simulations: the POWHEG method,” Journal of High Energy  
3121 Physics, vol. 11, p. 070, (2007).
- 3122 [101] S. Agostinelli et al., “GEANT4: A Simulation toolkit,” Nuclear Instruments  
3123 and Methods in Physics, vol. A506, pp. 250–303, (2003).
- 3124 [102] J. Allison et.al., “Recent developments in Geant4”, Nuclear Instruments and  
3125 Methods in Physics Research A 835 (2016) 186-225.
- 3126 [103] CMS Collaboration “Full Simulation Offline Guide”, <https://twiki.cern.ch/twiki/bin/view/CMSPublic/SWGuideSimulation>, last accessed 04.02.2018
- 3128 [104] A. Giammanco. “The Fast Simulation of the CMS Experiment” J. Phys.: Conf.  
3129 Ser. 513 022012 (2014)
- 3130 [105] A.M. Sirunyan et. al. “Particle-flow reconstruction and global event description  
3131 with the CMS detector”, JINST 12 P10003 (2017) <https://doi.org/10.1088/1748-0221/12/10/P10003>.

- 3133 [106] The CMS Collaboration. “ Description and performance of track and pri-  
 3134       mary vertex reconstruction with the CMS tracker”. JINST 9 P10009 (2014).  
 3135       doi:10.1088/1748-0221/9/10/P10009
- 3136 [107] J. Incandela. “Status of the CMS SM Higgs Search” July 4, 2012. Pdf slides.  
 3137       Retrieved from [https://indico.cern.ch/event/197461/contributions/1478917/attachments/290954/406673/CMS\\_4July2012\\_Final.pdf](https://indico.cern.ch/event/197461/contributions/1478917/attachments/290954/406673/CMS_4July2012_Final.pdf)
- 3139 [108] P. Billoir and S. Qian, “Simultaneous pattern recognition and track fitting by  
 3140       the Kalman filtering method”, Nucl. Instrum. Meth. A 294 219. (1990).
- 3141 [109] W. Adam, R. Fruhwirth, A. Strandlie and T. Todorov, “Reconstruction of  
 3142       electrons with the Gaussian sum filter in the CMS tracker at LHC”, eConf  
 3143       C 0303241 (2003) TULT009 [physics/0306087].
- 3144 [110] K. Rose, “Deterministic Annealing for Clustering, Compression, Classification,  
 3145       Regression and related Optimisation Problems”, Proc. IEEE 86 (1998) 2210.
- 3146 [111] R. Fruhwirth, W. Waltenberger and P. Vanlaer, “ Adaptive Vertex Fitting”,  
 3147       CMS Note 2007-008 (2007).
- 3148 [112] CMS collaboration, “Performance of CMS muon reconstruction in pp collision  
 3149       events at  $\sqrt{s} = 7 \text{ TeV}$ ”, JINST 7 P10002 2012, [arXiv:1206.4071].
- 3150 [113] Coco, Victor and Delsart, Pierre-Antoine and Rojo-Chacon, Juan and Soyez,  
 3151       Gregory and Sander, Christian, “Jets and jet algorithms”, Proceedings,  
 3152       HERA and the LHC Workshop Series on the implications of HERA for LHC  
 3153       physics: 2006-2008, pag. 182-204. <http://inspirehep.net/record/866539/files/access.pdf>, (2009), doi:10.3204/DESY-PROC-2009-02/54

- 3155 [114] M. Cacciari, G. P. Salam, and G. Soyez, “The anti- $k_t$  jet clustering algorithm,”  
3156 Journal of High Energy Physics, vol. 04, p. 063, (2008).
- 3157 [115] S. Catani, Y. L. Dokshitzer, M. H. Seymour, and B. R. Webber, “Longitudi-  
3158 nally invariant  $K_t$  clustering algorithms for hadron hadron collisions”, Nuclear  
3159 Physics B, vol. 406, pp. 187–224, (1993).
- 3160 [116] Y.L. Dokshitzer, G.D. Leder, S.Moretti, and B.R. Webber, “Better jet clustering  
3161 algorithms,” Journal of High Energy Physics, vol. 08, p. 001, (1997).
- 3162 [117] B. Dorney. “Anatomy of a Jet in CMS”. Quantum Diaries. June  
3163 1st, 2011. Retrieved from [https://www.quantumdiaries.org/2011/06/01/  
3164 anatomy-of-a-jet-in-cms/](https://www.quantumdiaries.org/2011/06/01/anatomy-of-a-jet-in-cms/)
- 3165 [118] The CMS Collaboration.“Event Displays from the high-energy collisions at 7  
3166 TeV”, May 2010, CMS-PHO-EVENTS-2010-007, Retrieved from [https://cds.  
3167 cern.ch/record/1429614.](https://cds.cern.ch/record/1429614)
- 3168 [119] The CMS collaboration. “Determination of jet energy calibration and transverse  
3169 momentum resolution in CMS”. JINST 6 P11002 (2011). [http://dx.doi.org/  
3170 10.1088/1748-0221/6/11/P11002](http://dx.doi.org/10.1088/1748-0221/6/11/P11002)
- 3171 [120] The CMS Collaboration, “Introduction to Jet Energy Corrections at  
3172 CMS.”. <https://twiki.cern.ch/twiki/bin/view/CMS/IntroToJEC>, last ac-  
3173 cessed 10.02.2018.
- 3174 [121] CMS Collaboration Collaboration. “Identification of b quark jets at the CMS  
3175 Experiment in the LHC Run 2”. Tech. rep. CMS-PAS-BTV-15-001. Geneva:  
3176 CERN, (2016). [https://cds.cern.ch/record/2138504.](https://cds.cern.ch/record/2138504)

- 3177 [122] CMS Collaboration Collaboration. “Performance of missing energy reconstruction  
3178 in 13 TeV pp collision data using the CMS detector”. Tech. rep. CMS-PAS-  
3179 JME16-004. Geneva: CERN, 2016. <https://cds.cern.ch/record/2205284>.
- 3180 [123] CMS Collaboration, “New CMS results at Moriond (Electroweak) 2013”,  
3181 Retrieved from [http://cms.web.cern.ch/sites/cms.web.cern.ch/files/styles/large/public/field/image/HIG13004\\_Event01\\_0.png?itok=LAWZzPHR](http://cms.web.cern.ch/sites/cms.web.cern.ch/files/styles/large/public/field/image/HIG13004_Event01_0.png?itok=LAWZzPHR)
- 3184 [124] CMS Collaboration, “New CMS results at Moriond (Electroweak) 2013”,  
3185 Retrieved from [http://cms.web.cern.ch/sites/cms.web.cern.ch/files/styles/large/public/field/image/TOP12035\\_Event01.png?itok=uMdnSqzC](http://cms.web.cern.ch/sites/cms.web.cern.ch/files/styles/large/public/field/image/TOP12035_Event01.png?itok=uMdnSqzC)
- 3188 [125] K. Skovpen. “Event displays highlighting the main properties of heavy flavour  
3189 jets in the CMS Experiment”, Aug 2017, CMS-PHO-EVENTS-2017-006. Re-  
3190 trieval from <https://cds.cern.ch/record/2280025>.
- 3191 [126] G. Cowan. “Topics in statistical data analysis for high-energy physics”.  
3192 arXiv:1012.3589v1
- 3193 [127] A. Hoecker et al., “TMVA-Toolkit for multivariate data analysis”  
3194 arXiv:physics/0703039v5 (2009)
- 3195 [128] L. Lista. “Statistical Methods for Data Analysis in Particle Physics”, 2nd  
3196 ed. Springer International Publishing. (2017) <https://dx.doi.org/10.1007/978-3-319-62840-0>

- 3198 [129] I. Antcheva et al., “ROOT-A C++ framework for petabyte data storage, sta-  
 3199       tistical analysis and visualization ,” Computer Physics Communications, vol.  
 3200       182, no. 6, pp. 1384â€¢1385, (2011).
- 3201 [130] Y. Coadou. “Boosted decision trees”, ESIPAP, Archamps, 9 Febru-  
 3202       ary 2016. Lecture. Retrieved from [https://indico.cern.ch/event/472305/contributions/1982360/attachments/1224979/1792797/ESIPAP\\_MVA160208-BDT.pdf](https://indico.cern.ch/event/472305/contributions/1982360/attachments/1224979/1792797/ESIPAP_MVA160208-BDT.pdf)
- 3205 [131] J.H. Friedman. “Greedy function approximation: A gradient boosting ma-  
 3206       chine”. Ann. Statist. Volume 29, Number 5 (2001), 1189-1232. [https://projecteuclid.org/download/pdf\\_1/euclid-aos/1013203451](https://projecteuclid.org/download/pdf_1/euclid-aos/1013203451).
- 3208 [132] W. Verkerke and D. Kirkby, “The RooFit toolkit for data modeling,” arXiv  
 3209       preprint physics, (2003).
- 3210 [133] CMS Collaboration, “Documentation of the RooStats-based statistics  
 3211       tools for Higgs PAG”. <https://twiki.cern.ch/twiki/bin/view/CMS/SWGuideHiggsAnalysisCombinedLimit>, last accessed on 08.04.2018.
- 3213 [134] F. James, M. Roos, “MINUIT: Function minimization and error analysis”. Cern  
 3214       Computer Centre Program Library, Geneve Long Write-up No. D506, 1989
- 3215 [135] J. Neyman and E. S. Pearson, “On the problem of the most efficient tests of  
 3216       statistical hypotheses”. Springer-Verlag, (1992).
- 3217 [136] A.L. Read. “Modified frequentist analysis of search results (the  $CL_s$  method),”  
 3218       (2000). CERN-OPEN-2000-205.
- 3219 [137] C. Palmer. “Searches for a Light Higgs with CMS”, CMS-CR-2012-215. <https://cds.cern.ch/record/1560435>.

- 3221 [138] A. Wald, “Tests of statistical hypotheses concerning several parameters when  
3222 the number of observations is large”, Transactions of the American Mathematical  
3223 society, vol. 54, no. 3, pp. 426–482, (1943).
- 3224 [139] G. Cowan, K. Cranmer, E. Gross, and O. Vitells, “Asymptotic formulae for  
3225 likelihood-based tests of new physics”, European Physical Journal C, vol. 71,  
3226 p. 1554, (2011).
- 3227 [140] S. S. Wilks, “The Large-Sample Distribution of the Likelihood Ratio for Testing  
3228 Composite Hypotheses”, Annals of Mathematical Statistics, vol. 9, pp. 60–62,  
3229 (03, 1938).
- 3230 [141] B. Hespel, F. Maltoni, and E. Vryonidou, “Higgs and Z boson associated pro-  
3231 duction via gluon fusion in the SM and the 2HDM”, JHEP 06 (2015) 065,  
3232 [https://dx.doi.org/10.1007/JHEP06\(2015\)065](https://dx.doi.org/10.1007/JHEP06(2015)065), arXiv:1503.01656.
- 3233 [142] ATLAS Collaboration, “Measurements of Higgs boson pro-  
3234 duction and couplings in diboson final states with the AT-  
3235 LAS detector at the LHC”, Phys. Lett. B726 (2013) 88–119,  
3236 doi:10.1016/j.physletb.2014.05.011, 10.1016/j.physletb.2013.08.010,  
3237 arXiv:1307.1427. [Erratum: Phys. Lett.B734,406(2014)].
- 3238 [143] CMS Collaboration, “Search for the associated production of a Higgs boson  
3239 with a single top quark in proton-proton collisions at  $\sqrt{s} = 8$  TeV”, JHEP 06  
3240 (2016) 177, doi:10.1007/JHEP06(2016)177, arXiv:1509.08159.
- 3241 [144] B. Stieger, C. Jorda Lope et al., “Search for Associated Production of a Single  
3242 Top Quark and a Higgs Boson in Leptonic Channels”, CMS Analysis Note CMS  
3243 AN-14-140, 2014.

- 3244 [145] M. Peruzzi, C. Mueller, B. Stieger et al., “Search for ttH in multilepton final  
3245 states at  $\sqrt{s} = 13$  TeV”, CMS Analysis Note CMS AN-16-211, 2016.
- 3246 [146] CMS Collaboration, “Search for H to bbar in association with a single top quark  
3247 as a test of Higgs boson couplings at  $\sqrt{s} = 13$  TeV”, CMS Physics Analysis  
3248 Summary CMS-PAS-HIG-16-019, 2016.
- 3249 [147] CMS Collaboration, “Search for production of a Higgs boson and a single top  
3250 quark in multilepton final states in proton collisions at  $\sqrt{s} = 13$  TeV”, CMS  
3251 Physics Analysis Summary CMS-PAS-HIG-17-005, 2016.
- 3252 [148] CMS Collaboration, “PdmV2016Analysis,” (2016). <https://twiki.cern.ch/twiki/bin/viewauth/CMS/PdmV2016Analysis#DATA>, last accessed 11.04.2016.
- 3254 [149] M. Peruzzi, F. Romeo, B. Stieger et al., “Search for ttH in multilepton final1  
3255 states at  $\sqrt{s} = 13$  TeV”, CMS Analysis Note CMS AN-17-029, 2017.
- 3256 [150] B. Maier, “SingleTopHiggProduction13TeV”, February, 2016. <https://twiki.cern.ch/twiki/bin/viewauth/CMS/SingleTopHiggsGeneration13TeV>.
- 3258 [151] B. WG, “BtagRecommendation80XReReco”, February, 2017. <https://twiki.cern.ch/twiki/bin/view/CMS/BtagRecommendation80XReReco>.
- 3260 [152] CMS Collaboration, “Identification of b quark jets at the CMS Experiment  
3261 in the LHC Run 2”, CMS Physics Analysis Summary CMS-PAS-BTV-15-001,  
3262 2016.
- 3263 [153] CMS Collaboration, “Baseline muon selections for Run-II.” <https://twiki.cern.ch/twiki/bin/view/CMSPublic/SWGuideMuonIdRun2>, last accessed on  
3264 24.02.2018.

- 3266 [154] G. Petrucciani and C. Botta, “Two step prompt muon identification”, January,  
3267 2015. [https://indico.cern.ch/event/368007/contribution/2/material/  
3268 slides/0.pdf](https://indico.cern.ch/event/368007/contribution/2/material/slides/0.pdf).
- 3269 [155] H. Brun and C. Ochando, “Updated Results on MVA eID with 13 TeV samples”,  
3270 October, 2014. [https://indico.cern.ch/event/298249/contribution/3/  
3271 material/slides/0.pdf](https://indico.cern.ch/event/298249/contribution/3/material/slides/0.pdf).
- 3272 [156] K. Rehermann and B. Tweedie, “Efficient Identification of Boosted Semileptonic  
3273 Top Quarks at the LHC”, JHEP 03 (2011) 059, [https://dx.doi:10.1007/  
3274 JHEP03\(2011\)059](https://dx.doi.org/10.1007/JHEP03(2011)059), arXiv:1007.2221.
- 3275 [157] CMS Collaboration. “Tag and Probe”, [https://twiki.cern.ch/twiki/bin/  
3276 view/CMS/TagAndProbe](https://twiki.cern.ch/twiki/bin/view/CMS/TagAndProbe), last accessed on 02.03.2018.